THÈSE DE DOCTORAT

DE

UNIVERSIDADE ESTADUAL PAULISTA "JÚLIO DE MESQUITA FILHO",
FACULDADE DE CIÊNCIAS FARMACÊUTICAS

ET DE

L'UNIVERSITE PARIS-SACLAY, L'UNIVERSITE PARIS SUD

Programa de Pós-graduação em Ciências Farmacêuticas
ÉCOLE DOCTORALE N°569-Innovation Thérapeutique, du fondamental à l'appliqué

Doutorado em Ciências Farmacêuticas
Spécialité de doctorat : Pharmacotechnie et biopharmacie

Par

Mlle Eloísa Berbel Manaia

Zinc oxide (ZnO) based quantum dots for bioimaging applications of lipid nanocarriers

Conception de Quantum dots à base d'oxyde de zinc (ZnO) pour des applications en bio-imagerie de nanosystèmes lipidiques

Pontos Quânticos à base de óxido de zinco (ZnO) para aplicações em bioimagem de nanocarreadores lipídicos

Thèse présentée et soutenue à Araraquara, le 25 may 2016:
Diréctеurs de thèse:
Mme Claudie Bourgaux, Chargée de recherche, Université Paris-Sud, Directeur de thèse
Mme Leila Aparecida Chiavacci Favorin, Professeur, UNESP-FCFAR, Directeur de thèse
Mme Renata C. K. Kaminski, Professeur, UFS, Co-Directeur de thèse
Composition du Jury:
M. Celso V. Santilli, Professeur, UNESP-IQ, Examinateur
Mme. Amélie Bochot, Professeure, Université Paris-Sud, Président du Jury
M. Damien Boyer, Maître de Conférences, SIGMA Clermont, Rapporteur
Mme. Márcia Carvalho de Abreu Fantini, Professeure, USP-IF, Rapporteur

Araraquara – SP
2016

THÈSE DE DOCTORAT

DE

UNIVERSIDADE ESTADUAL PAULISTA "JÚLIO DE MESQUITA FILHO", FACULDADE DE CIÊNCIAS FARMACÊUTICAS

ET DE

L'UNIVERSITE PARIS-SACLAY, L'UNIVERSITE PARIS SUD

Programa de Pós-graduação em Ciências Farmacêuticas
ÉCOLE DOCTORALE N°569 - Innovation Thérapeutique, du fondamental à l'appliqué

Doutorado em Ciências Farmacêuticas
Spécialité de doctorat : Pharmacotechnie et biopharmacie

Par

Mlle Eloísa Berbel Manaia

Zinc oxide (ZnO) based quantum dots for bioimaging applications of lipid nanocarriers

Conception de Quantum dots à base d'oxyde de zinc (ZnO) pour des applications en bio-imagerie de nanosystèmes lipidiques

Pontos Quânticos à base de óxido de zinco (ZnO) para aplicações em bioimagem de nanocarreadores lipídicos

Directeurs de thèse:
Mme Claudie Bourgaux, Chargée de recherche, Université Paris-Sud, Directeur de thèse
Mme Leila Aparecida Chiavacci Favorin, Professeur, UNESP-FCFAR, Directeur de thèse
Mme Renata C. K. Kaminski, Professeur, UFS, Co-Directeur de thèse

Tese apresentada ao programa de Pós Graduação em Ciências Farmacêuticas, Área de Pesquisa e Desenvolvimento de Fármacos e Medicamentos, da Faculdade de Ciências Farmacêuticas, Universidade Estadual Paulista Júlio de Mesquita Filho, como parte dos requisitos para obtenção do título de Doutora em Ciências Farmacêuticas.

Araraquara – SP
2016

Ficha Catalográfica
Elaborada Pelo Serviço Técnico de Biblioteca e Documentação
Faculdade de Ciências Farmacêuticas
UNESP – Campus de Araraquara

M266p Manaia, Eloísa Berbel
Pontos Quânticos à base de óxido de zinco (ZnO) para aplicações em bioimagem de nanocarreadores lipídicos / Eloísa Berbel Manaia. – Araraquara, 2016
175 f.

Tese (Doutorado) – Universidade Estadual Paulista. "Júlio de Mesquita Filho". Faculdade de Ciências Farmacêuticas. Programa de Pós Graduação em Ciências Farmacêuticas

Orientador: Leila Aparecida Chiavacci Favorin
Orientador no exterior: Claudie Bourgaux
Coorientador: Renata Cristina Kiatkoski Kaminski

1. ZnO. 2. Pontos quânticos. 3. Bioimagem. 4. Nanocarreadores lipídicos. I. Favorin, Leila Aparecida Chiavacci, orient. II. Bourgaux, Claudie, orient. III. Kaminski, Renata Cristina Kiatkoski, coorient. IV. Título.

CAPES: 40300005

ELOÍSA BERBEL MANAIA

PONTOS QUÂNTICOS À BASE DE ÓXIDO DE ZINCO (ZnO) PARA APLICAÇÕES EM BIOIMAGEM DE NANOCARREADORES LIPÍDICOS

Tese de Doutorado apresentada à Faculdade de Ciências Farmacêuticas da Universidade Estadual Paulista – UNESP, Campus de Araraquara como requisito para a obtenção do título de Doutor em Ciências Farmacêuticas

Araraquara, 25 de maio de 2016.

BANCA EXAMINADORA

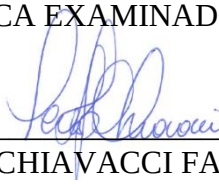

LEILA APARECIDA CHIAVACCI FAVORIN (Orientadora)

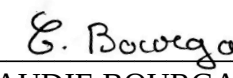

CLAUDIE BOURGAUX

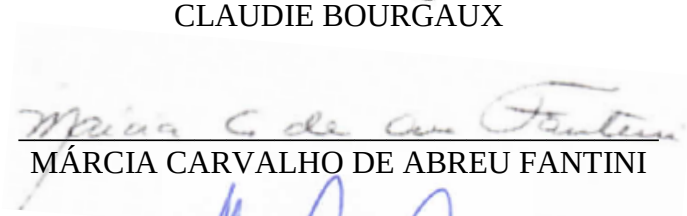

MÁRCIA CARVALHO DE ABREU FANTINI

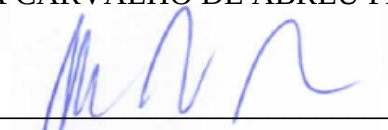

CELSO VALENTIM SANTILLI

DAMIEN BOYER

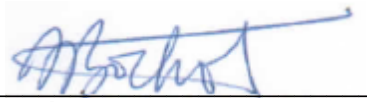

AMÉLIE BOCHOT

Title : Zinc oxide (ZnO) based quantum dots for bioimaging applications of lipid nanocarriers

Keywords : ZnO, Quantum Dots, bioimaing, and lipid nanocarriers

Abstract: Theranostic systems consist of a single device containing therapeutics and diagnosis agents and have increased attention in the actual researches because these devices can improve the disease therapy such as cancer, decrease the side effects and the toxicity in no-cancer cells and permit monitoring the treatment. The aim of this work was to develop theranostic systems consisted of lipid based nanocarriers containing ZnO based quantum dots (QDs) as cancer cell luminescent guides, and a model drug for cancer therapy. Firstly, it was study the synthesis of ZnO/ZnS QDs aiming to achieve improved luminescent properties. In this step, X-Rays Absorption Spectroscopy, together with other usual characterization techniques, could identify the synthesis condition in which core-shell structures were formed. Nevertheless, the emission of ZnO/ZnS QDs in the visible range was not promising. Therefore, Mg-doped ZnO QDs were synthesized and their luminescence went through a maximum for a 20 mol% nominal concentration of Mg^{2+} ions in the reaction medium. $Zn_{0.8}Mg_{0.2}O$ QDs presented quantum yield (QY) six times higher (QY = 64%) than undoped ones (QY = 10%). ZnO and $Zn_{0.8}Mg_{0.2}O$ QDs capped by oleic acid (OA) were synthesized and formed stable colloidal dispersions in chloroform and toluene. The QY of OA-$Zn_{0.8}Mg_{0.2}O$ was about 4 times (around 40%) higher than that of the OA-ZnO QDs. $Zn_{0.8}Mg_{0.2}O$ QDs and OA-$Zn_{0.8}Mg_{0.2}O$ QDs could be incorporated into lipid based nanocarriers of average hydrodynamic diameter around 100 – 220 nm. The luminescent solid lipid nanoparticles (SLN) were stable in different media at 37°C during 3 hours. The fluorescence association study showed enhanced emission of the J774 macrophage-like cells treated with 2 mg/mL of luminescent SLN during 50 min, suggesting partial internalization of the nanoparticles into the macrophages. The internalization study using the video-microscope and fluorescence microscope were not successfully, once the equipment condition used could not overcome the cells auto-fluorescence phenomena.

Titre : Conception de Quantum dots à base d'oxyde de zinc (ZnO) pour des applications en bio-imagerie de nanosystèmes lipidiques

Mots clés : ZnO, Quantum Dots, bioimagerie et nanosystèmes lipidiques

Résumé : Les systèmes théranostiques sont constitués d'un dispositif unique contenant des agents thérapeutiques et diagnostiques et attirent actuellement l'attention pour améliorer le traitement de maladies telles que le cancer ; ils pourraient réduire les effets secondaires (e.g. la toxicité pour les cellules non-cancéreuses) et permettre le suivi du traitement. Les quantum dots (QDs) sont utilisés comme agents d'imagerie *in vitro* et *in vivo*. Parmi ceux-ci, ZnO est moins cher, plus biocompatible et moins toxique que ceux utilisés couramment (SeCd, PbS, etc.). Le but de notre étude était de développer des systèmes théranostiques constitués de nanoparticules lipidiques contenant des QDs à base de ZnO comme agent luminescent, l'objectif final étant d'incorporer un principe actif pour le traitement du cancer. Nous avons d'abord étudié la synthèse de QDs de ZnO/ZnS (structure coeur/coquille) par le procédé sol-gel, afin d'améliorer les propriétés de luminescence de ZnO grâce à la passivation de la surface par le ZnS. Pour cela, deux voies de synthèse ont été explorées: le thioacétamide (TAA), utilisé comme source d'ions soufre, a été ajouté à (i) la solution de précurseur de l'acétate de zinc, et (ii) la suspension colloïdale de ZnO. Différentes concentrations de thioacétamide (TAA) ont été utilisées (1,5, 5 et 50 mM). Pour distinguer la formation de la structure coeur/coquille (ZnO / ZnS) d'un simple melange de particules de ZnO et ZnS, les échantillons ont été caractérisés par plusieurs techniques (DRX, XAS, SAXS, UV-vis, pH, HRTEM et PL). Parmi celles-ci, l'absorption des rayons X (XAS) a été essentielle pour montrer que seule la réaction effectuée à partir de la suspension colloïdale de ZnO contenant 5 mm de TAA donnait lieu à la structure ZnO/ZnS. Cependant, les QDs de ZnO/ZnS n'ont pas montré une intensité de l'émission dans le visible plus grande que celle des QDs de ZnO. Les QDs de ZnO ont donc été dopés pour générer des électrons ou des trous supplémentaires dans leur structure, entraînant des changements de leurs propriétés de luminescence. Différentes quantités de Mg (2,5, 5, 10 et 20% en mole) ont été ajoutées lors de la synthèse du ZnO par la voie sol-gel, afin d'obtenir des particules ayant une luminescence plus forte dans le visible. Plusieurs techniques (XRD, HRTEM, ICP-MS, SAXS, UV-Vis et PL) ont été utilisées pour déterminer les caractéristiques physico-chimiques des différents $Zn_{1-x}Mg_xO$ QDs obtenus. Il a été observé une diminution de la taille des particules avec l'augmentation de la concentration de Mg. Lors de l'ajout d'une concentration nominale de Mg^{2+} dans le milieu réactionnel de 20% molaire ($Zn_{0.8}Mg_{0.2}O$), le rendement quantique (QY) était six fois plus élevé (QY= 64%) que celui de la suspension de ZnO non dopé (QY= 10%). Pour utiliser les QDs dans un environnement biologique tout en conservant leurs propriétés de photoluminescence, leur surface est généralement modifiée par des substances hydrophiles pour les rendre stables dans l'eau, ou des substances hydrophobes pour permettre leur intégration dans des systèmes/nanoparticules à base de lipides ou de polymères. La surface des QDs de ZnO et $Zn_{0.8}Mg_{0.2}O$ a été recouverte par de l'acide oléique (AO) ; les QDs ainsi modifiés forment une dispersion colloïdale stable dans le chloroforme et le toluène. La spectroscopie Raman a confirmé la présence d'acide oleique à la surface des QDs. Le rendement quantique des QDs de $Zn_{0.8}Mg_{0.2}O$ recouverts d'AO était environ 4 fois plus élevé (QR = 40%) que celui des QDs de ZnO recouverts d'AO. Enfin, les QDs de $Zn_{0.8}Mg_{0.2}O$, recouverts ou non d'AO, ont été incorporés dans des nanoparticules lipidiques pour une utilisation ultérieure dans des études d'internalisation cellulaire. Des formulation à base de DPPC, DSPE-Peg et des nanoparticules lipidiques solides (SLN) contenant des QDs ont été préparées avec une taille hydrodynamique variant entre 100 et 220 nm. Les formulations à base de DSPE-Peg ont montré une intensité d'émission plus élevée dans le visible, comparé aux SLNs. L'étude de stabilité réalisée avec des SLNs luminescentes dans différents milieux (eau, PBS, PBS avec du Mg et du Ca, RPMI avec du sérum à 10%) à 37°C pendant 3 heures a montré que la taille ne changeait pas

fortement au cours du temps. Dans cette étude, la taille maximale était de l'ordre de 300 nm, montrant que même en présence de protéines, il ne se forme pas de gros agrégats. Trois méthodes ont été utilisées pour l'étude de l'internalisation cellulaire dans des macrophages J774. Lorsque la longueur d'onde d'excitation correspond à celle des QDs, les mesures d'intensité de fluorescence sur les suspensions de cellules ont montré une faible augmentation de l'intensité de l'émission visible pour les cellules incubées avec 2 mg/mL de SLNs luminescentes pendant 50 minutes, en comparaison avec les cellules témoins. Ce résultat suggère une internalisation partielle des SLNs dans les macrophages. Malheureusement, ces résultats n'ont pas pu être confirmés par vidéo-microscopie et microscopie de fluorescence sur les cellules parce que les conditions expérimentales (longueurs d'onde d'excitation et d'émission possibles) ne permettaient pas d'observer un signal supérieur à celui de l'auto-fluorescence des cellules.

En conclusion, cette étude a permis d'optimiser la composition et la synthèse par voie sol-gel de QDs à base de ZnO pour les rendre aptes à être utilisés comme sondes luminescentes dans des nanoparticules lipidiques. La relation entre leur structure et leurs propriétés de luminescence a été étudiée; les QDs dopés $Zn_{0.8}Mg_{0.2}O$, qui ont le rendement quantique le plus élevé, ont pu être incorporés dans des nanoparticules lipidiques pouvant contenir des agents thérapeutiques.

Título : Pontos Quânticos à base de óxido de zinco (ZnO) para aplicações em bioimagem de nanocarreadores lipídicos

Palavras-chaves : ZnO, Pontos Quânticos, bioimagem e nanocarreadores lipídicos

Resumo : Sistemas teranósticos consistem em um único dispositivo contendo agentes terapêuticos e de diagnóstico e tem ganhado atenção nas pesquisas atuais por melhorar o tratamento de doenças como câncer, podendo diminuir efeitos colaterais, diminuir toxicidade em células não cancerígenas e permitir o monitoramento do tratamento. Os pontos quânticos (PQs) vem sendo usado como agentes de imagem para realizar o monitoramento ótico em investigações *in vivo* e *in vitro*. Dentre eles, o ZnO tem se destacado por ser mais barato, mais biocompatível e menos tóxico do que os utilizados comumente (SeCd, PbS, etc). O objetivo deste trabalho foi desenvolver sistemas teranósticos constituídos de nanocarreadores à base de lipídeos contendo pontos quânticos a base de ZnO, como guias luminescentes de células cancerígenas, e um fármaco modelo para tratamento do câncer. Primeiramente, foi estudada a síntese de pontos quânticos de ZnO/ZnS (estrutura de casca/caroço) pelo processo sol-gel, a fim de melhorar as propriedades luminescentes do ZnO através da passivação da sua superfície provocada pelo ZnS. Para isto, as reações de síntese tiveram como base (i) a solução precursora de acetato de Zinco e (ii) a suspensão coloidal de ZnO. Além disso, foram variadas as concentrações de tioacetamida (TAA) (1.5, 5 e 50mM), usada como fonte de íons de enxofre. Para diferenciar a formação de estruturas casca/caroço (ZnO/ZnS) e não uma mistura de partículas de ZnO e ZnS, várias técnicas foram utilizadas para caracterizar as amostras (DRX, XAS, SAXS, UV-vis, pH, HRTEM e PL). Dentre elas, XAS foi crucial para identificar que somente a reação realizada a partir da suspensão coloidal de ZnO com TAA 5mM deu origem à estrutura de ZnO/ZnS do tipo casca/caroço. Entretanto, os PQs de ZnO/ZnS não apresentaram maior intensidade da emissão na região do visível quando comparado ao ZnO. Portanto, PQs de ZnO foram dopados com Mg para gerar elétrons ou buracos extras na sua estrutura levando a mudanças em suas propriedades luminescentes. Diferentes quantidades de Mg (2.5, 5, 10 e 20 % em mol) foram usadas durante a síntese de ZnO pelo processo sol-gel para poder obter, assim, partículas com maior luminescência na região do visível. DRX, HRTEM, ICP-MS, SAXS, UV-Vis e PL foram usadas a fim de avaliar as características físico-químicas dos diferentes $Zn_{1-x}Mg_xO$ obtidos. Observou-se a diminuição do tamanho das partículas com o aumento da concentração de Mg. Quando se utilizou 20 % em mols em concentração nominal de íons Mg^{2+} no meio reacional ($Zn_{0.8}Mg_{0.2}O$), o rendimento quântico (RQ) foi seis vezes maior (RQ = 64%) do que a suspensão de ZnO não dopado (RQ = 10%). Para utilizar os PQs em meio biológico mantendo sua propriedade fotoluminescente, sua superfície normalmente é modificada com substâncias hidrofílicas para torná-los estáveis em água, ou com substâncias hidrofóbicas para permitir sua incorporação em sistemas/carreadores à base de lipídeos ou polímeros. Os PQs de ZnO e de $Zn_{0.8}Mg_{0.2}O$ foram revestidos com ácido oleico (AO) formando uma dispersão coloidal estável em clorofórmio e tolueno. A espectroscopia RAMAN permitiu confirmar a modificação da superfície dos PQs pela presença dos grupamentos característicos do AO nessas amostras. O RQ do $Zn_{0.8}Mg_{0.2}O$ revestido com AO foi em torno de 4 vezes maior (RQ = 40%) que o RQ de ZnO revestido com AO. Por fim, os PQs de $Zn_{0.8}Mg_{0.2}O$ revestidos e não-revestidos com AO foram incorporados em nanocarreadores lipídicos para serem utilizados posteriormente nos estudos de internalização celular. Formulações à base de DPPC, DSPE-Peg e nanopartículas lipídicas sólidas (NLS) contendo PQs foram obtidos com diâmetro hidrodinâmico entre 100-220 nm. A formulação preparada com DSPE-Peg apresentou maior intensidade de emissão no visível quando comparadas com as NLS. O estudo de estabilidade realizado com as NLS luminescentes em diferentes meios (água, PBS, PBS com Mg e Ca, RPMI com soro à 10%) à 37°C durante 3 horas, mostrou que o tamanho delas não variou bruscamente no tempo analisado. Nesse estudo o tamanho máximo

encontrado foi de 300 nm, mostrando que na presença de proteínas, elas não formam grandes agregados que podem favorecer a fagocitose pelo sistema mononuclear. Foram utilizados três métodos para realizar o estudo de internalização celular. O estudo da associação de fluorescência mostrou aumento da intensidade de emissão no visível de células de macrófagos J774 tratadas com 2 mg/mL de NLS luminescente durante 50 min, comparado com as células sem tratamento. Este resultado sugere internalização parcial das NLS nos macrófagos. A vídeo-microscopia e a microscopia de fluorescência não tiveram sucesso para realizar este estudo, uma vez que as condições experimentais utilizadas não puderam superar o efeito de auto-fluorescência das células. Para concluir, a síntese de PQs à base de ZnO pelo processo sol-gel possibilitou estudar as estruturas e propriedades luminescentes destes, permitindo otimizar sua síntese para adequá-los para uso como guias luminescentes. Desta forma, $Zn_{0.8}Mg_{0.2}O$ com alto rendimento quântico foi incorporado em nanocarreadores lipídicos e sua aplicação como guia luminescente foi evidenciada através do teste de associação de fluorescência.

Acknowledgements

Firstly, I thank **God** for always guide me.

Bruno by his company, motivation, knowledge, help, good humor, love and affection.

To my family, especially my parents, **Cida** and **Osvaldo**, my sisters **Juliana** and **Mariele**, my brother in law **Eduardo** and my nieces **Sarah**, **Luana** and **Rafaela** by their love and encouragement.

I thank my supervisors Prof. Dr. **Leila Aparecida Chiavacci Favorin** and Dr. **Claudie Bourgaux** and my co-advisor Dr. **Renata C. K. Kaminski** for their dedication, supervision, motivation, and patience.

My friends of **CMAF laboratory Marina**, **Bruna Lallo**, **Bruna Chiari**, **Neima**, **Gabriela**, **João**, **Mariluci**, **Flavia**, **Aline** and **Natalia** for their help, support, and also **Mariana Sato, Jéssica and Alice**.

The friendships of **Institut GaIien Andreza**, **Any**, **André**, **Júnior**, **Thais**, **Benedict**, **Cristina**, **Leila**, **Chau**, **Boris**, **Frank**, **Elodie, Sarah** and also Dr. **François-Xavier Legrand**, Dr. **Vincent Faivre**, **Jean-Jacques**, **David**, Dr. **Angélina Angelova**, **Fany**, Dr. **Gillian Barratt**, **Claire**, **Alice**, **Fatima**, Dr. **Christine Vauthier**, Dr. **Didier Desmaele** and Dr. **Sylviane Lesieur**.

The Brazilian friends that I met in France **Sara Bachner**, **Rodrigo** (Dido), **Dani, Kellen** and all those that were visit me when I was in Paris **Má**, **Sarah**, **Cidinha**, **Patty**, **Marina**, **Roberto**, **Milena**, **Tia Rô**, **Carol**, **André** (Presidente), Mrs **Sonia**, Mr **Antônio, Gisele**, **Cavalim**,**Tia Eliana**, **Tia Eloísa**, **Daniel** and those that we met by chance **Marcel, Natália**, **Milana** and **Gledson.**

The Brazilian neighbors of 1, Rue Gustave Geffroy, **Sarah** and **Helena**, lovely women.

The **Chemical Institute** of UNESP/Araraquara, especially teachers Dr. **Celso V. Santilli**, Dr. **Sandra Helena Pulcineli**, Dr. **Peter Hammer**, the colleagues **Nalva**, **Aline**, **Bianca**, **Marlon, Rodrigo, Rodolfo** and specially **Marina** and **Amélie** for their supporting during HRTEM and EXAFS understandings, respectively, and the laboratory technicians **Sérgio, Rafael** and **Ricardo**.

The synchrotron **SOLEIL** for providing beamtime at the SAMBA beamline (project number: 20131299), Dr. **Valérie Briois** for her support during EXAFS experiments and all her knowledge, discussions, and help during my thesis; SWING beamline (project number: 20131299**) J. Perez**, **Y. Liatimi** and **Pierre Roblin** for their support during SAXS experiments; **Stéphanie Blanchandin** and **Karine Chaouchi** for WAXS measurements and their kindly support at the Chemistry Laboratory of SOLEIL.

The **LNLS** (project number: 14321) for SAXS measurements, Dr. **Florian Meneau** for his support during SAXS understanding, motivation and friendship, **LNNano** for HRTEM measurements.

The **Service of electronic microscopy** of the University Pierre et Marie Curie for HRTEM measurements.

The secretaries of **Post-Graduation Technique Section of Faculty of Pharmaceutical Sciences**, **Claudia**, **Daniela**, **Joyce**, **Flávia** and the secretary of **Doctoral School "Innovation thérapeutique du fondamental à l'appliqué"** Mme **Lucie Landry**.

FAPESP (Process number: 2012/07570-4 and BEPE process number: 2015/01198-4) and **PADC/FCF-UNESP** for the financial support.

My thesis was conducted at the Institut Galien of University Paris - Sud during one year supported by the International Cooperation Program **CAPES/COFECUB** (ME 767-13), financed by CAPES – Brazilian Federal Agency for Support and Evaluation of Graduate Education within the Ministry of Education of Brazil.

To all those who directly or indirectly contributed to the realization of this thesis, thank you very much.

List of Figures

List of tables

List of abbreviations

Ab: antibody

AET: aminoethanethiol-HCl

AFM : atomic force microscopy

CMC: critical micellar concentration

Cryo-TEM: cryogenic transmission electron microscopy

CT : Computed Tomography

DPPC: 1,2-dipalmitoyl-sn-glycero-3-phosphocholine

DSPE-Peg:1,2-distearoyl-sn-glycero-3-phosphoethanolamine-N-[amino(polyethylene glycol)-2000] ammonium salt

EGFR: epidermal growth factor receptor

EPR: enhanced permeation and retention

EXAFS: extended X-ray absorption fine structure

FT: Fourier transform

FWHM: full width at half maximum

GUV: giant unilamellar vesicles

HA: hyaluronic acid

HepG2: human liver carcinoma cells

HDS: hydroxy double salts

HRTEM: High Resolution Transmission Electron Microsocpy

ICP – MS: Inductively Coupled Plasma Mass Spectrometry

J774: murine phagocytic macrophage-like cell line

LCF: Linear Combination Fittings

LNC: lipid nanocapsules

LUV: large unilamellar vesicles

MHDA: 16-mercaptohexadecanoic acid

MLV: multilamellar vesicles

MOF: metal organic frameworks

MPS: mononuclear phagocyte system

MRI: magnetic resonance imaging

MUA: 11-mercaptoundecanoic acid

NCs: nanocarriers

NIR: near-infrared

NPs: Nanoparticles

OA: oleic acid

OA-ZnO QDs: ZnO quantum dots with oleic acid as surface modifier

OA- $Zn_{1-x}Mg_xO$ QDs: Mg-doped ZnO quantum dots with oleic acid as surface modifier

PBS: Phosphate-buffered saline

PEG: polyethylene glycol

PL: Photoluminescence

PLE : excitation photoluminescence

PREC: precursor

QDs: quantum dots

QD-LN: SLNs containing $Zn_{0.8}Mg_{0.2}O$ QDs

QELS: Quasi Elastic Ligth Scattering

QY: Quantum Yield

RES: reticuloendothelial system

RF: red phenol

Rg: radius of gyration

ROS: reactive oxygen species

RPMI: Roswell Park Memorial Institute, medium of cell culture

SAXS: Small Angle X-Ray Scattering

SLN: solid lipid nanoparticles

SR: synchrotron radiation

SUSP: Suspension

SUV: Small unilamellar vesicles

TAA: Thioacetamide

THF: tetrahydrofuran

UV-vis: ultravioleta-visible

XANES: X-ray absorption near-edge structure

XAS: X-Ray Absorptions Spectroscopy

XDR: X-Ray Diffraction

XES: X-ray emission spectroscopy

XPS: X-ray Photoelectron Spectroscopy

ZnO Susp: ZnO colloidal suspensions

$Zn_{1-x}Mg_xO$ QDs: Mg-doped ZnO quantum dots with x amount of Mg

CONTENT

CHAPTER VI – Final conclusions and Perspectives

INTRODUCTION

Introduction

The use of nanotechnology in the biomedical field is increasing due to the advantages of drug nanocarriers. For instance, nanoparticles loaded with drugs may improve the solubility and bioavailability of poorly soluble drugs, protect them from degradation, cross biological barriers, decrease drug toxicity against healthy cells by delivering the drug in target tissues. The drug loading capacity, biodistribution, pharmacokinetics and toxicity of nanoparticles depend on their composition, size, structure and surface properties. For example, nanoparticle surface modification by hydrophilic polymers or specific ligands has been explored to promote longer circulation time or to guide them to target tissue. Lipid based nanocarriers, such as liposomes, phospholid micelles and solid lipid nanoparticles, are widely imvestigated due to their biocompatibility and biodegradability.

Theranostic devices arise from the combination of therapeutic and imaging agents in a unique nanoparticle, in order to follow the nanoparticle biodistribution and to evaluate the disease evolution.

Numerous imaging agents can be used in theranostic nanoparticles, depending on the type of image: radionuclides for nuclear imaging, heavy elements for computed tomography, superparamagnetic metal oxides for magnetic resonance imaging and fluorescent dyes or quantum dots (QDs) for optical imaging. QDs have gained place because they present original properties, such as a large absorption spectrum, a narrow emission band and bright signal. Cadmiun (Cd) based QDs were the first and most explored QDs for bioimaging application; however, they present high toxicity as well as other heavy metal based QDs. To minimize the toxic effects, core-shell QDs and surface capped QDs were developed in order to prevent the release of heavy ions in the biological media. Moreover, coating QDs with a higher band gap semiconductor can eliminate surface defects, which minimizes the photoblinking effect, and QDs surface modification with organic molecules can provide colloidal stability in aqueous media or non-polar solvents. Nevertheless, nontoxic QDs, such as ZnO or ZnS QDs, began to be used due to their biocompatility and promising photoluminescent properties.

The photoluminescence of ZnO QDs is directly related to their size and surface defects. Because of these important characteristics, the synthesis route strongly interferes with the final properties of the material. Since 1980, researchers have studied the quantum confinement and luminescent properties of ZnO QDs synthesized using the sol-gel route,

which allows obtaining nanoparticles with size varying from 2 to 6 nm, displaying surface defects such as oxygen vacancies. However, the visible luminescence of ZnO QDs vanishes in the presence of water because they tend to aggregate, precipitate and their luminescent centers are destroyed. For this reason, the challenge is to keep their visible photoluminescence emission in biological media to allow their use in bioimaging.

The aim of this work was to develop ZnO based QDs with strong visible emission, stable in biological media or organic solvent that allow their later incorporation in lipid based nanocarriers, in order to achieve theranostic devices.

In the first part (Chapter III), ZnO/ZnS core-shell QDs were developed using a low-temperature sol-gel route. The formation of ZnS shell around the ZnO core could provide UV photoluminescence stability and prevent photoblinking and photobleaching undesirable effects. Numerous techniques, such as Small Angle X-Ray Scattering (SAXS), UV-Vis Spectroscopy, pH, X-Ray Absorption (XAS), High Resolution Transmission Electron Microscopy (HRTEM)), X-Ray Diffraction (XRD) were used to monitor the reactions and characterize the materials obtained. When characterized by Photoluminescence Spectroscopy, ZnO/ZnS core-shell QDs did not present an increase in the emission intensity in the visible range.

Because of ZnO/ZnS structures did not demonstrate desirable optical properties, the optimization of ZnO QDs for imaging was performed differently. Chapter IV described ZnO QDs doped with Mg^{2+} ions with enhanced luminescence emission. Specifically, we have shown that the maximum quantum yield (QY = 64%) for Mg precursor concentration of 20 mol% was six times higher than for undoped ZnO QDs (QY = 10%). Mg-doped ZnO QDs were characterized in order to establish a relationship between the composition and structure of the QDs and their luminescent properties.

The surface modification of the QDs was then performed using oleic acid (OA) to hinder their aggregation and to provide them colloidal stability in non-polar environment. Still in the Chapter IV, we could show that Mg-doped ZnO QDs capped by OA formed stable colloidal suspensions in toluene and chloroform, while preserving their photoluminescence with QY around 40 %, promising for bioimaging.

In the Chapter V, the OA surface modified Mg-doped QDs were incorporated in lipid based nanocarriers in order to analyze the nanoparticles structure, stability and luminescence. At low QD concentrations, QDs were embedded within 1,2-dipalmitoyl-sn-glycero-3-phosphocholine (DPPC) bilayers, without perturbing their stacking. 1,2-distearoyl-sn-glycero-

3-phosphoethanolamine-N-[amino(polyethylene glycol)-2000] ammonium salt (DSPE-Peg) /QDs formulations formed aggregates displaying a close-packed, layered structure, of QDs likely stabilized by a layer of DSPE-Peg. Solid lipid nanoparticles (SLN) loaded with QDs demonstrated good stability in biological media as shown by the absence of large aggregates. Cell internalization studies using luminescent SLN were performed using a macrophage-like cell line. However, cell autofluorescence prevented to unambiguously evidence the internalization of SLN into the cells.

CHAPTER I
Bibliography

Chapter I - Bibliography

I.1. Nanomedicine as a theranostic system

Nanomedicine consists of the use of nanoscale (1-1000 nm) strategies to diagnose and treat diseases at cellular and molecular level. New devices and drug delivery systems with various sizes, architectures and surface properties, made from diverse materials, have been developed to overcome the challenges of achieving efficient detection and treatment of serious diseases, such as cancer. Drug nanocarriers are based on lipids (micelles, liposomes, solid lipid nanoparticles, lipid nanocapsules, nanoemulsions), polymers (micelles, nanospheres or nanocapsules, dendrimers), proteins, oligosaccharides (cyclodextrins) as well as on inorganic materials (carbon nanotubes, gold, iron oxide, silica nanoparticles (NPs), metal organic frameworks (MOFs) and quantum dots) (DE JONG and BORM, 2008; MURA, NICOLAS and COUVREUR, 2013; FRANK et al., 2014). Figure I.1 shows schematically the structure of some nanocarriers used actually. Usually, the drug is encapsulated into polymeric/lipid nanoparticles and cyclodextrins nanocarriers (NCs), chemically linked to dendrimers and adsorbed in the carbon nanotubes and on inorganic nanoparticles, or chemically linked. Thus, drug fate depends on its carrier (LAMPRECHT, 2015). One limitation of these nanocarriers is their rather low drug-loading capacity. Of note, P. Couvreur and co-workers have recently developed an original concept (i.e. the “squalenoylation”) consisting in the chemical linkage of squalene (or even other terpenic moieties) to small drug molecules. Remarkably, squalenoylation led to prodrugs having the property to self-assemble in aqueous solution as stable monodisperse NPs (100-300 nm), in which drug loading could reach about 50% of the carrier weight. In most cases, nanoassemblies of the obtained bioconjugates displayed improved pharmaceutical profile compared to the parent drug (DESMAËLE, GREF and COUVREUR, 2012; MURA, NICOLAS and COUVREUR, 2013; FRANK et al., 2014).

Figure I.1. Schematic structures of the nanocarriers: (a) Polymeric nanoparticles, (b) Liposomes, (c) Lipid nanoparticles and nanoemulsions, (d) Micelles, (e) Cyclodextrins, (f) Dendrimers, (g) Carbon nanotubes, (h) Gold nanoparticles.

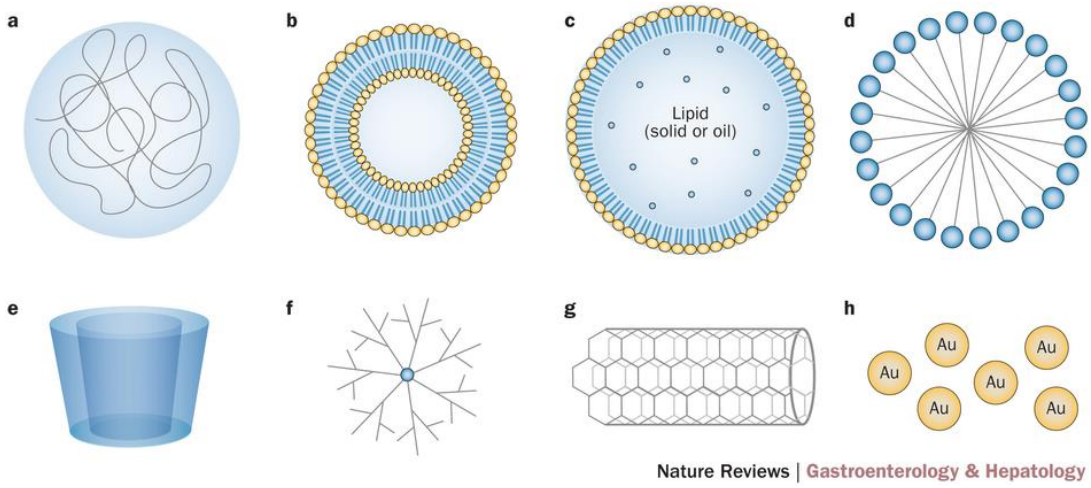

Figure from the article "Nanomedicines in gastroenterology and hepatology" (LAMPRECHT, 2015).

Nanocarriers impact the biodistribution and pharmacokinetics of drugs by modifying interactions with the biological environment. Therefore, they can improve the efficacy and reduce toxic side effects of drugs, increasing their therapeutic index. Moreover, nanocarriers can facilitate co-delivery of drugs to target sites with a controlled drug ratio, which may prove more effective than single drug therapy, for instance in case of drug resistance (BHASKAR et al., 2010).

Nanocarriers can improve poor water solubility of hydrophobic drugs which limits their bioavailability. They can protect therapeutic agents from enzymatic degradation or rapid excretion. They can be designed to allow a sustained and/or controlled drug release. Stimuli-responsive systems are sensitive to specific endogenous stimuli (pH, glutathione concentration, enzyme level) or external stimuli (temperature, light, ultrasound, magnetic or electric field) (MURA, NICOLAS and COUVREUR, 2013; FRANK et al., 2014). Finally, they can offer possibilities to target specific sites of action when their surface is functionalized with ligands.

Regarding cancer therapy via the intravenous route, nanocarriers can take advantage of the so-called enhanced permeation and retention effect (EPR): the leaky vasculature of some solid tumors, in combination with a weak lymphatic drainage, may induce a selective accumulation of nanoparticles in the target tissue, following extravasation from the vessels

(MATSUMURA and MAEDA, 1986; MAEDA, 2010). Drug nanocarriers displaying size above renal filtration size (6-10 nm) and up to 250 nm have shown extravasation and accumulation in the tumor interstitium, increasing their residence time, and cellular uptake (TORCHILIN, 2005; ACHARYA and SAHOO, 2011; FRANK et al., 2014). However, in the blood stream, the adsorption of the plasma proteins (opsonization) results in recognition of the nanoparticles by the macrophages of the reticuloendothelial system (RES) and rapid clearance. Opsonization depends on the size, shape and surface properties (charge, hydrophilicity) of the nanoparticles (FATTAL and TSAPIS, 2014). Surface modification with either natural polymers such as polysaccharides or synthetic polymers such as polyethylene glycol (PEG) reduces opsonization (NICOLAS et al., 2013). Indeed, the steric repulsion induced by the hydrophilic polymeric corona hinders protein binding, resulting in prolonged circulation and, thus, increased passive accumulation in tumors of the nanocarriers, due to the EPR effect (OWENS III and PEPPAS, 2006; RABANEL et al., 2012; ZHANG, HUANG e LI, 2014). Figure I.2 illustrates the EPR effect of drug-loaded nanocarriers (macromolecule) in a malignant tissue.

Figure I.2. Illustration of the EPR effect of drug-loaded nanocarriers (macromolecule) in a malignant tissue.

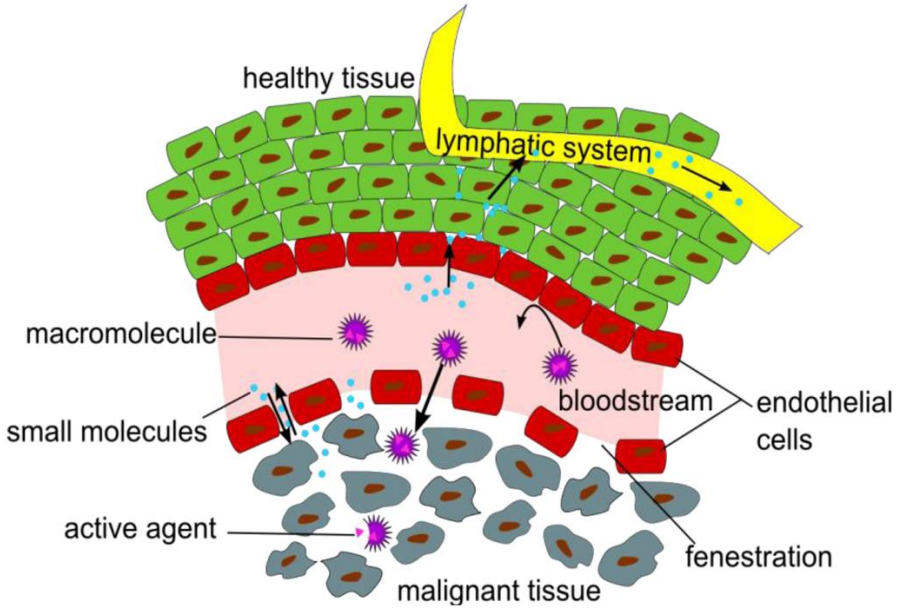

Figure from the article “Radiolabeling of Nanoparticles and Polymers for PET Imaging” (STOCKHOFE et al., 2014).

Nevertheless, passive targeting of tumors via the EPR effect remains limited. Indeed, the tumor vascularization and the fenestration of the vessels depend on the tumor type and stage of development. Heterogeneity of the tumor, increased interstitial fluid pressure or the extracellular matrix of certain tumors can limit NCs penetration into the tumor (MAEDA, 2010). Active targeting can be obtained by grafting targeting ligands (peptides, antibodies, aptamers, folic acid…) on the NCs surface to promote receptor recognition. Receptor-mediated endocytosis increases cellular uptake of NCs (RABANEL et al., 2012; FATTAL and TSAPIS, 2014).

Theranostic nanocarriers combine a diagnostic agent and the drug, allowing both imaging and treatment. They have been conceived for two types of applications: (i) *in vitro* analyses, e.g. cell internalization studies, (ii) *in vivo* monitoring of NC biodistribution and delivering of drug. Usually, the diagnostic agents used in theranostic systems are fluorescent dyes or quantum dots (QDs) for optical imaging, superparamagnetic iron oxides or gadolinium chelates for magnetic resonance imaging (MRI), radionuclides for nuclear imaging and heavy elements for computed tomography (YU, PARK and JON, 2012; MUTHU et al., 2014; YHEE, LEE e KIM, 2014).

Magnetic resonance imaging (MRI) is a non-invasive technique considered as one of the most powerful imaging techniques. It provides good spatial resolution, excellent soft tissue contrast and is easily translated from preclinical research to clinical applications. The MRI technique is based on the interaction of the magnetic moments of hydrogen nuclei of water present in tissues with a strong external magnetic field (MULDER et al., 2006; PENET et al., 2010). Many MRI contrast agents (Gd chelates, superparamagnetic iron oxide, and manganese) can be easily co-incorporated into nanocarriers (VIGLIANTI et al., 2006; TERRENO et al., 2010).

Nuclear imaging relies on trace amounts of radionuclides such as ^{131}I (half-life 8 days), ^{123}I (half-life 13.3 h), ^{111}In (half-life 67.3 h), ^{201}Tl (half-life 73 h) and ^{67}Ga (half-life 78 h). Radiolabeled ligands able to interact with molecular targets involved in the cancer disease can be used. However, low image resolution is induced by scattering of radiation by tissues (JOSHI and WANG, 2010; BAUM and KULKARNI, 2012; FERRO-FLORES et al., 2015).

The application of optical imaging, including confocal microscopy, two-photon microscopy and luminescence, is limited by the properties of biological media. Water, melanin, proteins (e.g. hemoglobin) strongly absorb visible and infrared light (in the 200-650 nm range). Moreover, reflection, refraction and scattering of photons and cell

autofluorescence make imaging difficult. Thus, imaging agents with visible emission can be used for surface imaging of thin sections or *in vitro* single cell layers and not for deeper tissues (>500 μm to cm) (WEISSLEDER, 2001; PANSARE et al., 2012). Absorption strongly decreases in the near-infrared (NIR) region (650-900 nm), called "biological window" for optical imaging and, therefore, fluorophores with NIR emission were developed (LI et al., 2009; HYUN et al., 2015). Figure I.3 presents the absorption coefficient of water, oxyhemoglobin (HbO_2) and hemoglobin (Hb), evidencing the most appropriate NIR imaging window. Optical probes such as organic dyes and quantum dots (CdSe, CdS, ZnO, ZnS, CdTe) have been used in theranostic devices (SMITH et al., 2008).

Figure I.3. Absorption coefficient of oxyhemoglobin, hemoglobin and water from 400 to 1000 nm. The inset shows the lowest absorption coefficient in the NIR region around 650–900 nm.

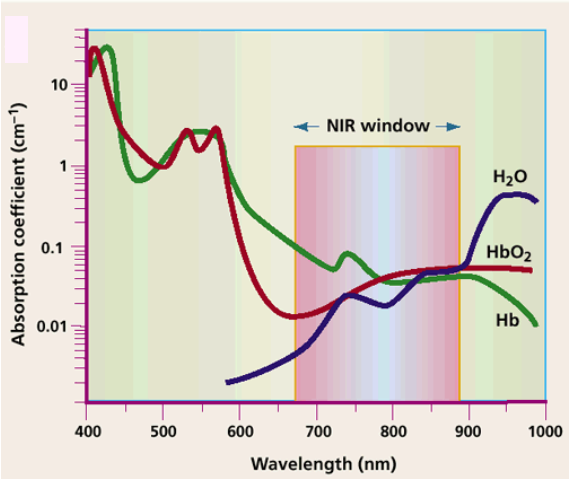

Figure adapted from the article "A clearer vision for in vivo imaging" (WEISSLEDER, 2001).

I.2. Lipid-based nanocarriers

Biocompatible nanocarriers, such as lipid-based nanoparticles, are desired for *in vivo* applications (PURI et al., 2009). We will therefore focus on nanocarriers such as liposomes that were the very first nanomedicines developed (GREGORIADIS and RYMAN, 1971), as well as phospholipid micelles, solid lipid nanoparticles and lipid nanocapsules. Figure I.4 presents schematically examples of lipid-based NCs.

Figure I.4. Schematic representation of lipid-based nanocarriers.

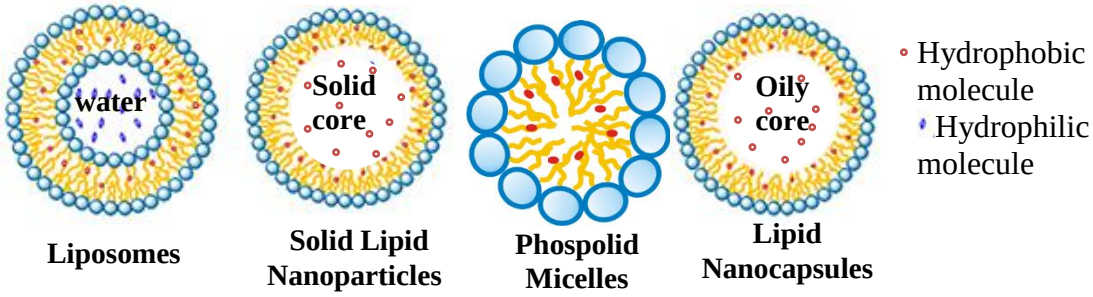

Figure adapted from the article "Cancer immunotherapy: nanodelivery approaches for immune cell targeting and tracking" (CONNIOT et al., 2014).

II.2.1. Liposomes

Liposomes are lipid spherical vesicles formed by one or more phospholipid bilayers enclosing an internal aqueous cavity. They can be classified as uni-, oligo-, and multilamellar vesicles, depending on the number of bilayers. They are formed by the self-assembly of amphiphilic phospholipids in an aqueous medium (BELOGLAZOVA et al., 2013; MUTHU et al., 2014). There are several methods to prepare liposomes, such as reverse phase evaporation technique, injection of phospholipids dissolved in an organic phase into an aqueous phase, detergent dialysis, and the thin lipid film hydration or Bangham method. The last one is a conventional method and the first described for preparing liposomes. It relies on the hydration of a thin film of lipids formed by evaporating the organic solvent used to solubilize them. The size and type of the liposomes depend on the preparation process (sonication, extrusion…). Small unilamellar vesicles (SUV), large or giant unilamellar vesicles (LUV, GUV) or multilamellar vesicles (MLV) can be obtained (BELOGLAZOVA et al., 2013; PATTNI, CHUPIN and TORCHILIN, 2015).

Liposomes can carry hydrophilic drugs in their aqueous compartment and hydrophobic or amphiphilic drugs in the bilayers. Their structure, reminiscent of plasma membranes, favors their internalization into the cells and drug transport across the cell membrane (WEN et al., 2012; BELOGLAZOVA et al., 2013; MUTHU et al., 2014). Their physical stability and the retention of drugs are the first issues associated with the *in vivo* use of liposomes. The efficacy of encapsulation and retention of drugs in liposomes depends both on the drug and on the nature of phospholipids. It has been shown that incorporation of cholesterol into the liposome bilayers could reduce the premature leakage of drugs ("burst effect") entrapped in the aqueous compartment (FATTAL and TSAPIS, 2014).

The "classical" liposomes, also called 1st generation liposomes are rapidly cleared

from blood circulation by uptake in macrophages, mainly in the liver and spleen. On the contrary, liposomes sterically stabilized with polymers such as PEG display long circulation half-life. These long-circulating liposomes are called "Stealth" liposomes or 2nd generation liposomes (ALLEN and CULLIS, 2013). They benefit from the EPR effect, as discussed before. A well-known example is that of doxorubicin. Doxil® was the first doxorubicin-loaded liposome approved by FDA and used in the clinic to treat cancer (GABIZON et al., 1994; BARENHOLZ, 2012). Pegylated liposomal doxorubicin markedly reduces the critical cardiotoxicity of free doxorubicin and enhances its activity due to an increase in the doxorubicin levels in the tumor. Another example of marketed liposomal formulation is that of amphotericin B, AmBisome® (HANN and PRENTICE, 2001).

The 3rd generation of liposomes consists of liposomes whose external surface carries targeting ligands to promote receptor recognition and internalization (RABANEL et al., 2012). Targeting efficiency is related to the overexpression of receptors at the cell surface. For instance, the RGD (arginine-glycine-aspartic acid) peptide specifically binds to fibronectin and integrins responsible for cell adhesion and overexpressed during angiogenesis. Functionalization of liposomes with antibodies (e.g., anti-EGFR, anti-VEGFR2 or anti-HER2) is a promising route for active targeting of tumors, as shown by doxorubicin-loaded immunoliposomes targeted against the epidermal growth factor receptor (EGFR) (TORCHILIN, 2005). Figure I.5 presents schematically the three generations of liposomes; other nanocarriers (e.g. SLNs) can be classified in the same way. Of note, active targeting of solid tumors can also be achieved by applying a magnetic field to liposomes loaded with magnetic nanoparticles (FORTIN-RIPOCHE et al., 2006).

Other advances include pH-sensitive liposomes (in solid tumors the extracellular pH is more acidic) and thermosensitive liposomes (drug release is induced by hyperthermia). Stimuli-sensitive liposomes rely on their lipid composition, selected in order to enable drug release in the required pH or temperature range (MURA, NICOLAS and COUVREUR, 2013).

Figure I.5. Schematic structures of the three generations of liposomes.

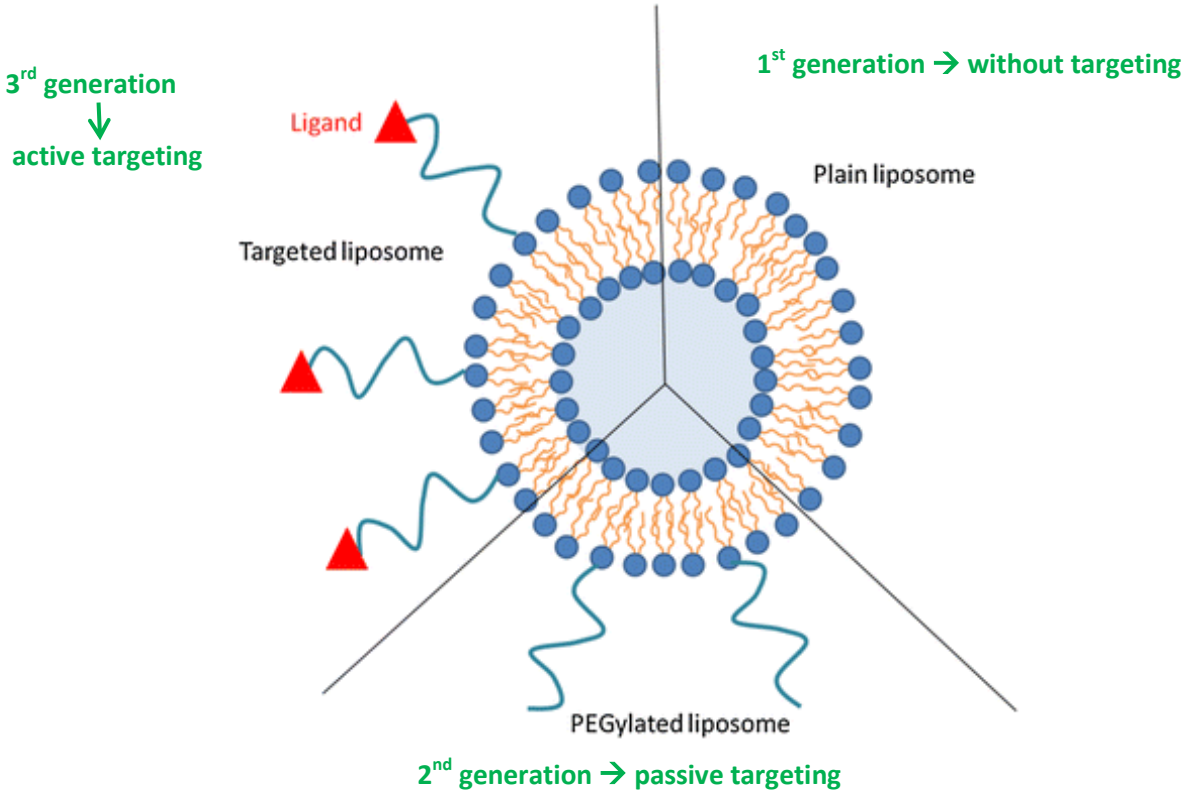

Figure adapted from the article "Nanomedicine technology: current achievements and new trends" (FATTAL and TSAPIS, 2014).

I.2.2. Micelles

Phospholipid-based micelles are spherical aggregates displaying a hydrophobic core surrounded by the hydrophilic phospholipid heads. They form spontaneously in aqueous media when the critical micellar concentration (CMC) is reached. They can encapsulate hydrophobic drugs in their core. Micelles have small sizes, usually less than 100 nm with a narrow size distribution. They can be used for parenteral administration, mainly for poorly soluble drugs, and are generally considered as a safe and biocompatible long-circulating drug delivery system when covered with a hydrophilic polymer shell. The morphology of the micelles (spheres, rods, vesicles, tubules, and lamellae) can significantly impact their pharmacokinetic properties, i.e. change their time of circulation in the body (KWON, 2006; PAPAGIANNAROS et al., 2009; FRANK et al., 2014; MUTHU et al., 2014; ZHANG, HUANG and LI, 2014). Like liposomes, micelles can be decorated with specific ligand allowing their active targeting.

I.2.3. Solid lipid nanoparticles (SLN)

As alternative to polymeric nanoparticles, researchers have focused on solid lipid nanoparticles (SLNs) nanocarriers since the beginning of the 90s (SIEKMANN and WESTESEN, 1992). SLNs have a core of lipids solid at body temperature, stabilized by a layer of surfactant. Lipids include triglycerides, complex glyceride mixtures, fatty acids (e.g. stearic acid) and waxes (e.g. cetyl palmitate). The methods of preparation can be high pressure homogenization (hot or cold), microemulsion technique and nanoprecipitation. High pressure homogenization is the basic production method for SLNs. Nanoprecipitation is a simple and fast technique with potential for scaling-up. In practice, the hydrophobic lipid is first dissolved into a polar solvent (usually ethanol, acetone or tetrahydrofuran). This solution is then added to a large amount of water with which the polar solvent is miscible in all proportions. The mixed binary solution becomes a non-solvent for the lipid and the lipid supersaturation leads to the formation of nanoparticles. The organic solvent can then be removed by evaporation. Hydrophobic drugs have been dissolved (solid solution) or dispersed into SLNs, which commonly present high drug loading capacity. Drug loading may result in changes of the SLN characteristics (e.g. degree of crystallinity and crystalline structure of the lipids). In turn, these characteristics impact drug release (DONG et al., 2012; MUTHU et al., 2014).

I.2.4. Lipid nanocapsules (LNC)

Lipid nanocapsules consist of an oily core (mainly triglycerides of capric and caprylic acids) surrounded by a tensioactive rigid membrane formed by surfactants derived from PEG and phospholipids. They can be prepared by a phase-inversion process from an O/W to a W/O emulsion which takes place as temperature is increased (phase inversion temperature, PIT process). This method is essentially based on the change in hydrophilicity of PEG as a function of temperature. The phase inversion temperature is defined as the “temperature or temperature range at which the hydrophilic and lipophilic properties of a nonionic surfactant just balance”. Cycles of heating and cooling, followed by dilution with cold water at the PIT, lead to the formation of LNCs. Their mean size is well controlled, and ranges from 20 to 100 nm. Their oily core favors hydrophobic drug encapsulation. Like the nanocarriers described before, they can be modified for active targeting (PELTIER et al., 2006; HUYNH et al., 2009; NICOLAS et al., 2013; SKANDRANI et al., 2014).

I.3. Quantum Dots for optical imaging

Quantum dots are emerging as a new class of luminescent probes for biology and medicine. QDs are nanometer-sized semiconductor particles, usually composed of atoms from groups II-VI, III-V or IV-VI of the periodic table (i.e. CdTe, CdSe, PbSe, GaAs, GaN, InP, and InAs). In comparison with organic dyes and fluorescent proteins, QDs have unique optical properties (HEYES et al., 2007; DAZZAZI et al., 2013). They display a broad absorption spectrum, a narrow symmetric emission peak, bright signal and resistance to photobleaching (FU et al., 2007). They are also good candidates for imaging due to their chemical stability and long luminescence lifetime, even when exposed to air (DAZZAZI et al., 2013). The most characteristic optical property of QDs is their size-dependent light emission, allowing simultaneous emission of several colors for a single wavelength of excitation (IOANNOU and GRIFFIN, 2010).

These outstanding properties result from the quantum confinement of the electron-hole pair (exciton), due to the absorption of a photon with energy above the semi-conductor band gap energy, for nanocrystals smaller than twice the exciton Bohr radius (HEYES et al., 2007; ISNAENI et al., 2011). Figure I.6 presents schematically the size-dependent luminescence properties of QDs, showing the higher energy required to excite smaller nanocrystals due to the reduced natural radius of the electron-hole pair and the quantized energy levels.

By controlling QD size and chemical composition emission it is therefore possible to tune emission from the UV to the near IR region.

Figure I.6. Schematic size-dependent luminescence properties of QDs: correlation between the electronic structure of QDs and the QD radius which leads to the blue shift of the emitted ration due to quantum confinement as the QD size decreases.

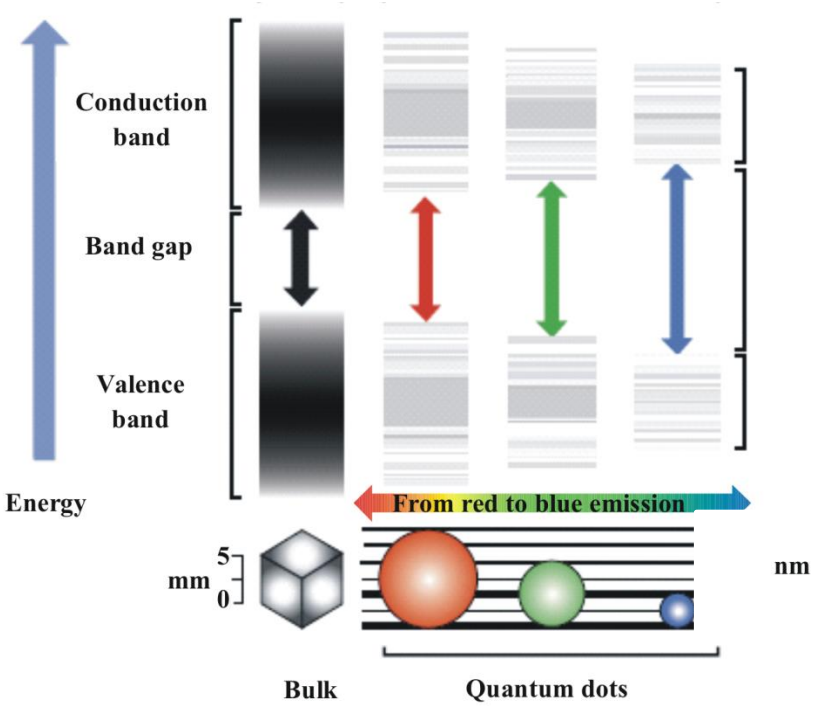

Figure adapted from the article "Nanotechnology and molecular cytogenetics: the future has not yet arrived" (IOANNOU and GRIFFIN, 2010).

I.3.1. Core-shell QDs

QD surface defects can act as traps for the electron or hole, hindering their radiative recombination. The non-radiative recombination of an electron-hole pair (exciton) results in "photoblinking" (ISNAENI et al., 2011). To minimize these effect of turning ON and OFF their photoluminescence, which limits their use in tracking applications, some groups have successfully obtained QDs with improved photoluminescence properties by forming a core-shell (WANG et al., 2009; CASSETTE et al., 2010; LUO et al., 2015). Coating NPs with a higher band gap semiconductor can passivate the core surface, eliminating surface-related defect states. ZnS has often been employed because of its wide band gap (3.66 eV), as shown by numerous publications. The first report in literature dealt with CdSe cores of 3 nm covered with 1-2 layers of ZnS, with a quantum yield of about 50% (HINES and GUYOT-SIONNEST, 1996).

Beside CdSe/ZnS core-shell QDs, CdSe/CdS core-shell QDs with core size varying from 1.2 to 1.5 nm presented narrow near-edge emission ranging from 445 to 517 nm and

improved quantum yield (60-80%), hence indicating the removal of the majority of surface traps (PAN et al., 2005). Figure I.7 shows solutions of CdSe/CdS QDs with different sizes and shell thicknesses. Moreover, non-blinking QDs with narrow multiple peaks emission spectra in the range of 600-700 nm were achieved by forming CdZnSe/ZnSe core-shell structures (WANG et al., 2009; CHEN et al., 2013).

Figure I.7. Solutions of CdSe/CdS core-shell QDs with different size and shell thickness under normal indoor light (no UV radiation).

Figure from the article "Synthesis of extremely small CdSe and highly luminescent CdSe/CdS core-shell nanocrystals via novel two- phase thermal approach" (PAN et al., 2005).

Beyond improving the luminescence properties of the QDs, the shell acts as a barrier between the core and the environment and can modify the charge and reactivity of the surface, as well as the colloidal stability and biocompatibility of the core material (REISS, PROTIÈRE and LI, 2009). Core-shell QDs can be also capped and functionalized with organic molecules according to their applications. Figure I.8 presents schematically the structure of a core-shell QD capped by amphiphilic molecules.

Figure I.8. Schematic structure of the core-shell quantum dot capped by amphiphilic molecules.

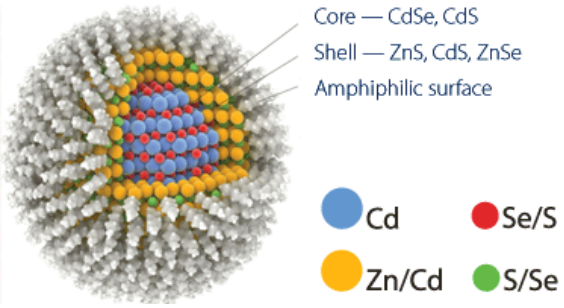

Figure from the website Nanodioed (NANODIODE, 2015).

I.3.2. Surface-modification of QDs with organic molecules

Due to their unique properties, QDs have applications in the field of bioimaging, biosensing and drug delivery. Prerequisite for every possible application is the proper surface modification of QDs, which determines their interactions with the environment. The surface coating of QDs with organic molecules may have different functions. It can (i) protect the QDs, reduce their toxicity and enhance their biocompatibility, (ii) improve the colloidal stability of QDs which have propensity to aggregate in biological media, (iii) allow their incorporation in drug delivery devices, e.g. polymeric or lipidic nanoparticles, (iv) allow tagging of a target molecule or a cell receptor, (v) carry drug molecules (JIN et al., 2011).

QD surface modification strategies include coating with a layer of small molecules (e.g; thiol containing molecules) (TANG et al., 2011; KOBAYASHI et al., 2014), a silica shell, a polymer shell (GILL, ZAYATS and WILLNER, 2008), encapsulation in phospholipid or amphiphilic copolymer micelles or in a phospholipid bilayer. These strategies are effective in enhancing QD stability and biocompatibility. Moreover, when QDs are functionalized with biomolecules such as ligands, antibodies, proteins or peptides they can bind with high specificity to many different cellular receptors and target molecules (SPERLING and PARAK, 2010; FRANK et al., 2014). However, modification of the QD surface may alter their luminescence properties.

I.3.3. In vitro imaging using QDs

Several studies used QDs for cell labelling and tracking. For example, carboxylic groups (16-mercaptohexadecanoic acid (MHDA, 90%), 11-mercaptoundecanoic acid (MUA, 95%), and aminoethanethiol-HCl (AET)) surface modified PbS and PbSe QDs were used to label specifically human colon cancer cells. In this case, the water-soluble QDs showed high (at least 10%) fluorescence quantum yield in NIR range (beyond 1000 nm) in biological media (HYUN et al., 2007). Pan et al. described the use of CdSe/ZnS QDs to label MCF-7 cell line. They used D-α-tocopheryl polyethylene glycol 3350 succinate to turn the QDs water-soluble and also to reduce their nonspecific cellular binding (PAN et al., 2014). DHLA-capped CdSe/ZnS QDs were developed for long-term multiple color imaging of live HeLa cells and AX2 cells. QDs did not affect the normal growth and differentiation of the cells for over 1 week. The two approaches for labeling cells were (i) internalization of the QDs by endocytosis (generalized labeling), (ii) selective labeling of cell surface proteins with QDs conjugated to antibodies (specific labeling). Besides, the use of different ligands grafted on

QDs with different colors of emission could allow tracking various cells in a mixture of cells (JAISWAL et al., 2003). Water-soluble avidin-conjugated CdSe/ZnS QDs were employed in numerous in vitro assays. Fluoro-immunoassays were performed by detecting protein toxin (staphylococcal enterotoxin B, cholera toxin) using these antibody conjugated QDs (GOLDMAN et al., 2002). Another application of QDs (CdSe/ZnS core/shell QDs capped with a paramagnetic coating and PEGylated lipids and functionalized with specific RGD peptides) was their use for multimodality imaging of markers of angiogenesis. These QDs were successfully targeted to human endothelial cells *in vitro* (MULDER et al., 2006). Moreover, CdSe QDs encapsulated into polymersomes could probe the internalization of polymersomes into human liver carcinoma cells (HepG2) (CAMBLIN et al., 2014). QDs associated with drug in an hybrid nanogel have already been used to targeted imaging and drug delivery (YANG et al., 2014). CdSe/ZnS core-shell QDs were capped by hydrophobic/ hydrophilic/hydrophobic peptide- based layers like a sandwich microstructure that allowed simultaneously hydrophobic and hydrophilic drug loading. The system presented temperature- and pH-sensitivity for drug release. Besides, RGD was used to target HeLa cells, being promising for application in cancer diagnosis, imaging, and therapy.

I.3.4. In vivo imaging using QDs

QDs have also been investigated as bioimaging agent for in vivo analysis (DUBERTRET et al., 2002; XIONG et al., 2008; DAOU et al., 2009). Nevertheless, the limitations of in vivo analysis (weak tissue penetration of low wavelength light, cell autofluorescence) make their use very challenging. Usually, in vivo applications require high sensitivity (NIR QDs with a high quantum yield), photostability (e.g., polymer coated QDs, QDs with proper composition), long circulation time (appropriate size, shape and surface of QDs) and low toxicity (e.g., conjugation of QDs with a target specific ligand). Han et al. developed three biocompatible QDs with different compositions (CdSe/CdZnS, CdSe/CdS, and InAs/CdZnS), conjugated with antibody (Ab-QDs) for in vivo single-cell bone investigation. They could observe the diffusion of the Ab-QDs along the bone marrow and the specific labeling of cells belonging to rare populations of hematopoietic stem and progenitor cells (HAN et al., 2015). Graphene QDs conjugated with hyaluronic acid (HA), as specific ligand, with maximum emission at 440 nm were used to study CD44 receptor overexpressed in tumor-bearing balb/c female mice. The tumor tissue presented bright fluorescence in the in vivo biodistribution investigation (ABDULLAH AL et al., 2013). Cancer targeting and

imaging in living animals were also achieved using an triblock copolymer-encapsulated and tumor-targeting bioconjugated CdSe/ZnS QDs. Nude mice with human prostate cancer were studied; QD probes accumulated mainly in the tumor sites by passive and active mechanisms. It was also possible to achieve sensitive and multicolor fluorescence imaging *in vivo* (GAO et al., 2004). Green and yellow emitting polymer-capped ZnO QDs were reported for the first time for in vivo mouse imaging five years ago. Intradermal and intravenous administrations were carried out and it was possible to observe QD fluorescence with the naked eye. Figure I.9 shows the mouse under UV light (λ_{exc} =330 nm) (A) 5 min after intradermal injection of green QDs, and (B) 60 min after intradermal injection of green and yellow QDs (PAN et al., 2011).

Figure I.9. A mouse under UV light (λexc =330 nm) (A) after 5 min after intradermal injection of green QDs, and (B) 60 min after intradermal injection of green and yellow QDs.

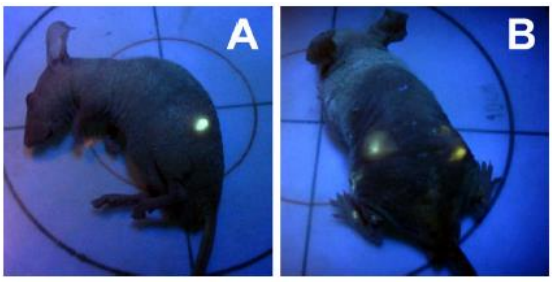

Figure from the article "The application of ZnO luminescent nanoparticles in labeling mice" (PAN et al., 2011).

I.3.5. ZnO QDs

Cd-based QDs are harmful to human health during their production and possibly to the environment (XIONG et al., 2008). Therefore, ZnO QDs are an excellent alternative to the ordinary quantum dots due to their biocompatibility (FU et al., 2007). Besides their biocompatibility, ZnO QDs are also cheaper, chemically stable towards air (ZHAO et al., 2012) and biodegradable (HAN et al., 2012). However, ZnO QDs have not been extensively explored as potential biological probes.

I.3.5.1. Sol-gel synthesis

When focusing on ZnO QDs, it is important to consider the beginning of their synthesis and study as colloidal suspensions. In the early 1980s Efros and Brus independently

observed striking differences of color for colloidal suspensions made of semiconductor nanocrystals displaying different sizes (BRUS, 1983; EFROS, 1982). As recalled in section I.3, the origin of this unusual property is the quantum confinement effect, related to the nanocrystal size. Obtaining quasi-monodisperse nanocrystals with the required size is thus crucial for the comprehension of their properties and applications.

Various physical and chemical procedures have been proposed to synthesize ZnO luminescent nanoparticles. Wet-chemical processes, such as controlled precipitation, hydrothermal or solvothermal methods, sol-gel route, are more attractive because they can be easily transposed to large scale production and are usually conducted at lower temperatures than those used in physical ones (e.g., HU et al., 2005a; HU et al., 2005a; HU, OSKAM and SEARSON, 2003).

The ZnO nanoparticle synthesis via sol–gel route started in the 1980s (BAHNEMANN et al, 1987) and until now it has been continuously investigated (SPANHEL and ANDERSON, 1991; LUO *et al.*, 2015). In 1991, Spanhel and Anderson proposed an innovative sol-gel synthesis of ZnO colloids (average crystallite size around 3-6 nm), relying on the base-catalyzed hydrolysis and condensation reaction of a solution of Zn acetate – derived precursor in ethanol (SPANHEL and ANDERSON, 1991). This process consists of two main steps: (i) preparation of the precursor by refluxing at 80°C an absolute ethanol solution of Zn acetate dihydrate ($Zn(Ac)_2 . 2H_2O$), (ii) formation of the ZnO nanoparticles by hydrolysis of the precursor and subsequent condensation reaction, induced by addition of a base.

Tokumoto et al have identified the primary clusters formed in the first step of this process. Through a detailed time-resolved EXAFS study combined with IR and UV-vis measurements carried out in solution, they proved the conversion of $Zn(Ac)_2 . 2H_2O$ into the tetrameric oxy-acetate $Zn_4O(Ac)_6$ precursor (TOKUMOTO et al, 2003). This precursor, based on a tetrahedron of 4 Zn^{2+} containing 1 oxygen, is structurally close to the ZnO wurtzite. Its transformation into ZnO could result from substitution of peripheral acetate ligands by hydrolysable groups, followed by subsequent oxolation (formation of Zn-O-Zn bridges). Figure I.10 presents schematically the wurtzite crystal structure of bulk ZnO. Tokumoto et al and Briois et al have further monitored the evolution of Zn-based species during the second step of the sol-gel synthesis, underlining the complexity of the process. The mixture of ZnO, unreacted Zn acetate ($Zn(Ac)_2$), and Zn hydroxy-acetate, a layered compound also called Zn hydroxy double salts (Zn-HDS) was characterized by time-resolved simultaneous UV-vis and

EXAFS measurements. The relative amounts of the compounds can be controlled by the sol-gel synthesis parameters (temperature, hydrolysis ratio, reaction duration…) (TOKUMOTO et al 2003, BRIOIS et al 2007). Recently, a deeper insight into the formation, growth and aggregation of ZnO QDs could be gained by time-resolved UV-vis/ SAXS and UV-vis/ EXAFS coupled measurements (CAETANO et al 2011).

Figure I. 10. Schematical structure of wurtzite ZnO, where Zn is the grey ball and O is the red ball, both Zn and O ions fourfold coordinated.

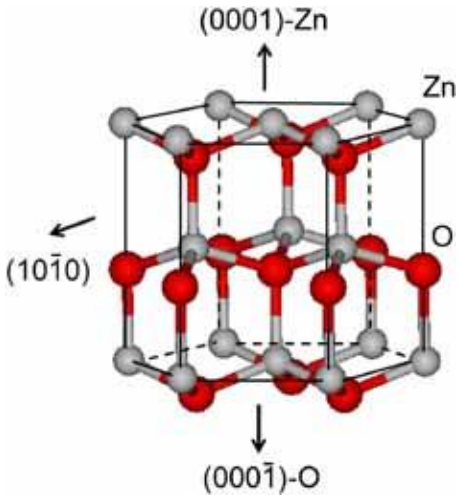

Figure from the article "Vibrational spectroscopic studies on pure and metal-covered metal oxide surfaces" (NOEI et al., 2011).

I.3.5.2. Photoluminescence properties

ZnO is an n-type semiconductor with a wide band gap of 3.37 eV and an exciton Bohr radius of about 3 nm. The intrinsic peak of bulk ZnO absorbance is therefore in the UV region, at about 365 nm. Reducing the ZnO crystal size below twice the Bohr radius shifts the wavelength of the absorption edge to lower values (corresponding to higher energy) due to quantum confinement. The typical exciton emission (photo-generated electrons recombine with the holes in the valence band) of ZnO QDs is thus in the UV range. In addition to this excitonic emission, a broad visible luminescence, usually around 500 nm, may be observed.

Despite many studies, the exact mechanisms of visible emission are still under debate. It is generally believed that this emission originates from defects such as oxygen vacancies. Two contributions have been suggested: (i) recombination of a shallowly trapped electron with a hole in a deep trap, (ii) recombination of an electron in an oxygen vacancy with a

photo-generated hole in the valence band. Figure I.11 presents schematically the mechanisms involved in the (a) UV and (b and c) visible emission. The existence of multiple defect-related transitions results in a broad emission. Consequently, the range and intensity of the visible emission are expected to strongly depend on the QD size, crystal lattice defects, surface state, capping groups and so on, and thus on the preparation technique (XIONG, 2010).

Figure I.11. Suggested mechanisms involved in the ZnO photoluminescent processes: (a) typical exciton emission (UV emission), (b) recombination of a shallowly trapped electron with a deeply trapped hole, and (c) recombination of a shallowly trapped hole with a deeply trapped electron (visible emission). In the maps VB and CB are the valence band and the conductance band, respectively.

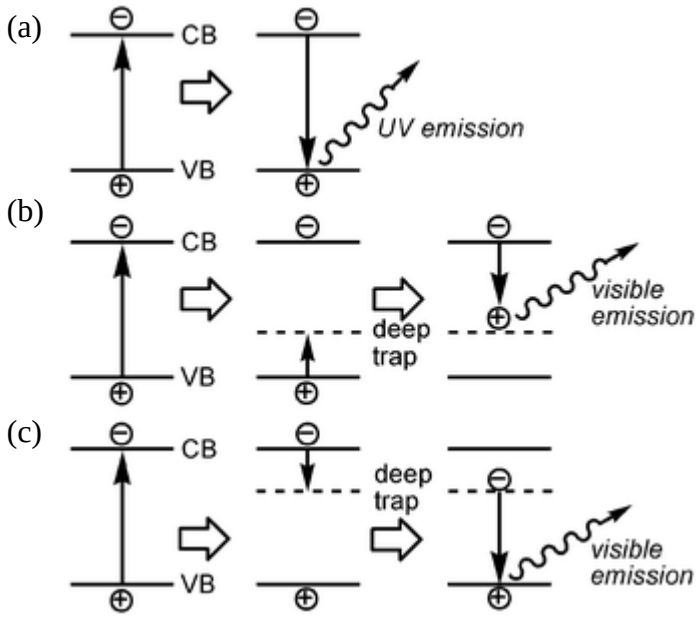

Figure from the article "Photoluminescent ZnO nanoparticles modified by polymers" (XIONG, 2010).

Figure I.12 shows the photoluminescence spectra of ZnO nanoparticles synthesized via hydrothermal route at different temperatures ((a) 50, (b) 100, (c) 150 and (d) 200°C). As the synthesis temperature increases, the nanoparticle size is larger, the surface to volume ratio decreases and nanoparticles present less surface defects; the visible emission therefore decreases, until vanishing.

Figure I.12. PL spectra of the ZnO nanoparticles synthesized at (a) 50, (b) 100, (c) 150 and (d) 200 °C, measured at room temperature with excitation wavelength 280 nm.

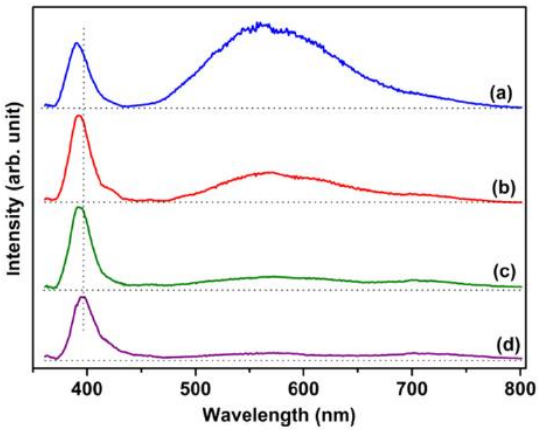

Figure from the article "Observation of band gap and surface defects of ZnO nanoparticles synthesized via hydrothermal route at different reaction temperature" (KUMAR and SAHARE, 2012).

ZnO QDs prepared by the sol-gel route tend to aggregate at room temperature, as evidenced by the red-shift of their UV-Vis absorption and PL spectrum. Moreover, their visible luminescence is quenched by water, in which they are unstable. Many surface modification strategies were employed to hinder their aggregation and provide them colloidal stability in different environments (e.g., aqueous media, lipidic or polymeric nanocarriers), while preserving their PL properties. For instance, ZnO QD surface was capped with polymers (XIONG et al., 2008; ZHANG et al., 2013; ABOULAICH et al, 2012; MOUSSODIA et al., 2010), oleic acid (FU et al., 2007), silanes (LI et al., 2015), silica (ZHANG et al. 2012), which turn them directly proper for biological media (hydrophilic) or make them appropriate for further incorporation into nanocarriers (hydrophobic). Remarkably, Li et al have recently designed ZnO QDs modified by silanes, displaying high stability in aqueous media and unexpectedly enhanced luminescence, about 10-fold higher than that of bare QDs. QDs synthesized by a modified sol-gel route were first shielded from water by a hydrophobic silane layer and then covered by a hydrophilic silane shell bearing amine groups. QDs with luminescence from blue to green-yellow were obtained (LI et al, 2015).

I.3.6. Doped ZnO QDs

The introduction of dopants in semiconductors can provide either extra electrons (n-type) or extra holes (p-type), modifying their properties. Dopant ions can either enlarge or narrow the band gap of the semiconductor, thereby tuning the emission colors. The common challenge is to ensure that the dopants are actually substituting host atoms in the QDs during crystal growth and that they are not expelled to the surface through a "self-purification" process. It is therefore important to choose dopants ions with the same valence state and ionic radius similar to that of the host QD (REISS, 2007). Furthermore, at the relatively low-temperatures at which solution phase syntheses are carried out, the dopant incorporation is mainly controlled by kinetic factors (BUONSANTI and MILLIRON, 2013). Erwin et al have shown the influence of three factors on doping kinetics: surface morphology, QD shape and the use of surfactants in the growth solution (ERWIN et al., 2005).

ZnO nanoparticles could be successfully doped with Mg, Cd, Co, Mn, Ni, Cu and Fe ions. Magnetic elements (Fe, Co, Mn and Ni) were chosen in an attempt to obtain probes with both fluorescent and magnetic properties. However, most of ZnO nanoparticles doped with these magnetic elements showed almost no luminescence in the visible region. Conversely, it has been reported that doping with Cd or Mg ions could enhance the luminescence of ZnO QDs (LUO et al, 2015; YOUSEFI et al, 2013). Figure I.13 shows schematically the diagram of Co-doped ZnO QDs structure.

Figure I.13. Schematic diagram of Co-doped ZnO QDs structure.

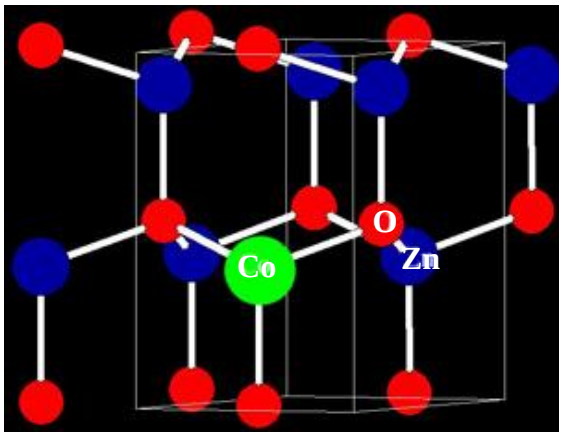

Figure from the article "Magnetic semiconductors: Intrinsic behavior" (ZHANG et al., 2009).

Wang et al have reported the changes in the optical properties of ZnO nanocrystals, with diameters in a range unaffected by quantum confinement effects, induced by doping with

Mg and Cd ions. A linear increase in the band gap from 3.30 to 3.66 eV was observed upon increasing Mg concentration from 0 to 15%, whereas the band gap decreased from 3.30 to 2.92 eV with the increase of Cd doping levels from 0 to 10%. The band edge emission shifted to the blue in the presence of Mg dopants whereas it showed a red shift upon Cd doping (WANG et al, 2006).

Spanhel et al studied the luminescent properties of the ZnO-doped nanoparticles using silica and erbium as dopants. They obtained materials with emission in the green-yellow range (silica-doped ZnO) (LORENZ et al., 1998) and in the near infra-red range (Er-doped ZnO) (SCHMIDT et al., 1998).

Liu et al have developed Gd-doped ZnO quantum dots as dual modal fluorescence and magnetic resonance imaging nanoprobes. Such QDs exhibited maximum luminescence coupled with a blue shift of the emission band (at about 550 nm) when the molar ratio Gd/Zn increased to 0.08. They labelled HeLa cells which could be imaged by both MRI and confocal fluorescence microscopy (LIU et al, 2011).

Other ZnO-based multimodal imaging probes have been designed for MRI and Computed Tomography (CT) imaging relying on the paramagnetic behavior of Gd and the strong X-ray absorption of Yb. These nanoprobes were functionalized with folate to increase their stability and biocompatibility (YIN et al, 2014).

I.3.7. Toxicity of quantum dots

The use of QDs for biological applications has raised great concern. The most commonly used QDs contain toxic heavy metal atoms such as cadmium, lead, arsenic, nickel, selenium, tellurium, etc. Beside their chemical composition, several physico-chemical factors, such as QD size, charge, concentration, shell coating, ligand functionalization, and stability, can affect QD cytotoxicity. In addition to their own properties, the environmental conditions will interfere on their stability, absorption, distribution, metabolism and excretion. For example, the tendency for QDs to aggregate, precipitate in cell culture media, bind non-specifically to cellular membranes and proteins, and induce the formation of reactive oxygen species (ROS) can be an important contribution to toxicity. Therefore, the potential toxicity of each type of QD for specific biological systems needs to be evaluated. Presently, the diversity of QDs and the disparity in experimental conditions (i.e., cell line, dose, duration, frequency of exposure, mechanisms of action) hampers the toxicological assessment of QDs (HARDMAN, 2006; DE JONG and BORM, 2008).

Usually, Cd-based QDs without shell coating present toxicity related to the release of highly toxic free Cd^{2+} ions, due to their degradation in biological media. Their toxicity against cells *in vitro* has been reported (e.g., CHO et al., 2007; KIRCHNER et al., 2005). *In vivo*, the liver is the first site of acute injury provoked by Cd^{2+} ions. Using primary hepatocytes as a liver model, Derfus et al found that CdSe QDs were indeed toxic; toxicity correlated with surface oxidation, decrease of QD size, and disruption of crystal lattice (DERFUS, CHAN and BHATIA, 2004).

When heavy metal ions-based QDs are coated with an inorganic and/or polymeric shell, their toxicity tends to be reduced. Numerous studies dealt with CdSe/ZnS QDs (CONTRERAS et al., 2013; WIECINSKI et al., 2013). ZnS shell decreased the release of cadmium ions from the core. These results were confirmed by studies on thiol-stabilized CdTe/CdS/ZnS QDs (SU et al., 2009). The same behavior was observed for CdTe/CdS/ZnS QDs without surface stabilizer in an aqueous medium (YAN et al., 2009). Derfus et al found that the addition of an organic coating (BSA) on the ZnS shell further minimizes the cytotoxicity of CdSe QDs, allowing long-term live cell labeling of hepatic tissue in vitro (DERFUS, CHAN and BHATIA, 2004). Kirchner et al showed that embedding CdSe QDs in a silica shell also dramatically hindered the release of Cd ions; in addition, the uptake of QDs by cells was reduced for PEG-silica coated CdSe QDs, which resulted in lower cytotoxicity (KIRCHNER et al., 2005). Taken together, these results suggest that the QD surface chemistry plays an important role for cytotoxicity. Water soluble InP/ZnS QDs were suggested as a safer alternative to CdSe/ZnS QDs. They demonstrated lower toxicity compared to CdSe/ZnS QDs for *in vitro* and *in vivo* biological applications. In this case the same amounts of $In_{(III)}$ and Cd^{2+} ions were released from the cores; however, $In_{(III)}$ ions are less toxic than the Cd^{2+} ones (BRUNETTI et al., 2013).

Finally, one alternative is the use of non-toxic element based QDs, such as ZnO, ZnS and ZnSe QDs. The influence of dopants on the toxicity of these QDs has been studied. Fluorine-doped hydroxyapatite (a well-known biocompatible material) was conjugated with Mn-doped ZnSe/ZnS QDs. This system presented low cytotoxicity during 24 h for cancer cells (ZHOU et al., 2014). Mn-doped ZnS QDs and their polyethylene glycol-coated counterparts caused damage neither to cell nuclei and mitochondria, nor to the liver, even after repeated administration in mice (YANG et al., 2015). Cu-doped QDs and QDs with Cu^{2+} ions chemisorbed at ZnO surface, both capped by polymer shell, were evaluated. Cu-doped ZnO QDs presented lower toxicity for *Escherichia coli* cells than QDs with Cu^{2+} ions

chemisorbed (MOUSSA et al., 2016).

To conclude, in depth analyses, like meta-analysis (OH et al., 2016), might be a good strategy to predict the QD toxicity.

I.4. REFERENCES

ABDULLAH AL; N. LEE, J.E.; IN, I.; LEE, H.; LEE, K. D.; JEONG, J. H.; PARK; S. Y. Target Delivery and Cell Imaging Using Hyaluronic Acid-Functionalized Graphene Quantum Dots. **Mol Pharm,** v. 10, n. 10, p. 3736-3744, 2013.

ABDULLAH, M.; MORIMOTO, T.; OKUYAMA, K. Generating Blue and Red Luminescence from ZnO/Poly(ethylene glycol) Nanocomposites Prepared Using an In-Situ Method. **Adv Funct Mater,** v. 13, n. 10, p. 800-804, 2003.

ABOULAICH, A., TILMACIU, C.-M., MERLIN, C., MERCIER, C., GUILLOTEAU, H., MEDJAHDI, G., SCHNEIDER, R. Physicochemical properties and cellular toxicity of (poly)aminoalkoxysilanes-functionalized ZnO quantum dots. **Nanotechnology**, v. 23, p. 335101:1-9, 2012.

ACHARYA, S.; SAHOO, S. K. PLGA nanoparticles containing various anticancer agents and tumour delivery by EPR effect. **Adv Drug Deliv Rev,** v. 63, n. 3, p. 170-183, 2011.

ALLEN, T. M.; CULLIS, P. R. Liposomal drug delivery systems: From concept to clinical applications. **Adv Drug Deliv Rev,** v. 65, n. 1, p. 36-48, 2013.

BAHNEMANN, D. W.; KORMANN, C.; HOFFMANN, M. R. Preparation and characterization of quantum size zinc oxide: a detailed spectroscopic study. **J Phys Chem,** v. 91, n. 14, p. 3789-3798, 1987.

BARENHOLZ, Y. Doxil® — The first FDA-approved nano-drug: Lessons learned. **J Control Release,** v. 160, n. 2, p. 117-134, 2012.

BAUM, R. P.; KULKARNI, H. R. THERANOSTICS: From Molecular Imaging Using Ga-68 Labeled Tracers and PET/CT to Personalized Radionuclide Therapy - The Bad Berka Experience. **Theranostics**, v. 2, n. 5, p. 437-447, 2012.

BELOGLAZOVA, N. V.; SHMELIN, P.S.; SPERANSKAYA, E.S.; LUCAS, B.; HELMBRECHT, C.; KNOPP, D.; NIESSNER, R.; DE SAEGER, S.; GORYACHEVA, I.Y. Quantum Dot Loaded Liposomes As Fluorescent Labels for Immunoassay. **Anal Chem,** v. 85, n. 15, p. 7197-7204, 2013.

BHASKAR, S. TIAN, F.; STOEGER, T.; KREYLING, W.; DE LA FUENTE, J. M.; GRAZÚ, V.; BORM, P.; ESTRADA, G.; NTZIACHRISTOS, V.; RAZANSKY, D. Multifunctional Nanocarriers for diagnostics, drug delivery and targeted treatment across

blood-brain barrier: perspectives on tracking and neuroimaging. **Part Fibre Toxicol,** v. 7, n. 1, p. 1-25, 2010.

BRIOIS, V. GIORGETTI, C.H.; BAUDELET, F.; BLANCHANDIN, S.; TOKUMOTO, M. S.; PULCINELLI, S. H.; SANTILLI, C. V. Dynamical Study of ZnO Nanocrystal and Zn-HDS Layered Basic Zinc Acetate Formation from Sol−Gel Route. **J Phys Chem C Nanomater Interfaces,** v. 111, n. 8, p. 3253-3258, 2007.

BRUNETTI, V. CHIBLI, H.; FIAMMENGO, R.; GALEONE, A.; MALVINDI, M. A.; VECCHIO, G.; CINGOLANI, R.; NADEAU, J. L.; POMPA, P. P. InP/ZnS as a safer alternative to CdSe/ZnS core/shell quantum dots: in vitro and in vivo toxicity assessment. **Nanoscale,** v. 5, n. 1, p. 307-317, 2013.

BRUS, L. E. A simple model for the ionization potential, electron affinity, and aqueous redox potentials of small semiconductor crystallites. **J Chem Phys,** v. 79, n. 11, p. 5566-5571, 1983.

BUONSANTI, R.; MILLIRON, D. J. Chemistry of Doped Colloidal Nanocrystals. **Chem Mater,** v. 25, n. 8, p. 1305-1317, 2013.

CAETANO, B. L. SANTILLI, C. V.; MENEAU, F.; BRIOIS, V.; PULCINELLI, S. H. In Situ and Simultaneous UV−vis/SAXS and UV−vis/XAFS Time-Resolved Monitoring of ZnO Quantum Dots Formation and Growth. **J Phys Chem C Nanomater Interfaces,** v. 115, n. 11, p. 4404-4412, 2011.

CAMBLIN, M.; DETAMPEL, P.; KETTIGER, H.; WU, D.; BALASUBRAMANIAN, V.; HUWYLER, J. Polymersomes containing quantum dots for cellular imaging. **Int J Nanomedicine,** v. 9, p. 2287-2298, 2014.

CASSETTE, E.; PONS, T.; BOUET, C.; HELLE, M.; BEZDETNAYA, L.; MARCHAL, F.; DUBERTRET, B. Cu−In−Se/ZnS Core/Shell Quantum Dots for In vivo Imaging. **Chem Mater,** v. 22, n. 22, p. 6117-6124, 2010.

CHEN, O.; ZHAO, J.; CHAUHAN, V. P.; CUI, J.; WONG, C.; HARRIS, D. K.; WEI, H.; HAN, H. S.; FUKUMURA, D.; JAIN, R. K.; BAWENDI, M. G. Compact high-quality CdSe–CdS core–shell nanocrystals with narrow emission linewidths and suppressed blinking. **Nat Mater,** v. 12, n. 5, p. 445-451, 2013.

CHO, S. J.; MAYSINGER, D.; JAIN, M.; RÖDER, B.; HACKBARTH, S.; WINNIK, F. M. Long-Term Exposure to CdTe Quantum Dots Causes Functional Impairments in Live Cells. **Langmuir,** v. 23, n. 4, p. 1974-1980, 2007.

COHN, A. W.; KITTILSTVED, K. R.; GAMELIN, D. R. Tuning the Potentials of "Extra" Electrons in Colloidal n-Type ZnO Nanocrystals via Mg2+ Substitution. **J Am Chem Soc,** v. 134, n. 18, p. 7937-7943, 2012.

CONNIOT, J. SILVA, J. M., FERNANDES, J. G., SILVA, L. C., GASPAR, R., BROCCHINI, S., FLORINDO, H. F., BARATA, T. S. Cancer immunotherapy: nanodelivery approaches for immune cell targeting and tracking. **Front Chem,** v. 2, p. 1-27, 2014.

CONTRERAS, E. Q.; CHO, M.; ZHU, H.; PUPPALA, H. L.; ESCALERA, G.; ZHONG, W.; COLVIN, V.L. Toxicity of Quantum Dots and Cadmium Salt to Caenorhabditis elegans after Multigenerational Exposure. **Environ Sci Technol,** v. 47, n. 2, p. 1148-1154, 2013.

DAOU, T. J.; LI, L.; REISS, P.; JOSSERAND, V.; TEXIER, I. Effect of Poly(ethylene glycol) Length on the in Vivo Behavior of Coated Quantum Dots. **Langmuir,** v. 25, n. 5, p. 3040-3044, 2009.

DAZZAZI, A.; COPPEL, Y.; IN, A.; CHASSENIEUX, C.; MASCALCHI, P.; SALOMÉ, L.; BOUHAOUSS, A.; KAHN, M. L.; GAUFFRE, F. Oligomeric and polymeric surfactants for the transfer of luminescent ZnO nanocrystals to water. **J Mater Chem C,** v. 1, n. 11, p. 2158-2165, 2013.

DE JONG, W. H.; BORM, P. J. A. Drug delivery and nanoparticles: Applications and hazards. **Int J Nanomedicine,** v. 3, n. 2, p. 133-149, 2008.

DERFUS, A. M.; CHAN, W. C. W.; BHATIA, S. N. Probing the Cytotoxicity of Semiconductor Quantum Dots. **Nano Lett,** v. 4, n. 1, p. 11-18, 2004.

DESMAËLE, D.; GREF, R.; COUVREUR, P. Squalenoylation: A generic platform for nanoparticular drug delivery. **J Control Release,** v. 161, n. 2, p. 609-618, 2012.

DONG, Y.; NG, W. K.; SHEN, S.; KIM, S.; TAN, R. B.. Solid lipid nanoparticles: Continuous and potential large-scale nanoprecipitation production in static mixers. **Colloids Surf B Biointerfaces.,** v. 94, n. 0, p. 68-72, 2012.

DUBERTRET, B.; SKOURIDES, P.; NORRIS, D. J.; NOIREAUX, V.; BRIVANLOU, A. H.; LIBCHABER, A. In Vivo Imaging of Quantum Dots Encapsulated in Phospholipid Micelles. **Science,** v. 298, n. 5599, p. 1759-1762, 2002.

EFROS, A.L. Interband absorption of light in a semiconductor sphere. **Sov Phys Semicond**, v.16, p. 772–775, 1982.

FATTAL, E.; TSAPIS, N. Nanomedicine technology: current achievements and new trends. **Clin Transl Imaging,** v. 2, n. 1, p. 77-87, 2014.

FERRO-FLORES, G.; OCAMPO-GARCÍA, B. E.; SANTOS-CUEVAS, C. L.; DE MARÍA RAMÍREZ, F.; AZORÍN-VEJA, E. P.; MELÉNDEZ-ALAFORT, L. Theranostic Radiopharmaceuticals Based on Gold Nanoparticles Labeled with ^{177}Lu and Conjugated to Peptides. **Curr Radiopharm,** v. 8, n. 2, p. 150-159, 2015.

FORTIN-RIPOCHE, J.-P.; MARTINA, M. S.; GAZEAU, F.; MÉNAGER, C.; WILHELM, C.; BACRI, J. C.; LESIEUR, S.; CLÉMENT, O. Magnetic Targeting of Magnetoliposomes to Solid Tumors with MR Imaging Monitoring in Mice: Feasibility. **Radiology,** v. 239, n. 2, p. 415-424, 2006.

FRANK, D.; TYAGI, C.; TOMAR, L.; CHOONARA, Y. E.; DU TOIT, L. C.; KUMAR, P.; PENNY, C.; PILLAY, V. Overview of the role of nanotechnological innovations in the detection and treatment of solid tumors. **Int J Nanomedicine,** v. 9, p. 589-613, 2014.

FU, Y.-S.; DU, X. W.; KULINICH, S. A.; QIU, J. S.; QIN, W. J.; LI, R.; SUN, J.; LIU, J. Stable Aqueous Dispersion of ZnO Quantum Dots with Strong Blue Emission via Simple Solution Route. **J Am Chem Soc,** v. 129, n. 51, p. 16029-16033, 2007.

GABIZON, A.; CATANE, R.; UZIELY, B.; KAUFMAN, B.; SAFRA, T.; COHEN, R.; MARTIN, F.; HUANG, A.; BARENHOLZ, Y. Prolonged Circulation Time and Enhanced Accumulation in Malignant Exudates of Doxorubicin Encapsulated in Polyethylene-glycol Coated Liposomes. **Cancer Res,** v. 54, n. 4, p. 987-992, 1994.

GAO, X.; CUI. Y.; LEVENSON, R. M.; CHUNG, L. W.; NIE, S. In vivo cancer targeting and imaging with semiconductor quantum dots. **Nat Biotech,** v. 22, n. 8, p. 969-976, 2004.

GILL, R.; ZAYATS, M.; WILLNER, I. Semiconductor Quantum Dots for Bioanalysis. **Angew Chem Int Ed Engl,** v. 47, n. 40, p. 7602-7625, 2008.

GOLDMAN, E. R.; BALIGHIAN, E. D.; MATTOUSSI, H.; KUNO, M. K.; MAURO, J. M.; TRAN, P. T.; ANDERSON, G. P. Avidin: A Natural Bridge for Quantum Dot-Antibody Conjugates. **J Am Chem Soc,** v. 124, n. 22, p. 6378-6382, 2002.

GREGORIADIS, G.; RYMAN, B. E. Liposomes as carriers of enzymes or drugs: a new approach to the treatment of storage diseases. **Biochem J,** v. 124, n. 5, p. 58P, 1971.

HAMMAD, T. M.; SALEM, J. K.; HARRISON. R. G.; HEMPELMANN, R.; HEJAZY. N. K. Optical and magnetic properties of Cu-doped ZnO nanoparticles. **J Mater Sci: Mater Electron,** v. 24, n. 8, p. 2846-2852, 2013.

HAN, H.-S.; NIEMEYER, E.; HUANG, Y.; KAMOUN, W. S.; MARTIN, J. D.; BHAUMIK, J.; CHEN, Y.; ROBERGE, S.; CUI, J.; MARTIN, M. R.; FUKUMURA, D.; JAIN, R. K.; BAWENDI, M. G.; DUDA, D.G. Quantum dot/antibody conjugates for in vivo cytometric imaging in mice. **Proc Natl Acad Sci U S A.,** v. 112, n. 5, p. 1350-1355, 2015.

HAN, L.-L.; CUI, L.; WANG, W.-H.; WANG, J.-L.; DU, X.-W. On the origin of blue emission from ZnO quantum dots synthesized by a sol–gel route. **Semicond Sci Technol,** v. 27, n. 6, p. 8, 2012.

HANN, I. M.; PRENTICE, H. G. Lipid-based amphotericin B: a review of the last 10 years of use. **Int J Antimicrob Agents,** v. 17, n. 3, p. 161-169, 2001.

HARDMAN, R. A Toxicologic Review of Quantum Dots: Toxicity Depends on Physicochemical and Environmental Factors. **Environ Health Perspect,** v. 114, n. 2, p. 165-172, 2006.

HEYES, C. D.; KOBITSKI, A. Y.; BREUS, V. V.; NIENHAUS, G. U. Effect of the shell on the blinking statistics of core-shell quantum dots: A single-particle fluorescence study. **Phys. Rev. B,** v. 75, n. 12, p. 125431, 2007.

HINES, M.; GUYOT-SIONNEST, P. Synthesis and Characterization of Strongly Luminescing ZnS-Capped CdSe Nanocrystals. **J Phys Chem,** v. 100, n. 2, p. 468-471, 1996.

HU, Z. RAMÍREZ, D. J. E., CERVERA, B. E. H., OSKAM, G., SEARSON, P. C. Synthesis of ZnO Nanoparticles in 2-Propanol by Reaction with Water. **J Phys Chem B,** v. 109, n. 22, p. 11209-11214, 2005a.

HU, Z., SANTOS, J. F. H., OSKAM, G., SEARSON, P. C. Influence of the reactant concentrations on the synthesis of ZnO nanoparticles. **J Colloid Interface Sci,** v. 288, n. 1, p. 313-316, 2005b.

HU, Z.; OSKAM, G.; SEARSON, P. C. Influence of solvent on the growth of ZnO nanoparticles. **J Colloid Interface Sci,** v. 263, n. 2, p. 454-460, 2003.

HUYNH, N. T.; PASSIRANI, C.; SAULNIER, P.; BENOIT, J. P. Lipid nanocapsules: A new platform for nanomedicine. **Int J Pharm,** v. 379, n. 2, p. 201-209, 2009.

HYUN, B.-R.; CHEN, H.; REY, D. A.; WISE, F. W.; BATT, C. A. Near-Infrared Fluorescence Imaging with Water-Soluble Lead Salt Quantum Dots. **J Phys Chem B,** v. 111, n. 20, p. 5726-5730, 2007.

HYUN, H.; PARK, M. H.; OWENS, E. A.; WADA, H.; HENARY, M.; HANDGRAAF, H. J.; VAHRMEIJER, A. L.; FRANGIONI, J. V.; CHOI, H. S. Structure-inherent targeting of near-infrared fluorophores for parathyroid and thyroid gland imaging. **Nat Med,** v. 21, n. 2, p. 192-197, 2015.

IOANNOU, D.; GRIFFIN, D. K. Nanotechnology and molecular cytogenetics: the future has not yet arrived. **Nano Revs,** v. 1, p. 10.3402/, 2010.

ISNAENI; KIM, K. H.; NGUYEN, D. L.; LIM, H.;NGA, P. T.; CHO, Y.-H. Shell layer dependence of photoblinking in CdSe/ZnSe/ZnS quantum dots. **Appl Phys Lett,** v. 98, n. 1, p. 012109-3, 2011.

JAISWAL, J. K.; MATTOUSSI, H.; MAURO, J. M.; SIMON, S. M. Long-term multiple color imaging of live cells using quantum dot bioconjugates. **Nat Biotech,** v. 21, n. 1, p. 47-51, 2003.

JIA, Z.; MISRA, R. D. K. Tunable ZnO quantum dots for bioimaging: synthesis and photoluminescence. **Mater Technol,** v. 28, n. 4, p. 221-227, 2013.

JIN, S.; HU, Y.; GU, Z.; LIU, L.; WU, H.-C. Application of Quantum Dots in Biological Imaging. **J Nanomater,** v. 2011, p. 13, 2011.

JOSHI, B. P.; WANG, T. D. Exogenous Molecular Probes for Targeted Imaging in Cancer: Focus on Multi-modal Imaging. **Cancers,** v. 2, n. 2, p. 1251-1287, 2010.

KIRCHNER, C.; LIEDL, T.; KUDERA, S.; PELLEGRINO, T.; MUÑOZ JAVIER, A.; GAUB, H. E.; STÖLZLE, S.; FERTIG, N.; PARAK, W. J. Cytotoxicity of Colloidal CdSe and CdSe/ZnS Nanoparticles. **Nano Lett,** v. 5, n. 2, p. 331-338, 2005.

KOBAYASHI, K.; WEI, J.; IIDA, R.; IJIRO, K.;NIIKURA, K. Surface engineering of nanoparticles for therapeutic applications. **Polym J,** v. 46, n. 8, p. 460-468, 2014.

KUMAR, S.; SAHARE, P. D. Observation of band gap and surface defects of ZnO nanoparticles synthesized via hydrothermal route at different reaction temperature. **Opt Commun,** v. 285, n. 24, p. 5210-5216, 2012.

KWON, S. R. C. A. G. S. Polymeric Micelles for Drug Delivery. **Curr Pharm Des,** v. 12, n. 36, p. 4669-4684, 2006.

LAMPRECHT, A. Nanomedicines in gastroenterology and hepatology. **Nat Rev Gastroenterol Hepatol,** v. 12, n. 4, p. 195-204, 2015.

LI, L.; DAOU, T. J.; TEXIER, I.;CHI, T. T. K.; LIEM, N. Q.; REISS, P. Highly Luminescent CuInS2/ZnS Core/Shell Nanocrystals: Cadmium-Free Quantum Dots for In Vivo Imaging. **Chem Mater,** v. 21, n. 12, p. 2422-2429, 2009.

LI, S., SUN, Z., LI, R., DONG, M., ZHANG, L., QI, W., ZHANG, X., WANG, H. ZnO Nanocomposites Modified by Hydrophobic and Hydrophilic Silanes with Dramatically Enhanced Tunable Fluorescence and Aqueous Ultrastability toward Biological Imaging Applications. **Sci Rep,** v. 5, p. 8475:1-8, 2015.

LIU, Y.; AI, K.; YUAN, Q.; LU, L. Fluorescence-enhanced gadolinium-doped zinc oxide quantum dots for magnetic resonance and fluorescence imaging. **Biomaterials,** v. 32, n. 4, p. 1185-1192, 2011.

LORENZ, C.; EMMERLING, A.; FRICKE, J.; SCHMIDT, T.; HILGENDOR, M.; SPANHEL, L.; MÜLLER, G. Aerogels containing strongly photoluminescing zinc oxide nanocrystals1. **J Non Cryst Solids,** v. 238, n. 1–2, p. 1-5, 1998.

LUO, J.; ZHAO, S.; WU, P.; ZHANG, K.; PENG, C.; ZHENG, S. Synthesis and characterization of new Cd-doped ZnO/ZnS core-shell quantum dots with tunable and highly visible photoluminescence. **J Mater Chem C,** v. 3, n. 14, p. 3391-3398, 2015.

MAEDA, H. Tumor-Selective Delivery of Macromolecular Drugs via the EPR Effect: Background and Future Prospects. **Bioconjug Chem,** v. 21, n. 5, p. 797-802, 2010.

MANAIA, E. B., KAMINSKI, R. C. K., CAETANO, B.L., BRIOIS, V., CHIAVACCI, L. A., BOURGAUX, C. Surface modified Mg-doped ZnO QDs for biological imaging. **Eur J Nanomed**, v. 7, p. 109-120 , 2015.

MATSUMURA, Y.; MAEDA, H. A New Concept for Macromolecular Therapeutics in Cancer Chemotherapy: Mechanism of Tumoritropic Accumulation of Proteins and the Antitumor Agent Smancs. **Cancer Res,** v. 46, n. 12 Part 1, p. 6387-6392, 1986.

MOUSSA, H.; MERLIN, C.; DEZANET, C.; BALAN, L.; MEDJAHDI, G.; BEN-ATTIA, M.; SCHNEIDER, R. Trace amounts of Cu2+ ions influence ROS production and cytotoxicity of ZnO quantum dots. **J Hazard Mater,** v. 304, p. 532-542, 2016.

MOUSSODIA, R.-O, BALAN, L., MERLIN, C., MUSTIN, C., SCHNEIDER, R. Biocompatible and stable ZnO quantum dots generated by functionalization with siloxane-core PAMAM dendrons. **J Mater Chem**, v. 20, p. 1147-1155, 2010.

MULDER, W. J.; KOOLE, R.; BRANDWIJK, R. J.; STORM, G.; CHIN, P. T.; STRIJKERS, G. J.; DE MELLO DONEGÁ, C.; NICOLAY, K.; GRIFFIOEN, A. W. Quantum Dots with a Paramagnetic Coating as a Bimodal Molecular Imaging Probe. **Nano Lett,** v. 6, n. 1, p. 1-6, 2006.

MURA, S.; NICOLAS, J.; COUVREUR, P. Stimuli-responsive nanocarriers for drug delivery. **Nat Mater,** v. 12, n. 11, p. 991-1003, 2013.

MUTHU, M. S.; LEONG, D. T.; MEI, L.; FENG, S. S. Nanotheranostics - Application and Further Development of Nanomedicine Strategies for Advanced Theranostics. **Theranostics**, v. 4, n. 6, p. 660-677, 2014.

NANODIODE, 2015. Disponível em: <http://en.rusnano.com/upload/OldNews/Files/33619/current.gif>. Acesso em: 30 mar.2016.

NICOLAS, J.; MURA, S.; BRAMBILLA, D.; MACKIEWICZ, N.; COUVREUR, P. Design, functionalization strategies and biomedical applications of targeted biodegradable/biocompatible polymer-based nanocarriers for drug delivery. **Chem Soc Rev,** v. 42, n. 3, p. 1147-1235, 2013.

NOEI, H., JIN, L., QIU, H., XU, M., GAO, Y., ZHAO, J., KAUER, M., WÖLL, C., MUHLER, M., WANG, Y. Vibrational spectroscopic studies on pure and metal-covered metal oxide surfaces. **Phys Status Solidi B Basic Solid State Phys**, v. 250, n. 6, p. 1204-1221, 2013.

NORBERG, N. S.; KITTILSTVED, K. R.; AMONETTE, J. E.; KUKKADAPU, R. K.; SCHWARTZ, D. A.; GAMELIN, D. R. Synthesis of Colloidal Mn2+:ZnO Quantum Dots and High-TC Ferromagnetic Nanocrystalline Thin Films. **J Am Chem Soc,** v. 126, n. 30, p. 9387-9398, 2004.

OH, E.; LIU, R.; NEL, A.; GEMILL, K. B.; BILAL, M.; COHEN, Y.; MEDINTZ, I. L. Meta-analysis of cellular toxicity for cadmium-containing quantum dots. **Nat Nanotechnol,** v. advance online publication, 2016.

OWENS III, D. E.; PEPPAS, N. A. Opsonization, biodistribution, and pharmacokinetics of polymeric nanoparticles. **Int J Pharm,** v. 307, n. 1, p. 93-102, 2006.

PAN, D.; WANG, Q.; JIANG, S.; JI, X.; AN, L. Synthesis of Extremely Small CdSe and Highly Luminescent CdSe/CdS Core–Shell Nanocrystals via a Novel Two-Phase Thermal Approach. **Adv Mater,** v. 17, n. 2, p. 176-179, 2005.

PAN, J.; WAN, D.; BIAN, Y.; GUO, Y.; JIN, F.; WANG, T.; GONG, T. Reduction of nonspecific binding for cellular imaging using quantum dots conjugated with vitamin E. **AIChE J,** v. 60, n. 5, p. 1591-1597, 2014.

PAN, Z.-Y.; LIANG, J.; ZHENG, Z. Z.; WANG, H. H.; XIONG, H. M. The application of ZnO luminescent nanoparticles in labeling mice. **Contrast Media Mol Imaging,** v. 6, n. 4, p. 328-330, 2011.

PANSARE, V.; HEJAZI, S.; FAENZA, W.; PRUD'HOMME, R. K.. Review of Long-Wavelength Optical and NIR Imaging Materials: Contrast Agents, Fluorophores and Multifunctional Nano Carriers. **Chem Mater.,** v. 24, n. 5, p. 812-827, 2012.

PAPAGIANNAROS, A.; LEVCHENKO, T.; HARTNER, W.; MONGAYT, D.; TORCHILIN, V. Quantum dots encapsulated in phospholipid micelles for imaging and quantification of tumors in the near-infrared region. **Nanomedicine,** v. 5, n. 2, p. 216-224, 2009.

PATTNI, B. S.; CHUPIN, V. V.; TORCHILIN, V. P. New Developments in Liposomal Drug Delivery. **Chemical Reviews,** v. 115, n. 19, p. 10938-10966, 2015.

PELTIER, S.; OGER, J. M.; LAGARCE, F.; COUET, W.; BENOÎT, J. P. Enhanced Oral Paclitaxel Bioavailability After Administration of Paclitaxel-Loaded Lipid Nanocapsules. **Pharm Res,** v. 23, n. 6, p. 1243-1250, 2006.

PENET, M.-F.; MIKHAYLOVA, M.; LI, C.; KRISHNAMACHARY, B.; GLUNDE, K.; PATHAK, A. P.; BHUJWALLA, Z. M.. Applications of molecular MRI and optical imaging in cancer. **Future Med Chem,** v. 2, n. 6, p. 975-988, 2010.

PRADHAN, A. K.; MUNDLE, R. M.; SANTIAGO, K.; SKUZA, J. R.; XIAO, B.; SONG, K. D.; BAHOURA, M.; CHEAITO, R.; HOPKINS, P. E. Extreme tunability in aluminum doped Zinc Oxide plasmonic materials for near-infrared applications. **Sci. Rep.,** v. 4, p. 1-6, 2014.

PURI, A.; LOOMIS, K.; SMITH, B.; LEE, J. H.; YAVLOVICH, A.; HELDMAN, E.; BLUMENTHAL, R.. Lipid-Based Nanoparticles as Pharmaceutical Drug Carriers: From Concepts to Clinic. **Crit Rev Ther Drug Carrier Syst.,** v. 26, n. 6, p. 523-580, 2009.

RABANEL, J. M.; AOUN, V.; ELKIN, I.; MOKHTAR, M.; HILDGEN, P. Drug-Loaded Nanocarriers: Passive Targeting and Crossing of Biological Barriers. **Curr Med Chem,** v. 19, n. 19, p. 3070-3102, 2012.

RATH, T.; KUNERT, B.; RESEL, R.; FRITZ-POPOVSKI, G.; SAF, R.; TRIMMEL, G. Investigation of Primary Crystallite Sizes in Nanocrystalline ZnS Powders: Comparison of Microwave Assisted with Conventional Synthesis Routes. **Inorg Chem,** v. 47, n. 8, p. 3014-3022, 2008.

REISS, P. ZnSe based colloidal nanocrystals: synthesis, shape control, core/shell, alloy and doped systems. **New J Chem,** v. 31, n. 11, p. 1843-1852, 2007.

REISS, P.; PROTIÈRE, M.; LI, L. Core/Shell Semiconductor Nanocrystals. **Small,** v. 5, n. 2, p. 154-168, 2009.

SCHMIDT, T.; MÜLLER, G.; SPANHEL, L. Activation of 1.54 μm Er3+ Fluorescence in Concentrated II−VI Semiconductor Cluster Environments. **Chem Mater,** v. 10, n. 1, p. 65-71, 1998.

SCHWARTZ, D. A.; NORBERG, N. S.; NGUYEN, Q. P.; PARKER, J. M.; GAMELIN, D. R. Magnetic Quantum Dots: Synthesis, Spectroscopy, and Magnetism of Co2+- and Ni2+-Doped ZnO Nanocrystals. **J Am Chem Soc,** v. 125, n. 43, p. 13205-13218, 2003.

SHARMA, S.; VYAS, R.; SHARMA, N.; SINGH, V.; SINGH, A.; KATARIA, V.; GUPTA, B. K.; VIJAY, Y. K. Highly efficient green light harvesting from Mg doped ZnO nanoparticles: Structural and optical studies. **J Alloys Compd,** v. 552, p. 208-212, 2013.

SIEKMANN, B.; WESTESEN, K. Sub-micron sized parenteral carrier systems based on solid lipid **Pharm. Pharmacol. Lett.,** v. 1, p. 123-126, 1992.

SKANDRANI, N.; BARRAS, A.; LEGRAND, D.; GHARBI, T.; BOULAHDOUR, H.; BOUKHERROUB, R.. Lipid nanocapsules functionalized with polyethyleneimine for plasmid DNA and drug co-delivery and cell imaging. **Nanoscale,** v. 6, n. 13, p. 7379-7390, 2014.

SMITH, A. M.; DUAN, H.; MOHS, A. M.; NIE, S. Bioconjugated quantum dots for in vivo molecular and cellular imaging. **Adv Drug Deliv Rev,** v. 60, n. 11, p. 1226-1240, 2008.

SPANHEL, L.; ANDERSON, M. A. Semiconductor clusters in the sol-gel process: quantized aggregation, gelation, and crystal growth in concentrated zinc oxide colloids. **J Am Chem Soc,** v. 113, n. 8, p. 2826-2833, 1991.

SPERLING, R. A.; PARAK, W. J. Surface modification, functionalization and bioconjugation of colloidal inorganic nanoparticles. **Philos Trans R Soc London, Ser A,** v. 368, n. 1915, p. 1333-1383, 2010.

STOCKHOFE, K.; POSTEMA, J. M.; SCHIEFERSTEIN, H.; ROSS, T. L. Radiolabeling of Nanoparticles and Polymers for PET Imaging. **Pharmaceuticals,** v. 7, n. 4, p. 392–418, 2014.

SU, Y.; HE, Y.; LU, H.; SAI, L.; LI, Q.; LI, W.; WANG, L.; SHEN, P.; HUANG, Q.; FAN, C. The cytotoxicity of cadmium based, aqueous phase – Synthesized, quantum dots and its modulation by surface coating. **Biomaterials,** v. 30, n. 1, p. 19-25, 2009.

SUN, L.-W.; SHI, H.-Q.; LI, W.-N.; XIAO, H.-M.; FU, S.-Y.; CAO, X.-Z.; LI, Z.-X.. Lanthanum-doped ZnO quantum dots with greatly enhanced fluorescent quantum yield. **J Mater Chem,** v. 22, n. 17, p. 8221-8227, 2012.

TANG, J.; KEMP, K. W.; HOOGLAND, S.; JEONG, K. S.; LIU, H.; LEVINA, L.; FURUKAWA, M.; WANG, X.; DEBNATH, R.; CHA, D.; CHOU, K. W.; FISCHER, A.; AMASSIAN, A.; ASBURY, J. B.; SARGENT, E. H. Colloidal-quantum-dot photovoltaics using atomic-ligand passivation. **Nat Mater,** v. 10, n. 10, p. 765-771, 2011.

TERRENO, E.; DASTRÙ, W.; DELLI CASTELLI, D.; GIANOLIO, E.; GENINATTI CRICH, S.; LONGO, D.; AIME, S. Advances in Metal-Based Probes for MR Molecular Imaging Applications. **Curr Med Chem,** v. 17, n. 31, p. 3684-3700, 2010.

TOKUMOTO, M. S., BRIOS, V.; SANTILLI, C. V.; PULCINELLI, S. H. Preparation of ZnO Nanoparticles: Structural Study of the Molecular Precursor. **J Solgel Sci Technol,** v. 26, n. 1-3, p. 547-551, 2003a.

TOKUMOTO, M. S.,PULCINELLI, S. H., SANTILLI, C. V. BRIOIS, V. Catalysis and Temperature Dependence on the Formation of ZnO Nanoparticles and of Zinc Acetate Derivatives Prepared by the Sol−Gel Route. **J Phys Chem B,** v. 107, n. 2, p. 568-574, 2003b.

TORCHILIN, V. P. Recent advances with liposomes as pharmaceutical carriers. **Nat Rev Drug Discov,** v. 4, n. 2, p. 145-160, 2005.

VIGLIANTI, B. L.; PONCE, A. M.; MICHELICH, C. R.; YU, D.; ABRAHAM, S. A.; SANDERS, L.; YARMOLENKO, P. S.; SCHROEDER, T.; MACFALL, J. R.; BARBORIAK, D. P.; COLVIN, O. M.; BALLY, M. B.; DEWHIRST, M. Chemodosimetry of in vivo tumor liposomal drug concentration using MRI. **Magn Reson Med,** v. 56, n. 5, p. 1011-1018, 2006.

WANG, X.; REN, X.; KAHEN, K.; HAHN, M. A.; RAJESWARAN, M.; MACCAGNANO-ZACHER, S.; SILCOX, J.; CRAGG, G. E.; EFROS, A. L.; KRAUSS, T. D. Non-blinking semiconductor nanocrystals. **Nature,** v. 459, n. 7247, p. 686-689, 2009.

WANG, Y. S.; THOMAS, P. J.; O'BRIEN, P. Optical properties of ZnO nanocrystals doped with Cd, Mg, Mn, and Fe ions. **J Phys Chem B,** v. 110, n. 43, p. 21412-21415, 2006.

WEI, X.; WANG, W.; CHEN, K. ZnO:Er,Yb,Gd Particles Designed for Magnetic-Fluorescent Imaging and Near-Infrared Light Triggered Photodynamic Therapy. **J Phys Chem C Nanomater Interfaces,** v. 117, n. 45, p. 23716-23729, 2013.

WEISSLEDER, R. A clearer vision for in vivo imaging. **Nat Biotech,** v. 19, n. 4, p. 316-317, 2001.

WEN, C.-J.; ZHANG, L. W.; AL-SUWAYEH, S. A.; YEN, T. C.; FANG, J. Y. Theranostic liposomes loaded with quantum dots and apomorphine for brain targeting and bioimaging. **Int J Nanomedicine,** v. 7, p. 1599-1611, 2012.

WIECINSKI, P. N.; METZ, K. M.; KING HEIDEN, T. C.; LOUIS, K. M.; MANGHAM, A. N.; HAMERS, R. J.; HEIDEMAN, W.; PETERSON, R. E.; PEDERSEN, J. A. Toxicity of Oxidatively Degraded Quantum Dots to Developing Zebrafish (Danio rerio). **Environ Sci Technol.,** v. 47, n. 16, p. 9132-9139, 2013.

WOLSKA, E.; KASZEWSKI, J.; KIEŁBIK, P.; GRZYB, J.; GODLEWSKI, M. M.; GODLEWSKI, M.. Rare earth activated ZnO nanoparticles as biomarkers. **Opt Mater,** v. 36, n. 10, p. 1655-1659, 2014.

WOOD, A.; GIERSIG, M.; HILGENDORFF, M.; VILAS-CAMPOS, A.; LIZ-MARZÁN, L. M.; MULVANEY, P.. Size Effects in ZnO: The Cluster to Quantum Dot Transition. **Aust J Chem,** v. 56, n. 10, p. 1051-1057, 2003.

WU, Y. L.; FU, S.; TOK, A. I.; ZENG, X. T.; LIM, C. S.; KWEK, L. C.; BOEY, F. C. A dual-colored bio-marker made of doped ZnO nanocrystals. **Nanotechnology,** v. 19, n. 34, p.1-9, 2008.

XIONG, H.-M. XU, Y.; REN, Q. G.; XIA, Y. Y. Stable Aqueous ZnO@Polymer Core−Shell Nanoparticles with Tunable Photoluminescence and Their Application in Cell Imaging. **J Am Chem Soc,** v. 130, n. 24, p. 7522-7523, 2008.

XIONG, H.-M. Photoluminescent ZnO nanoparticles modified by polymers. **J Mater Chem,** v. 20, n. 21, p. 4251-4262, 2010.

YAN, C.; TANG, F.; LI, L.; LI, H.; HUANG, X.; CHEN, D.; MENG, X.; REN, J. Synthesis of Aqueous CdTe/CdS/ZnS Core/shell/shell Quantum Dots by a Chemical Aerosol Flow Method. **Nanoscale Res Lett,** v. 5, n. 1, p. 189-194, 2009.

YANG, J.; YAO, M. H.; WEN, L.; SONG, J. T.; ZHANG, M. Z.; ZHAO, Y. D.; LIU, B. Multifunctional quantum dot-polypeptide hybrid nanogel for targeted imaging and drug delivery. **Nanoscale,** v. 6, n. 19, p. 11282-11292, 2014.

YANG, Y.; JIN, Y.; HE, H.; WANG, Q.; TU, Y.; LU, H.; YE, Z. Dopant-Induced Shape Evolution of Colloidal Nanocrystals: The Case of Zinc Oxide. **J Am Chem Soc,** v. 132, n. 38, p. 13381-13394, 2010.

YANG Y., LV, S-Y. YU, B., XU, S., SHEN, J., ZHAO, T., ZHANG, H. Hepatotoxicity assessment of Mn-doped ZnS quantum dots after repeated administration in mice. **Int J Nanomedicine,** v. 10, p. 5787-5796, 2015.

YHEE, J. Y.; LEE, S.; KIM, K. Advances in targeting strategies for nanoparticles in cancer imaging and therapy. **Nanoscale,** v. 6, n. 22, p. 13383-13390, 2014.

YIN, Q.; JIN, X.; YANG, G.; JIANG, C.; SONGA, Z.; SUN, G. Biocompatible folate-modified Gd3+/Yb3+-doped ZnO nanoparticles for dualmodal MRI/CT imaging. **RSC Adv,** v. 4, n. 96, p. 53561-53569, 2014.

YOUSEFI, R.; ZAK, A. K.; JAMALI-SHEINI, F. Growth, X-ray peak broadening studies, and optical properties of Mg-doped ZnO nanoparticles. **Mater Sci Semicond Process,** v. 16, n. 3, p. 771-777, 2013.

YU, M. K.; PARK, J.; JON, S. Targeting Strategies for Multifunctional Nanoparticles in Cancer Imaging and Therapy. **Theranostics**, v. 2, n. 1, p. 3-44, 2012.

LV, Y., XIAO, W. LI, W., XUE, J., DING, J. Controllable synthesis of ZnO nanoparticles with high intensity visible photoemission and investigation of its mechanism. **Nanotechnology,** v. 24, n. 17, p. 175702:1-10, 2013.

ZHANG, Z.H., WANG, X., XU, J.B., MULLER, S., RONNING, C. & LI., Q. Evidence of intrinsic ferromagnetism in individual dilute magnetic semiconductor nanostructures. **Nature Nanotech**. v. 4, p. 523-527 , 2009.

ZHANG, H-J., XIONG, H-M., REN, Q-G., XIA, Y-Y., KONG, J-L. ZnO@silica core–shell nanoparticles with remarkable luminescence and stability in cell imaging. **J Mater Chem**, v. 22, p. 13159-13165, 2012.

ZHANG, Z-Y., XU, Y-D., MA, Y-Y., QIU, L-L., WANG, Y., KONG, J-L., XIONG, H-M. Biodegradable ZnO@polymer Core–Shell Nanocarriers: pH-Triggered Release of Doxorubicin In Vitro. **Angew Chem Int Ed Engl**, v. 52, p. 4127-4131, 2013.

ZHANG, Y.; HUANG, Y.; LI, S. Polymeric Micelles: Nanocarriers for Cancer-Targeted Drug Delivery. **AAPS PharmSciTech**, New York**,** v. 15, n. 4, p. 862-871, 2014.

ZHAO, L.-H.; ZHANG, R.; ZHANGA, J.; SUN, S.-Q. Synthesis and characterization of biocompatible ZnO nanoparticles. **CrystEngComm,** v. 14, n. 3, p. 945-950, 2012.

ZHOU, R.; LI, M.; WANG, S.; WU, P.; WU, L.; HOU, X. Low-toxic Mn-doped ZnSe@ZnS quantum dots conjugated with nano-hydroxyapatite for cell imaging. **Nanoscale,** v. 6, n. 23, p. 14319-14325, 2014.

CHAPTER II
Materials and Methods

Chapter II - Materials and Methods

II.1. Materials

- Zinc acetate dihydrate, $ZnAc_2 \cdot 2H_2O$ (Qhemis, 98%);
- Thioacetamide, TAA (Sigma-Aldrich, 99.0%);
- Lithium hydroxide monohydrate, $LiOH \cdot H_2O$ (Vetec, 98%);
- Magnesium acetate tetrahydrate, $Mg(Ac)_2 \cdot 4\ H_2O$ (Alfa Aesar);
- Oleic acid (Alfa Aesar);
- Chloroform (VWR, BDH, Prolabo);
- Tetrahydrofuran, THF (VWR, BDH, Prolabo);
- Gelucire 50/13® (Gattefosse);
- 1,2-distearoyl-sn-glycero-3-phosphoethanolamine-N-[amino(polyethylene glycol)-2000] ammonium salt, DSPE-Peg 2000 (Avanti Lipids);
- 1,2-dipalmitoyl-sn-glycero-3-phosphocholine, DPPC (Avanti Lipids);
- Ethanol (Qhemis, 99.5%);
- Heptane (Synth, 99%);

All reagents were used as received, without further purification. Zinc oxide (Alfa Aesar) was used as standard. Figure II.1 presents the of DPPC, DSPE-Peg 2000 and oleic acid molecules.

Figure II.1. Molecule of (a) DPPC, (b) DSPE-Peg 2000, and (c) oleic acid.

(a)

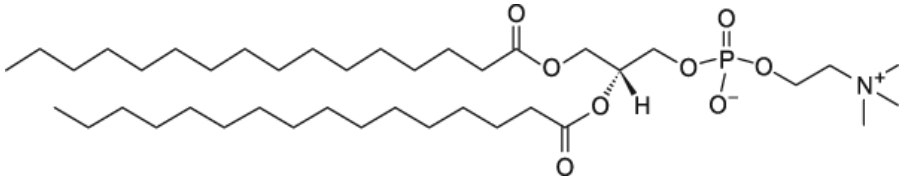

(b)

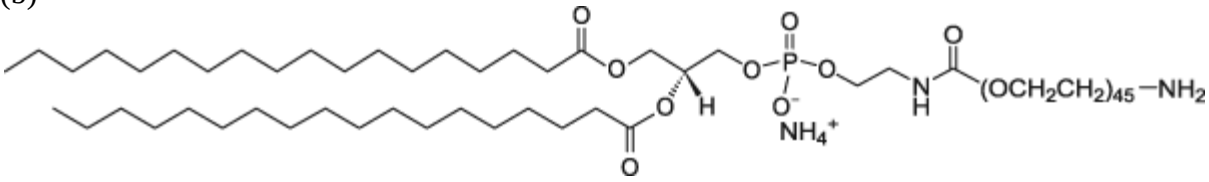

(c)

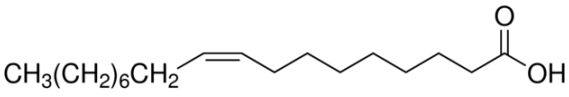

II.2. Synthesis

II.2.1. ZnO QDs

ZnO colloidal suspensions (ZnO Susp) were synthesised according to the sol-gel route proposed by Spanhel and Anderson (SPANHEL and ANDERSON, 1991). The $Zn_4O(Ac)_6$ tetrameric precursor (herein after referred to as ZnAc precursor) was first prepared by refluxing an absolute ethanol solution containing 0.05 M $ZnAc_2 \cdot 2H_2O$ during 2 h at 80 °C. Figure II.2 shows the experimental setup for ZnAc precursor preparation.

Figure II.2. Experimental setup for ZnAc precursor preparation.

The obtained transparent precursor solution was stored at ~ 4°C. ZnO colloidal suspensions were prepared by hydrolysis and condensation reactions, by adding under continuous stirring to the precursor a solution of 0.5 M of $LiOH \cdot H_2O$ in absolute ethanol.

The reactions were carried out either at 40°C for 5 s (chapter III) or at 60°C during 1 h (chapter IV). The ZnO colloidal suspensions were then cooled and stored at ~4°C to prevent any further growth. We used a nominal molar ratio [OH]/[Zn] = 0.5 in the chapter III and 1.4 in the chapter IV.

II.2.2. ZnS QDs

A ZnS colloidal suspension was synthesized by mixing 10 mL of ZnAc precursor with 10 mL of TAA 5mM ethanolic solution under continuous stirring at 60°C for 10 min. The suspension was then cooled and stored at ~4°C.

II.2.3. ZnO/ZnS core-shell QDs and ZnO and ZnS QDs mixtures

Two synthesis routes were explored in an attempt to prepare ZnO/ZnS core-shell QDs.

First, 10 mL of ZnO colloidal suspension was allowed to react with 10 mL of TAA ethanolic solution (as sulphur source) under continuous stirring at 60°C for 40 min. The suspension was then cooled and stored at ~4°C (Route 1).

The second route (Route 2) consisted in mixing 10 mL of the ZnAc precursor with 10 mL of TAA ethanolic solution and 500 μL of LiOH (0.5 M) in the same conditions than in Route 1. The addition of LiOH is required to maintain the same hydrolysis ratio than for the preparation of the ZnO colloidal suspension.

To investigate the effect of TAA on the formation of nanoparticles, different concentrations of TAA were used for the sulphidation process, while the other parameters remain unchanged. The final products prepared using Route 1 with different amounts of TAA (1.5 mM, 5 mM and 50 mM) were designed as SUSP_TAA1.5mM, SUSP_TAA5mM and SUSP_TAA50mM, respectively, and the final products prepared using the Route 2 with different amounts of TAA (1.5 mM, 5 mM and 50 mM) were designed as PREC_TAA1.5mM, PREC_TAA5mM and PREC_TAA50mM, respectively, where SUSP and PREC correspond to suspension and precursor respectively.

II.2.4. $Zn_{1-x}Mg_xO$ QDs

Mg doping was achieved by adding a $Mg(Ac)_2$ ethanol solution to the ZnAc precursor solution, keeping the total molar concentration [Zn+Mg] constant. The [LiOH]/[Zn+Mg] molar ratio was also kept constant (r = 1.4) . The other reaction conditions were similar to those described above for preparing undoped nanoparticles. The Mg precursor concentration was increased from 0.01 to 50 mol%. Samples are referred to using nominal Mg^{2+} mole fraction in the initial reaction mixture.

II.2.5. Powder obtainment

The as-synthesized colloidal suspensions (ZnO, ZnS, ZnO/ZnS, and $Zn_{1-x}Mg_xO$) were mixed with a "nonsolvent" heptane (MEULENKAMP, 1998) (1:4) to induce the precipitation of the QDs, and then centrifuged at 20 °C for 10 minutes (10000 rpm). The supernatant solution was discarded and the powder was dried under vacuum at room temperature. The dried powder was characterized by XRD and XAS.

II.2.6. Oleic acid-surface modified QDs: OA-ZnO QDs and OA-$Zn_{0.8}Mg_{0.2}O$ QDs

ZnO QDs capped by oleic acid (OA) were obtained by adding oleic acid (13mM, 18.8mM, 25mM or 36.7mM) to the ZnO QD suspension under vigorous stirring during 30 min at 60°C. The resulting turbid solutions were stored at 8°C overnight and then centrifuged (10 min at 10000 rpm). The supernatant was removed and the OA-ZnO QDs were washed with ethanol, in which they could not be dispersed, in order to remove the unreacted OA. Afterward, the washed OA-ZnO QDs were dried at room temperature under vacuum and put in suspension into chloroform or toluene.

II.3. QDs incorporation into lipid-based nanocarriers

II.3.1. Preparation of DPPC and DSPE-Peg 2000 –based formulations

Phospholipid – QD hybrids were prepared following the thin lipid film hydration protocol. Phospholipids and OA-$Zn_{0.8}Mg_{0.2}O$ QDs dispersed in chloroform were mixed to achieve a homogeneous distribution of QDs within the phospholipids. The organic solvent was evaporated under a N_2 stream and then under vacuum. The dry films were hydrated and the mixtures were vortexed.

II.3.2. Preparation of Solid Lipid Nanoparticles (SLN) containing QDs

SLNs containing $Zn_{0.8}Mg_{0.2}O$ QDs (QD-LN) were prepared into water, using simple nanoprecipitation technique (LEPELTIER, BOURGAUX and COUVREUR, 2014). Gelucire 50/13®, which is composed by 20% of mono-, di- and tri- acylglycerides of palmitic and stearic acid, 8% of free PEG 1500, and 72% of mono- and di-ester of PEG 1500, was used as lipid source. Gelucire 50/13® was dissolved in the $Zn_{0.8}Mg_{0.2}O$ QD colloidal ethanolic solution (without OA), and it was added drop-wise, under continuously stirring (10000 rpm) into Milli-Q water. To define the optimal conditions for the preparation of stable

nanoassemblies, we have tested the influence of various parameters: the QDs:Gelucire 50/13® ratio, the water:solvent volume ratio and the process used to eliminate ethanol. The Gelucire 50/13® was solubilized at room temperature, 50°C and 60°C.

Nanoprecipitation of the nanoassemblies occurred spontaneously. Two processes were used to eliminate ethanol: (i) the solvent was completely evaporated under vacuum at 45°C using a rotavapor; and (ii) the nanoparticle suspensions were introduced in a dialysis bag (Spectra Por Biotech membranes 132.720 MWCO 3,500) and dialyzed against Milli-Q water. The mean diameter of the nanoassemblies was determined by Quasi Elastic Ligth Scattering (QELS) in the Zetasizer Nano ZS Malvern; Malvern Instruments.

Formulations with OA-surface modified $Zn_{0.8}Mg0.2O$ QDs were also tested: the chloroform of the QD suspension (500 µL) was evaporated and either 500 µL of acetone or tetrahydrofuran (THF) were used to mix Gelucire and OA-QDs. Only the suspension with the QDs: Gelucire ratio 1:3 and THF: water ratio 1:3 was stable (formulation named THF).

II.4. Characterizations

X-ray scattering is a powerful technique providing structural information at different typical length scales. Wide-angle X-ray diffraction (XRD) describes the structure at an atomic scale (from about 1 to 10 Å) while small-angle X-ray scattering (SAXS) describes the organization of the sample in a range from 10 to about 1000 Å.

II.4.1. X-ray diffraction (XRD)

X-ray diffraction at wide angles enables to characterize the stacking of parallel atomic planes in a crystalline material. Indeed, X-rays are diffracted by a crystalline material at specific angles defined by the Bragg's law:

$$2d \sin \theta = n\lambda,$$

where n is an integer, λ is the X-ray wavelength, θ is the scattering angle and d is the interplanar distance (DONG and BOYD, 2011). Figure II.3 displays the wave behavior reflected off atomic planes following the Bragg's law.

Figure II.3. The Bragg description of diffraction in terms of the reflection of a plane wave (wavelength λ) incident at an angle θ to atomic planes of spacing d.

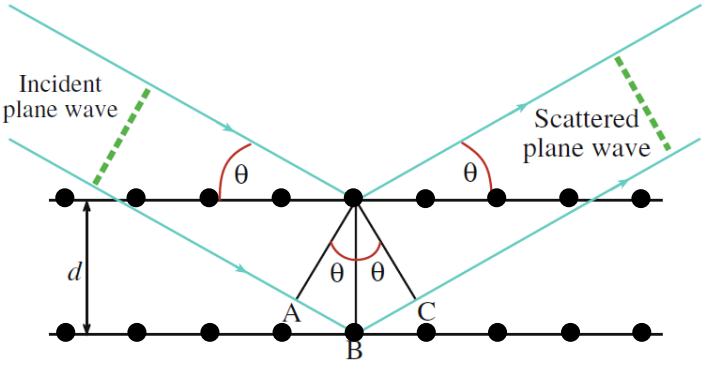

Figure adapted from the book "Transmission Electron Microscopy: A Textbook for Materials Science" (WILLIAMS and CARTER, 2009).

The broadening of the peaks can result from the limited crystal size and from defects in the crystal lattice. When it is assumed that the peak broadening is essentially due to size effects, the average nanocrystallite size can be evaluated using the Debye-Scherrer relation:

$$D = \kappa\lambda/\beta\cos\theta,$$

where D is the crystallite size, κ is a constant (shape factor), λ is the X-ray wavelength, β is the full-width-at-half-maximum of a characteristic diffraction peak, and θ is the diffraction angle (WEST, 1992). In this work, the Gaussian function was used to model the peaks involved in the crystallite size calculation.

XRD analysis of nanoparticles was performed on a Bruker D2 PHASER diffractometer, using the Cu Kα radiation, λ = 1.5418 Å, selected by a curved graphite monochromator and a fixed divergence slit of 1/8 deg. in a Bragg–Brentano configuration. The diffraction intensity data were measured in the 2θ range 5 - 70 deg. by the step counting method (0.1 deg. step and 3 s counting time).

II.4.2. Small-Angle X-ray Scattering (SAXS)

This technique can give information about the shapes and sizes of dispersed particles (such as biological molecules, polymer micelles, QDs) in a homogeneous medium. Besides the assessment of shape and size, SAXS can be used, also, to explore the spatial distribution of particles in a medium, giving details about their interactions, and orientation if the system is anisotropic. Both structure and interaction within the system can be investigated by

analyzing the intensity variation of X-rays scattering as a function of the scattering angle θ. These analyses can be figured out performing an independent or dependent model assay (DONG and BOYD, 2011; KOHLBRECHER and BRESSLER, 2014).

The sample is irradiated by a monochromatic and collimated X-ray beam and the X-ray detector records its scattering pattern. The scattered intensity is usually expressed as a function of the momentum transfer $q = 4\pi\sin\theta/\lambda$, where 2θ is the scattering angle and λ the wavelength of the incident beam (PETOUKHOV and SVERGUN, 2013). Figure II.4 presents (a) the schematic SAXS setup and (b) X-ray beam paths from the source to the detector, both elements located far away from the sample. The Fig II.4 (b) highlights the scattering vector q, which is defined as the difference between the wave-vectors $\vec{Q}$ and $\overrightarrow{Q_0}$, both with modulus equal to $2\pi/\lambda$, having the directions of the scattered and incident beam, respectively.

Figure II.4. (a) Schematic SAXS setup and (b) X-ray beam paths from the source to the detector, both elements located far away from the sample.

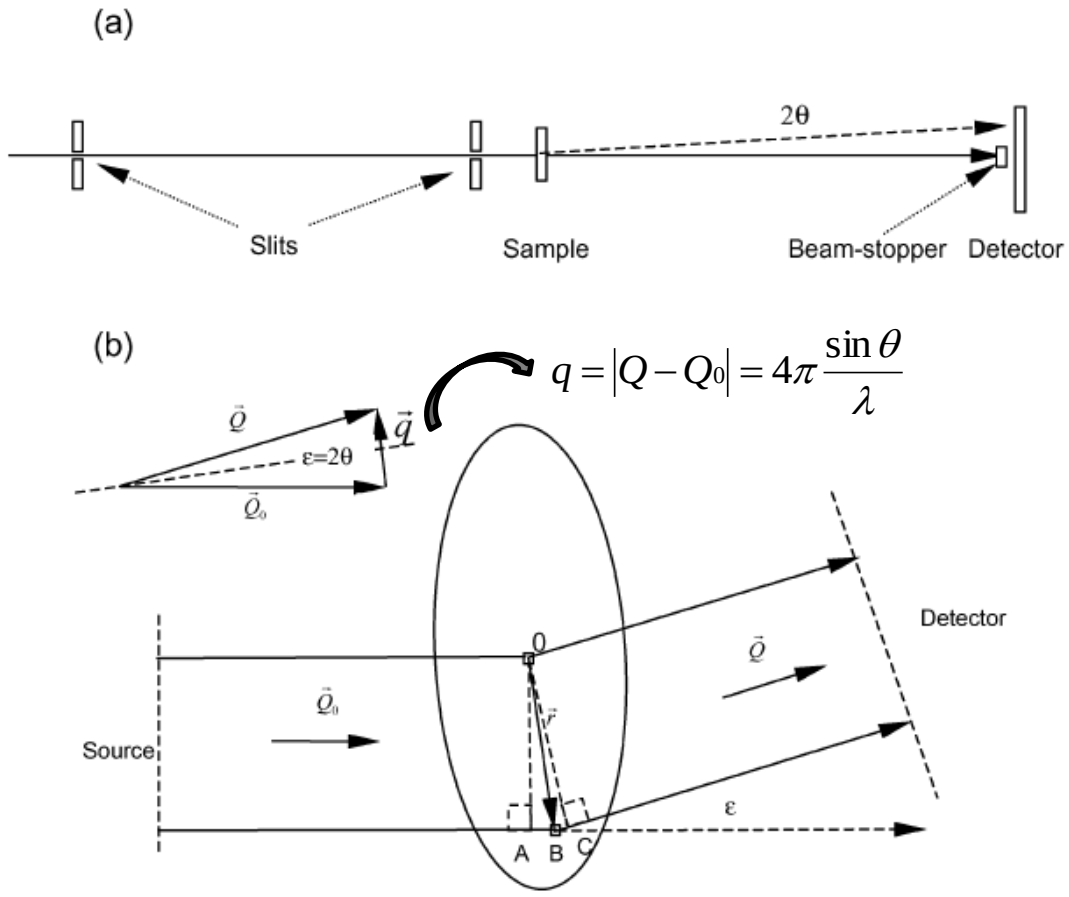

Figure adapted from the book "Handbook of Sol-Gel Science and Technology" (CRAIEVICH, 2005).

The scattering profile of non-interacting particles in a dilute solution carries information about the major geometrical parameters of the particle. The Guinier plot, ln($I(q)$) versus q^2 (which is linear at low q), gives information of the radius of gyration (Rg). The Guinier law is valid in the range $0< q<1/Rg$. The radius of gyration for a sphere with radius R is given by $Rg = \sqrt{3/5}$ R.

Compared to laboratory SAXS instruments, a synchrotron radiation (SR) source with high brightness enables the study of very dilute, or weakly scattering, samples, improves the data quality (well-resolved peaks and low background), reduces dramatically the acquisition time (hours to milliseconds) allowing *in situ* and time-resolved measurements as a function of various parameters (temperature…) (MULET, BOYD and DRUMMOND, 2013; NASCIMENTO et al., 2015; MANAIA et al., 2015,; INOBE et al., 2008; CHEMIN et al., 2009).

Synchrotron SAXS data collection were performed on the SAXS1 beamline of the Brazilian synchrotron source, LNLS, Campinas and also on the SWING beamline at the SOLEIL synchrotron source (Saint Aubin, France). A Pilatus 300k detector and a two-dimensional CCD detector were used at LNLS and SOLEIL, respectively. The scattered intensity was reported as a function of the scattering vector q. Silver behenate standard was used to calibrate the q range.

Data were normalised taking into account the beam decay, acquisition time and sample transmission. The scattered intensity of the sample holders, and the solvents (ethanol or water) were subtracted from the total intensity. The analysis of the SAXS data was carried out using the software package SASFIT (KOHLBRECHER and BRESSLER, 2014)

A special setup was used at SOLEIL. The nucleation and growth of pure ZnO and $Zn_{0.8}Mg_{0.2}O$ QDs have been followed in situ, using a home-made stopped-flow device. The freshly prepared precursor solution and the ethanolic LiOH solution, contained in two syringes, were simultaneously pushed by syringe pumps into two tubes, rapidly mixed at the Y-junction of these tubes and introduced into the thermostated X-ray capillary. Figure II.5 presents the setup used at SWING beamline.

Figure II.5. Schematical setup used at SWING beamline.

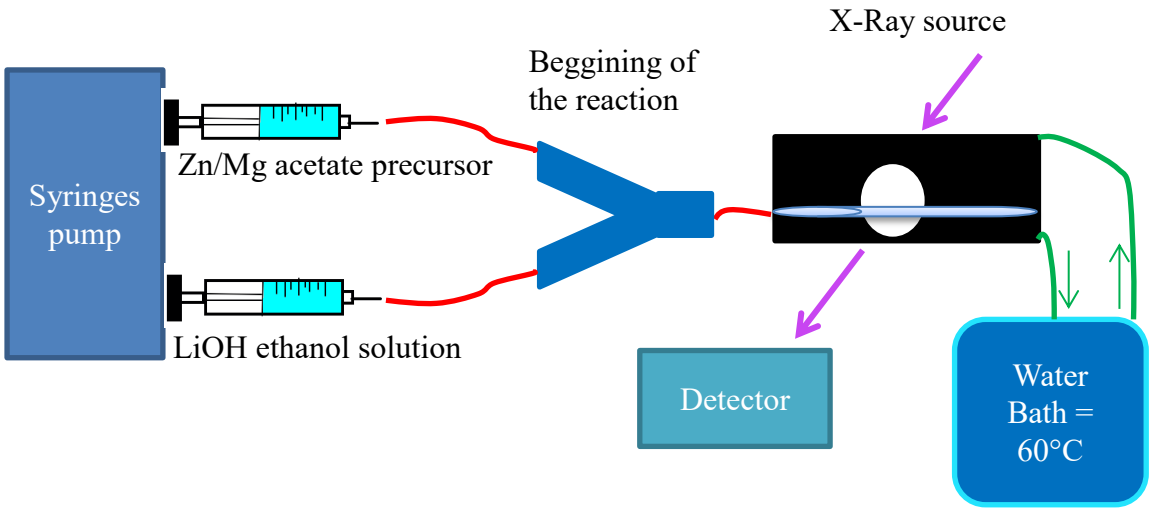

II.4.3. X-ray Absorption Spectroscopy (XAS)

The X-ray spectroscopy studies the transitions involved in absorption (XAS, X-ray absorption spectroscopy) or emission (XES, X-ray emission spectroscopy) of X-rays. These techniques allow characterizing the chemical nature and environment of atoms in molecules. Each particular element of periodic tables needs specific energy to absorb X-Ray. Therefore, synchrotron sources provide a large range of X-ray energies involving most elements in the periodic table. The energy of the X-rays used will determine the specific element that will be explored (YANO and YACHANDRA, 2009).

XAS measures the transitions from core electronic states of the metal (1s for Kedge, 2p for $L_{2,3}$ edges…) to the excited electronic (LUMO) and the continuum states, hence a photoelectron is generated with a kinetic energy (E_c) when X-Rays photon is absorbed by the matter. This phenomenon occurs when the photon energy ($h\upsilon$) is equal to the binding energy (E_0) of the core electron of an atom. This leads to an abrupt increase in the absorption coefficient (absorption edge) (BRIOIS et al., 2001).

The photoelectron generated may be viewed as an outgoing wave (particle-wave dualism) originated from the absorbing atom and it can suffer scattering interferences from the neighbors atoms. Two regimes can be observed according to E_c values:

High E_c: photoelectron presents weak life-time and about 10 Å of free pathway. Thus, it is involved mainly with the first and second neighbors, in single scattering process

modulated by constructive or destructive interferences backscattered from the neighbors. This regime ranges from 50 to 1000 eV above the edge.

Low E_c: photoelectron presents longer life-time and mean free pathway. Thus, it is involved in the scattering of atoms located at longer distances or scattered many times by the close atoms. This regime ranges from some eV below the edge to about 50 eV above the edge (BRIOIS et al., 2001).

The high Ec regime is known as extended X-ray absorption fine structure (EXAFS) which gives information about numbers, types, and distances to ligands and neighboring atoms from the absorbing element. EXAFS phenomenon $\chi(k)$, the oscillatory portion of the absorption coefficient, is current defined as the difference between the observed absorption coefficient $\mu(k)$ and the free-atom absorption coefficient $\mu_0(k)$, normalized by the free-atom contribution. By using the Fourier transform (FT) of this modulation it is possible to extract the distance between the absorbing atom and atoms to which it is bound. This distance presents typically a limit within 4–5 Å (YANO and YACHANDRA, 2009).

The low Ec regime is known as X-ray absorption near-edge structure (XANES) and gives information about electronic structure and symmetry of the metal site. The oxidation state of the metal can be determined from the K-edge energy, which refers to the transition from $1s \rightarrow np$ .The higher the oxidations state of the metal, higher the outer electrons are attracted to the positive nucleus and repelled by negative charged electrons, higher is the energy required to excite an electron from an orbital, thus, higher is the K-edge absorption energy. Information of metal symmetry can be obtained from the pre-egde peak, which is less intense and occurs at lower energies than the absorbed X-ray photon. It refers to the transition from $1s$ to $(n-1)d$ and increases when the ligand environment is perturbed from octahedral symmetry (YANO and YACHANDRA, 2009).

The figure II.6 exhibits a typical X-ray absorption, μx versus E, for Pd and shows the principle of X-ray absorption spectroscopy both in terms of XANES and EXAFS spectroscopy (GRUNWALDT and BAIKER, 2005).

Figure II.6. Illustration of a typical X-ray absorption, μx versus E, for Pd and a brief explanation of the principle of X-ray absorption spectroscopy both in terms of XANES and EXAFS spectroscopy.

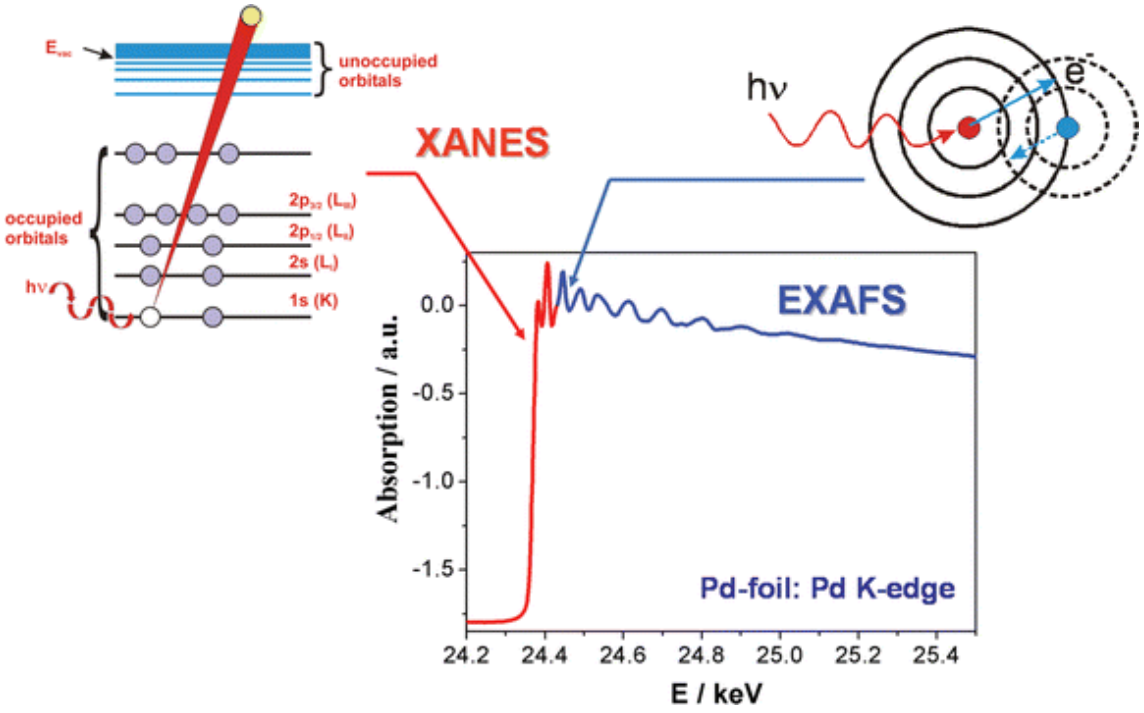

Figure from the article "In situ spectroscopic investigation of heterogeneous catalysts and reaction media at high pressure" (GRUNWALDT and BAIKER, 2005).

X-ray absorption data were collected at the SAMBA beamline at the Soleil synchrotron source using the fixed exit sagitally focusing Si (220) double crystal monochromator. The grazing incidence of the white and monochromatic beams on both Pd-coated collimating and focusing mirrors was set at 4 mrad, ensuring an efficient harmonic rejection. The beam size at the sample position was about 2 mm (H) 0.5 mm (V). Data were recorded in transmission mode using ionization chambers filled with a N_2/He gas mixture.

The analysis of the X-ray absorption data was carried out using the software package Athena and Artemis. To calibrate each data set in energy it was used the maximum of the first derivative of the zinc reference foil recorded simultaneously with the data. A linear background was fitted to the pre-edge region and subtracted from the spectra. A post-edge background using the AUTOBK algorithm was applied with a cutoff R bkg = 1.15 and k-weight = 3 in order to isolate the EXAFS oscillations $\chi(k)$. Then, the EXAFS data were Fourier transformed between 3.7 and 12 $Å^{-1}$ using a k^3 -weighting Kaiser- Bessel window

with a dk = 2 apodization window. EXAFS fitting of distances, coordination numbers and Debye−Waller factors were performed with the Artemis interface to IFeFFIT using least-squares refinements.

II.4.4. Inductively Coupled Plasma Mass Spectrometry (ICP-MS)

Mg^{2+} concentrations in doped QDs were determined using inductively coupled plasma mass spectrometry.

II.4.5. Raman Spectroscopy

The Raman spectra were collected in the backscattering configuration at room temperature with a commercial Kaiser Optical Systems RXN1 Raman spectrometer equipped with a near-IR laser diode working at 785 nm, operating with a power output of 50 mW. All the samples, apart from liquid oleic acid, were dried powders.

II.4.6. High Resolution Transmission Electron Microscopy

The HRTEM images were obtained with Philips microscope model CM 200 operating at 200 KeV at the LMA-IQ (UNESP – Araraquara) (chapter III) and with a JEOL JEM-2011 UHR scanning electron microscope operating at 200 keV, at the "Service of electronic microscopy" at the University Pierre and Marie Curie, Paris, France (chapter IV). A drop of the dilute colloidal suspension of QDs was deposited on a copper grid. Image analysis was carried out with the ImageJ and Digital Micrograph softwares.

II.4.7. UV-vis Spectroscopy

The absorption spectra were measured using a Cary Win 4000 UV-vis spectrophotometer with a cuvette of 1 mm optical path. The spectra of the QD colloidal suspensions were recorded between 200 and 400 nm, with a wavelength step of 1 nm, and an average counting time of 0.2 s per point. The UV-vis spectra were corrected from the absorption spectrum of ethanol.

Five aliquots of ZnO/ZnS QDs (chapter III) were collected at different times (1 min, 5 min, 10 min, 20 min and 40 min) of each reaction (Route 1 and Route 2) and diluted 8 times in ethanol to be detected without saturation of the detection.

The size of ZnO QDs was determined from the absorption spectra using the effective mass model derived by Brus (BRUS, 1983). Brus equation is based on "effective mass

approximation". In this approximation, it is considered that an exciton is confined to the spherical volume of the crystallite and the masses of electron and hole are replaced with effective masses (m_e^* and m_h^*) to define the wave function:

$$E_{g(QD)} = E_{bulk} + \frac{h^2}{8R^2}\left(\frac{1}{m_e^*} + \frac{1}{m_h^*}\right) - \frac{1.786e^2}{4\pi\varepsilon_0\varepsilon_r R^2}$$

where,

$E_{g(QD)}$ = band gap energy of quantum dot;

E_{bulk} = band gap energy of bulk semiconductor;

R = radius of quantum dot;

m_e^* = effective mass of excited electron;

m_h^*= effective mass of excited hole;

h = Planck's constant

ε_0 = permittivity of vacuum

ε_r = relative permittivity

For ZnO, E_{bulk} = 3.4 eV, m_e^* = 0.24 and m_h^*= 0.45.

Hence, the emission energy of QDs can be described in terms of the band gap energy (E_g), planck's constant (h), the radius of the quantum dot (R), the mass of the excited electron (m_e^*), and the mass of the electron hole (m_h^*). As the radius of the quantum dot affects the wavelength of the emitted light due to quantum confinement, changing QDs radius will change the emitted wavelength (CHUKWUOCHA, ONYEAJU and HARRY, 2012). To determine E_g (E_g= hc/λ, where c = speed of light in m/s), we have used the Nedelijkovic (NEDELIJKOVIC et al., 1993) method. Figure II.7 shows the determination of λ by Nedelijkovic method.

Figure II.7. ZnO QDs UV absorption spectra appointing λ determined by Nedelijkovic.

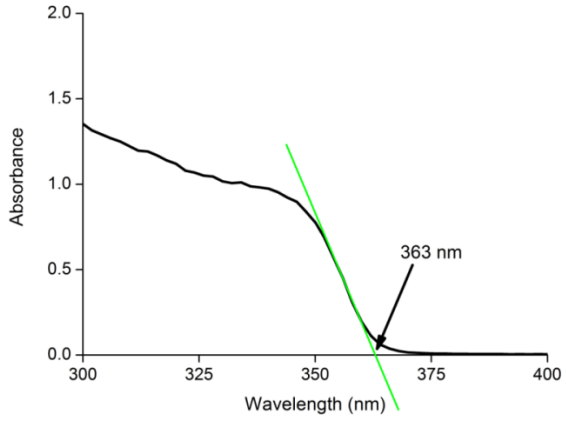

II.4.8. Photoluminescence Spectroscopy (PL)

The emission (PL) and excitation (PLE) photoluminescence spectra of QDs were recorded on a Luminescence spectrometer LS50B (Perkim Elmer) at room temperature with a Xenon lamp (20 kW) as the excitation source.

The same wavelength of excitation (λ_{exc} = 353 nm) was used to collect PL spectra of ZnO and ZnO/ZnS QDs; λ_{exc} = 302 nm was used for ZnS.

In the study of $Zn_{1-x}Mg_xO$ QDs, each sample was excited at the optimal wavelength, defined by the PLE spectrum.

The quantum yield (QY) determines the efficiency of the conversion of absorbed photons into emitted ones. Usually, the relative QY of the studied sample is compared with that of a reference fluorophore. In this work, a solution of Rhodamine 6G in ethanol (QY = 95%), often used as reference for green emission, was selected as the standard (SUN et al., 2012). According to the method described by Crosby and Demas (CROSBY and DEMAS, 1971), the QY is given by the following formula:

$$QY_x = QY_r[A_r(\lambda_r)/A_x(\lambda_x)](n_x^2/n_r^2)(D_x/D_r)$$

where A is the absorbance at the excitation wavelength (λ), n the refractive index of the solvent used and D the integrated fluorescence intensity (the area under the corrected emission curve). The subscripts r and x refer to the reference and sample solutions, respectively. To minimize the errors, the same excitation wavelength was chosen to measure the PL spectra of the Rhodamine 6G and QD ethanolic solutions and the two solutions had the same absorbance at this wavelength (A = 0.05).

The photoluminescence properties of the lipid-based formulations containing QDs were evaluated. UV-Vis measurements were performed with a Perkin Elmer Lambda35 UV/VIS Spectrometer and PL measurements were performed using the Fluorescence Spectrometer Perkin Elmer. We selected the formulations displaying good luminescence when observed under UV-lamp with naked eye. They were diluted to show the same absorbance in order to achieve the same QD concentration for comparing their PL properties.
PL properties of the cell line used to perform the internalization studies were also investigated: the cultured cells were detached mechanically, centrifuged and lysed in water by sonication.

II.4.9. Cryo microscopy

The morphology of some formulations was examined using cryogenic transmission electron microscopy (Cryo-TEM). A drop of the filtered (0.45 µm) sample was deposited on a carbon-coated copper grid. Excess liquid was removed with a blotting filter paper and the thin film remaining within the holes was quickly vitrified by immersion into liquid ethane. The sample was then transferred using liquid nitrogen to a cryo-sample holder and observed using a Cryo-TEM (JEOL 2100) electron microscope. The Cryo-TEM investigations were performed at the "Service de Microscopie Electronique de l'Institut de Biologie Intégrative" (IFR 83 CNRS, Paris).

II.4.10. Study of the Stability of SLN containing QDs

The stability of the formulation G4 (SLN of ratio 1:3 of $Zn_{0.8}Mg_{0.2}O$ QDs:Gelucire 50/13® and ratio 1:4 of ethanol:H_2O; Gelucire 50/13® solubilized at room temperature) was investigated in water, Phosphate-buffered saline (PBS) with and without calcium and Magnesium, RPMI without red phenol (RP), RPMI without RP with 10% of heat-inactivated fetal bovine serum FBS at 37 °C by determination of the mean particle size as a function of time using a Zetasizer Nano ZS Malvern; Malvern Instruments.

II.4.11. Cell culture and preparation

The J774A1 murine phagocytic macrophage-like cell line (ECACC catalogue number 91051511), was used to study the internalization of the luminescent nanoparticles by phagocytosis. The growth of cells was performed in culture bottles with RPMI 1640 medium (Sigma Aldrich), supplemented with 10% v/v heat-inactivated fetal bovine serum, antibiotics and antimycotics. The culture bottles were maintained in an incubator at 37 °C containing 5% CO_2. For experiments, cells were detached mechanically and plated in 6-well plates for the internalization studies. Passage-numbers 10–12 were used to perform the experiments.

II.4.12. Internalization Study

Three methods were used to study the internalization of the nanoparticles in the cells: determination of the fluorescence of cells after incubation with QDs, live-cell imaging using fluorescence video-microscopy and cell fluorescence microscopy. In all experiments the RPMI used during the experiment was devoid of red phenol to prevent interferences with the optical properties of the systems analyzed.

II.4.12.1. Determination of the fluorescence of cells

Cells were plated in 6-well plates containing 1mL of medium. After adherence, the medium was removed from each well and it was replaced by 1mL of medium and medium containing 1 mg and 2 mg of luminescent nanoparticles of the formulation G4, separately, as showed in the Figure II.8. Two replicate wells were used for each concentration.

Figure II.8. Schematic figure of the plate used to perform the determination of the fluorescence association by fluorescence spectroscopy.

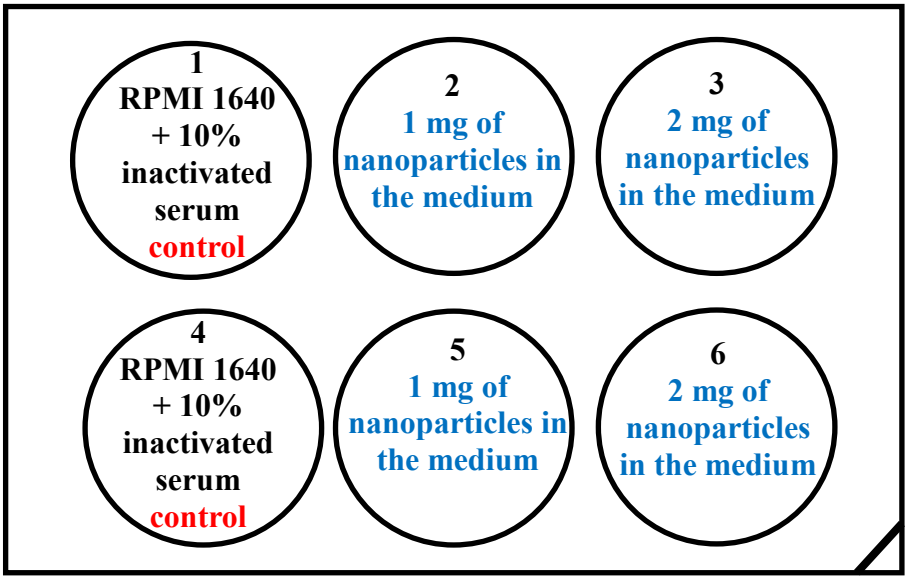

The plate was incubated during 50 min at 37°C with 5% CO_2. The supernatant was removed and the cells were washed once with 1mL PBS; subsequently 1mL of PBS was put to remove the cells mechanically. After the centrifugation step, the cells were lysed by the addition of 1 mL of Milli-Q water and the fluorescence was then measured with the spectrofluorimeter (λ_{exc} 340 and 365 nm).

II.4.12.2. Live-cell imaging using video-microscopy

Cells were plated in 6-well plates containing a cover slit #1.5 of 25 mm of diameter and 1mL of medium. After adherence of cells, the cover slit was first placed in a reusable 35 mm metal dish which was put in the adaptor of the microscope under controlled temperature (37 °C) and atmosphere (5% CO_2). Then, 1mL of medium containing 5mg/mL of luminescent nanoparticles of the formulation G11 (SLN of ratio 1:3 of $Zn_{0.8}Mg_{0.2}O$ QDs:Gelucire 50/13® and ratio 1:2 of ethanol:H_2O; Gelucire 50/13® solubilized at 50 °C) was incubated with the

cells and images were recorded from the beginning of the experiment. Photographies were recorded using the Videomicroscope Axio-Observer Z1 – Colibri –TIRF 3 with a 63X oil immersion objective of PlanApochromat. The filter used was the 61 HE GFP + HcRed: emission DBP 527/54 + 645/60 nm. The wavelength of the LED excitation used was 365 nm.

After these assays, one cover slit incubated during 40 minutes with 1mL of medium containing 2 mg/mL of luminescent nanoparticles of the formulation G11 was also observed. Further investigations were performed with the formulations THF and DPeg6 with different incubation times (i.e., 1, 2 and 3 h).

The acquisition time in all experiments was 3000 ms.

II.4.12.3. Fluorescence microscopy

Cells were plated in 6-well plates containing a cover slit #1.5 of 25 mm of diameter and 1mL of medium. After adherence, the medium was removed from each well and it was replaced by 1mL of medium and medium containing luminescent nanoparticles of the formulations DPeg6 (1.7 mg AO- $Zn_{0.8}Mg_{0.2}O$ QDs, 10 mg DSPE-Peg and 1 mL of H_2O), G12 (SLN of ratio 1:3 of $Zn_{0.8}Mg_{0.2}O$ QDs:Gelucire 50/13® and ratio 1:3 of ethanol:H_2O; Gelucire 50/13® solubilized at 50 °C), and THF (SLN of ratio 1:3 of OA-$Zn_{0.8}Mg_{0.2}O$ QDs:Gelucire 50/13® and ratio 1:3 of THF:H_2O; Gelucire 50/13® solubilized at room temperature) , separately, as shown in Figure II.9. The samples were prepared in this way: 500 µL of the formulation + 25 mg glucose (to achieve the same osmolality than the cells content) + 500 µL of medium. They were incubated for 4 hours and then observed in the Leitz Diaplan Fluorescent Microscope equipped with a CoolSnap ES charge-coupled device camera (Photometrics) and a band-pass excitation filter of 340–380 nm and a long-pass emission filter of 425 nm.

Figure II. 9. Schematic figure of the plate used to perform the cell treatment with luminescent nanoparticles for further observation by fluorescence microscope.

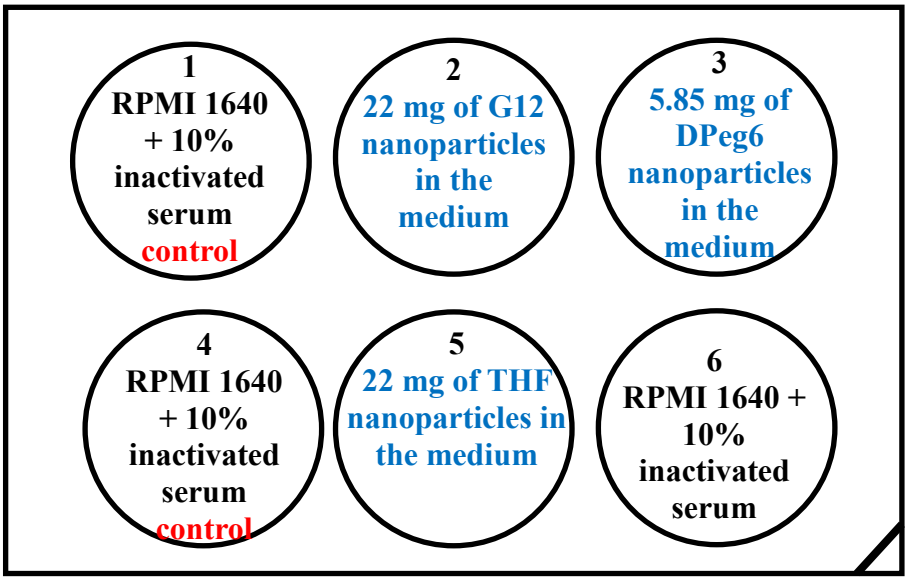

II.4. REFERENCES

BANCOS, S.; STEVENS, D. L.; TYNER, K. M. Effect of silica and gold nanoparticles on macrophage proliferation, activation markers, cytokine production, and phagocytosis in vitro. **Int J Nanomedicine,** v. 10, p. 183-206, 2015.

BRIOIS, V.; SERRINI, P.; CHIAVACCI, L.; PULCINELLI, S. H.; SANTILLI, C. V. EXAFS spectroscopy of nanocrystalline materials. In: NETWORK, T. R. (Ed.). **Recent Research and Development of Non-Crystalline Solids**. Kerala, India, v.1, 2001. p.21-35. ISBN 81-7895-028-6.

BRUS, L. E. A simple model for the ionization potential, electron affinity, and aqueous redox potentials of small semiconductor crystallites. **J Chem Phys,** v. 79, n. 11, p. 5566-5571, 1983.

CHEMIN, C.; PÉAN, J. M.; BOURGAUX, C.; PABST, G.; WÜTHRICH, P.; COUVREUR, P.; OLLIVON, M. Supramolecular organization of S12363-liposomes prepared with two different remote loading processes. **Biochim Biophys Acta,** v. 1788, n. 5, p. 926-935, 2009.

CHUKWUOCHA, E.; ONYEAJU, M.; HARRY, T. Theoretical Studies on the Effect of Confinement on Quantum Dots Using the Brus Equation. **World Journal of Condensed Matter Physics,** v. 2, n. 2, p. 96-100, 2012.

CRAIEVICH, A. F. **Handbook of Sol-Gel Science and Technology**; Norwell: Sakka, S., Almeida, R., Eds., 2005. vol.2, chapter II, p 161-189.

CROSBY, G. A.; DEMAS, J. N. Measurement of photoluminescence quantum yields. Review. **J Phys Chem,** v. 75, n. 8, p. 991-1024, 1971.

DONG, Y.-D.; BOYD, B. J. Applications of X-ray scattering in pharmaceutical science. **Int J Pharm,** v. 417, n. 1–2, p. 101-111, 2011.

GRUNWALDT, J.-D.; BAIKER, A. In situ spectroscopic investigation of heterogeneous catalysts and reaction media at high pressure. **Phys Chem Chem Phys,** v. 7, n. 20, p. 3526-3539, 2005.

INOBE, T.; TAKAHASHI, K.; MAKI, K.; ENOKI, S.; KAMAGATA, K.; KADOOKA, A.; ARAI, M.; KUWAJIMA, K. Asymmetry of the GroEL-GroES Complex under Physiological Conditions as Revealed by Small-Angle X-Ray Scattering. **Biophys J,** v. 94, n. 4, p. 1392-1402, 2008.

KOHLBRECHER, J.; BRESSLER, I. **SASfit**. Paul Scherrer Institut, Villigen, Switzerland. 0.94.1 2014.

LEPELTIER, E., BOURGAXU, C., COUVREUR P. Nanoprecipitation and the "Ouzo effect": Application to drug delivery devices. **Adv Drug Deliv Rev**, v.71, p. 86-97, 2014.

MANAIA, E. B.; KAMINSKI, R. C.; DE OLIVEIRA, A. G.; CORRÊA, M. A.; CHIAVACCI, L. A. Multifunction hexagonal liquid-crystal containing modified surface TiO_2 nanoparticles and terpinen-4-ol for controlled release. **Int J Nanomedicine,** v. 10, p. 811-819, 2015.

MEULENKAMP, E. A. Synthesis and Growth of ZnO Nanoparticles. **J Phys Chem B,** v. 102, n. 29, p. 5566-5572, 1998.

MULET, X.; BOYD, B. J.; DRUMMOND, C. J. Advances in drug delivery and medical imaging using colloidal lyotropic liquid crystalline dispersions. **J Colloid Interface Sci,** v. 393, p. 1-20, 2013.

NASCIMENTO, T. L.; HILLAIREAU, H.; NOIRAY, M.; BOURGAUX, C.; ARPICCO, S.; PEHAU-ARNAUDET, G.; TAVERNA, M.; COSCO, D.; TSAPIS, N.; FATTAL, E. Supramolecular Organization and siRNA Binding of Hyaluronic Acid-Coated Lipoplexes for Targeted Delivery to the CD44 Receptor. **Langmuir,** v. 31, n. 41, p. 11186-11194, 2015.

NEDELIJKOVIC, J. M.; PATEL, R. C.; KAUFMAN, P.; JOYCE-PRUDEN, C.; O'LEARY, N. Synthesis and optical properties of quantum-sized metal sulfide particles in aqueous solution. **J Chem Educ,** v. 70, n. 4, p. 342, 1993.

PETOUKHOV, M. V.; SVERGUN, D. I. Applications of small-angle X-ray scattering to biomacromolecular solutions. **Int J Biochem Cell Biol,** v. 45, n. 2, p. 429-437, 2013.

SPANHEL, L.; ANDERSON, M. A. Semiconductor clusters in the sol-gel process: quantized aggregation, gelation, and crystal growth in concentrated zinc oxide colloids. **J Am Chem Soc,** v. 113, n. 8, p. 2826-2833, 1991.

SUN, L.-W.; SHI, H.-Q.; LI, W.-N.; XIAO, H.-M.; FU, S.-Y.; CAO, X.-Z.; LI, Z.-X.. Lanthanum-doped ZnO quantum dots with greatly enhanced fluorescent quantum yield. **J Mater Chem,** v. 22, n. 17, p. 8221-8227, 2012.

WEST, A. R. **Solid State Chemistry and Its Applications**. New York: John Wiley and Sons, 1992.

WILLIAMS, D. B., CARTER, C. B. **Transmission Electron Microscopy. A Textbook for Materials Science**. New Your: Springer Science+Business Media, 2009. p. 49.

YANO, J.; YACHANDRA, V. K. X-ray absorption spectroscopy. **Photosynthesis Research,** v. 102, n. 2-3, p. 241-254, 2009.

CHAPTER III

Study of ZnO/ZnS core-shell formation by sol-gel process

Chapter III – Study of ZnO/ZnS core-shell QDs formation by sol-gel process

III.1. INTRODUCTION

Core-shell NPs consisting of two different semiconductors are currently attracting much interest due to the versatility of their structures and properties for potential applications in many fields such as electronics, optics and biological labeling or imaging (GHOSH CHAUDHURI and PARIA, 2011). The shell acts as a barrier between the core and the surrounding medium and can change the chemical reactivity and colloidal stability of the core. For example, surface modification can make NPs compatible with biological fluids and/or allow binding of specific ligands to target cell receptors. Forming a core-shell structure is also a strategy for improving the photoluminescence properties of semiconductor NPs (REISS et al., 2009). Coating NPs with a higher band gap semiconductor can passivate the core surface, eliminating surface-related defect states that induce non-radiative recombination of photogenerated electron-hole pairs (excitons), thereby lowering fluorescence quantum yield (QY) and giving rise to "blinking" (ISNAENI et al., 2011). This NP intermittent fluorescence might limit their use in tracking applications.

The surface-related effects are expected to be strongly enhanced in QDs, because of their very small size resulting in a high surface-to-volume ratio. Indeed, the quantum confinement effect, characterised by an increasing band gap with decreasing QD size and discrete energy levels, requires a QD size smaller than twice the Bohr exciton radius of the semiconductor (typically less than 10 nm). Non-blinking QDs, with narrow emission spectra and high quantum yield were achieved by forming core-shell structures (WANG et al., 2009a; CHEN et al., 2013). ZnS has often been chosen to overcoat QDs due to its wide band gap (3.66 eV), the largest among all II-VI semiconductors. For instance, the growth of a ZnS shell reduced blinking of CdSe QDs (an intermediate ZnSe layer was introduced between the CdSe core and the ZnS shell) (ISNAENI et al., 2011) and significantly improved the QY of CdSe and CuInSe QDs (DABBOUSI et al., 1997; CASSETTE et al., 2010).

Among (II-VI) semiconductors, ZnO is a cheap, wide band gap, material with outstanding electronic and optical properties. It is used in a wide range of applications such as photocatalysts (SADOLLAHKHANI et al., 2014), photodetectors (LIU et al., 2010), gas sensors (WANG et al., 2012), UV light emitting diodes and laser diodes (LIM et al., 2006).

More specifically, ZnO QDs are promising luminescent probes for bioimaging due to their biodegradability and very low toxicity *in vivo* (MOUSSODIA et al., 2010; JIA and MISRA, 2013; MATSUYAMA et al., 2013; XIONG, 2013). Over the last few years, various ZnO/ZnS core/shell structures have been prepared and their luminescent properties investigated. Beside chemical vapour or plasma laser deposition of ZnS on ZnO templates, many core-shell NPs were synthesised in solution at moderate temperatures via a partial chemical conversion of ZnO to ZnS in the presence of a sulphur source or via addition of both a sulphur source and a Zn precursor to preformed ZnO NPs. ZnO/ZnS core-shell nanocables (WANG et al., 2009b), nanorods (PANDA et al., 2007; WU et al., 2011), nanotubes (SHUAI and SHEN, 2011), nanowires (LIU et al., 2011) and nanospheres or powders (GENG et al., 2007; VERMA et al., 2009; NAM et al., 2011; SADOLLAHKHANI et al., 2014; SOOKHAKIAN et al., 2014) with dimensions in the *~25-200* nm range, were synthesised. Regarding the influence of the ZnS shell on the optical properties of the core, no general trend emerged. This might be due to different characteristics of the ZnS shell.

Very few investigations on ZnO/ZnS QDs synthesised in solution have been reported. Sharma and Chawla (SHARMA and CHAWLA, 2013) obtained core-shell nanoparticles, with thick shells, showing significant enhancement (~30%) of UV emission compared to ZnO NPs. Formation of hexagonal ZnS, instead of the usual cubic ZnS blende, suggested epitaxial growth over ZnO hexagonal wurtzite NPs. The core-shell structure of the NPs was further confirmed by HRTEM images. However, the distribution of NP sizes was large, ranging from few nm to about 30 nm. *Luo et* al (LUO et al., 2015) have recently prepared Cd-doped ZnO/ZnS core-shell QDs. The successful growth of the ZnS shell was evidenced by HRTEM images and its mean thickness (e.g. 1.37 nm) could be estimated from the monomodal size distributions of Cd-doped Zno QDs (with 6 nm average size) and Cd-doped ZnO/ZnS core-shell QDs (with 7.37 nm average size). At appropriate ZnS coating, the luminescence of the QDs strongly increased.

In this chapter we have investigated two low-temperature sol-gel synthesis routes aiming at obtaining ZnO/ZnS core-shell QDs. Briefly, the synthesis was carried out at 60°C using two different experimental procedures involving: (i) the reaction of a ZnO colloidal suspension with an ethanolic thioacetamide (TAA) solution, as sulphur source and (ii) the reaction of the Zn acetate precursor (TOKUMOTO et al., 2003) used for the synthesis of ZnO colloidal suspension with an ethanolic TAA solution. Different TAA concentrations were used in order to reveal the influence of this parameter on the so-formed particles. The

formation of ZnO/ZnS nanostructures was monitored by Small Angle X-Ray Scattering (SAXS) and UV-vis Spectroscopy techniques. They were further characterised by X-Ray diffraction (XRD), X-Ray Absorption Spectroscopy (XAS), High Resolution Transmission Electron Microscopy (HRTEM) and Photoluminescence Spectroscopy (PL). Very different ZnO-ZnS nanostructures were identified, depending on the synthesis conditions. The use of XAS, combined with the other characterisation techniques, was crucial to distinguish ZnO/ZnS core-shell QDs from mixtures of ZnO and ZnS NPs.

III.2. RESULTS

ZnO, ZnS and ZnO/ZnS core-shell QDs were synthesised by the hydrolysis and condensation reaction described in the chapter II (Sections II.2.1, II.2.2 and II.2.3). The organic compound thioacetamide was chosen as sulphur source due to its slow decomposition with a controlled release of sulphur ions.

III.2.1. X-Ray Diffraction (XRD)

Powder diffraction patterns are presented in Figure III.1 (a). The ZnO QDs, SUSP_TAA1.5mM, PREC_TAA1.5mM, SUSP_TAA5mM and PREC_TAA5mM mainly display the peaks characteristic of the ZnO hexagonal wurtzite structure marked in dashed black lines. The ZnS QDs, SUSP_TAA50mM, PREC_TAA50mM mainly display the peaks characteristic of the ZnS cubic zinc blende structure marked in dashed red lines. Figure III.1 (b) shows a zoom of the (111), (100), (002) and (101) diffraction peaks between $2\theta = 23°$ and $2\theta = 40°$ of the ZnO QDs, ZnS QDs, PREC_TAA5mM and SUSP_TAA5mM. With a careful observation, we can see that the samples using the TAA5mM present peaks characteristic of both ZnO and ZnS structures, suggesting that these samples contain ZnO and ZnS crystals. It is clear that the intensity of the peaks belonging to the ZnO QDs in the diffraction pattern of the SUSP_TAA5mM and PREC_TAA5mM samples is lower than that of ZnO QDs. As remarked before, these samples present a small wide peak around 29° related to ZnS structure, this suggests the coexistence of both phases in these samples. The same behaviour was observed by Sadollahkhani et al (SADOLLAHKHANI et al., 2014).

Figure III.1. (a)XRD profiles of ZnO and ZnS standards, ZnO and ZnS QDs, and ZnO/ZnS core-shell QDs with different concentration of the sulphur source. (b)Marked lines indicating the hexagonal wurtzite phase (black) and cubic zinc blende phase (red) are shown. Zoom of the peaks (111), (100), (002) and (101) in the 2θ ranging from 23 to 40 ° of the ZnO QDs, ZnS QDs, SUSP_TAA5mM and PREC_TAA5mM.

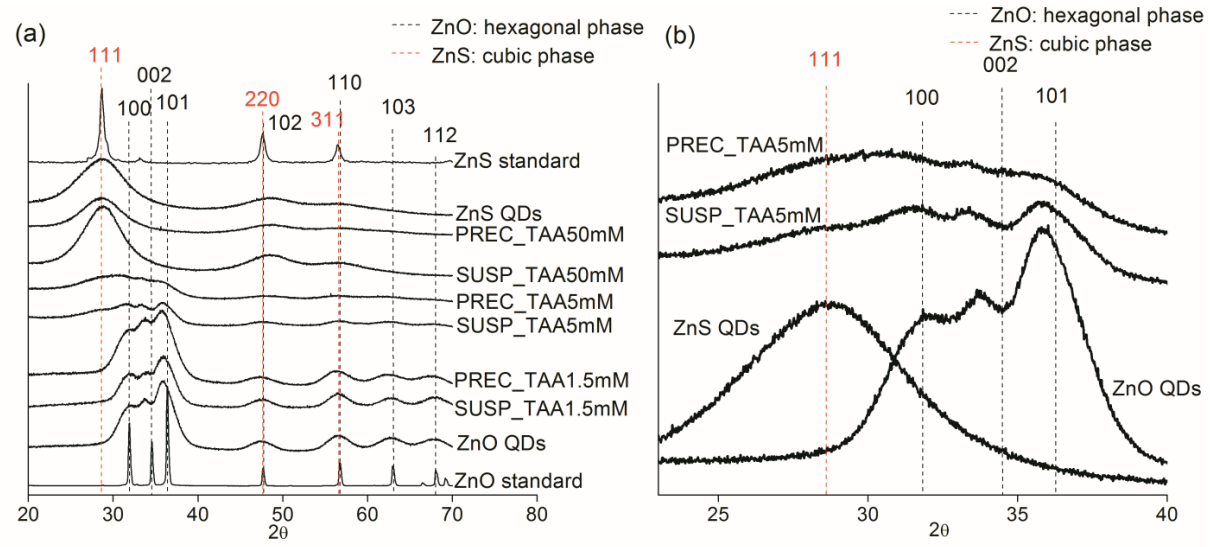

The average size of ZnO and ZnS nanocrystals could be estimated using the Debye-Scherrer relation (WEST, 1992) applied to the (100), (002) and (101) reflections of ZnO and (111) reflection of ZnS, respectively. ZnO and ZnS QDs presented a crystallite size about 5.3 and 1.4 nm, respectively.

III.2.2. X-ray Absorption Spectroscopy (XAS)

Figure III.2 (a) and (b) display the XANES spectra and Fourier Transforms of EXAFS spectra recorded for the different samples and compared to the standard references. Significant differences in shape and white lines positions can be observed between the standard ZnO and ZnS references which are also present in the samples. On the one hand, samples prepared with 1.5 mM of TAA display a XANES spectrum very similar to those recorded for ZnO-QDs and ZnO standard, irrespective of the preparation routes. This is a strong indication that these samples are mainly formed by ZnO nanoparticles, in agreement with XRD results. On the other hand, samples prepared with the highest TAA concentration (50 mM) display a XANES spectrum closer to the one characterizing ZnS standard whatever the preparation routes used herein. This suggests that for these samples, an effective exchange of oxygen by sulphur occurred during synthesis leading to nanoparticles presenting local

order arrangement comparable to ZnS. Finally, it is noteworthy that the XANES spectra of samples prepared with 5 mM of TAA depend on the preparation route. Comparison of FTs fully confirms the conclusions drawn from the XANES discussion. In fact the main contributions in the FTs display different R-space locations for ZnO and ZnS allowing us to make distinction between both structures. Indeed, ZnO is characterised by two main contributions corresponding to a first tetrahedral coordination shell at 1.96 Å and a second one related to the zinc second next neighbours at 3.23 Å (BRIOIS et al., 2007) whereas ZnS presents essentially a first tetrahedral sulphur coordination shell at 2.34 Å and a broad contribution with low intensity compared to ZnO corresponding to the zinc second next neighbours at 3.82 Å (CURCIO et al., 2015). Samples with ZnO QDs characteristics (PREC and SUPS_TAA1.5mM) and those with ZnS features (PREC and SUSP_TAA50mM) show FT peaks located to the same position than the respective standards. The samples prepared with intermediate TAA concentration (5 mM) are characterised by a first FT contribution with double maxima characteristic of the simultaneous presence of Zn-O and Zn-S contributions. Conclusive insights on the structural features of the samples were obtained by the least-square fitting procedures of the first coordination shell. So obtained structural parameters are gathered in Table III.1. As expected PREC and SUSP_TAA1.5mM are characterised by 3.6 (0.4) and 3.5 (0.5) oxygen atoms, respectively, at 1.98 (2) Å and PREC and SUSP_TAA 50mM are described with a coordination shell made of 3.1 (0.3) and 3.0(0.2) sulphur atoms, respectively, at 2.34 (2) Å and 1.3 (0.1) and 1.2 (0.1) oxygen atoms at 2.03 Å. It is interesting to note that no contribution at longer distances is observed on the FTs of the two TAA50mM samples. Those structural features allow us to conclude that only ZnO QDs are formed for the lowest TAA concentration. Satisfactory linear combination fittings using XANES of ZnO QDs and ZnS standards are obtained for reproducing the XANES spectra of the PREC and SUPS_TAA50mM in the 25:75 % proportion, respectively. This composition is in perfect agreement with the oxygen and sulphur coordination numbers presented in Table III.1 and allows for concluding that these samples are a mixture of both QDs: 25% of ZnO QDs and 75% of ZnS QDs. The lack of medium range order for both samples can be explained by the fact ZnS QDs (1.4 nm) are smaller than ZnO QDs (5.3 nm) making not visible the contribution of Zn-Zn second neighbours on the FT. Different conclusions about the structures of the samples prepared with intermediate TAA concentration are obtained depending on the preparation route. On the one hand, structural parameters and linear combination fitting for the PREC_TAA5mM show inverse proportion in the mixture of both

QDs phases compared to those obtained with 50 mM of TAA: i.e. 75% of ZnO QDs and 25% of ZnS QDs. In that case, as the main phase is the bigger one, a medium range order on the FT of this sample can be observed. Finally, the local order around Zn for the SUSP_TAA5mM displays a first coordination shell of 3.9 (1.1) oxygen atoms at 2.0 Å and 2.2 (1.0) sulphur atoms at 2.34 Å. Those values with a higher proportion of oxygen atoms around Zn is found compared to sulphur ones are ascribed as resulting from the formation of a core-shell structure where ZnO is the core capped by a ZnS shell. It is noteworthy that the proportions determined by LCF of the XANES spectrum for this sample used to mimic a mixture of ZnO QDs and ZnS QDs does not match the coordination numbers determined for this sample since a smaller proportion of ZnO QDs (37%) than ZnS QDs (63%) is found. The EXAFS results for Zn for the SUSP_TAA5mM sample is in agreement with the XRD conclusion for which a coexistence of ZnO and ZnS long range order was found. But contrary to the other samples for which this coexistences identified by EXAFS as the simultaneous presence of both QDs phases, the SUSP_TAA5mM sample is described as core-shell structure.

Figure III.2. (a) XANES spectra and (b) Fourier Transforms of EXAFS spectra recorded for the different samples and ZnO and ZnS standard references.

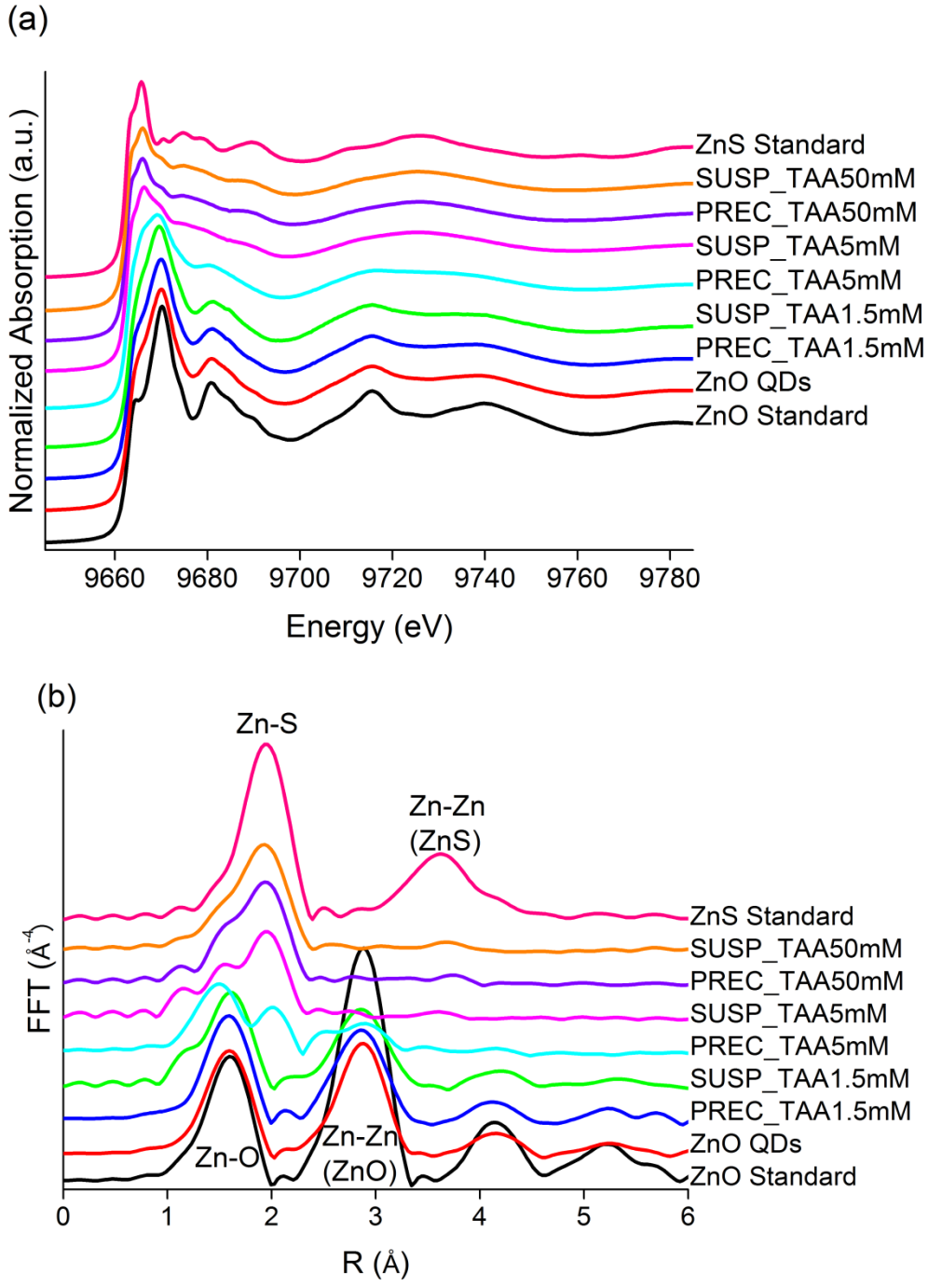

Table III. 1. EXAFS structural parameters for the first Zinc coordination sphere of ZnO, for the first Zinc coordination sphere of ZnS, and the percentages of ZnO and ZnS deduced from the Linear Combination Fittings (LCF) of XANES spectra.

Sample	N_O	R_{Zn-O}	σ^2_{Zn-O} ($Å^2$)	N_S	R_{Zn-S}	σ^2_{Zn-S} ($Å^2$)	R_{factor} (%)	***LCF***	
								% ZnO	**% ZnS**
ZnO Standard	4	1.97	0.004 (0.002)				0.03		
ZnO QDs	3.7 (0.4)	1.97	0.005 (0.001)				0.14		
SUSP_TAA1.5mM	3.6 (0.2)	1.99	0.006 (0.001)				0.03	98	2
PREC_TAA1.5mM	3.5 (0.5)	1.98	0.005 (0.002)				0.28	100	
SUSP_TAA5mM	3.9 (1.1)	2.00	0.007 (0.005)	2.2 (1.0)	2.34	0.007 (0.005)	0.27	37	63
PREC_TAA5mM	2.9 (0.4)	1.98	0.007 (0.002)	1.1 (0.2)	2.35	0.007 (0.002)	0.20	70	30
SUSP_TAA50mM	1.2 (0.1)	2.03	0.008 (0.001)	3.0 (0.2)	2.34	0.008 (0.001)	0.01	23	77
PREC_TAA50mM	1.3 (0.1)	2.03	0.008 (0.001)	3.1 (0.3)	2.34	0.008 (0.001)	0.02	22	78
ZnS Standard				4	2.34	0.006 (0.001)	0.04		

III.2.3. High resolution transmission electron microscopy

The structure of SUSP_TAA5mM studied using HRTEM is presented in Figure III.3 in low and high magnification ((a) and (b), respectively). In the Figure III.3 (a) it is possible to observe the crystallinity of the sample. The Figure III.3 (b) shows clearly the lattice fringes of ZnO and ZnS phases. The spacing of the fringes of ZnO and ZnS is marked in Figure III.3 (b), are approximately 0.26 nm (interspacing of the 002 lattice plane of wurtzite ZnO phase) and 0.31 nm (interplanar spacing of 111 plane of blende ZnS phase (WU et al., 2011)), respectively. This image (Figure III.3 (b)) looks like the micrographs presented by Luo et al (LUO et al., 2015) for a sample claimed by the authors as having a core-shell structure of ZnO/ZnS QDs. Thus, the HRTEM image confirms the XRD and XAS data: ZnS is covering the ZnO nanoparticles producing ZnO/ZnS core-shell QDs.

Figure III.3. HRTEM image of (a) SUSP_TAA5mM and (b) a zoom of the sample SUSP_TAA5mM which shows the interplanar spacing of ZnO and ZnS phases.

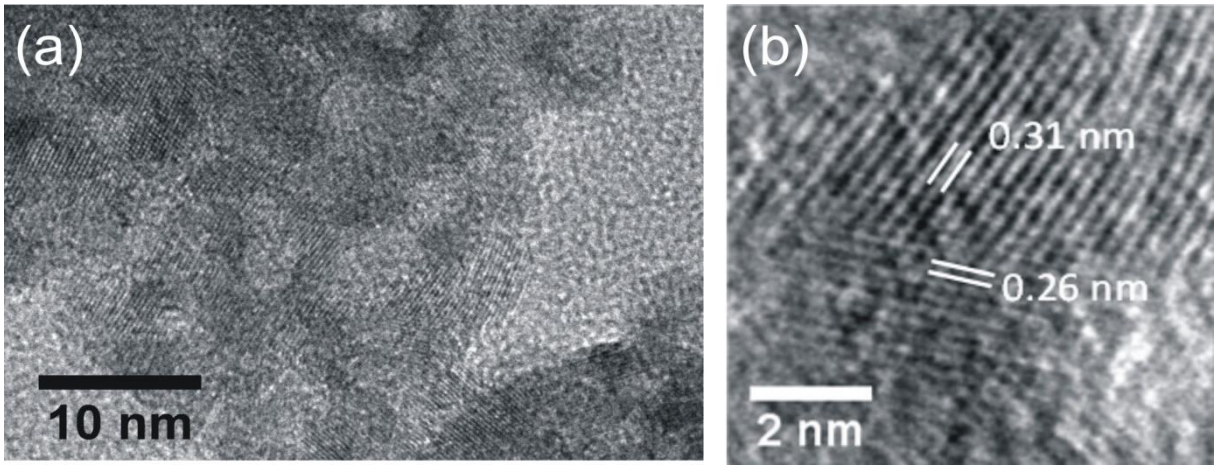

III.2.4. In situ UV-vis spectroscopy

The formation of the ZnO/ZnS core-shell QDs was studied by *in situ* UV–vis spectroscopy and SAXS. The Figure III.4 (a) shows the UV-vis spectra of ZnO QDs, ZnS QDs, the mixture of ZnO and ZnS QDs and (b) presents the UV-Vis spectra of the ethanolic solution of TAA. The excitonic peaks around 290 nm and 350 are characteristic of ZnS QDs (MEHTA et al., 2008) and ZnO QDs (CAETANO et al., 2011), respectively, and the band around 266 nm is a characteristic fingerprint of TAA.

Figure III.4. UV-vis spectra of (a) ZnO QDs, ZnS QDs and the mixture of ZnO and ZnS QDs and (b) ethanolic solution of TAA.

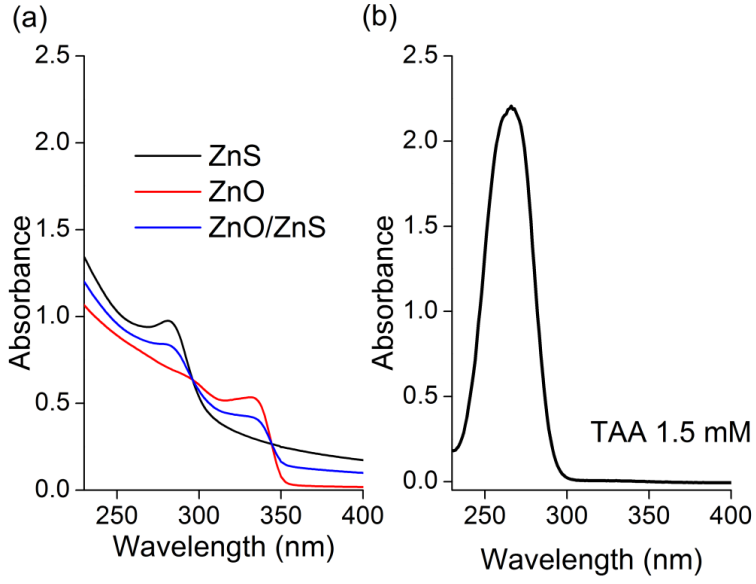

UV-vis absorption spectra measured at 1, 5, 10, 20 and 40 min of reactions using both preparation modes (Route 1 and Route 2) are shown in Figure III.5 (a to c and d to f, respectively). The size of ZnO QDs was calculated using the Brus equation (BRUS, 1983) for 1.5 and 5 mM TAA concentrations for both Routes and they are gathered in the Table III.2. With the lowest TAA concentrations, we observed a red-shift of the excitonic peak of ZnO corresponding to a growth of about 0.3 nm for both synthesis routes. Moreover, there is no ZnS excitonic peak, confirming the presence of ZnO nanoparticles only. For higher TAA concentrations, different behaviours are observed. PREC_TAA50mM (Figure III.5 (f)) does not present any ZnO excitonic peak whereas SUSP_TAA50mM (Figure III.5 (c)) does at the beginning of the reaction; which slowly decreases to finally vanishes as the reaction advances. This can be interpreted as the dissociation of the ZnO nanoparticles and formation of ZnS, according to the EXAFS results. To confirm the formation of ZnS nanoparticles, the SUSP_TAA50mM reaction product was washed in order to remove the unreacted TAA, which dominates the absorption spectrum in this wavelength range in Figures III.5 (c), and further suspended in ethanol before to be analyzed by UV spectroscopy. Figure III.6 (a) shows a zoom of selected UV-vis spectra measured at the indicated reaction time (min) in the region of the excitonic peak of ZnO QDs (330 to 360 nm) of the SUSP_TAA50mM reaction, and (b) UV-vis spectrum of SUSP_TAA50mM reaction product washed and re-suspended in ethanol. The peak around 290 nm fully confirms the formation of ZnS nanoparticles as main phase.

Table III.2. Initial (time = 1 min) and Final (time = 40 min) ZnO QDs Radius (nm) deduced from UV-vis spectra using Brus Equation, and Initial (time = 1 min) and Final (time = 40 min) Rg (nm) deduced from SAXS curves using Guinier Equation.

Sample	*Initial and Final ZnO QDs Radius (nm)*	*Initial and Final Rg (nm)*
ZnO QDs		2.4±0.008 - 2.8±0.011
SUSP_TAA1.5mM	2.2 - 2.4	1.9±0.004 - 2.7±0.012
PREC_TAA1.5mM	1.8 - 2.1	1.5±0.001 - 2.5±0.006
SUSP_TAA5mM	2.2 - 2.3	1.85±0.006 - ---
PREC_TAA5mM	1.7 - 2.0	1.6±0.003 - 3.9±0.049
SUSP_TAA50mM		2.1±0.208 - 6.7±0.123
PREC_TAA50mM		2.4±0.015 - 4.9±0.180
ZnS QDs		

For the intermediate TAA concentrations, SUSP_TAA5mM, we do not observe any displacement of the excitonic peak of ZnO as function of time, indicating that the size of the ZnO nanoparticles remains constant. This behaviour can be explained by the capping of a ZnS shell around the ZnO core preventing the growth of the latter. By the end of the reaction, both excitonic peaks of ZnO and ZnS are present. Whereas, for PREC_TAA5mM we observe the red shift of both excitonic peaks indicating the growth of two distinct populations, suggesting the presence of a mixture of ZnO and ZnS nanoparticles.

Figure III.5. Selected UV-vis spectra measured at the indicated reaction time (min) of the reactions using the Route 1 on the left ((a) SUSP_TAA1.5mM, (b) SUSP_TAA5mM and (c) SUSP_TAA50mM) and the Route 2 on the right ((d) PREC_TAA1.5mM, (e) PREC_TAA5mM and (f) PREC_TAA50mM).

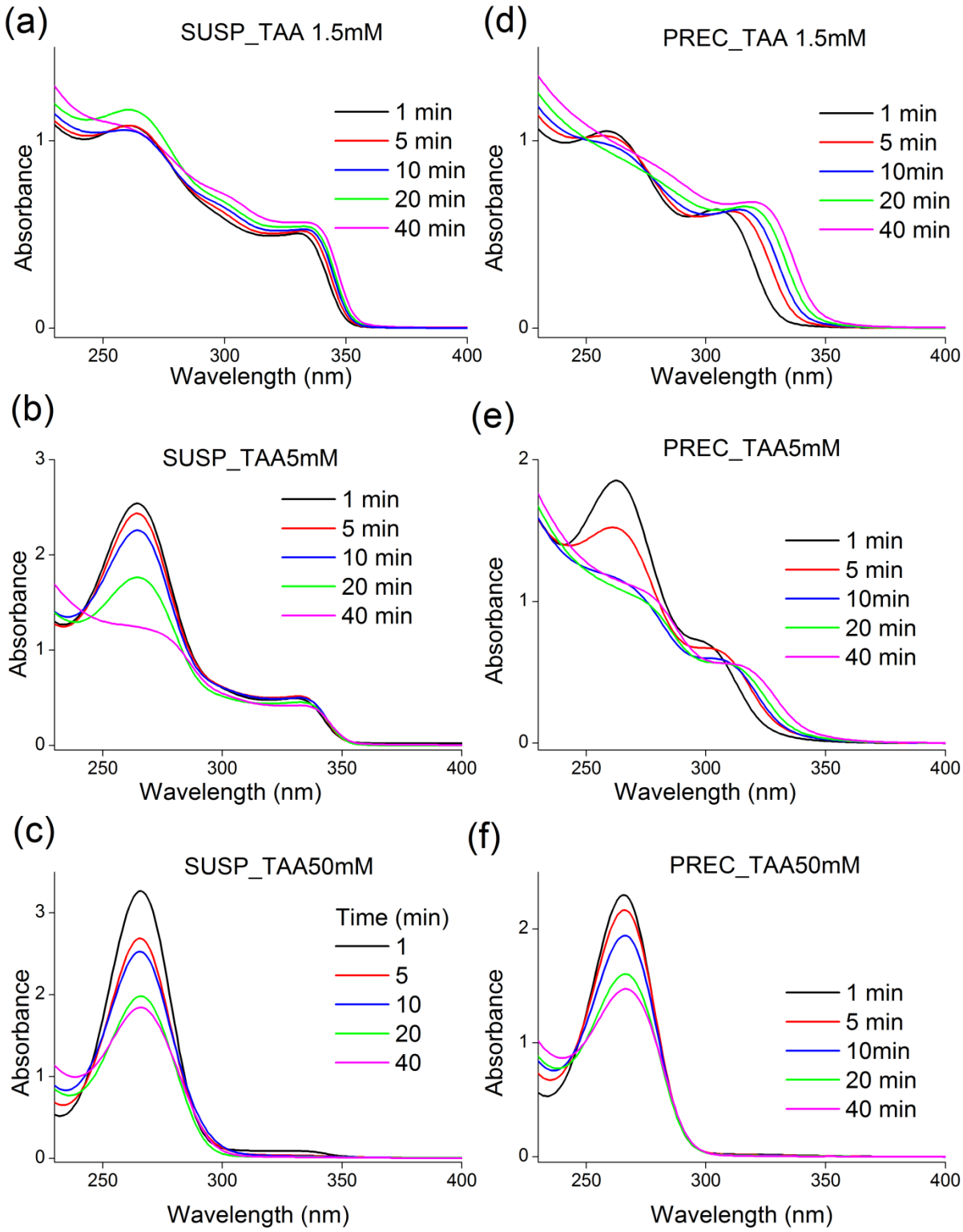

Figure III.6. (a) Zoom of selected UV-vis spectra measured at the indicated reaction time (min) in the region of the excitonic peak of ZnO QDs (330 to 360 nm) of the SUSP_TAA50mM reaction, and (b) UV-vis spectrum of SUSP_TAA50mM reaction product washed and re-suspended in etanol.

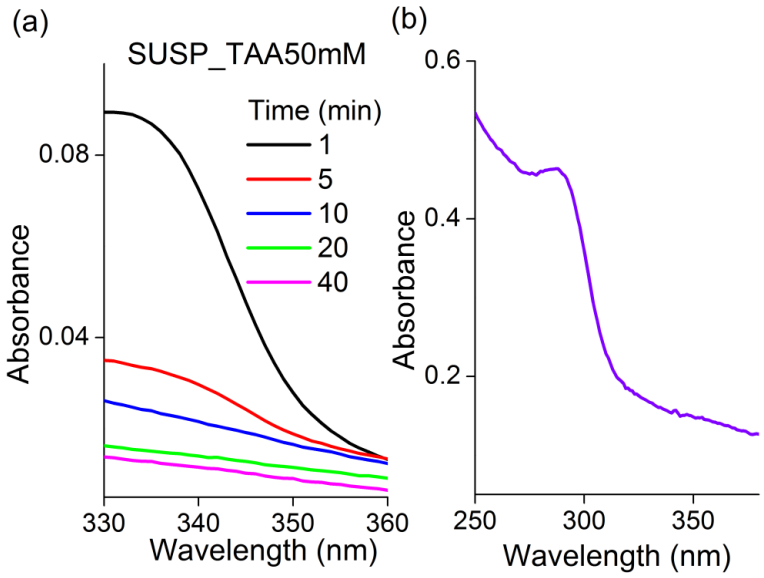

III.2.5. pH evolution

The time evolution of the pH during the reactions using Route 1 and Route 2 was monitored and is shown in Figures III.7 (a) and (b), respectively.

Figure III.7. Time evolution of the pH during the reactions using Route 1 (a) and Route 2 (b).

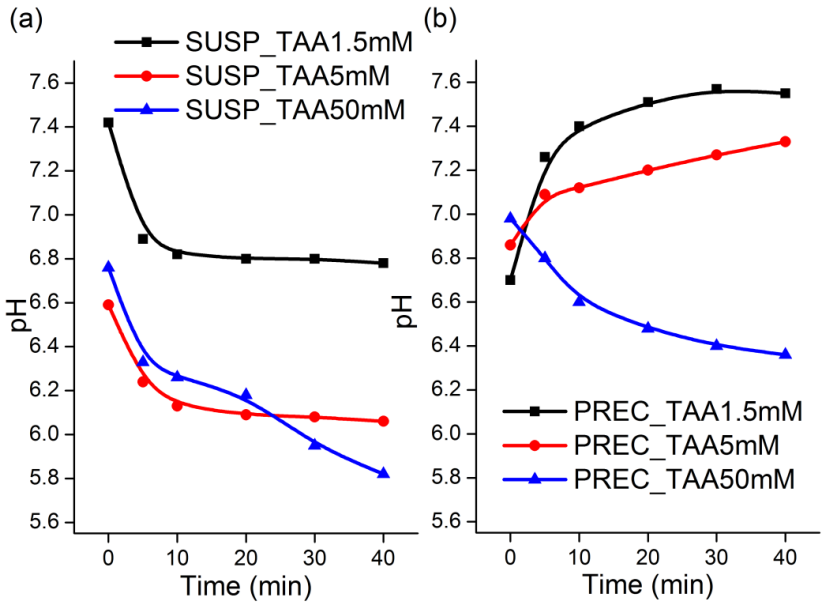

The ZnO QDs are soluble in acidic (MEULENKAMP, 1998) and basic media, thus in these environments the surface of the QDs starts to dissolve releasing Zn^{2+} ions into the solution. To form ZnS QDs, the TAA releases sulfur anions in the solution according to the reaction:

$CH_3CSNH_2 \rightarrow CH_3CN + 2H^+ + S^{2-}$

that will react with the Zn^{2+} and lead to the formation of ZnS QDs close to ZnO QDs:

$Zn^{2+} + S^{2-} \rightarrow ZnS$

SUSP_TAA1.5mM: the pH of the reaction varies from 7.4 to 6.8 and the solution is not acid enough to dissolve the ZnO QDs. Figure III.5 (a) shows the decrease of the TAA band with time, suggesting that the release of S^{-2} into the solution is accompanied by an increase of the absorbance intensity of the ZnO excitonic peak. ZnO QDs are not dissolved and the Zn^{+2} ions do not recombine with S^{2-} ions.

SUSP_TAA5mM: the pH decreases from 6.6 to 6.1 and the formation of ZnS QDs is evidenced by the excitonic peak at the end of the reaction (Figure III.5 (b)). The pH of the reaction is acid enough to dissolve ZnO QDs also evidenced by the decrease in the UV absorption around λ = 335 nm (Figure III.5 (b)), indicating the dissolution and loss of ZnO from the ZnO QDs (DAVID et al., 2012), forming ZnS nanoparticles. The ZnS nanoparticles could be also formed by the reaction between remaining ZnAc precursors molecules present yet in the medium and TAA, once the time (5 s) used to form the ZnO nanoparticles before the addition of sulphur source can be insufficient to promote the total conversion of precursor into ZnO nanoparticles.

SUSP_TAA50mM: the decrease of the pH is more accentuated, achieving 5.8 at the end of the reaction, inducing the total dissolution of ZnO as described in the Figure III.6 (a); the ZnO excitonic peak vanishes. With high TAA concentration, the Zn^{2+} ions can easily create bonds with the abundant sulphur source, resulting in the formation of ZnS QDs in higher proportion than ZnO QDs (NAM et al., 2011). The same behaviour is observed with the analog reaction using Route 2 synthesis, its pH reaches 6.4 at the end of the reaction and no ZnO QDs peak is observed because the reaction was started with ZnAc Prescursor.

The pH of the reactions using Route 2 synthesis was higher than that of Route 1. As the reaction of Route 2 started with the ZnAc precursor followed by the addition of TAA and LiOH, the possible presence of free OH^- ions in the solution might increase the pH. It is noteworthy that the pH of the reaction using intermediate TAA concentration is slightly lower than the reaction using lower TAA concentration due to higher release of H_2S by TAA. It is

important to remark that the same behaviour concerning the dissociation of ZnO with the increase of TAA concentration is observed in the reactions using Route 2: in the UV-vis spectra of PREC_TAA1.5mM and PREC_TAA5mM there is an increase and decrease, respectively, of the absorbance intensity of the ZnO excitonic peak.

Summarising: the smaller is the source of S, the less H_2S is released into the solution, the less acid is the medium, and weaker is the dissolution of ZnO, lowering the formation of ZnS.

III.2.6. In situ Small Angle X-ray Scattering

The growth of ZnO QDs and ZnO/ZnS core-shell QDs were further evidenced by time-resolved SAXS patterns, recorded from the beginning of the reactions. Figure III.8 (a) presents selected curves of the ZnO QDs. The ZnO suspension was injected in the sample holder and kept at 60°C during 40 min. At the beginning of the reaction, ZnO QDs curves display a plateau at low *q*-range (Guinier region). In the Guinier region, the scattered intensity can be approximated by $I(q) = I(0)\ exp(-Rg^2q^2/3)$ where *Rg* is the radius of gyration (Guinier radius) of the particles or aggregates (GUINIER and FOURNET, 1955). The Guinier plateau progressively shifts to lower *q* values until the end of the reaction, reflecting the increase in the nanoparticle size with time. The Guinier radius increases with the time from 2.4 to 2.8 nm at the end of the reaction, see Table III.2.

Figure III.8 displays selected curves of the reactions Route 1 (b, c and d) and Route 2 (e, f and g). The reactions using TAA 1.5 mM (both routes) and TAA 5 mM (Route 2) present similar kinetic behaviours as for ZnO QDs: the presence of a Guinier region, and a progressive displacement to lower *q* region of this plateau, indicating the increase of the nanoparticles size. The reaction using TAA 5 mM (Route 1) showed also a characteristic Guinier region until 20 min of reaction, moving towards the low *q*-region finally vanishing. Figure III.9 shows the time evolution of the *Rg* during 40 min of the reactions, except for the reaction SUSP_TAA5mM which presented the plateau in the Guinier region only up to 20 min. The reactions carried out using Route 2 synthesis present smaller size at the beginning of the reactions due to the fact that the reactions started with the ZnAc precursor. The primary particles are forming in the first instants of the reactions with lower size compared to the Route 1 synthesis which were started with the ZnO suspensions of *Rg* = 2.4 nm. The final nanoparticles sizes prepared by Route 1 are higher than those prepared by Route 2. The higher increase of the size of final SUSP_TAA5mM suggests the overcoating of the ZnO by ZnS.

For samples prepared with higher TAA concentration the SAXS curves show the presence of a plateau at Guinier region and a progressive displacement to lower *q* values of this plateau, indicating the increase of the size of the nanoparticles. However at higher *q* values another linear regime can be observed indicating the presence of a second population of nanoparticles formed after 5 minutes for PREC_TAA50mM and 10 minutes for SUSP_TAA50mM. This second population of nanoparticles presents smaller *Rg* values of around 1.0 nm that remains constant with time of reaction independently of the route of synthesis. The second population can be attributed to the ZnS QDs as already discussed in XAS results.

Figure III.8. Selected in situ SAXS profiles measured at the indicated reaction time (min) of ZnO QDs (a) and the reactions using the Route 1 (b, c and d) and the Route 2 (e, f and g).

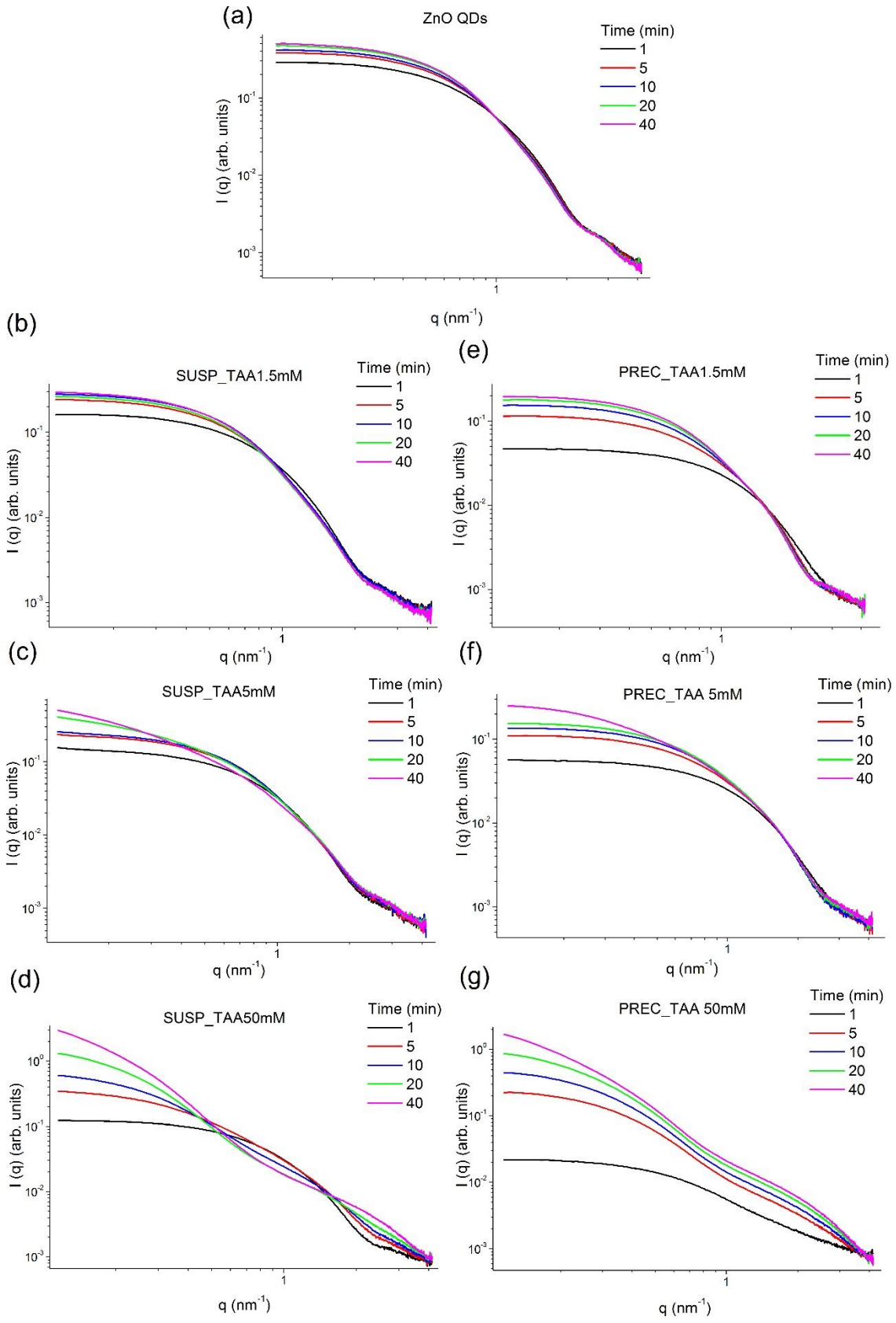

Figure III.9. Time evolution of the Rg (nm) during 40 min of the reactions (except for the reaction SUSP_TAA5mM which presented the plateau in the Guinier region up to 20 min).

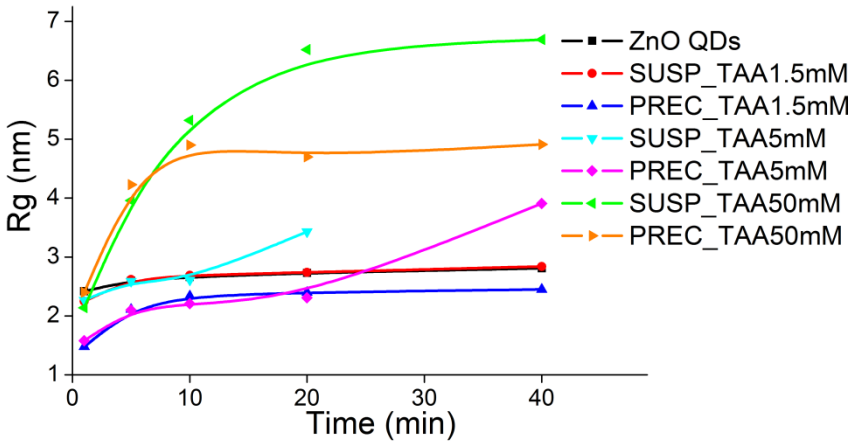

III.2.7. Photoluminescence

PL spectra of the ZnO QDs and the different samples prepared, excited at 353 nm, are shown in Figure III.10. The ZnO QDs presented a broad green emission centered on 520 nm. The samples prepared with TAA1.5mM and TAA5mM presented two emitting bands including the same of the ZnO QDs and a small UV emission peak at 390 nm.

Figure III.10. PL spectra of the ZnO QDs, samples prepared using the Route 1 (SUSP_TAA1.5mM, SUSP_TAA5mM and SUSP_TAA50mM) and the Route 2 (PREC_TAA1.5mM, PREC_TAA5mM and PREC_TAA50mM) excited at 353 nm.

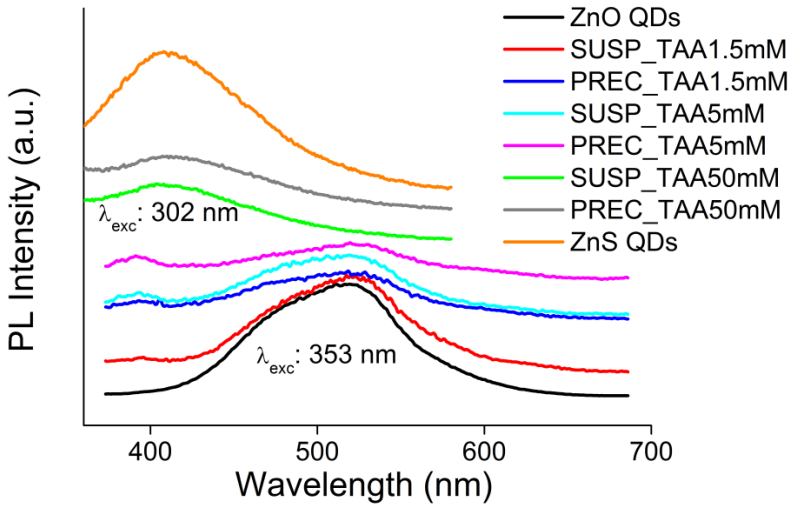

Generally, the UV emission originates from the recombination of photogenerated free excitons with holes in the valence band or in traps near the valence band. The broad visible luminescence has commonly been attributed to the singly ionized oxygen vacancy and results from the recombination of electrons which are close to the conduction band with the trapped holes in the interstitial oxygen vacancies (XIONG, 2010). The PL spectrum of ZnO/ZnS core-shell QDs structure (SUSP_TAA5mM) shows an enhanced UV emission (393 nm) and a reduced green emission, as compared to that of ZnO QDs. This behaviour indicates that with the increase of TAA concentration, the ZnO surface defects are decreasing gradually by filling up the oxygen vacancies via S atoms. The increase of the presence of ZnS, a wider band gap semiconductor material, covering the ZnO QDs passivates the surface electronic states of the ZnO QDs, leading to the enhancement of the UV luminescence. This same behaviour has been observed in many works, with the increase of the ZnS amount (NAM et al., 2011; SHUAI and SHEN, 2011; SADOLLAHKHANI et al., 2014). For PREC_TAA5mM, we can observe a very low increase of UV emission and a reduction of green emission compared to PREC_TAA1.5mM. These results corroborate to XAS ones, once the presence of ZnO and ZnS distinct QDs do not lead to surface passivation of them.

The samples prepared with TAA50mM presented PL spectra very different from the others: there is a peak characteristic of ZnS QDs centered around 420 nm which is well reported for ZnS emission due to sulphur vacancies (SHARMA et al., 2010), indicating mainly the presence of ZnS QDs, which corroborates with XRD, HRTEM, XAS, and UV results.

III.3. DISCUSSIONS

Capping ZnO with a semiconductor presenting larger bandgap energy such as CdS, ZnSe or ZnS (THUY and LIEM, 2013), may improve their photoluminescence properties. This procedure is applied to reduce their sensitivity of the optical properties towards changes in the local environment of the nanoparticle surface. Moreover, it is possible to enhance their stability against photodegradation, photobleaching and to improve their fluorescence quantum yield (REISS et al., 2009; CHEN et al., 2013).

Luo et al (LUO et al., 2015) have recently reported a Cd-doped ZnO/ZnS core–shell quantum dots using also the TAA as sulphur source to form ZnS shell. They investigated the final material by UV-vis spectroscopy and attributed the red shift of the excitonic peak with the increase of the TAA concentration to the leakage of excitons from the ZnO core to the

ZnS shell. In our case, we collected UV-vis spectra during the nanoparticles formation and we observed the red-shift of the ZnO excitonic peak as a function of time for low and intermediate TAA concentrations (except for SUSP_TAA5mM, discussed below). This behaviour can be attributed to the nanoparticles size increase. This latter has also been evidenced by SAXS. Of note, the final size calculated from UV spectra are smaller than that calculated from SAXS, because the radius calculated by Brus considers only the singular ZnO QDs and the *Rg* calculated by Guinier considers the size of the nanoparticle that can be an agglomerate of ZnO and/or ZnS QDs formed during the reactions.

The pH of the reaction helped us to identify the dissolution phenomena for the different samples. For samples with the lowest TAA concentration, where no intense pH variation was detected, the dissolution of ZnO was not observed. This fact can be also observed by an increase of the ZnO excitonic peak intensity in the absorbance spectra. The final pH of the SUSP_TAA1.5mM and SUSP_TAA5mM suspensions were about 6.8 and 6.0, respectively, justifying the higher dissolution of ZnO when using TAA5mM. The dissolution of the ZnO with the decrease of the pH has already been investigated by David et al. (DAVID et al., 2012) which evaluated different ZnO nanoparticle sizes changing the solution parameters. They described a similar behaviour as the one observed in the present work: a substantial decrease in the UV absorption intensity of ZnO excitonic peak when the pH was decreased from 8.8 to 7.7 due to ZnO dissolution.

In our study it was observed the higher proportions of ZnS QDs in the reactions containing higher concentration of TAA. Higher amount of TAA provoked the increase of H_2S into the solution leading to the release of Zn^{+2} ions by the dissolution of ZnO nanoparticles and combining Zn^{2+} ions with S^{2-} ions. In the same way, Nam et al (NAM et al., 2011) and Luo et al (LUO et al., 2015) also related ions exchange between ZnO surface and H_2S with the formation of ZnS shell in nanoparticles bigger than 200 nm, and about 8 nm, respectively. Thus, this methodology of capping ZnO with ZnS shell can be used not only for bigger particles, but also for quantum dots.

Basic characterisation techniques can be used to identify the core overcoating. UV-vis and PL spectroscopy are extremely sensitive to nanoparticle surface modifications, nevertheless, they can mainly give indirect information of the shell formation and must be completed by structural investigations, such as X-ray diffraction or Transmission Electron Microscopy. The last one is used for direct proof of successful shell growth by the increase of the nanoparticle diameter; however, this analysis must be very accurate before and after the

shell deposition and is very limited depending on the core size and shell thickness. Other sophisticated characterisation techniques can be used, such as X-ray Photoelectron Spectroscopy (XPS) and Extended X-ray Absorption Fine Structure (EXAFS). This latter has been used to identify the nature and binding modes of the nanoparticles (REISS et al., 2009).

The EXAFS results obtained for all the samples are in agreement with UV-vis, XRD, SAXS, HRTEM and pH evolution results:

TAA 1.5 mM: the XANES and EXAFS data analysis revealed that these samples are mainly formed by ZnO nanoparticles (98% and 100% of ZnO in Route 1 and Route 2, respectively), irrespective to the preparation routes.

TAA 5 mM: XANES/EXAFS data revealed different behaviours as function of the preparation route. For PREC_TAA5mM the structural parameters and linear combination fitting show the presence of a mixture of 70% of ZnO QDs and 30% of ZnS QDs. In that case, as the main phase is the bigger one, the ZnO QDs are mainly presented in the medium confirming the results of UV-vis, XRD and pH evolution. In the Route 2, the TAA and LiOH are added to the ZnAC precursor and hydrolysis and condensation reactions occur to form both ZnO and ZnS species. In this case a competition between reactions to form ZnO and ZnS is established and the concentration of TAA is not high enough to mostly provoke ZnS species. This behaviour is different for Route 1 when the TAA is added after the ZnO formation. For SUSP_TAA5mM the local order around Zn revealed a higher proportion of oxygen atoms around Zn compared to sulphur ones resulting to the formation of a core-shell structure where ZnO is the core capped by a ZnS shell. It is noteworthy that the proportions determined by LCF of the XANES spectrum for this sample used to mimic a mixture of ZnO QDs and ZnS QDs does not match the coordination numbers determined by EXAFS data analyses. The presence of a core-shell structure for this sample is confirmed by UV-vis and HRTEM results; the excitonic peak of ZnO, observed in the UV-vis spectra, is not displaced to higher wavelengths suggesting that the ZnO nanoparticles growth is stopped by the ZnS shell deposition.

TAA 50mM: combined XANES/EXAFS data show the presence of majoritarian ZnS phases (~78%), independent of the route of synthesis. Figure III.11 shows time evolution of (a) the pH, ZnO and TAA UV-vis absorbance intensity of the SUSP_TAA50mM and (b) the pH and TAA UV-vis absorbance intensity of the PREC_TAA50mM. In the Route 1, we can observe the pH variation in three steps (Figure III.11(a)): (i) 1 – 10 min, an intense decrease of pH due to the decrease of TAA peak which acidify the medium with H_2S and starts the

ZnO dissolution; (ii) 10 - 20 min, a decrease of the TAA concentration and ZnO dissolution is observed, however, the pH presents a plateau related to the ZnO dissolution that induces the balance displacement with the Zn^{2+} presence (BIAN et al., 2011); (iii) 20-40 min, the ZnO presence is almost zero (stop the balance displacement), TAA decomposition is kept until the end of the reaction (high concentration of H_2S in the medium), therefore the pH decreases continuously. Route 2 presents a better correlation of the pH decrease with the TAA decomposition (Fig. III.11 (b)). The pH range variation is higher than Route1 due to the LiOH presence in the medium; besides part of the H^+ will react with LiOH and no base will react with the ZnAc precursor to form ZnO.

Figure III.11. Time evolution of (a) the pH, ZnO and TAA UV-vis absorbance intensity of the SUSP_TAA50mM and (b) the pH and TAA UV-vis absorbance intensity of the PREC_TAA50mM.

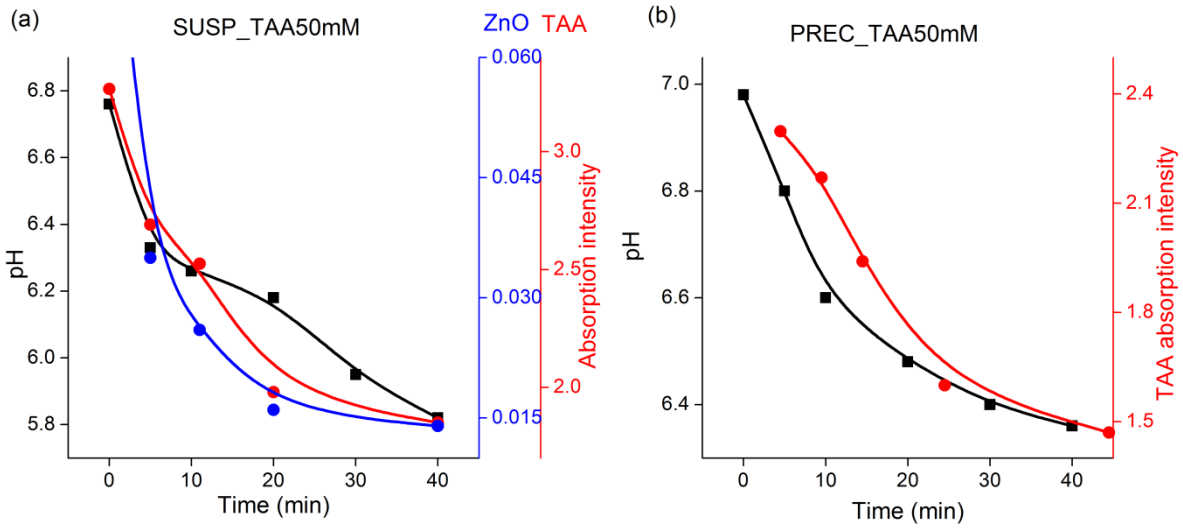

The PL emission spectra revealed an increase of UV emission (393 nm) and a decrease of green emission for samples containing smaller and intermediate TAA amounts as compared to that of ZnO QDs, however the presence of a core-shell structure was not decisive to improve the UV or visible emission. Time resolved photoluminescence studies are necessary to obtain more information about the photostability of the samples and correlate the structural aspects of the core-shell QDs with photoluminescence properties.

III.4. CONCLUSIONS

ZnO/ZnS cores-shell QDs were synthesised by low temperature sol-gel route. We could observe the formation of ZnO/ZnS core-shell QDs when the reactions started with ZnO colloidal suspension mixed with TAA 5 mM (Route1). For sample prepared with TAA 5 mM by Route 2 a mixture of ZnO and ZnS phases was observed. For samples prepared with lower and higher TAA concentrations ZnO or ZnS phase is mainly formed, respectively. The association of XAS technique with usual characterisation techniques used to determine core-shell formation was crucial to distinguish ZnO/ZnS core-shell from ZnO and ZnS mixtures.

III.5. REFERENCES

BIAN, S.-W.; MUDUNKOTUWA, I. A.; RUPASINGHE, T.; GRASSIAN, V. H. Aggregation and Dissolution of 4 nm ZnO Nanoparticles in Aqueous Environments: Influence of pH, Ionic Strength, Size, and Adsorption of Humic Acid. **Langmuir,** v. 27, n. 10, p. 6059-6068, 2011.

BRIOIS, V. GIORGETTI, C.H.; BAUDELET, F.; BLANCHANDIN, S.; TOKUMOTO, M. S.; PULCINELLI, S. H.; SANTILLI, C. V. Dynamical Study of ZnO Nanocrystal and Zn-HDS Layered Basic Zinc Acetate Formation from Sol−Gel Route. **J Phys Chem C Nanomater Interfaces,** v. 111, n. 8, p. 3253-3258, 2007.

BRUS, L. E. A simple model for the ionization potential, electron affinity, and aqueous redox potentials of small semiconductor crystallites. **J Chem Phys,** v. 79, n. 11, p. 5566-5571, 1983.

CAETANO, B. L. SANTILLI, C. V.; MENEAU, F.; BRIOIS, V.; PULCINELLI, S. H. In Situ and Simultaneous UV−vis/SAXS and UV−vis/XAFS Time-Resolved Monitoring of ZnO Quantum Dots Formation and Growth. **J Phys Chem C Nanomater Interfaces,** v. 115, n. 11, p. 4404-4412, 2011.

CASSETTE, E.; PONS, T.; BOUET, C.; HELLE, M.; BEZDETNAYA, L.; MARCHAL, F.; DUBERTRET, B. Synthesis and Characterization of Near-Infrared Cu−In−Se/ZnS Core/Shell Quantum Dots for In vivo Imaging. **Chem Mater,** v. 22, n. 22, p. 6117-6124, 2010.

CHEN, O.; ZHAO, J.; CHAUHAN, V. P.; CUI, J.; WONG, C.; HARRIS, D. K.; WEI, H.; HAN, H. S.; FUKUMURA, D.; JAIN, R. K.; BAWENDI, M. G. Compact high-quality CdSe–CdS core–shell nanocrystals with narrow emission linewidths and suppressed blinking. **Nat Mater,** v. 12, n. 5, p. 445-451, 2013.

CURCIO, A. L.; BERNARDI, M. I. B.; MESQUITA, A. Local structure and photoluminescence properties of nanostructured Zn1-xMnxS material. **Phys Status Solidi Rapid Res Lett.,** v. 12, n. 12, p. 1367-1371, 2015.

DABBOUSI, B. O.; RODRIGUEZ-VIEJO, J.; MIKULEC, F. V.; HEINE, J. R.; MATTOUSSI, H.; OBER, R.; JENSEN, K. F.; BAWENDI, M. G. (CdSe)ZnS Core−Shell Quantum Dots: Synthesis and Characterization of a Size Series of Highly Luminescent Nanocrystallites. **J Phys Chem B,** v. 101, n. 46, p. 9463-9475, 1997.

DAVID, C. A.; GALCERAN, J.; REY-CASTRO, C.; PUY, J.; COMPANYS, E.; SALVADOR, J.; MONNÉ, J.; WALLACE, R.; VAKOUROV, A. Dissolution Kinetics and Solubility of ZnO Nanoparticles Followed by AGNES. **J Phys Chem C Nanomater Interfaces,** v. 116, n. 21, p. 11758-11767, 2012.

GENG, J.; LIU, B.; XU, L.; HU, F. N.; ZHU, J. J. Facile Route to Zn-Based II−VI Semiconductor Spheres, Hollow Spheres, and Core/Shell Nanocrystals and Their Optical Properties. **Langmuir,** v. 23, n. 20, p. 10286-10293, 2007.

GHOSH CHAUDHURI, R.; PARIA, S. Core/Shell Nanoparticles: Classes, Properties, Synthesis Mechanisms, Characterization, and Applications. **Chem Rev,** v. 112, n. 4, p. 2373-2433, 2011.

GUINIER, A.; FOURNET, G. **Small Angle Scattering of X-rays**. New-York: Wiley, 1955.

ISNAENI; KIM, K. H.; NGUYEN, D. L.; LIM, H.;NGA, P. T.; CHO, Y.-H. Shell layer dependence of photoblinking in CdSe/ZnSe/ZnS quantum dots. **Appl Phys Lett,** v. 98, n. 1, p. 012109-3, 2011.

JIA, Z.; MISRA, R. D. K. Tunable ZnO quantum dots for bioimaging: synthesis and photoluminescence. **Mater Technol,** v. 28, n. 4, p. 221-227, 2013.

LIM, J. H.; KANG, C. K.; KIM, K. K.; PARK, I. K.; HWANG, D. K.; PARK, S. J. UV Electroluminescence Emission from ZnO Light-Emitting Diodes Grown by High-Temperature Radiofrequency Sputtering. **Adv Mater,** v. 18, n. 20, p. 2720-2724, 2006.

LIU, K.; SAKURAI, M.; AONO, M. ZnO-Based Ultraviolet Photodetectors. **Sensors (Basel, Switzerland),** v. 10, n. 9, p. 8604-8634, 2010.

LIU, L.; CHEN, Y.; GUO, T.; ZHU, Y.; SU, Y.; JIA, C.; WEI, M.; CHENG, Y. Chemical Conversion Synthesis of ZnS Shell on ZnO Nanowire Arrays: Morphology Evolution and Its Effect on Dye-Sensitized Solar Cell. **ACS Appl Mater Interfaces,** v. 4, n. 1, p. 17-23, 2011.

LUO, J.; ZHAO, S.; WU, P.; ZHANG, K.; PENG, C.; ZHENG, S. Synthesis and characterization of new Cd-doped ZnO/ZnS core-shell quantum dots with tunable and highly visible photoluminescence. **J Mater Chem C,** v. 3, n. 14, p. 3391-3398, 2015.

MATSUYAMA, K.; IHSAN, N.; IRIE, K.; MISHIMA, K.; OKUYAMA, T.; MUTO, H. Bioimaging application of highly luminescent silica-coated ZnO-nanoparticle quantum dots with biotin. **J Colloid Interface Sci,** v. 399, p. 19-25, 2013.

MEHTA, S. K.; KUMAR, S.; CHAUDHARY, S.; BHASIN, K. K.; GRADZIELSKI, M. Evolution of ZnS Nanoparticles via Facile CTAB Aqueous Micellar Solution Route: A Study on Controlling Parameters. **Nanoscale Res Lett,** v. 4, n. 1, p. 17-28, 2008.

MEULENKAMP, E. A. Size Dependence of the Dissolution of ZnO Nanoparticles. **J Phys Chem B,** v. 102, n. 40, p. 7764-7769, 1998.

MOUSSODIA, R.-O, BALAN, L., MERLIN, C., MUSTIN, C., SCHNEIDER, R. Biocompatible and stable ZnO quantum dots generated by functionalization with siloxane-core PAMAM dendrons. **J Mater Chem**, v. 20, p. 1147-1155, 2010.

NAM, W.; LIM, Y. S.; SEO, W.-S.; CHO, H. K.; LEE, J. Y. Control of the shell structure of ZnO–ZnS core-shell structure. **J Nanopart Res,** v. 13, n. 11, p. 5825-5831, 2011.

PANDA, S. K.; DEV, A.; CHAUDHURI, S. Fabrication and luminescent properties of c-axis oriented ZnO-ZnS core-shell and ZnS nanorod arrays by sulfidation of aligned ZnO nanorod arrays. **J Phys Chem C Nanomater Interfaces,** v. 111, n. 13, p. 5039-5043, 2007.

REISS, P.; PROTIÈRE, M.; LI, L. Core/Shell Semiconductor Nanocrystals. **Small,** v. 5, n. 2, p. 154-168, 2009.

SADOLLAHKHANI, A.; KAZEMINEZHAD, I.; LU, J.; NUR, O.; HULTMAN, L.; WILLANDER, M. Synthesis, structural characterization and photocatalytic application of ZnO@ZnS core-shell nanoparticles. **RSC Adv,** v. 4, n. 70, p. 36940-36950, 2014.

SHARMA, M.; KUMAR, S.; PANDEY, O. P. Study of energy transfer from capping agents to intrinsic vacancies/defects in passivated ZnS nanoparticles. **J Nanopart Res,** v. 12, n. 7, p. 2655-2666, 2010.

SHARMA, S.; CHAWLA, S. Enhanced UV emission in ZnO/ZnS core shell nanoparticles prepared by epitaxial growth in solution. **Electronic Materials Letters,** v. 9, n. 3, p. 267-271, 2013.

SHUAI, X. M.; SHEN, W. Z. A Facile Chemical Conversion Synthesis of ZnO/ZnS Core/Shell Nanorods and Diverse Metal Sulfide Nanotubes. **J Phys Chem C Nanomater Interfaces,** v. 115, n. 14, p. 6415-6422, 2011.

SOOKHAKIAN, M.; AMIN, Y. M.; BASIRUN, W. J.; TAJABADI, M. T.; KAMARULZAMAN, N. Synthesis, structural, and optical properties of type-II ZnO–ZnS core–shell nanostructure. **J Lumin,** v. 145, n. 0, p. 244-252, 2014.

THUY, U. T. D., LIEM, N. Q. Transition from type-I to type-II CdTe/CdS core/shell quantum dots synthesized in water at low temperature. **J Nanosci Nanotechnol,** v. 4, n. 4, p. 045010, 2013.

TOKUMOTO, M. S., BRIOS, V.; SANTILLI, C. V.; PULCINELLI, S. H. Preparation of ZnO Nanoparticles: Structural Study of the Molecular Precursor. **J Solgel Sci Technol,** v. 26, n. 1-3, p. 547-551, 2003.

VERMA, P.; PANDEY, A. C.; BHARGAVA, R. N. Synthesis and characterisation: Zinc oxide–sulfide nanocomposites. **Physica B Condens Matter,** v. 404, n. 21, p. 3894-3897, 2009.

WANG, X.; REN, X.; KAHEN, K.; HAHN, M. A.; RAJESWARAN, M.; MACCAGNANO-ZACHER, S.; SILCOX, J.; CRAGG, G. E.; EFROS, A. L.; KRAUSS, T. D. Non-blinking semiconductor nanocrystals. **Nature,** v. 459, n. 7247, p. 686-689, 2009a.

WANG, Y., GUO, Q., LIN, S., CHEN, B., ZHENG, D. Growth and properties of ZnO/ZnS core/shell nanostructures. **Journal of Physics: Conference Series,** v. 152, n. 1, p. 012018, 2009b.

WANG, L.; KANG, Y.; LIU, X.; ZHANG, S.; HUANG, W.; WANG, S. ZnO nanorod gas sensor for ethanol detection. **Sens Actuators B Chem,** v. 162, n. 1, p. 237-243, 2012.

WEST, A. R. **Solid State Chemistry and Its Applications**. New York: John Wiley and Sons 1992.

WU, D.; JIANG, Y.; YUAN, Y.; WU, J.; JIANG, K. ZnO–ZnS heterostructures with enhanced optical and photocatalytic properties. **J Nanopart Res,** v. 13, n. 7, p. 2875-2886, 2011.

XIONG, H.-M. Photoluminescent ZnO nanoparticles modified by polymers. **J Mater Chem,** v. 20, n. 21, p. 4251-4262, 2010.

XIONG, H.-X. ZnO Nanoparticles Applied to Bioimaging and Drug Delivery. **Adv Mater,** v. 25, n. 37, p. 5329-5335, 2013.

CHAPTER IV

Surface modified Mg-doped ZnO QDs for biological imaging

Chaper IV – Surface modified Mg-doped ZnO QDs for biological imaging

IV.1. INTRODUCTION

In this chapter, we report the design of ZnO-based QDs with strong visible luminescence, promising for labeling of lipidic nanoparticles which could be used as theranostic devices. Specifically, we have shown that (i) Mg-doped ZnO QDs prepared using the sol-gel method exhibited enhanced visible luminescence, (ii) the maximum quantum yield was obtained for Mg precursor concentration of 20 mol%, (iii) Mg-doped ZnO QDs capped by oleic acid formed stable colloidal suspensions in toluene and chloroform, while preserving their photoluminescence.

Usual QDs are made of CdSe, CdTe, InAs and InP. Depending on their composition and size, their emission ranges from near UV to near IR. They need appropriate surface modification, such as coating with amphiphilic molecules, to be dispersible in an aqueous solution. When functionalized with ligands such as antibodies or peptides, QDs can be used to label different types of cellular targets or detect biomarkers (MICHALET et al., 2005; WANG et al., 2010). Recently, nanoparticles containing QDs have been investigated as theranostic devices for simultaneous imaging and drug delivery (XIE et al., 2010). For instance, doxorubicin has been loaded, along with QDs, into micelles, aptamers, and liposomes (BAGALKOT et al., 2007; PARK et al., 2008; TIAN et al., 2011).

However, the potential cytotoxicity of first generation QDs is a major concern for biological applications (CHANG et al., 2006; KLAINE et al., 2008; LEWINSKI et al., 2008; SU et al., 2009). In this context, luminescent nanoparticles of ZnO are currently attracting great interest as potential labels for bio-imaging because of their biodegradability and very low toxicity in vivo, although ZnO nanoparticles are able to release Zn^{2+} ions and produce destructive reactive oxygen species (ROS), as shown by cytotoxicity tests in vitro (MOUSSODIA et al., 2010; JIA and MISRA, 2013; XIONG, 2013). ZnO is an n-type semi-conductor with a wide band gap of 3.37 eV at room temperature and a Bohr exciton radius of ~ 2.34 nm. The typical excitonic emission, arising from recombination of photo-generated electrons with holes in the valence band or in traps near the valence band, is thus observed in the UV range. Remarkably, the photoluminescence spectrum of ZnO nanocrystals also displays a broad visible emission, more suitable for biological imaging, which has been

ascribed to point defects such as O and Zn vacancies or interstitials and related to surface oxygen-containing moieties, such as OH groups (ZHANG et al., 2010). However, the understanding of the exact mechanism for visible emission is still lacking.

Because of the role of defects and surface chemistry, the synthesis technique is expected to strongly influence the luminescence of ZnO. In general, the visible emission of thin films or particles synthesized at high temperature or annealed is very weak whereas nanoparticles prepared by the sol-gel route exhibit stronger defect-induced visible luminescence. A typical sol-gel route is the hydrolysis and condensation of a precursor in ethanolic solution (Zn salt solution) catalyzed by a base (CAETANO et al., 2011). However, the obtained ZnO QDs display a low quantum yield and are unstable in water and in non-polar solvents. Surface modification is further required to prevent growth and aggregation of QDs and to ensure their colloidal stability in different environments (XIONG, 2010). Obtaining ZnO QDs with high quantum yield while preserving their visible luminescence upon surface modification remain a challenge because of the sensitivity of photoluminescence to subtle changes of synthesis parameters and environment.

It has been reported that doping with Mg^{2+} ions can enhance the luminescence of ZnO. Most of previous researches have focused on Mg-doped ZnO thin films and particles annealed at high temperature, with high UV emission but weak visible luminescence (LIN et al., 2008; XIONG et al., 2009; DING et al., 2010; YOUSEFI et al., 2010; VIJAYALAKSHMI and KARTHICK, 2013).

In this chapter, Mg-doped ZnO QDs were characterized by elemental analysis, transmission electronic microscopy, small- and wide-angle X-ray scattering, Raman spectroscopy, UV-vis absorption and photoluminescence emission. The aim was to establish a relationship between the composition and structure of the QDs and their luminescent properties.

IV.2. RESULTS

Mg-doped ZnO QDs were synthesized by the hydrolysis and condensation reaction described in the Chapter II (Section II.2.1 and II.2.4). Surface modification of the QDs was performed using oleic acid (OA) to hinder their aggregation and to provide them colloidal stability in different environments (Section II.2.6). Different quantities of OA were added to the QD suspensions. In all cases the QDs capped by OA formed stable colloidal dispersions in chloroform or toluene.

Preliminary measurements having shown that the visible luminescence of Mg-doped ZnO QDs went through a maximum for a 20 mol% nominal concentration of Mg^{2+} ions in the reaction medium, our investigations focused on the structure and properties of QDs obtained with Mg^{2+} concentration increasing from 2.5 up to 20%. Formulations with concentrations higher than 20 mol% of Mg did not present an increase of the visible emission intensity.

IV.2.1. Inductively Coupled Plasma Mass Spectrometry (ICP-MS)

Actual atomic concentrations of Mg in doped QDs, determined using ICP-MS, are reported in Table IV.1. These data evidence a low incorporation of Mg^{2+} ions into ZnO QDs. The Mg^{2+} concentration varied from 0.41 to 2.94 % (w/w).

IV.2.2. X-ray powder diffraction (XRD)

Figure IV.1 (a) shows powder wide-angle X-ray diffraction patterns, recorded between 2θ = 5 deg and 70 deg, of ZnO reference, ZnO QDs and Mg-doped ZnO QDs. They display peaks characteristic of the ZnO hexagonal wurtzite structure. No peak characteristic of the MgO rock salt phase (e.g. at 42.5 deg) is detected whatever the concentration of Mg^{2+} ions.

Table IV.1. Amount of Mg incorporated into ZnO QDs obtained by ICP, Crystallite size deduced from X-ray diffraction peaks using the Debye-Scherrer relation, Bandgap measured using UV-vis absorption, Wavelength of the PLE peak maximum, Wavelength of the PL emission peak maximum, Quantum Yield of each sample.

Nominal (%) Mg-doped ZnO	(% w/w) Mg incorporated into ZnO	(mol%) Mg incorporated into ZnO	Crystallite size (nm)	Bandgap (eV)	λ_{ex} (nm)	λ_{em} (nm)	QY (%)
0			3.3	3.37	365	520	10.2
2.5	0.41	1.37	2.7	3.42	363	520	5.0
5	0.72	2.41	2.3	3.52	358	512	16.7
10	1.98	6.63	2.2	3.60	350	476	27.8
20	2.94	9.85	2.0	3.71	342	470	64.8

Figure IV.1. (a) XRD profiles of the ZnO standard and nanocrystals from the reactions with 0, 2.5, 5, 10 and 20 % of Mg precursor concentration, indicating the hexagonal wurtzite phase and (b) zoom of the peak (100) in the 2θ ranging from 30 to 34.

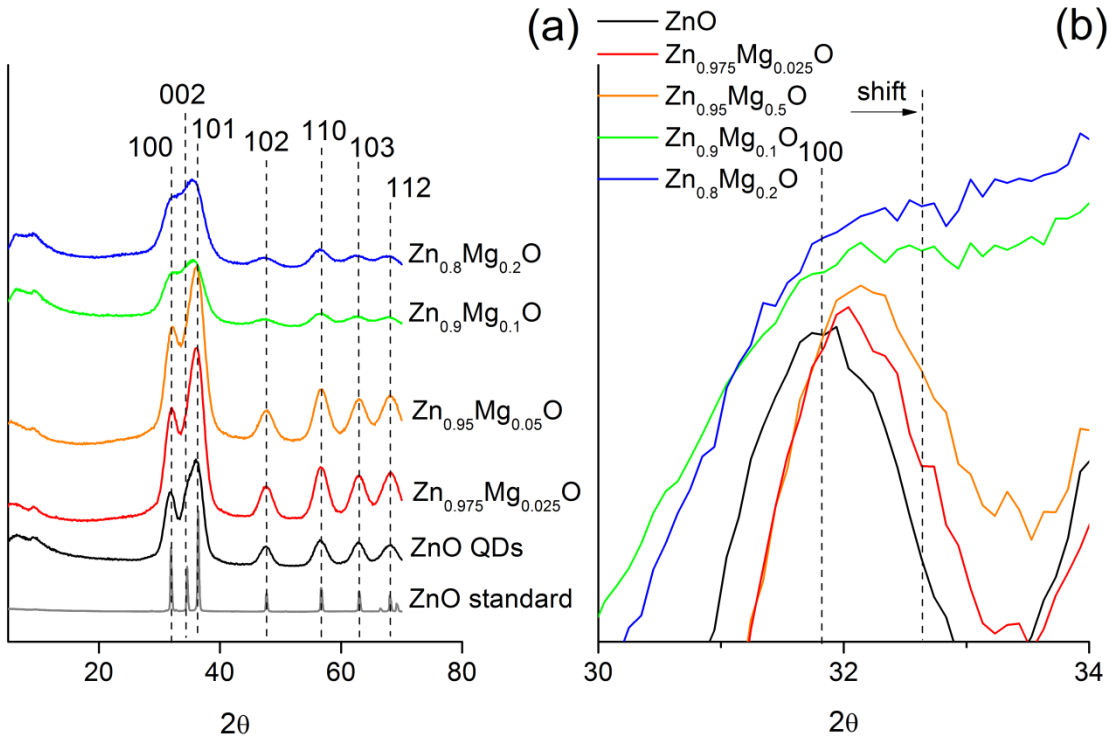

The broadening of the peaks of Mg-doped ZnO QDs could result from a decrease in crystallinity and/or crystal size, promoted by the presence of Mg. Assuming that this broadening is mainly due to size effects, the average size of nanocrystals could be estimated using the Debye-Scherrer relation (WEST, 1992) applied to the (100) reflection:

$$D = \frac{\kappa\lambda}{\beta\cos\theta}$$

where D is the crystal size; k is a constant (shape factor, 0.89 for spherical nanoparticles), λ is the X-ray wavelength, β is the Full-Width-at-Half-Maximum (FWHM) of the diffraction peak and 2θ is the diffraction angle. The size of the nanocrystals decreased from 3.3 nm for ZnO to 2.0 nm for $Zn_{0.8}Mg_{0.2}O$. Figure IV.1 (b) shows a zoom of the (100) diffraction peak between 2θ = 30 deg and 2θ = 34 deg. Mg^{2+} ions shift the (100) peak to slightly higher angles, suggesting a weak decrease of the lattice parameters. This small change, whose extent depends on the Mg concentration, is expected to reflect the substitution of some Zn^{2+} ions by Mg^{2+} ions in the crystalline lattice, as the Mg^{2+} ions have a slightly smaller ionic radius (0.57 Å for Mg^{2+} ions compared to 0.60 Å for Zn^{2+} ions). At high Mg concentrations the peak shifts are obscured by the large width of the peaks.

IV.2.3. High Resolution Transmission electron microscopy (HRTEM)

The size and morphology of ZnO and $Zn_{0.8}Mg_{0.2}O$ nanoparticles were also studied using HRTEM (Figure IV.2). HRTEM images show nanocrystals with approximately spherical shapes and average diameters of about 4 nm for ZnO QDs. The average size of $Zn_{0.8}Mg_{0.2}O$ QDs, whose structure appears less ordered, is slightly smaller. Overall, these data are in agreement with XRD data.

Figure IV.2. HRTEM images of undoped ZnO QDs (a) and $Zn_{0.8}Mg_{0.2}O$ QDs (b).

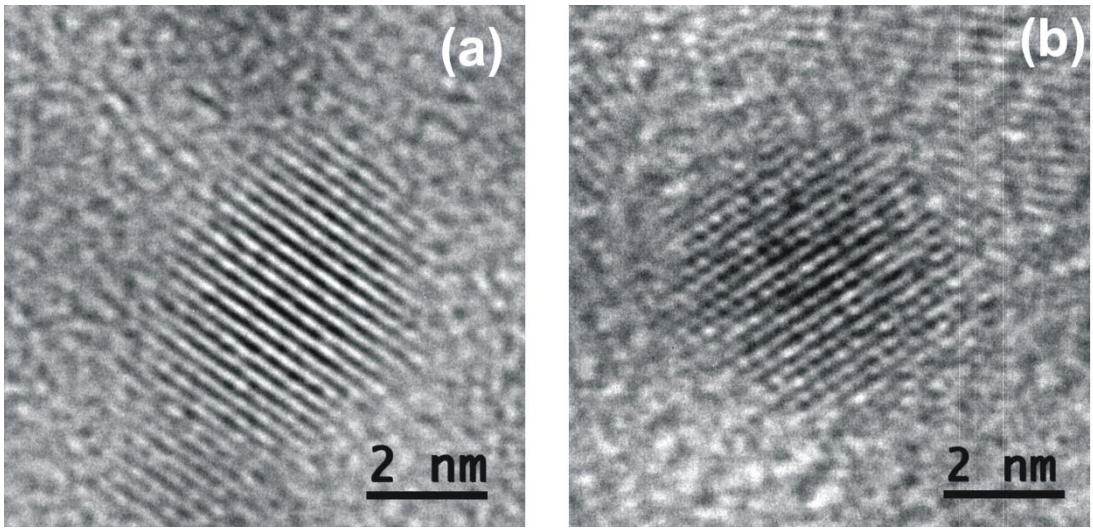

IV.2.4. Small-Angle X-ray Scattering (SAXS)

The influence of Mg on the growth of nanoparticles was further evidenced by time-resolved SAXS patterns, recorded from the beginning of the reaction using 200 ms as acquisition time. Figure IV.3 (a) and Figure IV.4 (a) present three-dimensional stacked log-log plots of the SAXS curves as a function of time, corresponding to the formation of ZnO and $Zn_{0.8}Mg_{0.2}O$ QDs, respectively. Selected curves of ZnO and $Zn_{0.8}Mg_{0.2}O$ QDs formation are shown in Figure IV.3 (b) and Figure IV.4 (b), respectively. The two systems exhibit clearly different time evolution.

Figure IV.3. Three-dimensional stacked log-log plots of the SAXS curves as a function of time recorded in situ during the formation of ZnO QDs (a) and selected in situ SAXS profiles measured at the indicated reaction time (min) (b).

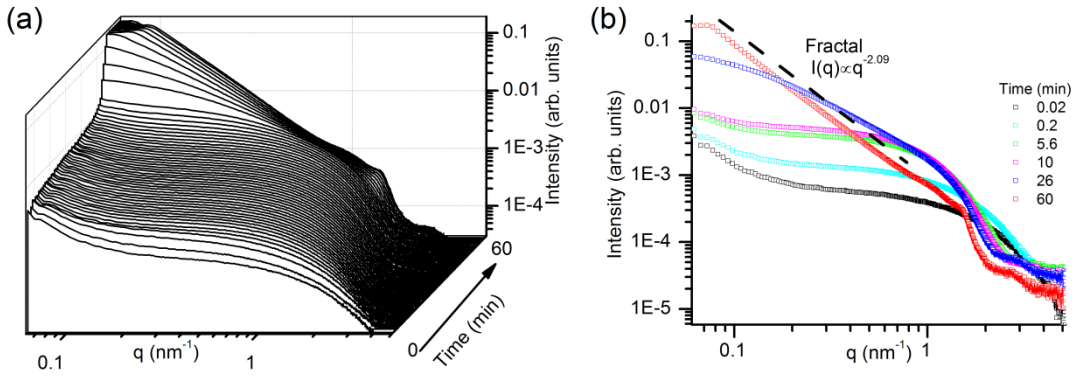

Figure IV.4. Three-dimensional stacked log-log plots of the SAXS curves as a function of time recorded in situ during the formation of $Zn_{0.8}Mg_{0.2}O$ QDs (a) and selected in situ SAXS profiles measured at the indicated reaction time (min) (b).

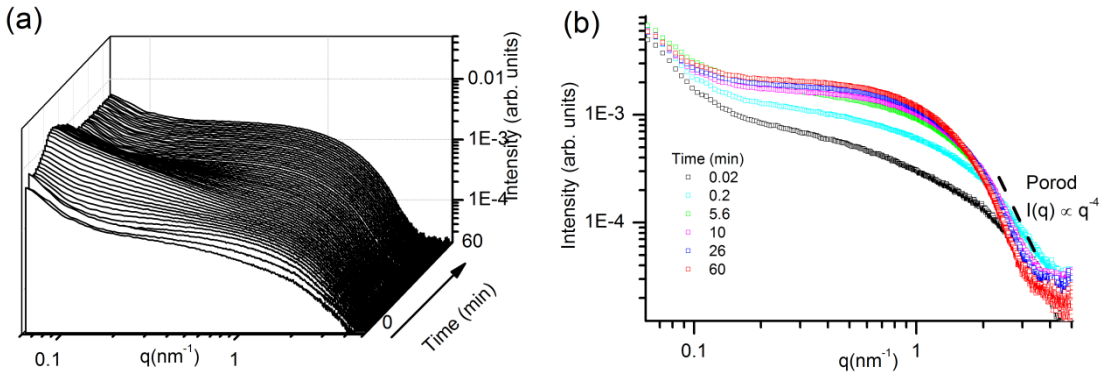

At the beginning of the reaction, ZnO curves display a plateau at low *q*-range (Guinier region), indicative of the scattering of non-interacting particles. In the Guinier region, the scattered intensity can be approximated by $I(q) = I(0)\ exp(-Rg^2q^2/3)$ where *Rg* is the radius of gyration (Guinier radius) of the particles (GUINIER and FOURNET, 1955). The Guinier plateau progressively shifts to lower *q* values, reflecting the increase in the nanoparticle size with time. The curves display an oscillation at high *q* values, which can arise from the form factor of spherical particles. The SAXS profiles could be fitted by the form factor of homogeneous spheres with Gaussian radius distribution. The Table IV.2 displays the values of the variables *N* (particle number density), *s* (polidispersitiy) and *X0* (mean radius) used to fit the curves in each time and the values of I(0) obtained by Guinier equation. Besides, a

background was added to fit the curves. The radii of gyration *Rg* are consistent with the mean radii of the nanoparticles *R*, as deduced from the fits (for a sphere *Rg* is defined as $Rg = (3/5)^{½} R$) (Figure IV.5 (a)). The size of the nanoparticles increased steeply during the first minutes of the reaction, up to 3 nm after 3 min. After about 15 min the size of the primary particles, which has reached 4 nm, no longer evolved.

Table IV.2. Variables *N* (particle number density), *s* (polidispersity), and *X0* (mean radius) used to fit the ZnO and $Zn_{0.8}Mg_{0.2}O$ SAXS curves and the values of I(0) obtained by Guinier equation.

Time (min)	ZnO QDs				$Zn_{0.8}Mg_{0.2}O$ QDs			
	N	***s***	***X0 (Å)***	***I(0)***	***N***	***s***	***X0 (Å)***	***I(0)***
0.02833	$4x10^{-11}$	2.35	8.14	0.0006				
0.20774	$4.07x10^{-11}$	3.03	8.89	0.001				
0.47735	$2.35x10^{-11}$	2.9	11.04	0.002	$3.3x10^{-11}$	1.61	10	
1.54106	$1.728x10^{-11}$	2.84	12.84	0.003	$2.5x10^{-11}$	1.61	11	
2.56666	$1.3x10^{-11}$	3.25	13.96	0.003	$2.5x10^{-11}$	1.61	11	
4.19909	$1.1x10^{-11}$	2.95	15.2	0.004	$2.5x10^{-11}$	2.14	11.3	
7.4952				0.004	$2.5x10^{-11}$	2.84	10.78	0.0016
10.99				0.005	$2.5x10^{-11}$	3	10.78	0.0017
13.30515	$1.42x10^{-11}$	3.83	17.1	0.006	$2.5x10^{-11}$	3	10.78	0.0018
17.71083	$1.42x10^{-11}$	3.83	17.1		$2.5x10^{-11}$	3	10.78	
25.92265					$2.5x10^{-11}$	3	10.78	0.0019
28.51159	$1.42x10^{-11}$	3.83	17.1					
34.49	$1.42x10^{-11}$	3.83	17.1		$2.1x10^{-11}$	3.45	11	0.002
45.88					$2.1x10^{-11}$	3.45	11	0.002
61.04					$2.6x10^{-11}$	3.5	11	0.0021
67.15					$2.6x10^{-11}$	3.5	11	0.0021

Figure IV. 5. Comparison of the time evolution of the radius of gyration (Rg) determined by the Guinier region and the radius of Sphere (R) determined by the sphere model of (a) ZnO QDs and (b) $Zn_{0.8}Mg_{0.2}O$ QDs.

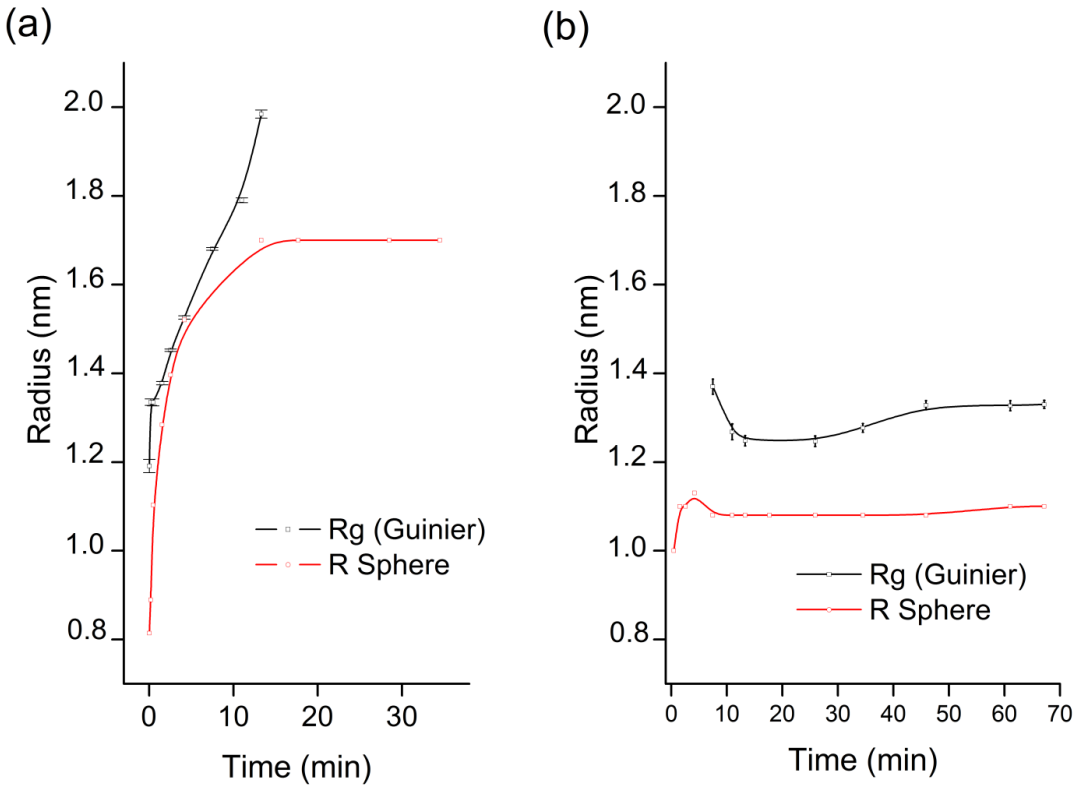

At the end of the reaction, after about 50 min, the intensity scattered at low q values strongly increases and the Guinier plateau disappears. In the low q region, a linear decay of log$I$ is observed in the log$I$ versus log$q$ plot: $I(q) \propto q^{-\alpha}$ (CRAIEVICH, 2005) with $\alpha = 2.09$. This behaviour evidences the formation of fractal aggregates with fractal dimension α, defined as the exponent that relates the mass M of an object to a characteristic dimension R: $M \propto R^{\alpha}$. The $\alpha = 2.09$ fractal dimension is characteristic of structures formed by reaction-limited cluster-cluster aggregation (RLCCA). The aggregation rate is limited by the time needed to overcome the repulsive barrier between two clusters. Compared to the diffusion-limited cluster-cluster aggregation (DLCCA), the RLCCA mechanism corresponds to slower colloid aggregation, yielding more compact clusters due to the lower sticking probability (BRINKER and SCHERER, 1990).

This linear decrease in log$I$ as a function of log$q$ is observed between q values corresponding to the primary particle size and the fractal aggregate size, respectively. As

shown by the curve oscillation in the high *q* range, the mean radius of the primary particles remains constant, at about 2 nm, until the end of the reaction. Consequently, the formation of ZnO QDs involves two main steps: the nucleation and growth, up to a size of ~ 4 nm, of elementary nanoparticles during the ten first min of the reaction, followed by the formation of fractal aggregates with fractal dimension $\alpha = 2.09$.

The structures giving rise to the first $Zn_{0.8}Mg_{0.2}O$ SAXS profiles collected during the synthesis of $Zn_{0.8}Mg_{0.2}O$ QDs could not be identified. After about 5 min, the SAXS curves could also be fitted by the form factor of homogeneous spheres with Gaussian radius distribution. The growth of nanoparticles is rapidly stopped after the nucleation step. Nanoparticles remain smaller than ZnO ones. A further small increase in size is observed at the end of the reaction. The intensity *I*(*0*), proportional to the number of nanoparticles in the medium, increases continuously during the first 60 min of the reaction. Of note, unlike ZnO nanoparticles, $Zn_{0.8}Mg_{0.2}O$ QDs do not form fractal aggregates with time, suggesting that the nanoparticles have different surface properties.

IV.2.5. Raman Spectroscopy

Raman scattering carried out on QDs allows obtaining information on the surface species and on the modifications of the optical phonon spectrum, as compared to ZnO bulk crystal values (Figure IV.6 (a) and (b)). The spectrum of ZnO standard shows a prominent peak at 439 cm^{-1} and weak peaks at 332 cm^{-1}, 380 cm^{-1}, 410 cm^{-1}, 581 cm^{-1} and 666 cm^{-1}, in agreement with previous studies (CUSCÓ et al 2007). The peak at 439 cm^{-1} is characteristic of the wurtzite lattice; the sharp line shape is indicative of high crystalline order. This peak becomes less intense in ZnO QDs while the intensity of the 410 cm^{-1} band increases, appearing as a shoulder of the peak at 439 cm^{-1}. More importantly, in $Zn_{0.8}Mg_{0.2}O$ QDs the weak 439 cm^{-1}peak is involved in a broad band, reflecting the diminution of crystallinity induced by Mg incorporation.

The presence of oleic acid (OA) attached on the surface of QDs is unambiguously evidenced by the intense and well resolved peaks at 1265 cm^{-1}, 1301 cm^{-1} and 1655 cm^{-1} which cannot overlap with peaks arising from other species. These peaks correspond to δ(=CH) deformations, $\delta(CH_2)_n$ deformations and υ(C=C) stretching vibrations of unsaturated fatty acids, respectively (DE JELDER et al., 2007). Other peaks assigned to OA are listed in Table IV.3.

Figure IV.6. Raman spectra of ZnO standard, ZnO QDs, $Zn_{0.8}Mg_{0.2}O$ QDs, OA, OA-ZnO QDs and OA- $Zn_{0.8}Mg_{0.2}O$ QDs with indications of the principal vibrations (a) from 200 to 800 cm^{-1} and (b) from 800 to 1800 cm^{-1}.

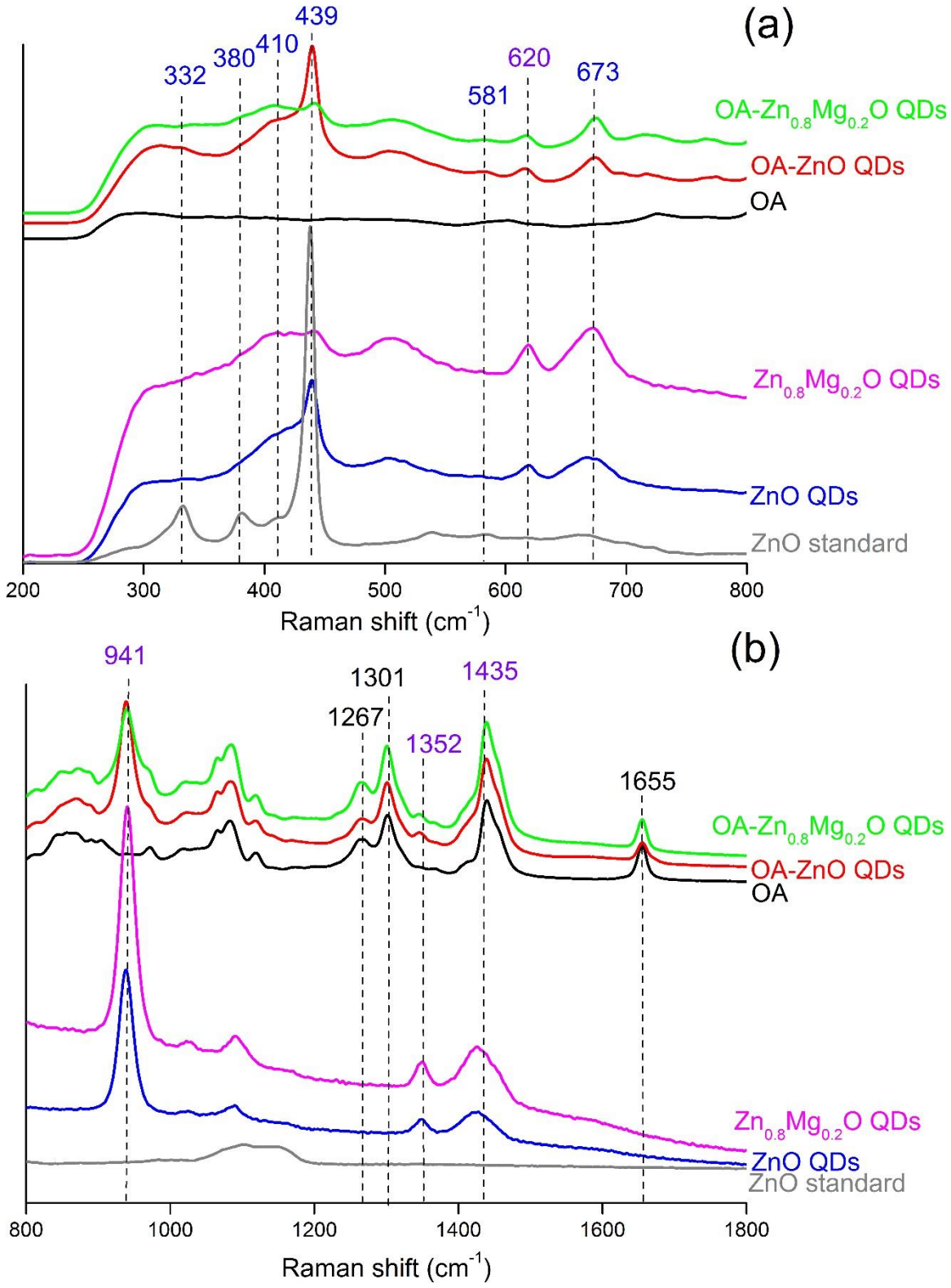

Table IV. 3. Raman shift (cm^{-1}) and assignment of the main vibrations observed in the following samples: ZnO standard, ZnO QDs, $Zn_{0.8}Mg_{0.2}O$ QDs, OA, OA-ZnO QDs and OA-$Zn_{0.8}Mg_{0.2}O$ QDs. Raman shifts are compared with values from References (TANDON et al., 2000; KOLEVA e STOILOVA, 2002; CUSCÓ et al., 2007; DE GELDER et al., 2007).

Raman shift (cm^{-1})	**Origin**	**Reference (cm^{-1})**	**Assignment**	**Reference**
332	ZnO	332	E_2(high) –E_2 (low)	CUSCO
380	ZnO	380	A_1(TO)	CUSCO
410	ZnO	408	E_1(TO)	CUSCO
439	ZnO	437	E_2(high)	CUSCO
581	ZnO	584	E_1(LO)	CUSCO
620	Acetate	621	$Y_{15}(B_2)$; out of plane	KOLEVA
673	ZnO/Acetate	666/671	TA+LO/ $\upsilon_5(A_1)$; OCO sym. bend	CUSCO/ KOLEVA
941	Acetate	942	υ_4 (A_1),C−C strech	KOLEVA
1065	OA	1063	υ_{as}(CC), chain ordered	TANDON
1085	OA	1082	υ(CC), chain ordered	TANDON
1116	OA	1118	υ(CC), chain ordered	TANDON
1267	OA	1265	δ(=CH)	DE GELDER
1301	OA	1301	$\delta(CH_2)_n$	DE GELDER
1435	Acetate	1435	$\upsilon_2(A_1)$; CO sym. strech	KOLEVA
1439	OA	1438	CH_2 scissoring	TANDON
1655	OA	1655	υ(C=C)	DE GELDER

Beside peaks originating from the optical phonon spectrum of QDs and OA molecules capping their surface, Raman spectra of QDs exhibit a prominent peak at 940 cm^{-1} and weak broad peaks at 1352 cm^{-1} and 1435 cm^{-1}, which could be attributed to acetate ions. These peaks correspond to υ(C-C) stretching, $\delta(CH_3)$ symmetric bending and υ(CO) symmetric stretching, respectively (KOLEVA and STOILOVA, 2002). Raman measurements support the incorporation of Mg^{2+} ions in ZnO lattice and demonstrate that the QD surface is efficiently capped with OA. They also evidence the presence of acetate surface groups.

IV.2.6. UV-vis and Photoluminescence Spectroscopy (PL)

The optical properties of the ZnO and $Zn_{0.8}Mg_{0.2}O$ QD colloidal suspensions were studied by UV–vis absorption and PL spectroscopy. UV-vis absorption spectra of ZnO and Mg-doped ZnO QD suspensions are shown in Figure IV.7. The absorption edge shifts from 340 nm to 305 nm with Mg concentration increasing from 0 to 20 mol%. This progressive

blue-shift is indicative of the band gap widening upon Mg doping. The band gap energy was estimated to be the energy at which the absorbance of the absorption edge reached half of its maximum value (BRUS, 1986). An increase from 3.37 eV to 3.71eV is observed, consistent with previous studies (Table IV.1).

Figure IV.7. Absorption spectra of the undoped and 2.5, 5, 10 and 20% Mg doped ZnO colloidal suspensions.

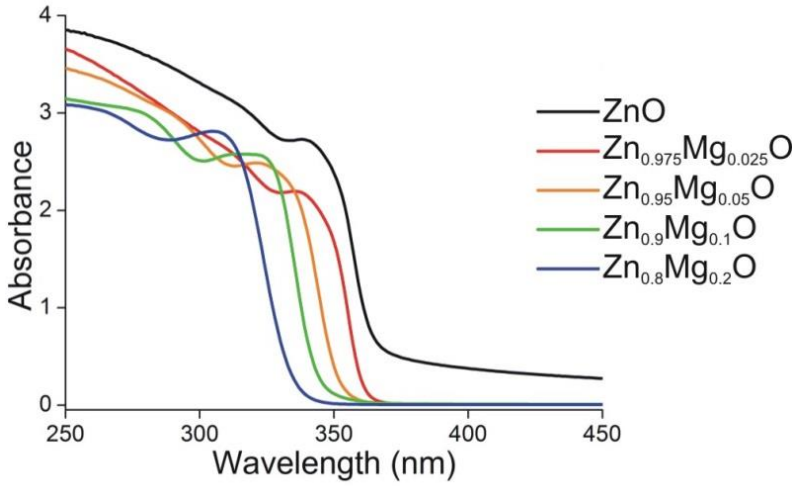

Usually, the PL spectra of ZnO exhibit two components. One is the exciton, or band-edge, emission in the UV range, the other is visible emission, also called deep-level emission, due to the existence of defects which are mainly located on the ZnO surface. Nanoparticles prepared by the sol-gel route exhibit mainly visible luminescence whereas their UV emission is weak. On the contrary, highly crystalline ZnO displays strong band-edge luminescence. In our study, only a weak UV emission peak at ~380 nm was observed when the ZnO QDs where excited at 342 nm. The intensity of the UV emission peak further decreased and became negligible when the concentration of Mg in QDs increased, in agreement with a previous report (YOUSEFI et al., 2013). $Zn_{1-x}Mg_xO$ QDs were excited at low wavelength, between 324 nm and 346 nm. We have therefore focused on the visible emission, by selectively exciting the defect states. Photoluminescence excitation (PLE) spectra were measured with detection at a wavelength where the visible emission was maximum (Table IV.1), revealing an increase in the peak energy with increasing Mg doping level (Figure IV.8). This dependence is in line with that of the absorption spectra.

Photoluminescence emission spectra were then collected by exciting each QD suspension at the wavelength corresponding to the maximum of the PLE spectrum (Fig IV.8). The emission spectra exhibit two broad bands at 400-495 nm and 495-590 nm, whose relative intensities depend on Mg^{2+} concentration. The intensity of the first band is enhanced at high Mg^{2+} concentration. The luminescence increases when Mg^{2+} concentration rises from 5% to 20%. The quantum yields of the different samples are reported in Table IV.1. Remarkably, the quantum yield (QY) of $Zn_{0.8}Mg_{0.2}O$ colloidal suspension (64%) is about 6 times higher than that of the ZnO suspension (QY = 10%).

Figure IV. 8. PLE and PL spectra of the undoped and 2.5, 5, 10 and 20 mol% Mg doped ZnO colloidal suspensions. The inset shows the photography of the undoped (right) and $Zn_{0.8}Mg_{0.2}O$ (left) colloidal suspensions under UV lamp (λexc = 365 nm).

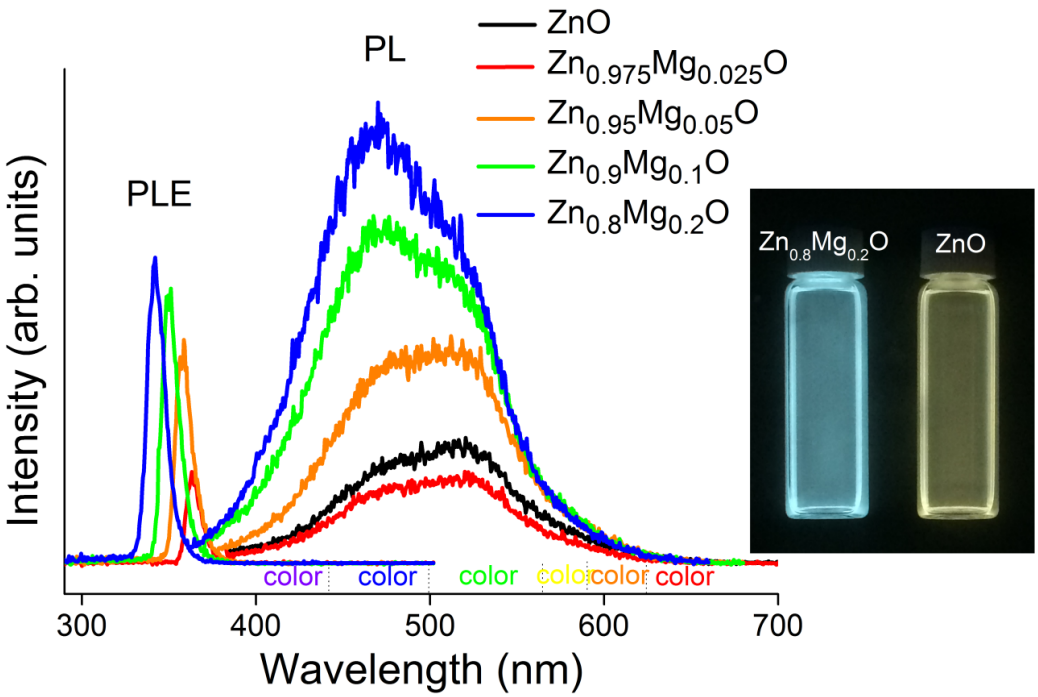

Figure IV.9 shows the emission spectra of ZnO and $Zn_{0.8}Mg_{0.2}O$ QDs capped by OA dispersed in chloroform excited at 345 nm and 341 nm, respectively. The emission wavelength range is not affected by OA. The corresponding QY values are reported in Table IV.4. It can be seen that OA reduced the QY of doped ZnO QDs from 64% to about 40%.

Figure IV.9. PL spectra of the OA-ZnO QDs and OA- $Zn_{0.8}Mg_{0.2}O$ QDs dispersed in chloroform. The insets show the photographs of each sample under UV lamp (λexc = 365 nm).

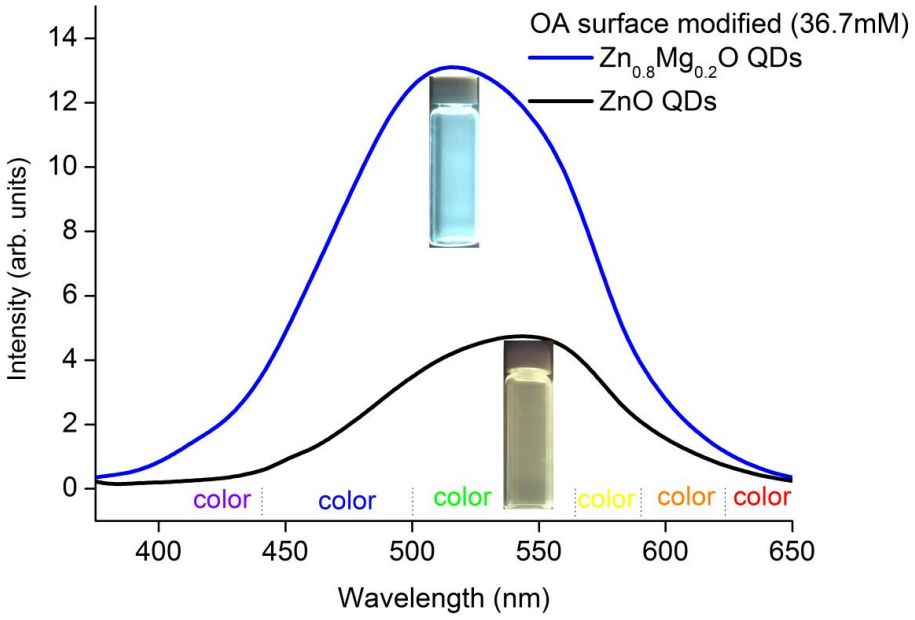

Table IV.4. Quantum Yield (QY) of the ZnO and $Zn_{0.8}Mg_{0.2}O$ QDs capped with oleic acid (OA).

Sample	QY (%)
ZnO 50mM OA 13 mM	5.76
ZnO 50mM OA 36.7 mM	11.86
$Zn_{0.8}Mg_{0.2}O$ 50mM OA 13mM	41.56
$Zn_{0.8}Mg_{0.2}O$ 50mM OA 36.7mM	38.22

IV.3. DISCUSSIONS

Doping ZnO is an effective approach to modify its properties. The introduction of dopant ions can either enlarge or narrow the band gap of the semiconductor, thereby tuning the emission colors. Furthermore, doping ZnO nanoparticles with ions such as Mn^{2+}, Ni^{2+} or Co^{2+} is known to impart magnetic properties to the material (SCHWARTZ et al., 2003; NORBERG et al., 2004).

Effective dopant incorporation is a critical issue. If dopant ions are excluded during ZnO crystal growth or just adsorbed on the surface, the desired properties may be compromised. The close radii of Mg^{2+} (0.57 Å) and Zn^{2+} (0.60 Å) contribute to the solid

solubility of Mg^{2+} in ZnO since Mg^{2+} ions may replace Zn^{2+} ions in the wurtzite lattice. However, both the ratio of actual Mg amount in nanoparticles to nominal concentration in the reaction medium and the maximum Mg doping were found extremely sensitive to the conditions of sample preparation in previous studies. Generally, higher Mg^{2+} contents were achieved when the nanocrystal synthesis was performed at high temperature.

Yang et al reported a dopant content of 22.6 mol%, for a nominal 50% content in the reaction mixture. Doped nanocrystals with different shapes were obtained by alcoholysis of Zn stearate and Mg stearate in 1-octadecene at 270°C (YANG et al., 2010). Cohn et al achieved a dopant content of 18%, close to the nominal content, by heating nanocrystals in dodecylamine at 160°C for about 20 min after hydrolysis and condensation reaction in DMSO at 50°C (COHN et al., 2012). In contrast, Mg content as low as 0.03%, for a Mg concentration in the initial solution of 20%, was obtained by Ghosh et al using sol-gel process at 70°C (GHOSH and RAYCHAUDHURI, 2011). In all cases the wurtzite ZnO phase was maintained. In the present study, the actual Mg content was always much lower than the nominal precursor concentration in the reaction medium. When synthesis was carried out with a [LiOH]/[Zn+Mg] molar ratio r = 1.4, the maximum Mg^{2+} substitution achieved was 2.94% (w/w) for an initial Mg concentration of 20 mol%. Synthesis performed with a different molar ratio, r = 0.5, yielded a concentration of 0.56%. These findings suggested that kinetic factors, likely related to relative precursor reactivities, could limit Mg incorporation in the host ZnO crystal. Generally, it has been emphasized that the growth rate of the host crystal and the rate of deposition of dopant ions should be balanced to achieve effective doping during crystal growth (BUONSANTI and MILLIRON, 2013).

The presence of Mg^{2+} ions affected the growth and size of the NPs, along with their structure. Mg^{2+} addition decreased the final size of QDs and inhibited their fractal aggregation, suggesting a modification of their surface properties. As evidenced by X-ray diffraction, HRTEM images and Raman spectra, doped QDs displayed a less crystalline, more disordered wurtzite structure than ZnO QDs.

The incorporation of Mg widened the band gap of doped ZnO QDs primarily by decreasing their size since NPs smaller than ~ 6 nm are sensitive to quantum confinement. Moreover, it is known that doping with Mg widens the band gap of ZnO (YANG et al., 2010; YOUSEFI et al., 2013). According to Cohn et al, the introduction of Mg^{2+} ions raises the conduction band potential and lowers the valence band potential of ZnO (COHN et al., 2012). The two effects (quantum confinement and intrinsic effect of Mg) could not be separated.

The visible emission spanned the 400-590 nm range, featuring two broad bands at 400-495 nm and 495-590 nm whose relative intensities depended on Mg^{2+} concentration. Different relaxation processes, radiative or non-radiative, can take place upon photoexcitation of a ZnO nanoparticle. Two mechanisms have been proposed for the ZnO visible emission: i) recombination of an electron in the valence band with a hole in a deep trap, ii) recombination of an electron in singly ionized oxygen vacancy (i.e deeply trapped) with a photo-generated hole in the valence band (XIONG, 2010). The green-yellow luminescence of ZnO is usually attributed to singly ionized oxygen vacancies (VAN DIJKEN et al., 2000; LIU et al., 2006; YOUSEFI and KAMALUDDIN, 2009; ZHANG et al., 2010; LAYEK et al., 2011; XU et al., 2013). It has been shown by PL microscopy probing luminescence profile at single QD level that the visible emission of ZnO QDs is intrinsically broad. The broad bandwidth does not mainly arise from the NP size (or composition herein) distribution but from multiple transitions involving closely spaced energy levels, inherent to every QD, lying between the valence band and the conduction band (LAYEK et al., 2011). The increase in QY upon Mg^{2+} doping can be explained by the increased concentration of inner and surface defects, in particular oxygen vacancies, and by the decrease in QD size. Because of the larger surface-to-volume ratio, smaller QDs entail the formation of more numerous surface defects. The surface state is expected to strongly influence the luminescence of ZnO QDs. For instance, correlations have been observed between the presence of surface hydroxide moieties and visible luminescence intensity. As observed by Felbier et al, when surface oxygen containing species, such as OH groups, were desorbed under vacuum, the visible emission vanished while the UV emission was significantly enhanced (FELBIER et al., 2014). Of note, the decrease in QY when $Zn_{0.8}Mg_{0.2}O$ QDs are capped by oleic acid is consistent with the hypothesis of the role of OH groups in visible emission. The number of OH surface groups is expected to decrease if they react with oleic acid. The difference in relative intensities of the two broad bands at 400-495 nm and 495-590 nm suggests the existence of different types of defects and/or different paths for electron-hole recombination as a function of Mg concentration.

IV.4. CONCLUSIONS

Mg-doped ZnO QDs were synthesized by a hydrolysis and condensation reaction. Mg^{2+} ions could be incorporated into the ZnO wurtzite lattice owing to the very close values of the Mg^{2+} and Zn^{2+} ion radii. However, the dopant ions strongly influenced the growth and final size of ZnO nanocrystals. Doping with Mg^{2+} ions widened the band gap of ZnO QDs and enhanced their visible luminescence. The luminescence went through a maximum for a 20 mol% nominal concentration of Mg^{2+} ions in the reaction medium. With increasing proportion of Mg^{2+} ions, both the absorption and emission spectra experienced a blue shift. $Zn_{0.8}Mg_{0.2}O$ QDs capped by oleic acid (OA) formed stable colloidal dispersions in chloroform and toluene, with strong visible luminescence, promising for biological imaging.

IV.5. REFERENCES

BAGALKOT, V.; ZHANG, L.; LEVY-NISSENBAUM, E.; JON, S.; KANTOFF, P. W.; LANGER, R.; FAROKHZAD, O. C. Quantum Dot−Aptamer Conjugates for Synchronous Cancer Imaging, Therapy, and Sensing of Drug Delivery Based on Bi-Fluorescence Resonance Energy Transfer. **Nano Lett,** v. 7, n. 10, p. 3065-3070, 2007.

BRINKER, C. J.; SCHERER, G. W. **Sol-Gel Sciences. The Physics and Chemistry of Sol-Gel Processing.** San Diego: Academic Press, Inc, p. 908, 1990.

BRUS, L. Electronic wave functions in semiconductor clusters: experiment and theory. **J Phys Chem,** v. 90, n. 12, p. 2555-2560, 1986.

BUONSANTI, R.; MILLIRON, D. J. Chemistry of Doped Colloidal Nanocrystals. **Chem Mater,** v. 25, n. 8, p. 1305-1317, 2013.

CAETANO, B. L. SANTILLI, C. V.; MENEAU, F.; BRIOIS, V.; PULCINELLI, S. H. In Situ and Simultaneous UV−vis/SAXS and UV−vis/XAFS Time-Resolved Monitoring of ZnO Quantum Dots Formation and Growth. **J Phys Chem C Nanomater Interfaces,** v. 115, n. 11, p. 4404-4412, 2011.

CHANG, E.; THEKKEK, N.; YU, W. W.; COLVIN, V. L.; DREZEK, R.. Evaluation of Quantum Dot Cytotoxicity Based on Intracellular Uptake. **Small,** v. 2, n. 12, p. 1412-1417, 2006.

COHN, A. W.; KITTILSTVED, K. R.; GAMELIN, D. R. Tuning the Potentials of "Extra" Electrons in Colloidal n-Type ZnO Nanocrystals via Mg^{2+} Substitution. **J Am Chem Soc,** v. 134, n. 18, p. 7937-7943, 2012.

CRAIEVICH, A. F. **Handbook of Sol-Gel Science and Technology**. Norwell, MA: Kluwer Publishers, p.161-189, 2005.

DING, R.; XU, C.; GU, B.; SHI, Z.; WANG, H.; BA, L.; XIAO, Z. Effects of Mg Incorporation on Microstructure and Optical Properties of ZnO Thin Films Prepared by Sol-gel Method. **J Mater Sci Technol,** v. 26, n. 7, p. 601-604, 2010.

FELBIER, P.; YANG, J.; THEIS, J.; LIPTAK, R. W.; WAGNER, A.; LORKE, A.; BACHER, G.; KORTSHAGEN, U. Highly Luminescent ZnO Quantum Dots Made in a Nonthermal Plasma. **Adv Funct Mater,** v. 24, n. 14, p. 1988-1993, 2014.

GHOSH, M.; RAYCHAUDHURI, A. K. Optical Properties of Mg-Substituted ZnO Nanoparticles Obtained by Solution Growth. **IEEE Trans Nanotehcnol,** v. 10, n. 3, p. 555-559, 2011.

GUINIER, A.; FOURNET, G. **Small Angle Scattering of X-rays**. New-York: Wiley, 1955.

JIA, Z.; MISRA, R. D. K. Tunable ZnO quantum dots for bioimaging: synthesis and photoluminescence. **Mater Technol,** v. 28, n. 4, p. 221-227, 2013.

KLAINE, S. J.; ALVAREZ, P. J.; BATLEY, G. E.; FERNANDES, T. F.; HANDY, R. D.; LYON, D. Y.; MAHENDRA, S.; MCLAUGHLIN, M. J.; LEAD, J. R. Nanomaterials in the environment: Behavior, fate, bioavailability, and effects. **Environ Toxicol Chem,** v. 27, n. 9, p. 1825-1851, 2008.

KOLEVA, V.; STOILOVA, D. Infrared and Raman studies of the solids in the $Mg(CH_3COO)_2$–$Zn(CH_3COO)_2$–H_2O system. **J Mol Struct,** v. 611, n. 1–3, p. 1-8, 2002.

LAYEK, A.; DE, S.; THORAT, R.; CHOWDHURY, A. Spectrally Resolved Photoluminescence Imaging of ZnO Nanocrystals at Single-Particle Levels. **J Phys Chem Lett,** v. 2, n. 11, p. 1241-1247, 2011.

LEWINSKI, N.; COLVIN, V.; DREZEK, R. Cytotoxicity of Nanoparticles. **Small,** v. 4, n. 1, p. 26-49, 2008.

LIN, Y.-J.; WU, P.-H.; TSAI, C.-L.; LIU, C.-J.; LIN, Z.-R.; CHANG, H.-C.; LEE, C.-T. Effects of Mg incorporation on the optical properties of ZnO prepared by the sol-gel method. **J Appl Phys,** v. 103, p. 113709, 2008.

LIU, D.-P.; LI, G. D.; SU, Y.; CHEN, J. S. Highly Luminescent ZnO Nanocrystals Stabilized by Ionic-Liquid Components. **Angew Chem Int Ed Engl,** v. 45, n. 44, p. 7370-7373, 2006.

MICHALET, X.; PINAUD, F. F.; BENTOLILA, L. A.; TSAY, J. M.; DOOSE, S.; LI, J. J.; SUNDARESAN, G.; WU, A. M.; GAMBHIR, S. S.; WEISS, S. Quantum Dots for Live Cells, in Vivo Imaging, and Diagnostics. **Science,** v. 307, n. 5709, p. 538-544, 2005.

MOUSSODIA, R.-O, BALAN, L., MERLIN, C., MUSTIN, C., SCHNEIDER, R. Biocompatible and stable ZnO quantum dots generated by functionalization with siloxane-core PAMAM dendrons. **J Mater Chem**, v. 20, p. 1147-1155, 2010.

NORBERG, N. S.; KITTILSTVED, K. R.; AMONETTE, J. E.; KUKKADAPU, R. K.; SCHWARTZ, D. A.; GAMELIN, D. R. Synthesis of Colloidal Mn2+:ZnO Quantum Dots and High-TC Ferromagnetic Nanocrystalline Thin Films. **J Am Chem Soc,** v. 126, n. 30, p. 9387-9398, 2004.

PARK, J.-H.; VON MALTZAHN, G.; RUOSLAHTI, E.; BHATIA, S. N.; SAILOR, M. J. Micellar Hybrid Nanoparticles for Simultaneous Magnetofluorescent Imaging and Drug Delivery. **Angew Chem Int Ed Engl,** v. 47, n. 38, p. 7284-7288, 2008.

SCHWARTZ, D. A.; NORBERG, N. S.; NGUYEN, Q. P.; PARKER, J. M.; GAMELIN, D. R. Magnetic Quantum Dots: Synthesis, Spectroscopy, and Magnetism of Co2+- and Ni2+-Doped ZnO Nanocrystals. **J Am Chem Soc,** v. 125, n. 43, p. 13205-13218, 2003.

SU, Y.; HE, Y.; LU, H.; SAI, L.; LI, Q.; LI, W.; WANG, L.; SHEN, P.; HUANG, Q.; FAN, C. The cytotoxicity of cadmium based, aqueous phase – Synthesized, quantum dots and its modulation by surface coating. **Biomaterials,** v. 30, n. 1, p. 19-25, 2009.

TIAN, B.; AL-JAMAL, W. T.; AL-JAMAL, K. T.; KOSTARELOS, K. Doxorubicin-loaded lipid-quantum dot hybrids: Surface topography and release properties. **Int J Pharm,** v. 416, n. 2, p. 443-447, 2011.

VAN DIJKEN, A.; MEULENKAMP, E. A.; VANMAEKELBERGH, D.; MEIJERINK, A. The Kinetics of the Radiative and Nonradiative Processes in Nanocrystalline ZnO Particles upon Photoexcitation. **J Phys Chem B,** v. 104, n. 8, p. 1715-1723, 2000.

VIJAYALAKSHMI, K.; KARTHICK, K. Influence of Mg doping on the microstructure and PL emission of wurtzite ZnO synthesized by microwave processing. **J Mater Sci Mater Electron,** v. 24, n. 6, p. 2067-2071, 2013.

WANG, C.; GAO, X.; SU, X. In vitro and in vivo imaging with quantum dots. **Anal Bioanal Chem,** v. 397, n. 4, p. 1397-1415, 2010.

WEST, A. R. **Solid State Chemistry and Its Applications**. New York: John Wiley and Sons 1992.

XIE, J.; LEE, S.; CHEN, X. Nanoparticle-based theranostic agents. **Adv Drug Deliv Rev,** v. 62, n. 11, p. 1064-1079, 2010.

XIONG, H.-M.; SHCHUKIN, D. G.; MÖHWALD, H.; XU, Y.; XIA, Y. Y. Sonochemical Synthesis of Highly Luminescent Zinc Oxide Nanoparticles Doped with Magnesium(II). **Angewandte Chemie,** v. 121, n. 15, p. 2765-2769, 2009.

XIONG, H.-M. Photoluminescent ZnO nanoparticles modified by polymers. **J Mater Chem,** v. 20, n. 21, p. 4251-4262, 2010.

XIONG, H.-M. ZnO Nanoparticles Applied to Bioimaging and Drug Delivery. **Adv Mater**, v. 25, p. 5329–5335, 2013.

XU, X.; XU, C.; WANG, X.; LIN, Y.; DAI, J.; HU, J. Control mechanism behind broad fluorescence from violet to orange in ZnO quantum dots. **CrystEngComm,** v. 15, n. 5, p. 977-981, 2013.

YANG, Y.; JIN, Y.; HE, H.; WANG, Q.; TU, Y.; LU, H.; YE, Z. Dopant-Induced Shape Evolution of Colloidal Nanocrystals: The Case of Zinc Oxide. **J Am Chem Soc,** v. 132, n. 38, p. 13381-13394, 2010.

YOUSEFI, R.; SHEINI, F. J.; MUHAMAD, M. R.; MORED, M. A. Characterization and field emission properties of ZnMgO nanowires fabricated by thermal evaporation process. **Solid State Sciences,** v. 12, n. 7, p. 1088-1093, 2010.

YOUSEFI, R.; KAMALUDDIN, B. Fabrication and characterization of ZnO and ZnMgO nanostructures grown using a ZnO/ZnMgO compound as the source material. **Appl Surf Sci,** v. 256, n. 1, p. 329-334, 2009.

YOUSEFI, R.; ZAK, A. K.; JAMALI-SHEINI, F. Growth, X-ray peak broadening studies, and optical properties of Mg-doped ZnO nanoparticles. **Mater Sci Semicond Process,** v. 16, n. 3, p. 771-777, 2013.

ZHANG, L.; YIN, L.; WANG, C.; LUN, N.; QI, Y.; XIANG, D. Origin of Visible Photoluminescence of ZnO Quantum Dots: Defect-Dependent and Size-Dependent. **J Phys Chem C Nanomater Interfaces,** v. 114, n. 21, p. 9651-9658, 2010.

CHAPTER V

Incorporation of QDs in lipid-based nanocarriers: Preliminary results

V.1. INTRODUCTION

Nanocarriers offer unique possibilities to combine drug delivery and bioimaging using probes. However, to fully realize the promise they hold, nanocarriers must be able to be internalized within the targeted cells. There are various mechanisms of cell internalization that strongly depend on the characteristics of nanocarriers such as size, shape, surface charge and chemistry. Nanocarrier cellular uptake may be caused by non-specific adsorption on the plasma membrane or by (specific) interactions with cell surface-receptors, thereby triggering different internalization pathways. When nanocarriers interact with the membrane via non-specific (hydrophobic and electrostatic) interactions, they can enter the cell through macropinocytosis: they are enveloped by actin-driven plasma membrane protrusions. Alternatively, formation of ligand-receptor complexes can lead to endocytosis of the nanocarrier. Endocytic pathways include clathrin-mediated, caveolae-mediated endocytosis, and other clathrin- and caveolae-independent endocytosis (HILLAIREAU and COUVREUR, 2009). Figure V.1 ilustrates the principal endocytic pathways in mammalian cells.

Figure V.1. Principal nanocarrier internalization pathways in mammalian cells: (a) Phagocytosis, an actin-based mechanism, closely associated with opsonization; (b) Clathrin-mediated endocytosis, associated with the formation of a clathrin lattice; (c) Caveolae-mediated endocytosis, typical flask-shaped invaginations of the membrane coated with caveolin dimers; (d) Macropinocytosis, also an actin-based pathway, less selective than phagocytosis; (e) Other endocytosis pathways, independent of both clathrin and caveolae-mediation.

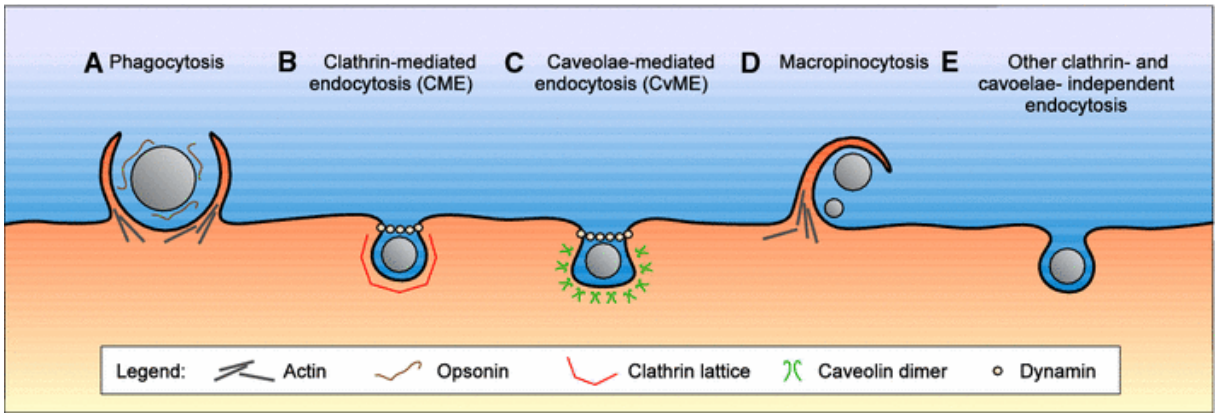

Figure from the article: "Nanocarriers' entry into the cell: relevance to drug delivery" (HILLAIREAU and COUVRER, 2009).

For a specialized set of cells, namely macrophages, monocytes and neutrophils, nanocarriers can also be internalized via phagocytosis. These cells constitute the first line of defense of the organism against nanoparticles and pathogens such as bacteria by removing them from the bloodstream. Drug delivery to these cells is relevant for many intracellular bacterial infections. Indeed, many pathogenic bacteria use macrophages as a "sanctuary", leading to the recurrence of systemic infections. It is also relevant for the treatment of tumors located in an organ of the reticuloendothelial system (RES), also named the mononuclear phagocyte system (MPS), (e;g., hepatocarcinoma and liver metastasis). In other cases, the rapid clearance of nanoparticles from the bloodstream by macrophages is an obstacle to the targeted delivery of drugs (ABED and COUVREUR, 2014; ADEREM and UNDERHILL, 1999; SALEM et al., 2005).

The phagocytic pathway of entry into macrophages involves three distinct steps: opsonization, adhesion of the opsonized particles to the macrophages, internalization of the particles. Opsonization consists of the adhesion of proteins, called opsonins, on the particle surface (HILLAIREAU and COUVREUR, 2009).

The aim of the present chapter was to obtain lipidic nanocarriers containing Mg-doped ZnO QDs as imaging agents for *in vitro* internalization studies in the J774 murine macrophage-like cell line. We have tried to incorporate QDs into different lipids or mixtures of lipids, in order to identify candidates for bioimaging and, ultimately, drug delivery. We have considered three different mixed lipid-QD structures: bilayer-QD, micelle-QD, and SLN (solid lipid nanoparticle)-QD structures. We have therefore tried to embed Mg-doped ZnO QDs within DPPC bilayers, DSPE-Peg micelles and nanoparticles consisting of Gelucire.

V.2. RESULTS AND DISCUSSIONS

V.2.1. DPPC-based formulations

In excess water, the zwitterionic molecules of DPPC spontaneously form bilayers whose structure and long-range organization depend on temperature. As temperature is increased from room temperature, DPPC displays successively three lamellar phases, the gel phase $L_{\beta'}$ (below Tp = 36°C), the gel ripple phase $P_{\beta'}$ and, finally, the liquid-crystalline phase L_{α} (above Tm = 42°C). In the $L_{\beta'}$ phase the chains are fully extended, packed in a pseudo-hexagonal lattice and tilted with respect to the lipid bilayer plane. Above the main transition Tm, in the L_{α} phase, the chains have a liquid-like conformation. Small-angle X-ray scattering

(SAXS) patterns give information on the long range bilayer organization in the different phases. The regular stacking of the bilayers gives rise to reflections equally spaced. The *d-spacing*, which corresponds to the sum of the bilayer thickness and water layer thickness, can be deduced from the position of the Bragg peaks: $d = 2\pi/q_1$. Of note, fewer orders of diffraction (2 instead of 4) are observed for the fluid L_α phase, due to the suppression of higher orders by Helfrich fluctuations of membranes. The *d-spacing* slightly increases from 63.8 Å in the gel phase to 67.3 Å in the fluid phase, reflecting the higher hydration of the fluid phase.

Table V.1 presents the composition of the DPPC based formulations containing OA surface- modified Mg-doped ZnO QDs, the QD/DPPC ratio (w/w) and the *d-spacing* at 30 and 50°C calculated from the SAXS patterns. Increasing amounts of OA-$Zn_{0.8}Mg_{0.2}O$ QDs were mixed with DPPC (see Table V.1) and the SAXS patterns of the samples in excess water were recorded at 30°C and 50°C, i.e., below and above the main transition temperature of DPPC.

Table V.1. OA-$Zn_{0.8}Mg_{0.2}O$ QDs, DPPC and water quantities used in the liposomes formulations, QD/DPPC ratio (mg/mg) and *d-spacing* at 30 and 50 °C.

Formulations	**AO-$Zn_{0.8}Mg_{0.2}O$ QDs (mg)**	**DPPC (mg)**	**H_2O (mL)**	**QD/ DPPC ratio (mg/mg)**	***d-spacing* (30°C) (Å)**	***d-spacing* (50°) (Å)**
D0		20			63.8	67.3
D1	0.05	40	0.25	0.00125	64.1	67.3
D2	0.1	40	0.25	0.0025	64.1	67.3
D3	0.25	40	0.5	0.00625	63.7	
D4	0.5	40	0.5	0.0125	63.7	
D5	1	40	0.25	0.025	63.5	67.6
D6	2	40	0.25	0.05	39.6	40.4
D7	5	40	0.3	0.125	43.9	44.0

Figures V.2 and V.3 present the SAXS patterns of the formulations D0-D7 at 30 and 50 °C, respectively. Formulations D1-D4 display sharp Bragg peaks, indicative of a lamellar

phase; in these samples, the presence of the AO-$Zn_{0.8}Mg_{0.2}O$ QDs does not perturb the stacking of bilayers, as shown by the *d-spacing* identical to that of DPPC. In contrast, formulations D5-D7 exhibit a strong scattering at small angles, suggesting the formation of large aggregates. Moreover, in samples D6 and D7, containing large amounts of QDs, only weak reflections, corresponding to small repeat distances, superimpose on the strong scattering at small angles.

Figure V.2. SAXS patterns of DPPC based liposomes formulations collected at 30°C.

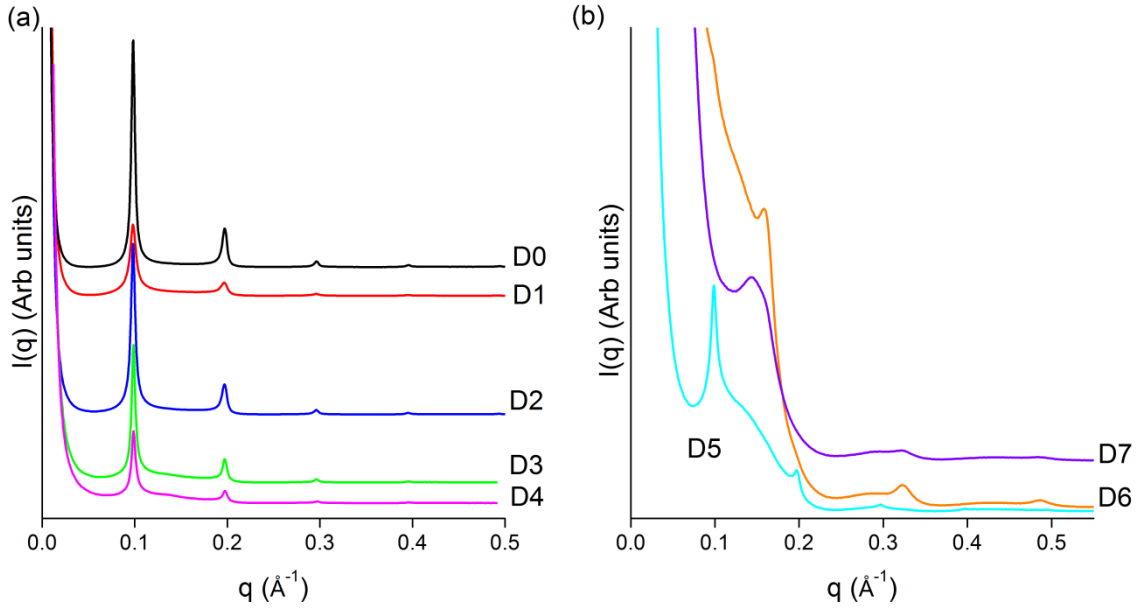

Figure V.3. SAXS patterns of DPPC based liposomes formulations collected at 50°C.

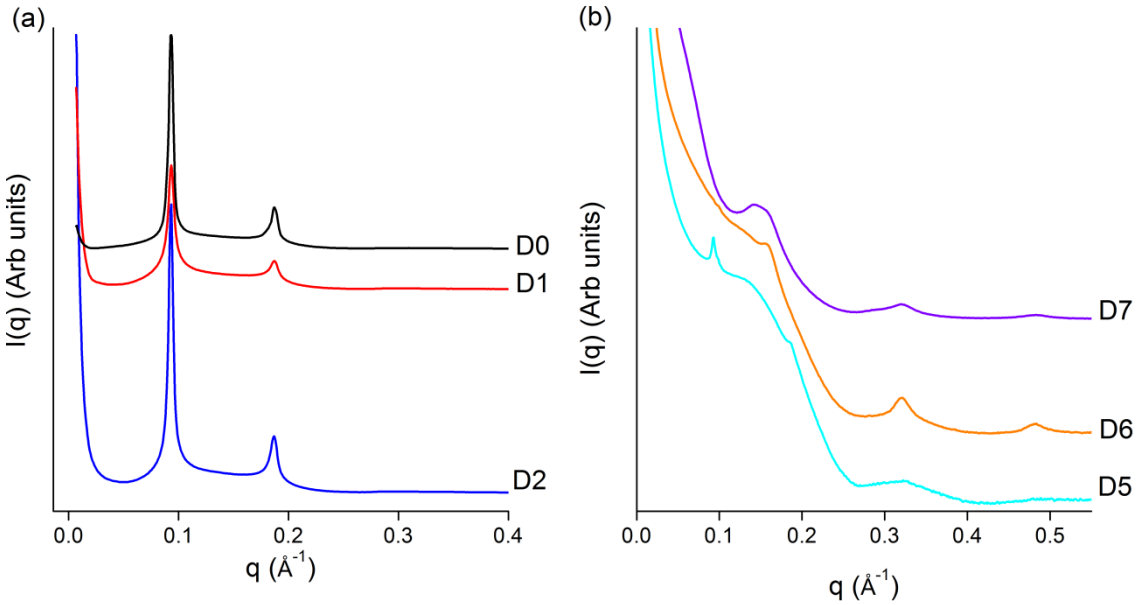

Figure V.4 shows Cryo-TEM pictures of a formulation similar to D5 in a large excess of water, after extrusion. Liposomes with a rather angular shape and thick and dark membranes can be observed, suggesting the incorporation of QDs into the DPPC bilayers.

Figure V. 4. Cryo-TEM images of formulation similar to D5 in a large excess of water, after extrusion.

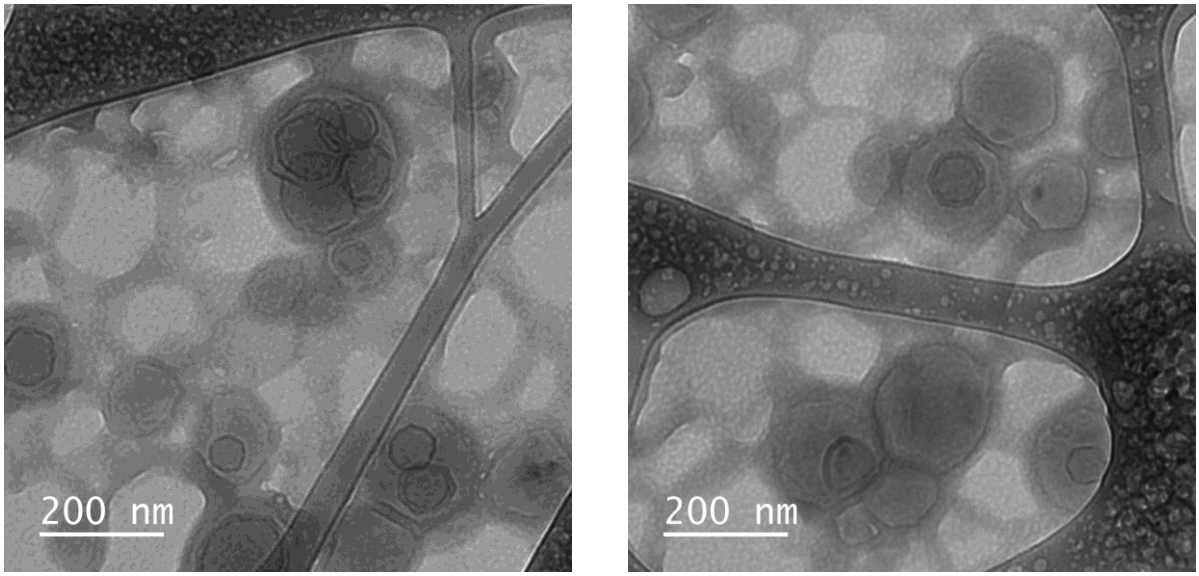

Wi et al have predicted the stability of QDs in a DOPC bilayer as a function of their size by evaluating the interfacial free energy of deformation of the lipid monolayers surrounding a QD. According to that work, only QDs with a diameter smaller than a critical size, comparable to the thickness of the lipid bilayer, can be embedded in the bilayer. This was confirmed by experimental reports. Gopalakrisnan et al, Al-Jamal et al and Wi et al have successfully inserted small QDs into lipid bilayers: TOPO-coated CdSe QDs with overall diameters ~ 4-5 nm in DMPC bilayers (GOPALAKRISHNAN et al., 2006), TOPO-coated CdSe/ZnS QDs with about the same diameters in DOPC (AL-JAMAL et al., 2008), and HDA-coated CdSe with core diameters between ~2 and ~2.65 nm in DOPC (WI et al., 2012). On the other hand, QDs with an overall size of 6-7 nm could not be incorporated (AL-JAMAL et al., 2008; WI et al., 2012). Of note, higher amounts of HDA-coated CdSe QDs were loaded in Asolectin (a mixture of phospholipids) than in DOPC bilayers.

Our results suggest that, at low QD concentrations, a fraction at least of QDs (with core diameters ~3 nm) are embedded within DPPC bilayers, whereas at high QD/ DPPC ratios hybrid aggregates are formed by closely packed QDs stabilized by DPPC.

V.2.2. DSPE-Peg based formulations

DSPE-Peg based formulations were prepared, varying the QD/DSPE-Peg ratio as reported in Table V.2. Figure V.5 shows the SAXS patterns of DSPE-Peg based formulations at 30 °C.

Table V.2. OA-$Zn_{0.8}Mg_{0.2}O$ QDs, DSPE-Peg and water quantities used in the formulations, QD/DSPE-Peg ratio (mg/mg) and *d-spacing* at 10, 30 and 50 °C.

Formulations	AO-$Zn_{0.8}Mg_{0.2}O$ QDs (mg)	DSPE-Peg (mg)	H_2O (mL)	QD/ DSPE-Peg ratio (mg/mg)	*d-spacing* (10 °C) (Å)	*d-spacing* (30°C) (Å)	*d-spacing* (50°C) (Å)
DPeg0		10	0.3				
DPeg1	15	10	0.2	1.5		37.6	38.3
DPeg2	10	9	0.5	1.1	38.4	38.8	
DPeg3	10	18	0.5	0.55	38.5	38.9	
DPeg4	10	36	0.5	0.27		39.3	
DPeg5	5	25	0.2	0.2		38.2	39.3
DPeg6	1.7	10	1	0.17			

Figure V.5. SAXS patterns of DSPE-Peg based formulations collected at 30 °C.

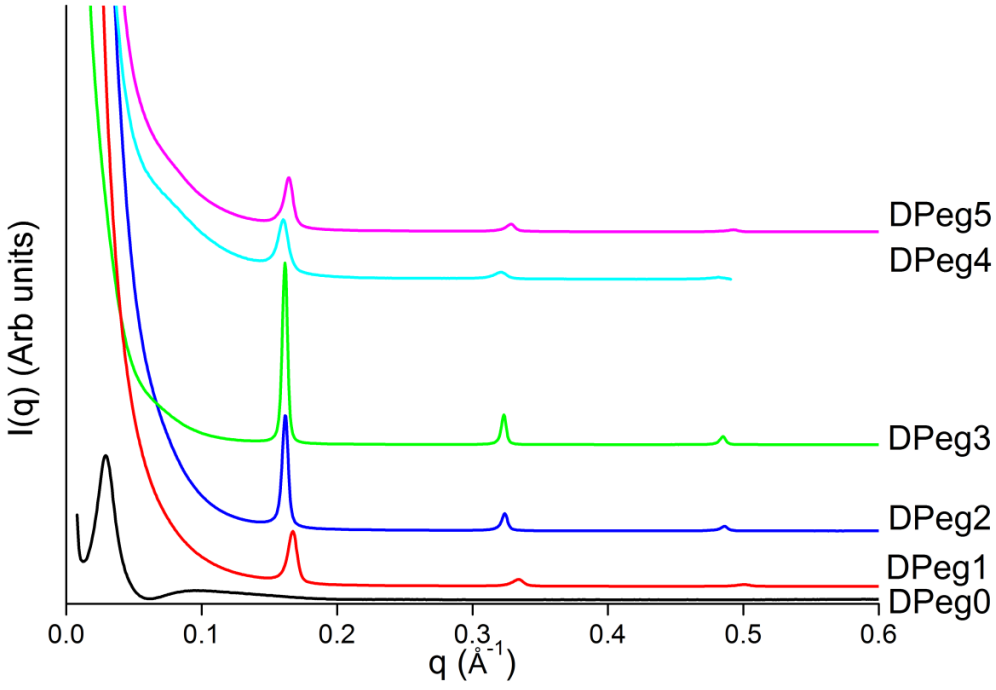

The amphiphilic DSPE-Peg 2000 molecules self-assemble in water as spherical micelles, formed by a DSPE core surrounded by a hydrophilic PEG corona. The SAXS curve labeled DPeg0 in Fig V.5 is characteristic of micelles in the semi-dilute regime: it displays a broad reflection around q = 0.1 $Å^{-1}$, arising from the micelle form factor, along with a correlation peak at q = 0.029 $Å^{-1}$, yielding the average distance between micelles (d = 216.5 Å). Johnsson et al reported a micelle hydrodynamic diameter of 13.4 nm, as measured by DLS, and a core diameter of 6.4 nm, thus able to accommodate small QDs (JOHNSSON et al., 2001).

We have investigated formulations with significantly different QD/DSPE-Peg ratios in an attempt to obtain two types of structures: (i) micelles containing isolated QDs at low QD/DSPE-Peg ratios, (ii) larger nanoparticles involving several QDs at higher QD/ DSPE-Peg ratios.

Indeed, Dubertret et al have encapsulated individual CdSe/ZnS core-shell QDs (diameter ~4 nm) in the hydrophobic core of a micelle composed of DSPE-Peg or DSPE-Peg and DPPC (DUBERTRET et al., 2002). In contrast, Shroeder et al prepared large particles, with a mean diameter size of ~ 50-100 nm, containing many TOPO-coated CdSe QDs (diameter 2.6 or 2.9 nm) in each, which they referred to as "lipodots". The aggregates were surrounded by a phospholipid monolayer of DSPE-Peg and DPPC (SCHROEDER et al., 2007) .

Very surprisingly, all samples gave rise to the same type of SAXS patterns, displaying diffuse scattering at small angles (q < 0.1 $Å^{-1}$) and sharp equidistant peaks at q_1 = 0.16 $Å^{-1}$, q_2 = 0.32 $Å^{-1}$, q_3 = 0.48 $Å^{-1}$. These peaks are indicative of a close-packed (maybe layered) structure, with a repeat distance of about 38.5 Å, almost independent of the QD/DSPE-Peg ratio and temperature. Only a slight increase of d was observed between 10°C and 30°C or 30°C and 50°C. It can be suggested that QDs capped by OA might self-assemble as large aggregates stabilized by a layer of DSPE-Peg. The observed repeat distance is consistent with the size of QDs. Of note, the scattering of coexisting micelles, with or without QDs, could be masked by the strong scattering at small angles.

The samples prepared with OA-$Zn_{0.8}Mg_{0.2}O$ QDs and DPPC/DSPE-Peg mixtures displayed the same characteristics, supporting our interpretation. Table V.3 presents the composition of the samples prepared with DPPC/DSPE-Peg and AO-$Zn_{0.8}Mg_{0.2}O$ QDs, the QD/lipid ratio (w/w) and the *d spacing* at 30 and 50°C calculated from the SAXS patterns. Figures V.6 present the SAXS patterns of the formulations DDPeg0-DDPeg3 at (a) 30 and (b)

50 °C, respectively.

Table V.3. OA-$Zn_{0.8}Mg_{0.2}O$ QDs, DPPC, DSPE-Peg and water quantities used in the formulations, QD/lipids ratio (mg/mg) and *d-spacing* at 30 and 50 °C.

Formu-lations	AO-$Zn_{0.8}Mg_{0.2}O$ QDs (mg)	DPPC (mg)	DSPE-Peg (mg)	H_2O (mL)	QD/Lipids ratio (mg/mg)	*d-spacing* (30 °C) (Å)	*d-spacing* (50 °C) (Å)
DDPeg0		6	14.8	0.5			
DDPeg1	10	1.5	3.7	0.5	1.92	38.5	38.9
DDPeg2	10	3	7.4	0.5	0.96	38.5	38.9
DDPeg3	5	6	14.8	0.15	0.24	37.9	38.8

Figure V.6. SAXS patterns of DSPE-Peg/DPPC based formulations recorded at (a) 30°C (continuous lines) and (b) 50°C (dotted lines).

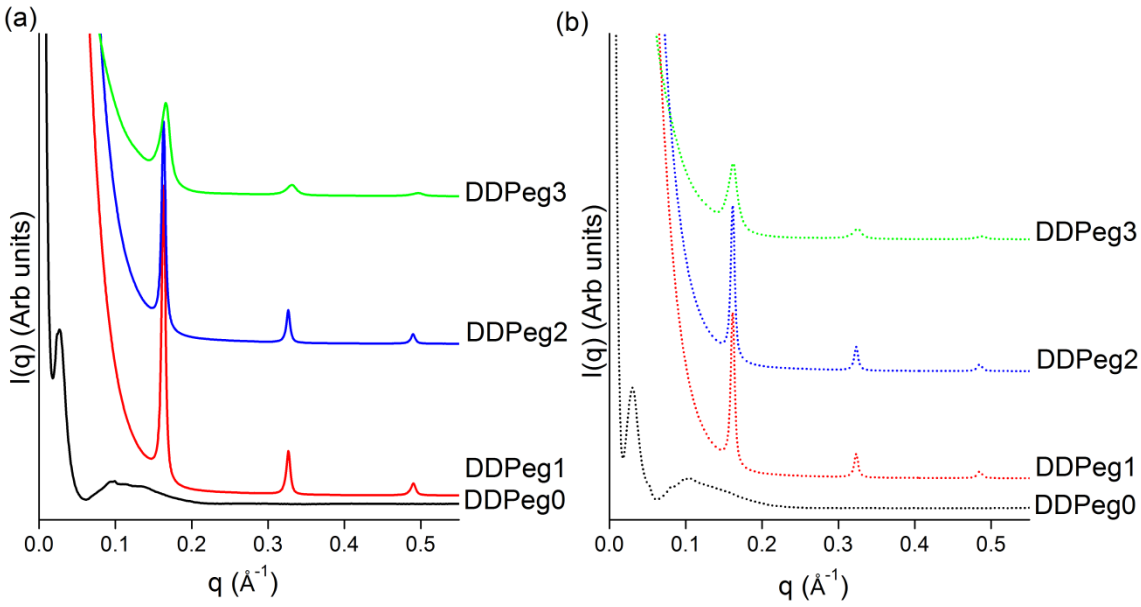

Figure V.7 presents Cryo-TEM images of DPeg6 formulation. It seems that micelles coexist with nanoparticles with size around 180-200 nm, which could be aggregates of QDs stabilized by DSPE-Peg.

Figure V. 7. Cryo-TEM images of formulation DPeg6.

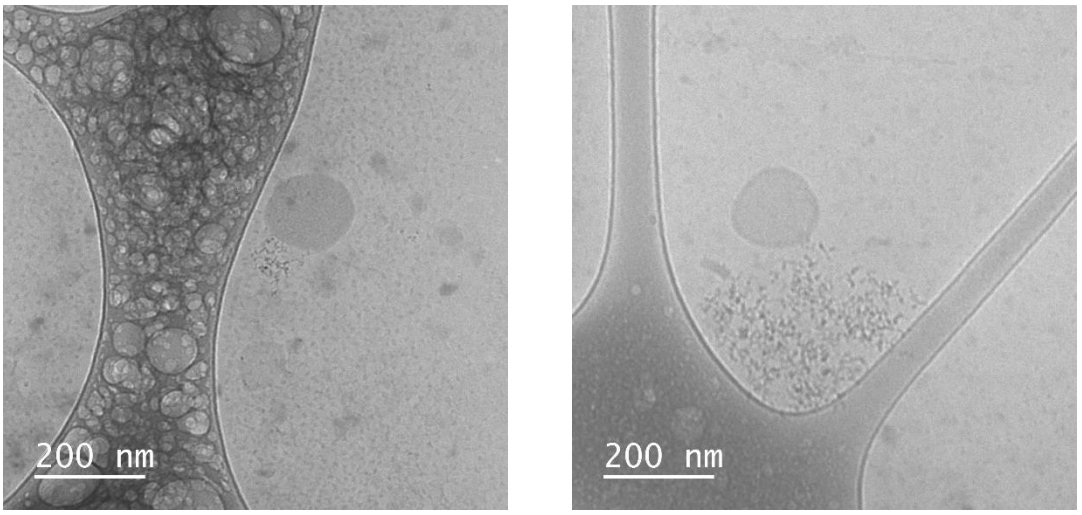

Figure V.8 illustrates the dried film (a), the hydrated film under visible light (b) and under UV lamp (λ_{exc} = 356nm) (c) of the DPeg6 formulation.

Figure V.8. Photos of (a) the dried film, (b) the hydrated film under visible light and (c) under UV lamp (λexc = 356nm) of the DPeg6 formulation.

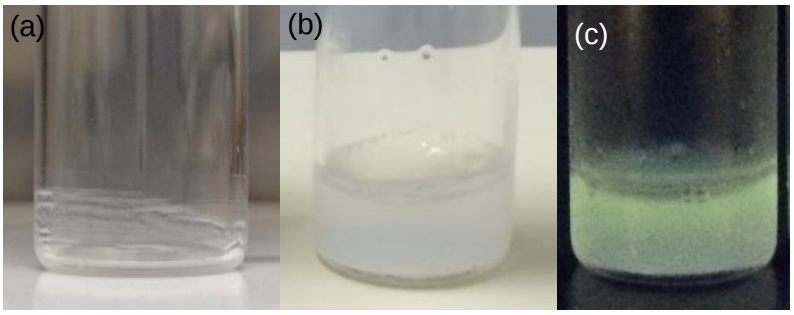

V.2.3. Solid lipid nanoparticles

Nanoprecipitation is a straightforward process for preparing nanoparticles (NPs) from hydrophobic organic compounds such as lipids or polymers. In general, the hydrophobic solute is first dissolved into a polar organic solvent (usually ethanol, acetone or THF). This solution is then added to a large volume of water with which the polar solvent is miscible in all proportions. The mixed binary solution becomes a non-solvent for the hydrophobic

molecules and supersaturation of solutes triggers their precipitation as nanoparticles. The characteristics of the NPs, such as size, size distribution and stability, result mainly from the complex interplay between the concentration of the hydrophobic solute in the polar organic solvent, the non-solvent-to-solvent volume ratio, and the kinetics of mixing of the initial solution and the non-solvent. Under appropriate conditions, nanoprecipitation can generate a dispersion of nanoparticles with a unimodal size distribution in the 50-300 nm range (LEPELTIER, BOURGAUX, COUVREUR, 2014).

SLNs of Gelucire50/13®, a pharmaceutical excipient, embedding $Zn_{0.8}Mg_{0.2}O$ QDs have been prepared by nanoprecipitation into water of an ethanolic solution of Gelucire mixed with QDs, taking advantage of the stability of as-synthesized QDs (without OA surface modification) in ethanol and of the Gelucire solubility in this solvent. After nanoprecipitation, ethanol was removed by evaporation or dialysis.

As detailed in "Materials and Methods" (Chapter II, Section II.3.2), numerous conditions of preparation were tested with the aim to form monodisperse nanoparticles. However, we could not achieve a narrow unimodal size distribution in the desired range when QDs were present in the formulations. Samples were therefore filtered (0.45 µm) to overcome this problem.

Table V.4 gathers the concentrations of $Zn_{0.8}Mg_{0.2}O$ QDs and Gelucire50/13® in the initial solutions, the $Zn_{0.8}Mg_{0.2}O$ QDs:Gelucire 50/13® ratios, and the ethanol:water volume ratios used for nanoprecipitation. After filtration, the nanoparticle size varied from ~120 nm to ~160 nm.

Table V.4. $Zn_{0.8}Mg_{0.2}O$ QDs and Gelucire concentrations, ratio of $Zn_{0.8}Mg_{0.2}O$ QDs:Gelucire 50/13® and ethanol:water used.

Formulations	$Zn_{0.8}Mg_{0.2}O$ QDs concentration (mg/mL)	Gelucire 50/13® Concentration (mg/mL)	Ratio of $Zn_{0.8}Mg_{0.2}O$ QDs:Gelucire 50/13®	Ratio of ethanol:H_2O Vol/vol
G1*	11	22	1:2	1:2
G2*	11	22	1:2	1:1
G3*	11	22	1:2	1:4
G4*	11	33	1:3	1:4
G5*	11	33	1:3	1:2
G6*	11	33	1:3	1:1
G7*	11	44	1:4	1:4
G8*	11	44	1:4	1:2
G9*	11	44	1:4	1:1
G10*	7.5	22.5	1:3	1:4
G11**	11	33	1:3	1:2
G12**	11	33	1:3	1:3
G13***	11	33	1:3	1:2
G14***	11	33	1:3	1:3

*Temperature used to solubilize Gelucire 50/13® = room temperature; rotavapor for ethanol elimination

** Temperature used to solubilize Gelucire 50/13®= 50°C; dialysis for ethanol elimination

*** Temperature used to solubilize Gelucire 50/13®= 60 °C; dialysis for ethanol elimination

The formulation named THF, obtained by nanoprecipitation into water of a THF solution of Gelucire mixed with OA- $Zn_{0.8}Mg_{0.2}O$ QDs, was also tested. The suspension with the QDs:Gelucire ratio 1:3 and THF:water ratio 1:3 was stable and yielded nanoparticles with mean size around 200 nm after filtration.

Figure V.9 presents the Cryo-TEM images of the formulations G12 and THF, respectively. These images reveal that (i) the formulation G12 shows isolated QDs and SLNs having irregular shapes, with probably QDs on their surface; (ii) the formulation THF shows SLNs with more contrasted cores that could contain QDS.

Figure V.9. Cryo-TEM images of formulations (a) G12, and (b) THF.

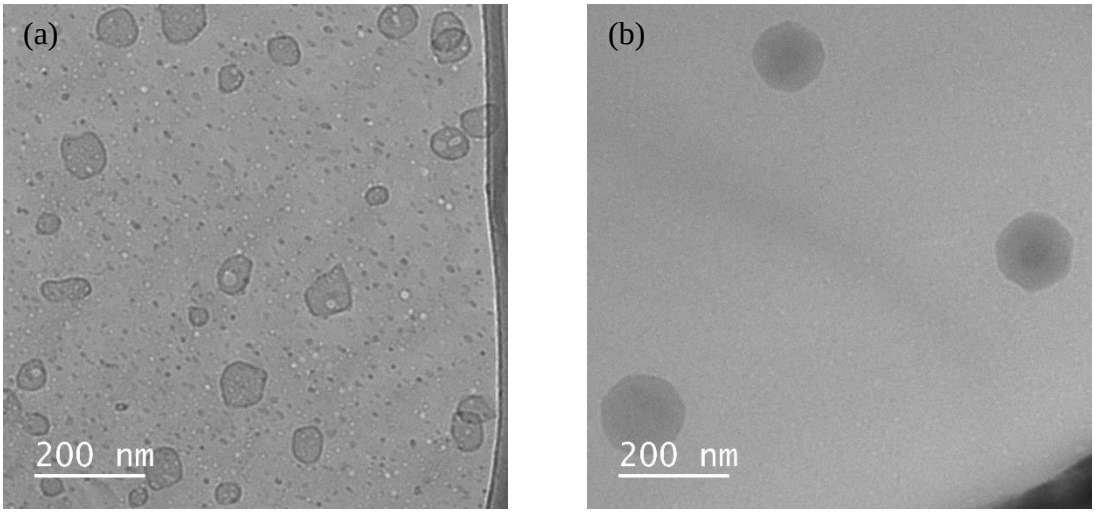

V.2.4. PL Studies

Figure V.10 presents the photography of the formulations G1-G9 under UV lamp (λ_{exc} = 356 nm).

Figure V.10. Photos of the formulations G1-G9 (from left to right) under UV lamp (λexc = 356nm).

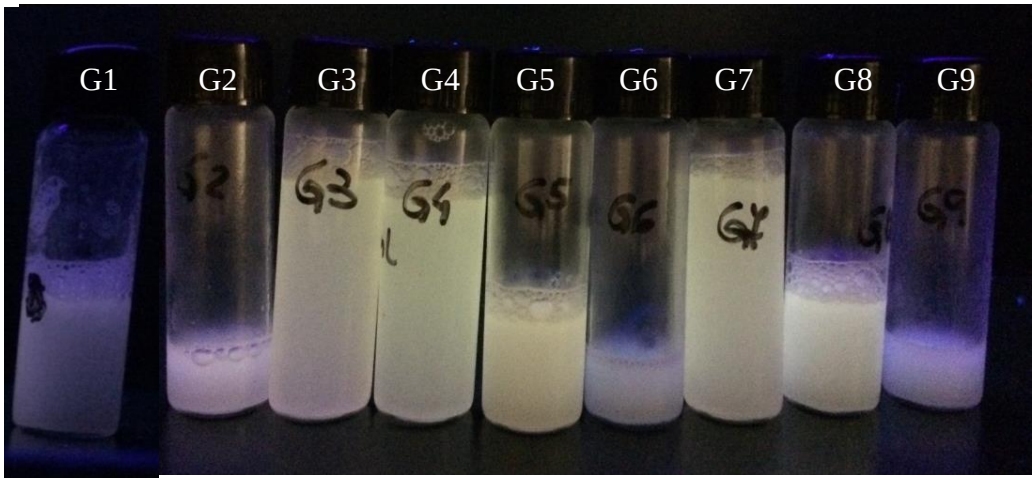

Formulations DPeg6, G4 and G8 were chosen for further studies. Fig V.11 shows the UV absorbance of these samples, after dilution to achieve the same QD concentration. All samples present an excitonic peak around 350 nm characteristic of ZnO nanoparticles.

Figure V.11. Absorption spectra of the diluted formulations G4, G8, and DPeg6.

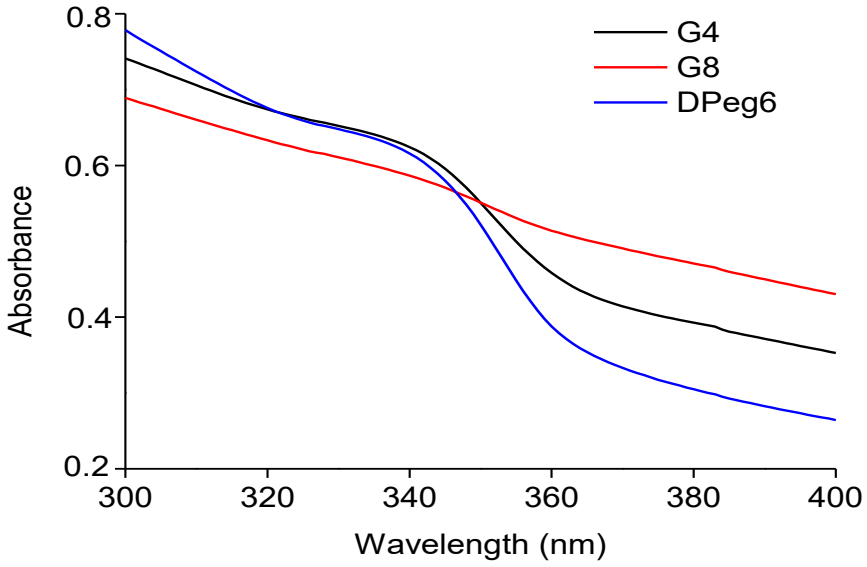

Fig V.12 (a) and (b) shows the photoluminescence excitation (PLE) and emission (PL) spectra, respectively, of these samples. In parallel, the PL properties of the cells were also investigated. Figure V.13 shows the absorption spectra of water and of the aqueous J774 cell suspension. The cell suspension absorbs around 270 nm, suggesting no interferences with the luminescent formulations.

Figure V.12. (a) PLE and (b) PL spectra of the formulations G4, G8 and DPeg6.

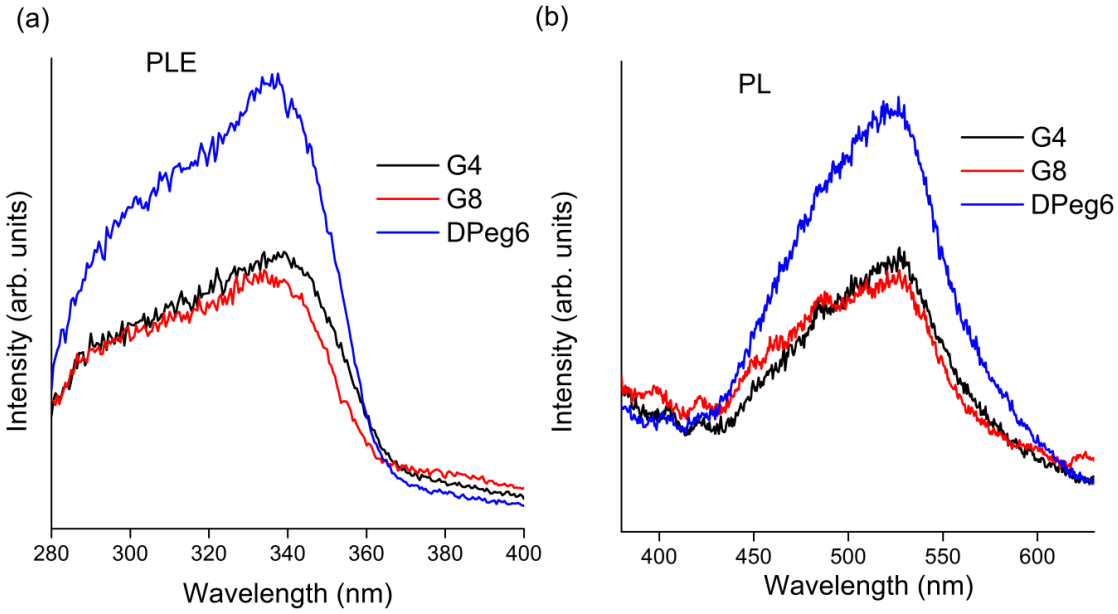

Figure V.13. Absorption spectra of the water and cells suspension.

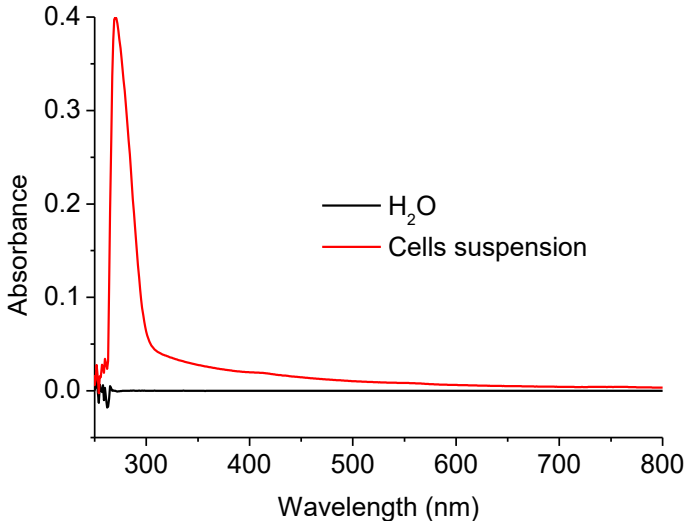

Figure V.14 shows (a) PL spectra of the cell suspension excited at 270, 340, 350, and 365 nm and (b) a zoom of the PL spectra for excitation at 340, 350, and 365 nm. The emission of the cells excited at these wavelengths remains low in the 400-600 nm region (emission region of the DPeg6, G4, G8 formulations when excited at the optimal wavelength ~340-350 nm).

Figure V.14. PL spectra of (a) cells suspension excited at 270, 340, 350, and 365 nm and (b) a zoom in the PL spectra excited at 340, 350, and 365 nm.

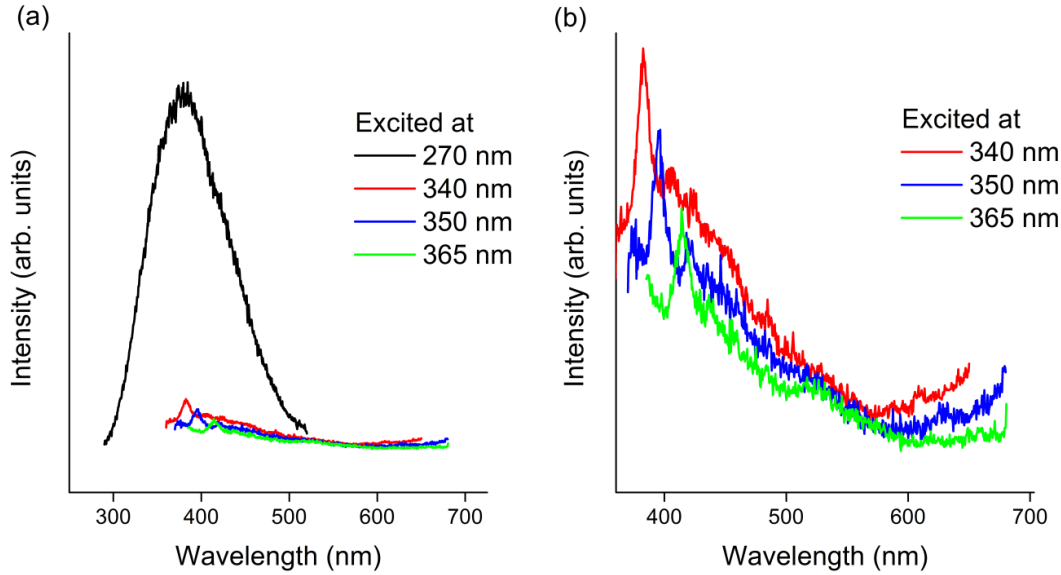

V.2.5. Nanoparticle stability studies

The aggregation of nanoparticles is known to induce cytotoxicity. Furthermore, when nanoparticles are placed in a complex biological medium, the formation of the so-called protein corona on the nanoparticle surface can suppress the nanoparticle's ability to bind to the targeted receptors on cells (GARCÍA et al., 2015). Thus, the investigation of the aggregate formation with serum proteins is crucial to evaluate the ability of transferring nanoparticles to target cells.

The stability of the formulation G4 was studied in water and in different biological media. Figure V.15 shows the evolution of the mean size of the formulation G4 in different media with time. Nanoparticles were stable when dispersed in water and PBS with and without calcium and magnesium: their mean size did not vary significantly for 3 hours. On the other hand, the nanoparticle size increased when they were incubated in the medium used to cultivate the cells, RPMI with 10% of hot-inactivated FBS. Moreover, the size distribution was broader and the polydispersity significantly increased. Serum is a complex fluid that contains a variety of proteins, with concentrations up to 0.07 g/mL, albumin being the major protein present (GARCÍA et al., 2015). These proteins can interact with the nanoparticles, inducing aggregation. However, this aggregation remained limited.

Figure V.15. Evolution of the mean size of the formulation G4 in different media during the time.

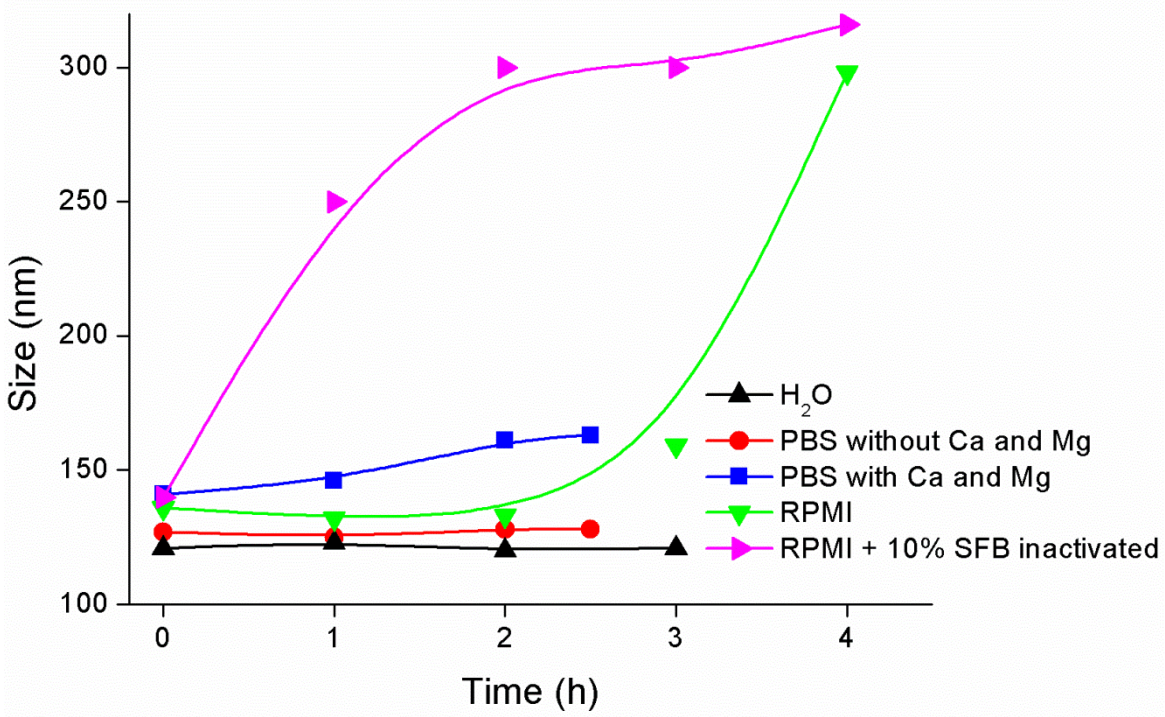

V.2.6. Cell internalization studies

One of the advantages of theranostic systems is the possibility to investigate the cell internalization of the nanocarrier containing the drug. In the present study, QDs were embedded into lipid-based nanocarriers with the aim to incorporate, in a near future, a model drug. Therefore, three different assays were carried out to evaluate the cell internalization of the formulations.

The PL measurement of the lysed cells was carried out after incubation with different concentrations of the formulation G4, during 50 min at 37°C and 5% CO_2. Figure V.16 shows the PL spectra of the cells without treatment and cells treated with 1 and 2 mg/mL of G4 nanoparticles excited at (a) 340 nm and (b) 365 nm. The PL emission intensity of the lysed cells without treatment and treated with 1 mg/mL of G4 nanoparticles were the same, whatever the wavelength of excitation. On the other hand, the lysed cells treated with 2 mg/mL of G4 nanoparticles presented slightly higher emission intensity than cells without treatment, whatever the wavelength of excitation, suggesting the internalization of some luminescent nanoparticles.

Figure V.16. PL spectra of lysed cells without treatment, cells treated with 1 and 2 mg/mL of G4 nanopaticles excited at (a) 340 nm and (b) 365 nm.

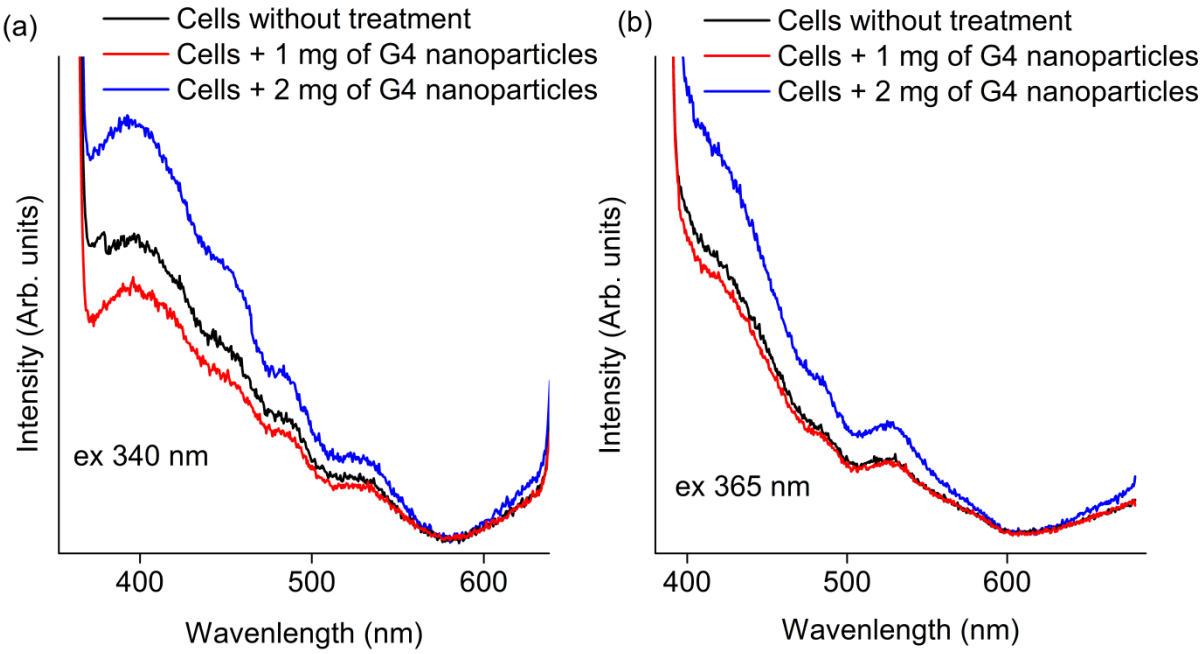

This experiment was based on Jaulin et al. studies (JAULIN et al., 2000), which evaluated the cell internalization of polymeric nanoparticles by macrophages (J774), showing noticeable internalization of nanoparticles only in the first 40 minutes of incubation. Maybe, in our case the cell internalization should be investigated with a prolonged cell incubation time or more concentrated samples to observe significant PL intensity differences between treated and non-treated cells. More investigations will be performed using this promising technique.

Attempts have also been made to monitor the cell internalization of luminescent nanoparticles using live-cell video-microscopy imaging and fluorescence microscopy. However, at the wavelength of excitation available for the video-microscopy (365 nm), the luminescence of the nanoparticles in the 450-550 nm range was very weak, of the same order of magnitude than the auto-fluorescence of the J774 cells. Likewise, the auto-fluorescence of cells hindered the observation of nanoparticles by fluorescence microscopy. Thus, the equipment and, probably, nanoparticle concentration into cells did not allow to unambiguously evidence cell internalization.

V.3. CONCLUSIONS

$Mg_{0.2}Zn_{0.8}O$ QDs and OA- $Mg_{0.2}Zn_{0.8}O$ QDs could be incorporated into lipid-based systems of average hydrodynamic diameter around 100 – 220 nm. The luminescent SNLs were stable in biological media without serum at 37°C during 3 hours, presenting no significant variation in their average size. In general, cryo-microscopic images suggested the incorporation of QDs into the SLNs. The optimal excitation wavelength of the luminescent nanoparticles was around 334-350 nm, emitting in the green visible region (500-550 nm). The J774 cell line, used in the internalization studies, lysed in water presented weak emission between 500-600 nm. The fluorescence association study showed faintly enhanced emission of the cells treated with 2 mg/mL of G4 formulation during 50 min, suggesting very weak internalization of the nanoparticles into the macrophages. The internalization of the nanoparticles into the cells could not be further confirmed by fluorescence microscopy due to the auto-fluorescence phenomena of cells and the weakness of nanoparticle signals.

V.4. REFERENCES

ABED, N.; COUVREUR, P. Nanocarriers for antibiotics: A promising solution to treat intracellular bacterial infections. **Int J Antimicrob Agents**, v. 43, p. 485-496.

ADEREM, A.; UNDERHILL, D. M. MECHANISMS OF PHAGOCYTOSIS IN MACROPHAGES. **Annu Rev Immunol,** v. 17, n. 1, p. 593-623, 1999.

AL-JAMAL, W. T.; AL-JAMAL, K. T.; TIAN, B.; LACERDA, L.; BOMANS, P. H.; FREDERIK, P. M.; KOSTARELOS, K. Lipid−Quantum Dot Bilayer Vesicles Enhance Tumor Cell Uptake and Retention in Vitro and in Vivo. **ACS Nano,** v. 2, n. 3, p. 408-418, 2008.

DUBERTRET, B.; SKOURIDES, P.; NORRIS, D. J.; NOIREAUX, V.; BRIVANLOU, A. H.; LIBCHABER, A. In Vivo Imaging of Quantum Dots Encapsulated in Phospholipid Micelles. **Science,** v. 298, n. 5599, p. 1759-1762, 2002.

GARCÍA, I.; SÁNCHEZ-IGLESIAS, A.; HENRIKSEN-LACEY, M.; GRZELCZAK, M.; PENADÉS, S.; LIZ-MARZÁN, L. M. Glycans as Biofunctional Ligands for Gold Nanorods: Stability and Targeting in Protein-Rich Media. **J Am Chem Soc,** v. 137, n. 10, p. 3686-3692, 2015.

GOPALAKRISHNAN, G.; DANELON, C.; IZEWSKA, P.; PRUMMER, M.; BOLINGER, P. Y.; GEISSBÜHLER, I.; DEMURTAS, D.; DUBOCHET, J.; VOGEL, H.Multifunctional Lipid/Quantum Dot Hybrid Nanocontainers for Controlled Targeting of Live Cells. **Angew Chem Int Ed Engl,** v. 45, n. 33, p. 5478-5483, 2006.

HILLAIREAU, H.; COUVREUR, P. Nanocarriers' entry into the cell: relevance to drug delivery. **Cell Mol Life Sci,** v. 66, n. 17, p. 2873-2896, 2009.

JAULIN, N.; APPEL, M.; PASSIRANI, C.; BARRATT, G.; LABARRE, D. Reduction of the Uptake by a Macrophagic Cell Line of Nanoparticles Bearing Heparin or Dextran Covalently Bound to Poly(methyl methacrylate). **J Drug Target,** v. 8, n. 3, p. 165-172, 2000.

JOHNSSON, M.; HANSSON, P.; EDWARDS, K. Spherical Micelles and Other Self-Assembled Structures in Dilute Aqueous Mixtures of Poly(Ethylene Glycol) Lipids. **J Phys Chem B,** v. 105, n. 35, p. 8420-8430, 2001.

LEPELTIER, E.; BOURGAUX, C.; COUVREUR, P. Nanoprecipitation and the "Ouzo effect": Application to drug delivery devices. **Adv Drug Deliv Rev,** v. 71, p. 86-97, 2014.

SALEM, I. I.; FLASHER, D. L.; DÜZGÜNEŞ, N. Liposome-Encapsulated Antibiotics1. In: (Ed.). **Methods Enzymol**, 2005. v. 391, p.261-291.

SCHROEDER, J. E.; SHWEKY, I.; SHMEEDA, H.; BANIN, U.; GABIZON, A. Folate-mediated tumor cell uptake of quantum dots entrapped in lipid nanoparticles. **J Control Release,** v. 124, n. 1–2, p. 28-34, 2007.

WI, H. S.; KIM, S. J.; LEE, K.; KIM, S. M.; YANG, H. S.; PAK, H. K. Incorporation of quantum dots into the lipid bilayer of giant unilamellar vesicles and its stability. **Colloids Surf B Biointerfaces,** v. 97, n. 0, p. 37-42, 2012.

CHAPTER VI
Final conclusions and perspectives

Chapter VI – Final conclusions and perspectives

VI.1. Final conclusions

The aim of this thesis was to explore ZnO based QDs as bioimaging agents due to their promising photoluminescent properties, when synthesized via sol-gel route, and low toxicity compared to the usual QDs, which contain heavy metals such as Cd, Pb, etc.

In a first step, attempts were made to improve the photoluminescence properties of ZnO QDs by synthesizing ZnO/ZnS core-shell QDs and doping ZnO QDs with Mg^{2+} ions. Hereafter, QD surface modification was achieved for later incorporation in lipid based nanocarriers. Finally, the study of the structure, stability, photoluminescence properties and cell internalization of lipid nanocarriers loaded with QDs was carried out.

We could monitor the reactions tentatively used for obtaining ZnO/ZnS core-shell QDs and characterize the final products. We could observe that a small amount of TAA in the reaction medium was not sufficient to produce ZnS; an intermediate amount of TAA led to the formation of both species (ZnO and ZnS); and higher quantities of TAA gave mainly rise to ZnS nanoparticles. Figure VI.1 shows schematically the final products starting from either ZnAc precursor or ZnO colloidal suspensions mixed with three different TAA concentrations. The samples obtained in each reaction could be characterized by UV-vis, XRD and XAS techniques; however, it is noteworthy that only XAS allowed identifying core-shell structure when the reaction proceeded in ZnO colloidal suspension mixed with TAA 5 mM (Route1).

Figure VI.1. Schematical final products obtained in the reactions starting from ZnO colloidal suspensions (Route 1) and ZnAc precursor (Route 2) using three TAA concentrations (1.5, 5 and 50mM).

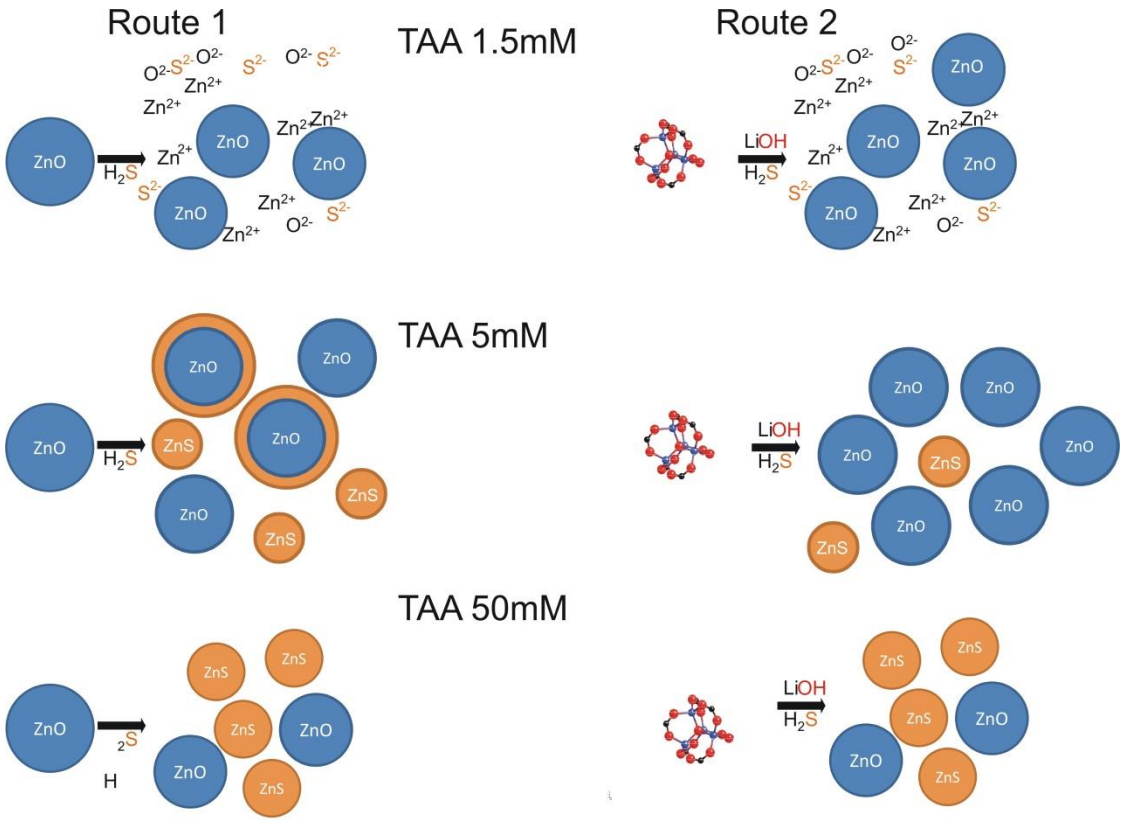

ZnO/ZnS QDs showed a rather weak photoluminescence in the visible range, compared to ZnO QDs, without displaying a significantly increased emission in the UV range. Therefore, doping of Zno QDs with Mg ions was performed in an attempt to optimize their luminescence.

Mg-doped ZnO QDs were synthesized, preserving the wurtzite lattice of ZnO. The higher was the amount of dopant incorporated into ZnO structure, smaller was the size of nanoparticles. Mg ions incorporated into ZnO QDs strongly changed their growth, preventing the formation of fractal aggregates. We could increase the QY of ZnO QDs six times by using 20 mol% (nominal concentration) of Mg^{2+} ions in the reaction medium. The modification of their surface was also required to incorporate them into lipid-based nanocarriers. The ZnO and $Zn_{0.8}Mg_{0.2}O$ QDs could be successfully capped by oleic acid (OA), forming stable colloidal dispersions in chloroform and toluene and keeping strong visible luminescence. Figure VI.2 presents schematically the structures of ZnO and $Zn_{0.8}Mg_{0.2}O$ QDs with and

without OA coating, their photographs and respective QY. This part of the work has already been published in the European Journal of Nanomedicine, 7(2): 109–120, 2015 (Annexe).

Figure VI.2. Schematical structures of ZnO and $Zn_{0.8}Mg_{0.2}O$ QDs with and without OA capping, their photographs and respective QY.

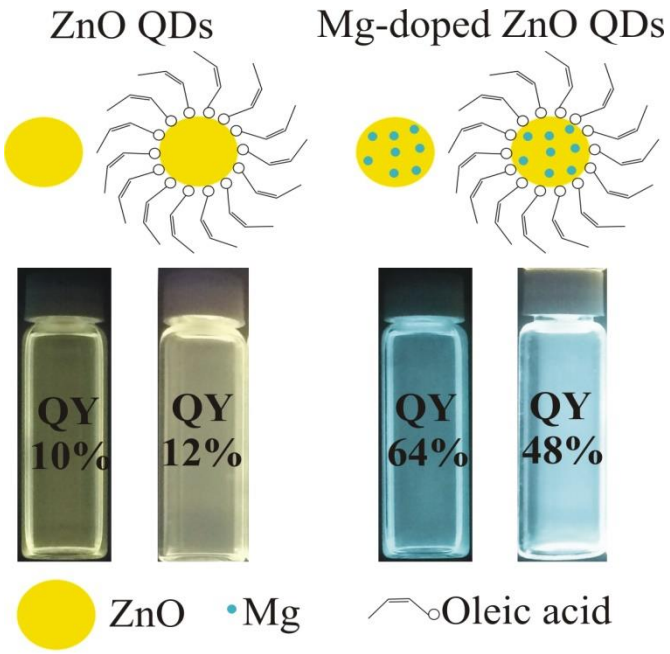

Finally, we have tried to incorporate highly luminescent $Zn_{0.8}Mg_{0.2}O$ and OA-$Zn_{0.8}Mg_{0.2}O$ QDs into lipid-based nanocarriers.

Figure VI.3 shows examples of photographs of liposomes, DSPE-Peg based formulations and SLNs, loaded with QDs. As observed in this figure, liposomes presented lower luminescence compared to the DSPE-Peg formulation and SLN. SLNs were fairly stable in biological media, as shown by the absence of large aggregates. However, further investigations are needed to optimize the preparation and photoluminescence properties of the different nanocarriers for bioimaging applications.

Figure VI.3. Photographs of QDs loaded liposomes, a DSPE-Peg based formulation and an example of SLN (from left to right, respectively) under UV lamp.

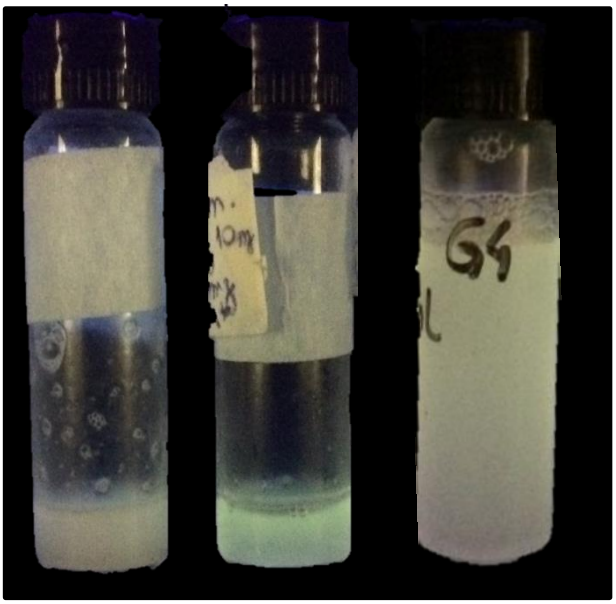

VI.2. Perspectives

ZnO/ZnS nanoparticles surface could be characterized by XPS, Zeta potential and isoeletric potential to confirm the modification of their surface by the ZnS shell deposition around the ZnO core.

Doping with Mg^{2+} ions widened the band gap of ZnO QDs and enhanced their visible luminescence. While studying Mg-doped ZnO QDs we could observe that Mg^{2+} ions interfere directly with the growth of the nanoparticles, inducing disorder in the ZnO lattice, decreasing the final size of the QDs and hindering their aggregation. However, we could not determine their location into ZnO QDs (in the core and/or at the surface). EXAFS and XANES spectra could be recorded at the Mg edge to identify the environment of Mg ions (nature and number of neighbors, distance between them). Indeed, no significant differences could be evidenced at the Zn edge between ZnO QDs and Mg-doped Zno QDs. First experiments have been performed at LUCIA beamline at SOLEIL Synchrotron source. Work is in progress.

Regarding DPPC-based formulations which preserve the DPPC bilayer structure, atomic force microscopy (AFM) could be used to investigate the homogeneity of the repartition of QDs in the bilayers and the potential presence of QD aggregates. Further investigations are needed to better control the size and size distribution of the different nanocarriers, improve their luminescence and characterize their structure.

For cell internalization studies, the limitations due to the cell auto-fluorescence phenomena might be overcome if ZnO QDs were excited at the optimal excitation wavelength with high intensity beam and short exposure time. Appropriate setups are available at the DISCO beamline at SOLEIL. Besides, the luminescent nanoparticle formulation, concentration and time of incubation with cells should be optimized.

ANNEXES

DE GRUYTER Eur. J. Nanomed. 2015; 7(2): 109–120

Eloísa Berbel Manaia, Renata Cristina Kiatkoski Kaminski, Bruno Leonardo Caetano, Valérie Briois, Leila Aparecida Chiavacci and Claudie Bourgaux*

Surface modified Mg-doped ZnO QDs for biological imaging

Abstract: Nanocrystals of ZnO are currently attracting great interest as potential labels for biological applications, such as theranostic devices, due to their luminescent properties and low toxicity in vivo. It has been reported that doping with Mg^{2+} ions could enhance the luminescence of ZnO quantum dots (QDs). In the present study Mg-doped ZnO QDs were synthesized by a hydrolysis and condensation reaction. Surface modification of the QDs was performed using oleic acid (OA) to hinder their aggregation and to provide them colloidal stability in non-polar environments. Mg^{2+} ions could be incorporated into the ZnO wurtzite lattice owing to the very close values of the Mg^{2+} and Zn^{2+} ion radii. However, the dopant ions strongly influenced the growth and final size of ZnO nanocrystals, as evidenced by time-resolved synchrotron SAXS measurements. The presence of Mg prevented the aggregation of the primary nanoparticles. Doping with Mg^{2+} ions widened the band gap of ZnO QDs and enhanced their visible luminescence. With increasing proportion of Mg^{2+} ions, both the absorption and emission spectra experienced a blue shift. The luminescence went through a maximum for a 20 mol% nominal concentration of Mg^{2+} ions in the reaction medium. The quantum yield (QY) of 20 mol% Mg-doped ZnO colloidal suspension (64%) was about 6 times higher than that of the ZnO suspension (10%). Mg-doped ZnO QDs capped by OA formed stable colloidal dispersions in chloroforme, with strong visible fluorescence (QY=38%), promising for biological imaging.

Keywords: biological imaging; Mg-doped ZnO quantum dots; SAXS; sol-gel process.

DOI 10.1515/ejnm-2014-0047
Received November 16, 2014; accepted March 12, 2015

***Corresponding author: Claudie Bourgaux,** University Paris-Sud, Institut Galien, CNRS, UMR 8612, LabEX LERMIT, F-92296 Châtenay-Malabry, France, Phone: +33 1 46 83 58 68, Fax: +33 1 46 83 53 12, E-mail: claudie.bourgaux@u-psud.fr

Eloísa Berbel Manaia: Faculty of Pharmaceutical Sciences of São Paulo State University, UNESP, Araraquara-Jaú Interstate Highway, Km 1, Araraquara, SP, Brazil; University Paris-Sud, Institut Galien, CNRS, UMR 8612, LabEX LERMIT, F-92296 Châtenay-Malabry, France

Renata Cristina Kiatkoski Kaminski: Sergipe Federal University, Campus Itabaiana, Av. Vereador Olimpio Grande, s/n, Itabaiana, SE, Brazil

Bruno Leonardo Caetano: Chemistry Institute of São Paulo State University, UNESP, Prof. Francisco Degni Street, 55, Araraquara, SP, Brazil

Valérie Briois: Synchrotron SOLEIL, L'Orme des Merisiers, BP48, Saint Aubin, 91192 Gif-sur Yvette, France

Leila Aparecida Chiavacci: Faculty of Pharmaceutical Sciences of São Paulo State University, UNESP, Araraquara-Jaú Interstate Highway, Km 1, Araraquara, SP, Brazil

Introduction

At the nanoscale, the optoelectronic properties of semiconductor crystals depend on their size. For crystals smaller than twice the Bohr exciton radius (the so-called quantum dots, QDs), the semi-conductor band gap widens as the nanocrystal size decreases, owing to quantum confinement effects. Consequently, the radiative recombination of an electron from the conduction band with a hole from the valence band leads to the emission of a photon whose wavelength can be tuned by changing the nanocrystal size. The creation of an electron-hole pair (or exciton) is induced by the absorption of a photon with energy above that of the band gap, resulting in a broad absorption spectrum. Both the absorption and emission spectra of QDs experience a blue shift with QD decreasing size (1).

Usual QDs are made of CdSe, CdTe, InAs and InP. Depending on their composition and size, their emission ranges from near UV to near IR. They need appropriate surface modification, such as coating with amphiphilic molecules, to be dispersible in an aqueous solution. When functionalized with ligands such as antibodies or peptides, QDs can be used to label different types of cellular targets or detect biomarkers (2, 3). Recently, nanoparticles containing QDs have been investigated as theranostic devices for simultaneous imaging and drug delivery (4). For instance, doxorubicine has been loaded, along with QDs, into micelles, aptamers, and liposomes (5–7).

However, the potential cytotoxicity of first generation QDs is a major concern for biological applications (8–11). In this context, luminescent nanoparticles of ZnO are currently attracting great interest as potential labels for bio-imaging because of their biodegradability and very low toxicity in vivo, although ZnO nanoparticles are able to release Zn^{2+} ions and produce destructive reactive oxygen species (ROS), as shown by cytotoxicity tests in vitro (12–14). ZnO is an n-type semi-conductor with a wide band gap of 3.37 eV at room temperature and a Bohr exciton radius of ~2.34 nm. The typical excitonic emission, arising from recombination of photo-generated electrons with holes in the valence band or in traps near the valence band, is thus observed in the UV range. Remarkably, the photoluminescence spectrum of ZnO nanocrystals also displays a broad visible emission, more suitable for biological imaging, which has been ascribed to point defects such as O and Zn vacancies or interstitials and related to surface oxygen-containing moieties, such as OH groups (15). However, the understanding of the exact mechanism for visible emission is still lacking.

Because of the role of defects and surface chemistry, the synthesis technique is expected to strongly influence the luminescence of ZnO. In general, the visible emission of thin films or particles synthesized at high temperature or annealed is very weak whereas nanoparticles prepared by the sol-gel route exhibit stronger defect-induced visible luminescence. A typical sol-gel route is the hydrolysis and condensation of a precursor in ethanolic solution (Zn salt solution) catalyzed by a base (16). However, the obtained ZnO QDs display a low quantum yield and are unstable in water and in non-polar solvents. Surface modification is further required to prevent growth and aggregation of QDs and to ensure their colloidal stability in different environments (17). Obtaining ZnO QDs with high quantum yield while preserving their visible luminescence upon surface modification remain a challenge because of the sensitivity of photoluminescence to subtle changes of synthesis parameters and environment.

It has been reported that doping with Mg^{2+} ions can enhance the luminescence of ZnO. Most of previous researches have focused on Mg-doped ZnO thin films and particles annealed at high temperature, with high UV emission but weak visible luminescence (18–22).

In the present study, we report the design of ZnO-based QDs with strong visible luminescence, promising for labeling of lipidic nanoparticles which could be used as theranostic devices. Specifically, we have shown that (i) Mg-doped ZnO QDs prepared using the sol-gel method exhibited enhanced visible luminescence, (ii) the maximum quantum yield was obtained for Mg precursor concentration of 20 mol%, (iii) Mg-doped ZnO QDs capped by oleic acid formed stable colloidal suspensions in toluene and chloroform, while preserving their photoluminescence.

Mg-doped ZnO QDs were characterized by elemental analysis, transmission electronic microscopy, small- and wide-angle X-ray scattering, Raman spectroscopy, UV-Vis absorption and photoluminescence emission. The aim was to establish a relationship between the composition and structure of the QDs and their luminescent properties.

Materials and methods

Materials

Zinc acetate dihydrate, $ZnAc_2{\cdot}2H_2O$ (Alfa Aesar), lithium hydroxide monohydrated, $LiOH{\cdot}H_2O$ (Alfa Aesar), magnesium acetate tetrahydrate, $Mg(Ac)_2{\cdot}4\ H_2O$ (Alfa Aesar), oleic acid (Alfa Aesar), ethanol (VWR, BDH, Prolabo), chloroform (VWR, BDH, Prolabo) and heptane (Carlo Erba Reagents), were used as received, without further purification. Zinc oxide powder (Alfa Aesar) was used as standard.

Synthesis

ZnO QDs: ZnO colloidal suspensions were synthesized by hydrolysis and condensation at 60°C of a precursor solution (Zn_4OAc_6 ethanolic solution) upon mixing with a LiOH ethanolic solution, following the sol-gel route proposed by Spanhel and Anderson (23).

The Zn_4OAc_6 tetrameric precursor was first prepared by refluxing an absolute ethanol solution with 0.05 M $ZnAc_2{\cdot}2H_2O$ concentration for ~2 h at 80°C. The thus-obtained transparent precursor solution was stored at ~4°C. Meanwhile, $LiOH{\cdot}H_2O$ absolute ethanol solution (0.5 M) was prepared by ultrasonic mixing. Hydrolysis and condensation reactions were carried out in a flask containing the precursor solution thermostated at 60°C. LiOH solution was dropped into the precursor solution and the reaction medium was then continuously stirred for 30 min. Afterward, the ZnO colloidal suspension was cooled and stored at ~4°C to prevent any further growth process. The nominal molar ratio [OH]/[Zn] was 1.4.

Mg-ZnO QDs: Mg doping was achieved by adding a $Mg(Ac)_2$ ethanol solution to the Zn precursor solution, keeping the total molar concentration [Zn+Mg] constant. The [LiOH]/[Zn+Mg] molar ratio was also kept constant. The reaction conditions were similar to those described above for preparing undoped nanoparticles. The Mg precursor concentration was increased from 2.5 to 20 mol%. Samples are referred to using nominal Mg^{2+} mole fraction in the initial reaction mixture (e.g. 20% Mg-ZnO).

OA-ZnO QDs: ZnO QDs capped by oleic acid (OA) were obtained by adding oleic acid to the ZnO QDs suspension (13 mM, 18.8 mM, 25 mM or 36.7 mM OA concentration) under vigorous stirring during 30 min at 60°C. The resulting turbid solutions were stored at 8°C overnight

and then centrifuged (10 min at 10,000 rpm, 13000 *g*). The supernatant was removed and the OA-ZnO QDs were washed with ethanol, in which they could not be dispersed, in order to remove the unreacted OA. Afterward, the washed OA-ZnO QDs were dried at room temperature under vacuum and put in suspension into chloroform or toluene.

OA-Mg-ZnO QDs: The surface modification of the 20% Mg-ZnO QDs, which showed optimal photoluminescence properties, was achieved in the same way.

Powder obtention: Doped or undoped ZnO QDs could be recovered from the ethanolic suspensions thanks to an extraction procedure using heptane. The as-synthesized colloidal suspensions were mixed with a "non-solvent" heptane (2:4) (1:4) to induce the precipitation of the QDs, and then centrifuged at 20°C for 10 min (10,000 rpm, 13000 *g*). The supernatant was discarded and the powder was dried under vacuum at room temperature. The dried powder was used for X-ray powder diffraction characterization, Mg quantification and Raman spectroscopy analyses.

Characterization

Inductively coupled plasma mass spectrometry (ICP-MS): Mg^{2+} concentrations in doped QDs were determined using inductively coupled plasma mass spectrometry at the Institut des Sciences Analytiques, Villeurbanne.

High resolution transmission electron microscopy (HRTEM): HRTEM investigations were performed with a JEOL JEM-2011 UHR scanning electron microscope operating at 200 keV, at the "Service of electronic microscopy" at the University Pierre and Marie Curie, Paris, France. A drop of the dilute colloidal suspension of QDs was deposited on a copper grid. Image analysis was carried out with the ImageJ software.

X-ray powder diffraction (XRD): XRD analysis of nanoparticles was performed on a Bruker D2 PHASER diffractometer, using the Cu Kα radiation, λ=1.5418 Å, selected by a curved graphite monochromator and a fixed divergence slit of 1/8° in a Bragg-Brentano configuration. The diffraction intensity data were measured in the 2θ range 5–70° by the step counting method (0.1° step and 3 s counting time).

Small-angle X-ray scattering (SAXS): SAXS experiments were performed on the SWING beamline, operated at 10.5 keV, at the SOLEIL synchrotron source (Saint Aubin, France).

For two compositions, pure ZnO and 20 % Mg-ZnO, the nucleation and growth of nanoparticles have been followed in situ, using a home-made stopped-flow device. The freshly prepared precursor solution and the ethanolic LiOH solution, contained in two syringes, were simultaneously pushed by syringe pumps into two tubes, rapidly mixed at the Y-junction of these tubes and introduced into the thermostated X-ray capillary. The temperature of the sample holder was set to 60°C. Time-resolved SAXS patterns could be recorded from the first seconds of the reaction. The acquisition time of each curve was 200 ms. The dead time between two acquisitions was adjusted to take into account the evolution of the nanoparticle growth rate during synthesis.

SAXS patterns were collected by a two-dimensional CCD detector with a sample-to-detector distance of 1727 mm. The scattered intensity was reported as a function of the scattering vector $q=4\pi \sin\theta/\lambda$, where 2θ is the scattering angle and λ the wavelength of the incident beam. The calibration of the q range (0.0062–0.64 $Å^{-1}$) was carried out with silver behenate.

Intensity values were normalized to account for beam intensity, acquisition time and sample transmission. Each scattering pattern was then integrated circularly to yield the intensity as a function of q. The scattered intensity from a capillary filled with ethanol was subtracted from the sample scattering curves. The analysis of the SAXS data was carried out using the software package SASFIT (25).

Raman spectroscopy: The Raman spectra were collected in the backscattering configuration at room temperature with a commercial Kaiser Optical Systems RXN1 Raman spectrometer equipped with a near-IR laser diode working at 785 nm, operating with a power output of 50 mW. All the samples, apart from liquid oleic acid, were dried powders.

Spectroscopy UV: The absorption spectra were measured using a Cary Win 4000 UV-Vis spectrophotometer with a cuvette of 1 mm optical path. The spectra of the QDs suspensions were recorded between 250 and 450 nm, with a wavelength step of 1 nm, and an average counting time of 0.2 s per point. The UV-vis spectra were corrected from the absorption spectrum of ethanol.

Photoluminescence spectroscopy (PL): The emission (PL) and excitation (PLE) photoluminescence spectra were recorded on a Luminescence spectrometer LS50B (Perkin-Elmer) at room temperature with a Xe lamp (20 kW) as the excitation source. For PL measurements, each sample was excited at the optimal wavelength, defined by the PLE spectrum (Table 1).

The quantum yield (QY) determines the efficiency of the conversion of absorbed photons into emitted ones. Usually, the relative QY of the studied sample is compared with that of a reference fluorophore. In this work, a solution of Rhodamine 6G in ethanol (QY=95%), often used as reference for green emission, was selected as the standard (26). According to the method described by Crosby and Demas (27), the QY is given by the following formula:

$$QY_x = QY_r [A_r(\lambda_r)/A_x(\lambda_x)](n_x^2/n_r^2)(D_x/D_r)$$

where A is the absorbance at the excitation wavelength (λ), n the refractive index of the solvent used and D the integrated fluorescence intensity (the area under the corrected emission curve). The subscripts r and x refer to the reference and sample solutions, respectively. To minimize the errors, the same excitation wavelength was chosen to measure the PL spectra of the Rhodamine 6G and QD solutions and the two solutions had the same absorbance at this wavelength (A=0.05).

Results

Mg-doped ZnO QDs were synthesized by the hydrolysis and condensation reaction described above. Surface modification of the QDs was performed using oleic acid (OA) to hinder their aggregation and to provide them colloidal stability in different environments. Different quantities of

Table 1: Amount of Mg incorporated into ZnO QDs obtained by ICP, crystallite size deduced from X-ray diffraction peaks using the Debye-Scherrer relation, bandgap measured using UV/Vis absorption, wavelength of the PLE peak maximum, wavelength of the PL emission peak maximum, quantum yield of each sample.

Initial Mg mole fraction	Mg incorporated into ZnO, %	Crystallite size, nm	Bandgap, eV	λ_{ex}, nm	λ_{em}, nm	QY, %
0		3.3	3.37	365	520	10.2
2.5	0.41	2.7	3.42	363	520	5.0
5	0.72	2.3	3.52	358	512	16.7
10	1.98	2.2	3.60	350	476	27.8
20	2.94	2.0	3.71	342	470	64.8

OA were added to the QD suspensions. In all cases the QDs capped by OA formed stable colloidal dispersions in chloroform or toluene.

Preliminary measurements having shown that the visible luminescence of Mg-ZnO QDs went through a maximum for a 20 mol% nominal concentration of Mg^{2+} ions in the reaction medium, our investigations focused on the structure and properties of QDs obtained with Mg^{2+} concentration increasing up to 20%.

Actual atomic concentrations of Mg in doped QDs, determined using ICP-MS, are reported in Table 1. These data evidence a low incorporation of Mg^{2+} ions into ZnO QDs. The Mg^{2+} concentration varied from 0.41 to 2.94%.

Figure 1A shows powder wide-angle X-ray diffraction patterns, recorded between $2\theta=5°$ and 70°, of ZnO reference, ZnO QDs and Mg-ZnO QDs. They display peaks characteristic of the ZnO hexagonal wurtzite structure. No peak characteristic of the MgO rock salt phase (e.g., at 42.5°) is detected whatever the concentration of Mg^{2+} ions.

The broadening of the peaks of Mg-ZnO QDs could result from a decrease in crystallinity and/or crystal size, promoted by the presence of Mg. Assuming that this broadening is mainly due to size effects, the average size of nanocrystals could be estimated using the Debye-Scherrer relation (28) applied to the (100) reflection:

$$D=\frac{\kappa\lambda}{\beta\cos\theta}$$

where D is the crystal size; k is a constant (shape factor, 0.89 for spherical nanoparticles), λ is the X-ray wavelength, β is the full width at half maximum (FWHM) of the diffraction peak and 2θ is the diffraction angle. The size of the nanocrystals decreased from 3.3 nm for ZnO to 2.0 nm for 20% Mg-ZnO. Figure 1B shows a zoom of the (100) diffraction peak between $2\theta=30°$ and $2\theta=34°$. Mg^{2+} ions shift the (100) peak to slightly higher angles, suggesting a weak decrease of the lattice parameters. This small change, whose extent depends on the Mg

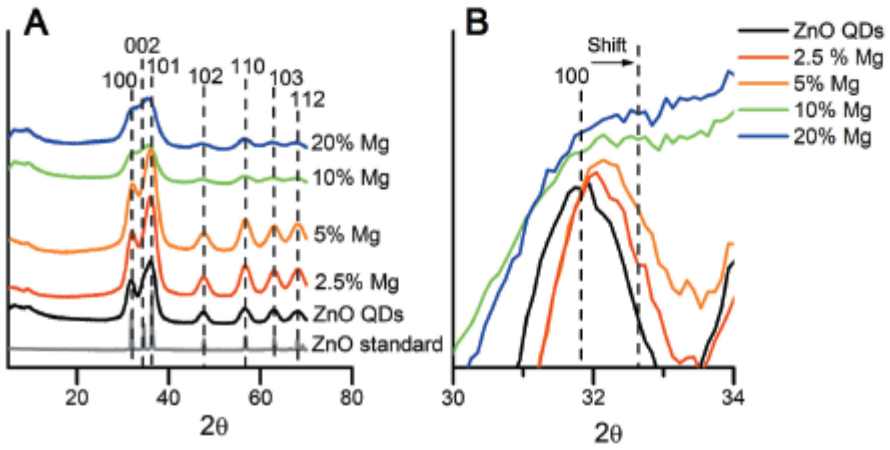

Figure 1: (A) XRD profiles of ZnO standard and 0, 2.5, 5, 10 and 20% of Mg-ZnO QDs, showing the presence of the hexagonal wurtzite phase (B) zoom of the (100) peak in the 30°–34° 2θ range.

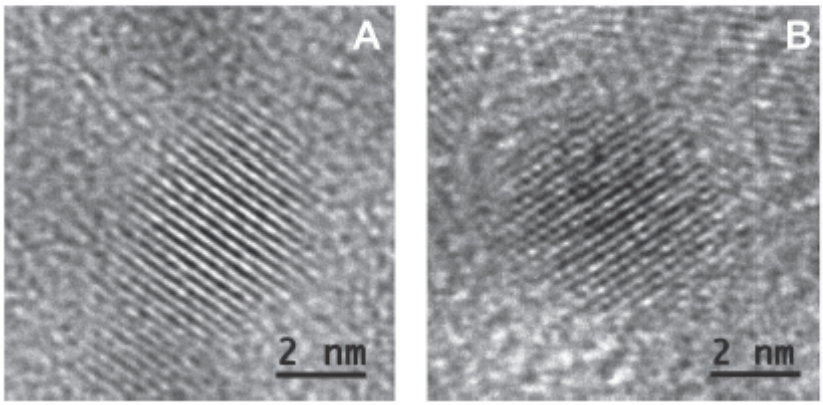

Figure 2: HRTEM images of undoped ZnO QDs (A) and 20% Mg-ZnO QDs (B).

concentration, is expected to reflect the substitution of some Zn^{2+} ions by Mg^{2+} ions in the crystalline lattice, as the Mg^{2+} ions have a slightly smaller ionic radius (0.57 Å for Mg^{2+} ions compared to 0.60 Å for Zn^{2+} ions). At high Mg concentrations the peak shifts are obscured by the large width of the peaks.

The size and morphology of ZnO and 20% Mg-ZnO nanoparticles were also studied using HRTEM (Figure 2). HRTEM images show nanocrystals with approximately spherical shapes and average diameters of about 4 nm for ZnO QDs. The average size of Mg-ZnO QDs, whose structure appears less ordered, is slightly smaller. Overall, these data are in agreement with XRD data.

The influence of Mg on the growth of nanoparticles was further evidenced by time-resolved SAXS patterns, recorded from the beginning of the reaction. Figures 3A and 4A present three-dimensional stacked log-log plots of the SAXS curves as a function of time, corresponding to the formation of ZnO and 20% Mg-ZnO QDs, respectively. Selected curves of ZnO and 20% Mg-ZnO QDs formation are shown in Figures 3B and 4B, respectively. The two systems exhibit clearly different time evolution.

At the beginning of the reaction, ZnO curves display a plateau at low q-range (Guinier region), indicative of the scattering of non-interacting particles. In the Guinier region, the scattered intensity can be approximated by $I(q)=I(0)\exp(-Rg^2q^2/3)$ where Rg is the radius of gyration (Guinier radius) of the particles (29). The Guinier plateau progressively shifts to lower q-values, reflecting the increase in the nanoparticle size with time. The curves display an oscillation at high q-values, which can arise from the form factor of spherical particles. The SAXS profiles could be fitted by the form factor of homogeneous spheres with Gaussian radius distribution. The radii of gyration Rg are consistent with the mean radii of the nanoparticles R, as deduced from the fits [for a sphere Rg is defined as $Rg=(3/5)^{1/2}R$] (Figure 5A). The size of the nanoparticles increased steeply during the first minutes of the reaction, up to 3 nm after 3 min. After about 15 min the size of the primary particles, which has reached 4 nm, no longer evolved.

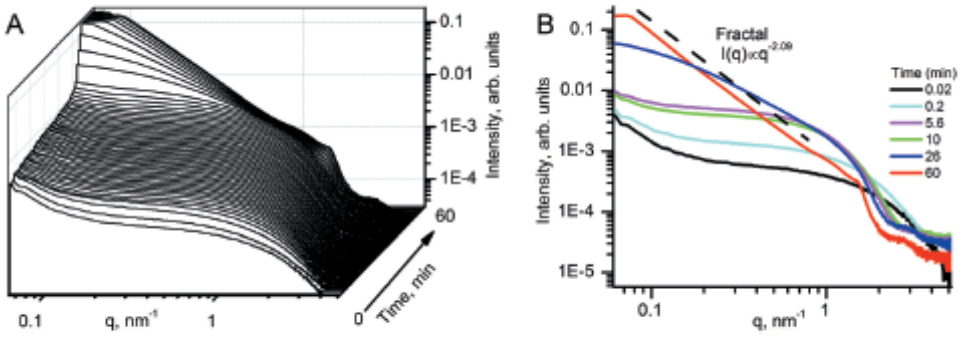

Figure 3: Three-dimensional stacked log-log plots of the SAXS curves as a function of time recorded in situ during the formation of ZnO QDs (A) and selected in situ SAXS profiles measured at the indicated reaction time (min) (B).

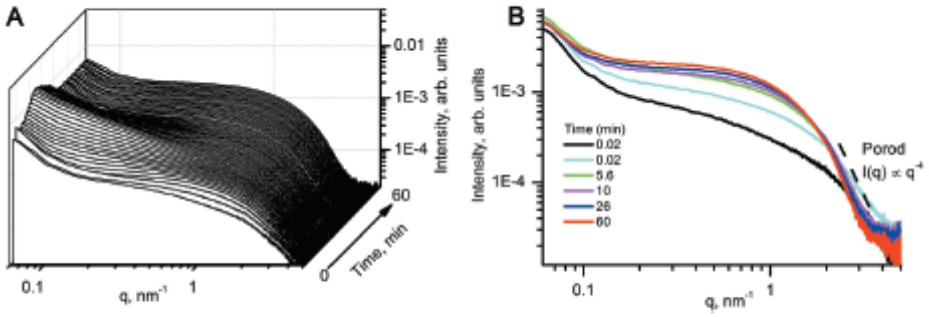

Figure 4: Three-dimensional stacked log-log plots of the SAXS curves as a function of time recorded in situ during the formation of 20% Mg-doped ZnO QDs (A) and selected in situ SAXS profiles measured at the indicated reaction time (min) (B).

At the end of the reaction, after about 50 min, the intensity scattered at low q-values strongly increases and the Guinier plateau disappears. In the low q region, a linear decay of log$I$ is observed in the log$I$ vs. log$q$ plot: $I(q) \propto q^{-\alpha}$ (30) with α=2.09. This behaviour evidences the formation of fractal aggregates with fractal dimension α, defined as the exponent that relates the mass M of an object to a characteristic dimension R: $M \propto R^{\alpha}$. The α=2.09 fractal dimension is characteristic of structures formed by reaction-limited cluster-cluster aggregation (RLCCA). The aggregation rate is limited by the time needed to overcome the repulsive barrier between two clusters. Compared to the diffusion-limited cluster-cluster aggregation (DLCCA), the RLCCA mechanism corresponds to slower colloid aggregation, yielding more compact clusters due to the lower sticking probability (31).

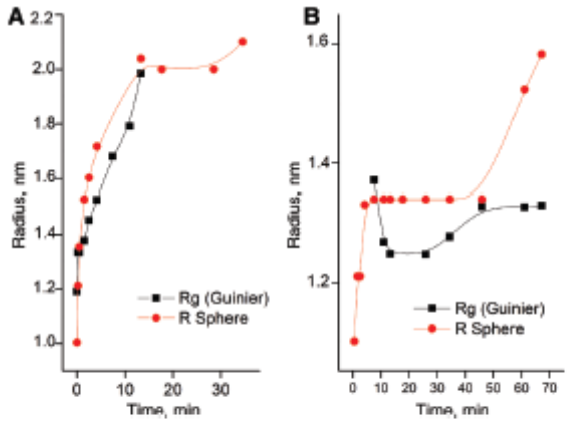

Figure 5: Comparison of the time evolution of the radius of gyration (Rg), determined in the Guinier region, and the radius (R), deduced from the fit of curves by the form factor of spheres, of nanoparticles: (A) ZnO QDs and (B) 20% Mg-ZnO QDs.

This linear decrease in log$I$ as a function of log$q$ is observed between q-values corresponding to the primary particle size and the fractal aggregate size, respectively. As shown by the curve oscillation in the high q range, the mean radius of the primary particles remains constant, at about 2 nm, until the end of the reaction. Consequently, the formation of ZnO QDs involves two main steps: the nucleation and growth, up to a size of ~4 nm, of elementary nanoparticles during the ten first min of the reaction, followed by the formation of fractal aggregates with fractal dimension α=2.09.

The structures giving rise to the first Mg-ZnO SAXS profiles collected during the synthesis of Mg-ZnO QDs could not be identified. After about 5 min, the SAXS curves could also be fitted by the form factor of homogeneous spheres with Gaussian radius distribution. The growth of nanoparticles is rapidly stopped after the nucleation step. Nanoparticles remain smaller than ZnO ones. A further small increase in size is observed at the end of the reaction. The intensity $I(0)$, proportional to the number of nanoparticles in the medium, increases continuously during the first 60 min of the reaction. Of note, unlike ZnO nanoparticles, Mg-ZnO QDs do not form fractal aggregates with time, suggesting that the nanoparticles have different surface properties.

Raman scattering carried out on QDs allows obtaining information on the surface species and on the modifications of the optical phonon spectrum, as compared to ZnO bulk crystal values (Figure 6A and B).

The spectrum of ZnO standard shows a prominent peak at 439 cm^{-1} and weak peaks at 332 cm^{-1}, 380 cm^{-1}, 410 cm^{-1}, 581 cm^{-1} and 666 cm^{-1}, in agreement with previous studies (32). The peak at 439 cm^{-1} is characteristic of the wurtzite lattice; the sharp line shape is indicative of high crystalline order. This peak becomes less intense in ZnO QDs while the intensity of the 410 cm^{-1} band increases, appearing as a shoulder of the peak at 439 cm^{-1}.

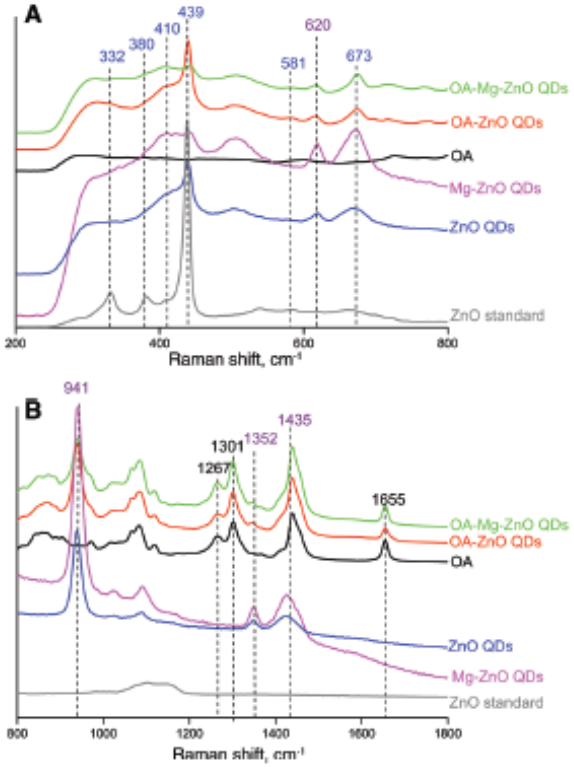

Figure 6: Raman spectra of ZnO standard, ZnO QDs, Mg-ZnO QDs, OA, OA-ZnO QDs and OA-Mg ZnO QDs with indications of the principal vibrations (A) from 200 to 800 cm^{-1} and (B) from 800 to 1800 cm^{-1}.

More importantly, in Mg-ZnO QDs the weak 439 cm^{-1} peak is involved in a broad band, reflecting the diminution of crystallinity induced by Mg incorporation.

The presence of oleic acid (OA) attached on the surface of QDs is unambiguously evidenced by the intense and well resolved peaks at 1265 cm^{-1}, 1301 cm^{-1} and 1655 cm^{-1} which cannot overlap with peaks arising from other species. These peaks correspond to δ(=CH) deformations, $\delta(CH_2)_n$ deformations and ν(C=C) stretching vibrations of unsaturated fatty acids, respectively (33). Other peaks assigned to OA (34) are listed in Table 2.

Beside peaks originating from the optical phonon spectrum of QDs and OA molecules capping their surface, Raman spectra of QDs exhibit a prominent peak at 940 cm^{-1} and weak broad peaks at 1352 cm^{-1} and 1435 cm^{-1}, which could be attributed to acetate ions. These peaks correspond to ν(C–C) stretching, $\delta(CH_3)$ symmetric bending and ν(CO) symmetric stretching, respectively (35). Raman measurements support the incorporation of Mg^{2+} ions in ZnO lattice and demonstrate that the QD surface is efficiently capped with OA. They also evidence the presence of acetate surface groups.

The optical properties of the ZnO and Mg-ZnO QD colloidal suspensions were studied by UV-Vis absorption and PL spectroscopy. UV-vis absorption spectra of ZnO and Mg-doped ZnO QD suspensions are shown in Figure 7. The absorption edge shifts from 340 nm to 305 nm with Mg concentration increasing from 0 to 20 mol%. This progressive blue-shift is indicative of the band gap widening upon Mg doping. The band gap energy was estimated to be the energy at which the absorbance of the absorption edge reached half of its maximum value (36). An increase from 3.37 eV to 3.71 eV is observed, consistent with previous studies (Table 1).

Usually, the PL spectra of ZnO exhibit two components. One is the exciton, or band-edge, emission in the UV range, the other is visible emission, also called deep-level emission, due to the existence of defects which are mainly located on the ZnO surface. Nanoparticles prepared by the sol-gel route exhibit mainly visible luminescence whereas their UV emission is weak. On the contrary, highly crystalline ZnO displays strong band-edge luminescence. In our study, only a weak UV emission peak at ~380 nm was observed when the ZnO QDs where excited at 342 nm. The intensity of the UV emission peak further decreased and became negligible when the concentration of Mg in QDs increased, in agreement with a previous report (37). Mg-doped QDs were excited at low wavelength, between 324 nm and 346 nm. We have therefore focused on the visible emission, by selectively exciting the defect states. Photoluminescence excitation (PLE) spectra were measured with detection at a wavelength where the visible emission was maximum (Table 1), revealing an increase in the peak energy with increasing Mg doping level (Figure 8). This dependence is in line with that of the absorption spectra.

Photoluminescence emission spectra were then collected by exciting each QD suspension at the wavelength corresponding to the maximum of the PLE spectrum (Figure 8). The emission spectra exhibit two broad bands at 400–495 nm and 495–590 nm, whose relative intensities depend on Mg^{2+} concentration. The intensity of the first band is enhanced at high Mg^{2+} concentration. The luminescence increases when Mg^{2+} concentration rises from 5% to 20%. The quantum yields of the different samples are reported in Table 1. Remarkably, the quantum yield (QY) of 20 mol% Mg-doped ZnO colloidal suspension (64%) is about 6 times higher than that of the ZnO suspension (10%).

Figure 9 shows the emission spectra of ZnO and 20% Mg-ZnO QDs capped by OA dispersed in chloroform excited at 345 nm and 341 nm, respectively. The emission wavelength range is not affected by OA. The corresponding

Table 2: Raman shift (cm^{-1}) and assignment of the main vibrations observed in the following samples: ZnO standard, ZnO QDs, Mg-ZnO QDs, OA, OA-ZnO QDs and OA-Mg-ZnO QDs. Raman shifts are compared with values from References (32–35).

Raman shift, cm^{-1}	Origin	Reference, cm^{-1}	Assignment	Reference
332	ZnO	332	E_2 (high)–E_2 (low)	Cusco
380	ZnO	380	A_1(TO)	Cusco
410	ZnO	408	E_1(TO)	Cusco
439	ZnO	437	E_2(high)	Cusco
581	ZnO	584	E_1(LO)	Cusco
620	Acetate	621	$Y_{1,5}(B_2)$; out of plane	Koleva
673	ZnO/acetate	666/671	TA+LO/$\upsilon_5(A_2)$; OCO sym. bend	Cusco/Koleva
941	Acetate	942	υ_4 (A_2), C–C strech	Koleva
1065	OA	1063	υ_{as}(CC), chain ordered	Tandon
1085	OA	1082	υ(CC), chain ordered	Tandon
1116	OA	1118	υ(CC), chain ordered	Tandon
1267	OA	1265	δ(=CH)	De Gelder
1301	OA	1301	$\delta(CH_2)_n$	De Gelder
1435	Acetate	1435	$\upsilon_3(A_2)$; CO sym. strech	Koleva
1439	OA	1438	CH_2 scissoring	Tandon
1655	OA	1655	υ(C=C)	De Gelder

QY values are reported in Table 3. It can be seen that OA reduced the QY of doped ZnO QDs from 64% to about 40%.

Discussion

Doping ZnO is an effective approach to modify its properties. The introduction of dopant ions can either enlarge or narrow the band gap of the semiconductor, thereby tuning the emission colors. Furthermore, doping ZnO nanoparticles with ions such as Mn^{2+}, Ni^{2+} or Co^{2+} is known to impart magnetic properties to the material (38, 39).

Effective dopant incorporation is a critical issue. If dopant ions are excluded during ZnO crystal growth or just adsorbed on the surface, the desired properties may be compromised. The close radii of Mg^{2+} (0.57 Å) and Zn^{2+} (0.60 Å) contribute to the solid solubility of Mg^{2+} in ZnO since Mg^{2+} ions may replace Zn^{2+} ions in the wurtzite lattice. However, both the ratio of actual Mg amount in nanoparticles to nominal concentration in the reaction medium and the maximum Mg doping were found extremely sensitive to the conditions of sample preparation in previous studies. Generally, higher Mg^{2+} contents were achieved when the nanocrystal synthesis was performed at high temperature.

Yang et al reported a dopant content of 22.6 mol%, for a nominal 50% content in the reaction mixture. Doped nanocrystals with different shapes were obtained

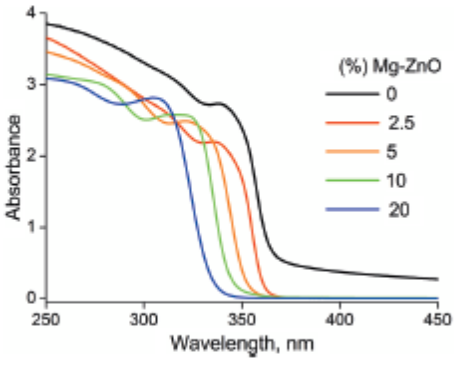

Figure 7: Absorption spectra of ZnO and 2.5, 5, 10 and 20% Mg-ZnO colloidal suspensions.

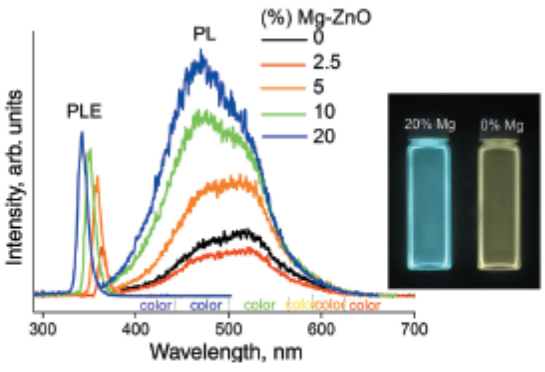

Figure 8: PLE and PL spectra of ZnO and 2.5, 5, 10 and 20% Mg-ZnO colloidal suspensions. The inset shows the photography of ZnO (right) and 20% Mg-ZnO (left) colloidal suspensions under UV lamp (λ_{exc}=365 nm).

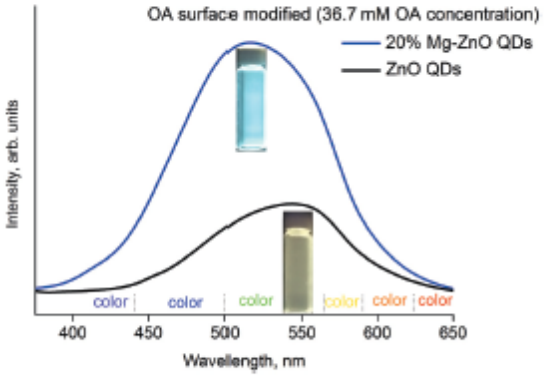

Figure 9: PL spectra of the OA-ZnO QDs and OA-Mg-ZnO QDs dispersed in chloroform. The insets show the photographs of each sample under UV lamp (λ_{exc}=365 nm).

by alcoholysis of Zn stearate and Mg stearate in 1-octadecene at 270°C (40). Cohn et al achieved a dopant content of 18%, close to the nominal content, by heating nanocrystals in dodecylamine at 160°C for about 20 min after hydrolysis and condensation reaction in DMSO at 50°C (41). In contrast, Mg content as low as 0.03%, for a Mg concentration in the initial solution of 20%, was obtained by Ghosh et al using sol-gel process at 70°C (42). In all cases the wurtzite ZnO phase was maintained. In the present study, the actual Mg content was always much lower than the nominal precursor concentration in the reaction medium. When synthesis was carried out with a [LiOH]/[Zn+Mg] molar ratio r=1.4, the maximum Mg^{2+} substitution achieved was 2.94% for an initial Mg concentration of 20%. Synthesis performed with a different molar ratio, r=0.5, yielded a concentration of 0.56%. These findings suggested that kinetic factors, likely related to relative precursor reactivities, could limit Mg incorporation in the host ZnO crystal. Generally, it has been emphasized that the growth rate of the host crystal and the rate of deposition of dopant ions should be balanced to achieve effective doping during crystal growth (43).

Table 3: Quantum Yield (QY) of the ZnO and 20% Mg-ZnO QDs capped with oleic acid (OA).

Sample	QY, %
ZnO 50 mM OA 13 mM	5.76
ZnO 50 mM OA 36.7 mM	11.86
Mg ZnO 50 mM OA 13 mM	41.56
Mg ZnO 50 mM OA 36.7 mM	38.22

The presence of Mg^{2+} ions affected the growth and size of the NPs, along with their structure. Mg^{2+} addition decreased the final size of QDs and inhibited their fractal aggregation, suggesting a modification of their surface properties. As evidenced by X-ray diffraction, HRTEM images and Raman spectra, doped QDs displayed a less crystalline, more disordered wurtzite structure than ZnO QDs.

The incorporation of Mg widened the band gap of doped ZnO QDs primarily by decreasing their size since NPs smaller than ~6 nm are sensitive to quantum confinement. Moreover, it is known that doping with Mg widens the band gap of ZnO (37, 40). According to Cohn et al., the introduction of Mg^{2+} ions raises the conduction band potential and lowers the valence band potential of ZnO (41). The two effects (quantum confinement and intrinsic effect of Mg) could not be separated.

The visible emission spanned the 400–590 nm range, featuring two broad bands at 400–495 nm and 495–590 nm whose relative intensities depended on Mg^{2+} concentration. Different relaxation processes, radiative or non-radiative, can take place upon photoexcitation of a ZnO nanoparticle. Two mechanisms have been proposed for the ZnO visible emission: i) recombination of an electron in the valence band with a hole in a deep trap, ii) recombination of an electron in singly ionized oxygen vacancy (i.e., deeply trapped) with a photo-generated hole in the valence band (Xiong, 2010). The green-yellow luminescence of ZnO is usually attributed to singly ionized oxygen vacancies (15, 44–48). It has been shown by PL microscopy probing luminescence profile at single QD level that the visible emission of ZnO QDs is intrinsically broad. The broad bandwidth does not mainly arise from the NP size (or composition herein) distribution but from multiple transitions involving closely spaced energy levels, inherent to every QD, lying between the valence band and the conduction band (44). The increase in QY upon Mg^{2+} doping can be explained by the increased concentration of inner and surface defects, in particular oxygen vacancies, and by the decrease in QD size. Because of the larger surface-to-volume ratio, smaller QDs entail the formation of more numerous surface defects. The surface state is expected to strongly influence the luminescence of ZnO QDs. For instance, correlations have been observed between the presence of surface hydroxide moieties and visible luminescence intensity. As observed by Felbier et al., when surface oxygen containing species, such as OH groups, were desorbed under vacuum, the visible emission vanished while the UV emission was significantly enhanced (49). Of note, the decrease in QY when Mg-doped QDs are capped by oleic acid is consistent with the hypothesis of

the role of OH groups in visible emission. The number of OH surface groups is expected to decrease if they react with oleic acid. The difference in relative intensities of the two broad bands at 400–495 nm and 495–590 nm suggests the existence of different types of defects and/or different paths for electron-hole recombination as a function of Mg concentration.

Conclusions

Mg-ZnO QDs were synthesized by a hydrolysis and condensation reaction. Mg^{2+} ions could be incorporated into the ZnO wurtzite lattice owing to the very close values of the Mg^{2+} and Zn^{2+} ion radii. However, the dopant ions strongly influenced the growth and final size of ZnO nanocrystals. Doping with Mg^{2+} ions widened the band gap of ZnO QDs and enhanced their visible luminescence. The luminescence went through a maximum for a 20 mol% nominal concentration of Mg^{2+} ions in the reaction medium. With increasing proportion of Mg^{2+} ions, both the absorption and emission spectra experienced a blue shift. Mg-ZnO QDs capped by oleic acid (OA) formed stable colloidal dispersions in chloroform and toluene, with strong visible luminescence, promising for biological imaging.

List of non-standard abbreviations

Mg-ZnO QDs, Mg-doped ZnO quantum dots; OA-ZnO QDs, ZnO quantum dots with oleic acid as surface modifier; OA-Mg-ZnO QDs, Mg-doped ZnO quantum dots with oleic acid as surface modifier.

Acknowledgments: The authors thank D. Desmaële for his help during synthesis, the synchrotron SOLEIL for providing beamtime at the SWING beamline (project number: 20131299) J. Perez, Y. Liatimi and P. Roblin for their support during SAXS experiments, S. Blanchandin for WAXS measurements, the Service of electronic microscopy of the University Pierre et Marie Curie for HRTEM measurements, and FAPESP and PADC/FCF-UNESP for the financial support. This work was conducted during a scholarship of E. Berbel Manaia supported by the International Cooperation Program CAPES/COFECUB (ME 767-13) at the University Paris – Sud, financed by CAPES – Brazilian Federal Agency for Support and Evaluation of Graduate Education within the Ministry of Education of Brazil.

References

1. Reid PJ, Fujimoto B, Gamelin DR. A simple ZnO nanocrystal synthesis illustrating three-dimensional quantum confinement. J Chem Educ 2013;91:280–2.
2. Michalet X, Pinaud FF, Bentolila LA, Tsay JM, Doose S, Li JJ, et al. Quantum dots for live cells, in vivo imaging, and diagnostics. Science 2005;307:538–44.
3. Wang C, Gao X, Su X. In vitro and in vivo imaging with quantum dots. Anal Bioanal Chem 2010;397:1397–415.
4. Xie J, Lee S, Chen X. Nanoparticle-based theranostic agents. Adv Drug Deliv Rev 2010;62:1064–79.
5. Tian B, Al-Jamal WT, Al-Jamal KT, Kostarelos K. Doxorubicin-loaded lipid-quantum dot hybrids: surface topography and release properties. Int J Pharm 2011;416:443–7.
6. Park JH, von|Maltzahn G, Ruoslahti E, Bhatia SN, Sailor MJ. Micellar hybrid nanoparticles for simultaneous magnetofluorescent imaging and drug delivery. Angew Chem Int Ed 2008;47:7284–8.
7. Bagalkot V, Zhang L, Levy-Nissenbaum E, Jon S, Kantoff PW, Langer R, et al. Quantum dot-aptamer conjugates for synchronous cancer imaging, therapy, and sensing of drug delivery based on bi-fluorescence resonance energy transfer. Nano Lett 2007;7:3065–70.
8. Su Y, He Y, Lu H, Sai L, Li Q, Li W, et al. The cytotoxicity of cadmium based, aqueous phase – synthesized, quantum dots and its modulation by surface coating. Biomaterials 2009;30:19–25.
9. Chang E, Thekkek N, Yu WW, Colvin VL, Drezek R. Evaluation of quantum dot cytotoxicity based on intracellular uptake. Small 2006;2:1412–7.
10. Lewinski N, Colvin V, Drezek R. Cytotoxicity of nanoparticles. Small 2008;4:26–49.
11. Klaine SJ, Alvarez PJ, Batley GE, Fernandes TF, Handy RD, Lyon DY, et al. Nanomaterials in the environment: behavior, fate, bioavailability, and effects. Environ Toxicol Chem 2008;27:1825–51.
12. Jia Z, Misra RD. Tunable ZnO quantum dots for bioimaging: synthesis and photoluminescence. Mater Tech 2013;28:221–7.
13. Xiong HM. ZnO nanoparticles applied to bioimaging and drug delivery. Adv Mater 2013;25:5329–35.
14. Moussodia RO, Balan L, Merlin C, Mustin C, Schneider R. Biocompatible and stable ZnO quantum dots generated by functionalization with siloxane-core PAMAM dendrons. J Mater Chem 2010;20:1147–55.
15. Zhang L, Yin L, Wang C, lun N, Qi Y, Xiang D. Origin of visible photoluminescence of ZnO quantum dots: defect-dependent and size-dependent. J Phys Chem C 2010;114:9651–8.
16. Caetano BL, Santilli CV, Meneau F, Briois VR, Pulcinelli SH. In Situ and Simultaneous UV-vis/SAXS and UV-vis/XAFS time-resolved monitoring of ZnO quantum dots formation and growth. J Phys Chem C 2011;115:4404–12.
17. Xiong HM. Photoluminescent ZnO nanoparticles modified by polymers. J Mater Chem 2010;20:4251–62.
18. Vijayalakshmi K, Karthick K. Influence of Mg doping on the microstructure and PL emission of wurtzite ZnO synthesized by microwave processing. J Mater Sci Mater Electron 2013;24:2067–71.
19. Xiong HM, Shchukin DG, Möhwald H, Xu Y, Xia YY. Sonochemical synthesis of highly luminescent zinc oxide nanoparticles doped with magnesium(II). Angew Chem 2009;121:2765–9.

20. Lin YJ, Wu PH, Tsai CL, Liu CJ, Lin ZR, Chang HC, et al. Effects of Mg incorporation on the optical properties of ZnO prepared by the sol-gel method. J Appl Phys 2008;103:113709.
21. Ding R, Xu C, Gu B, Shi Z, Wang H, Ba L, et al. Effects of Mg incorporation on microstructure and optical properties of ZnO thin films prepared by sol-gel method. J Mater Sci Technol 2010;26:601–4.
22. Yousefi R, Jamali Sheini F, Muhamad MR, More MA. Characterization and field emission properties of ZnMgO nanowires fabricated by thermal evaporation process. Solid State Sci 2010;12:1088–93.
23. Spanhel L, Anderson MA. Semiconductor clusters in the sol-gel process: quantized aggregation, gelation, and crystal growth in concentrated zinc oxide colloids. J Am Chem Soc 1991;113:2826–33.
24. Meulenkamp EA. Synthesis and growth of Zno nanoparticles. J Phys Chem B 1998;102:5566–72.
25. Kohlbrecher J, Bressler I. SASfit. Paul scherrer institut, Villigen: Switzerland. 2014.
26. Sun LW, Shi HQ, Li WN, Xiao HM, Fu SY, Caoc XZ, et al. Lanthanum-doped ZnO quantum dots with greatly enhanced fluorescent quantum yield. J Mater Chem 2012;22:8221–7.
27. Crosby GA, Demas JN. Measurement of photoluminescence quantum yields. Rev J Phys Chem 1971;75:991–1024.
28. West AR. Solid state chemistry and its applications. New York: John Wiley and Sons, 1992.
29. Guinier A, Fournet G. Small angle scattering of X-rays. New York: Wiley, 1955.
30. Craievich AF. In: Handbook of sol-gel science and technology. Sakka A, Almeida R, editors. Norwell, MA: Kluwer Publishers, 2005.
31. Brinker CJ, Scherer GW. Sol-gel sciences. The physics and chemistry of sol-gel processing. San Diego: Academic Press, Inc., 1990.
32. Cuscó R, Alarcón-Lladó E, Ibáñez J, Artús L. Temperature dependence of Raman scattering in ZnO. Phys Rev B 2007;75:165202.
33. De Gelder J, De Gussem K, Vandenabeele P, Moens L. Reference database of Raman spectra of biological molecules. J Raman Spectrosc 2007;38:1133–47.
34. Tandon P, Förster G, Neubert R, Wartewig S. Phase transitions in oleic acid as studied by X-ray diffraction and FT-Raman spectroscopy. J Mol Struct 2000;524:201–15.
35. Koleva V, Stoilova D. Infrared and Raman studies of the solids in the Mg(CH3COO)2-Zn(CH3COO)2-H2O system. J Mol Struct. 2002;611:1–8.
36. Brus L. Electronic wave functions in semiconductor clusters: experiment and theory. J Phys Chem 1986;90:2555–60.
37. Yousefi R, Zak AK, Jamali-Sheini F. Growth, X-ray peak broadening studies, and optical properties of Mg-doped ZnO nanoparticles. Mater Sci Semicond Process 2013;16:771–7.
38. Schwartz DA, Norberg NS, Nguyen QP, Parker JM, Gamelin DR. Magnetic quantum dots: synthesis, spectroscopy, and magnetism of Co^{2+}- and Ni^{2+}-doped ZnO nanocrystals. J Am Chem Soc 2003;125:13205–18.
39. Norberg NS, Kittilstved KR, Amonette JE, Kukkadapu RK, Schwartz DA, Gamelin DR. Synthesis of colloidal Mn^{2+}:ZnO quantum dots and high-TC ferromagnetic nanocrystalline thin films. J Am Chem Soc 2004;126:9387–98.
40. Yang Y, Jin Y, He H, Wang Q, Tu Y, Lu H, et al. Dopant-induced shape evolution of colloidal nanocrystals: the case of zinc oxide. J Am Chem Soc 2010;132:13381–94.
41. Cohn AW, Kittilstved KR, Gamelin DR. Tuning the potentials of "Extra" electrons in colloidal n-Type ZnO nanocrystals via Mg^{2+} substitution. J Am Chem Soc 2012;134:7937–43.
42. Ghosh M, Raychaudhuri AK. Optical properties of Mg-substituted ZnO nanoparticles obtained by solution growth. Nanotech IEEE Trans Nanotechnol 2011;10:555–9.
43. Buonsanti R, Milliron DJ. Chemistry of doped colloidal nanocrystals. Chem Mater 2013;25:1305–17.
44. Layek A, De S, Thorat R, Chowdhury A. Spectrally resolved photoluminescence imaging of ZnO nanocrystals at single-particle levels. J Phys Chem Lett 2011;2:1241–7.
45. van Dijken A, Meulenkamp EA, Vanmaekelbergh D, Meijerink A. The kinetics of the radiative and non-radiative processes in nanocrystalline ZnO particles upon photoexcitation. J Phys Chem B 2000;104:1715–23.
46. Xu X, Xu C, Wang X, Lin Y, Dai J, Hu J. Control mechanism behind broad fluorescence from violet to orange in ZnO quantum dots. Cryst Eng Comm 2013;15:977–81.
47. Liu DP, Li GD, Su Y, Chen JS. Highly luminescent ZnO nanocrystals stabilized by ionic-liquid components. Angew Chem Int Ed 2006;45:7370–3.
48. Yousefi R, Kamaluddin B. Fabrication and characterization of ZnO and ZnMgO nanostructures grown using a ZnO/ZnMgO compound as the source material. Appl Surf Sci 2009;256:329–34.
49. Felbier P, Yang J, Theis J, Liptak W, Wagne A, Lorke A, et al. Highly Luminescent ZnO quantum dots made in a non-thermal plasma. Adv Funct Mater 2014;24:1988–93.

Bionotes

Eloísa Berbel Manaia
Faculty of Pharmaceutical Sciences of São Paulo State University, UNESP, Araraquara-Jaú Interstate Highway, Km 1, Araraquara, SP, Brazil
University Paris-Sud, Institut Galien, CNRS, UMR 8612, LabEX LERMIT, F-92296 Châtenay-Malabry, France

Eloísa Berbel Manaia is currently preparing her PhD thesis in co-direction between the Faculty of Pharmaceutical Sciences, São Paulo State University (Brazil) and the Faculty of Pharmacy, Institut Galien, University Paris Sud (France). The topic of her PhD thesis and her research interest focus on the development of QDs based on ZnO for application in bioimaging and also in theranostic systems using lipid nanocarriers. She is particularly interested in nanomedicine, diagnostic molecules and drug delivery systems.

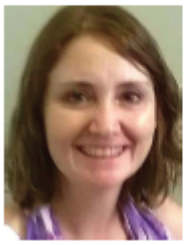

Renata Cristina Kiatkoski Kaminski
Sergipe Federal University, Campus Itabaiana, Av. Vereador Olimpio Grande, s/n, Itabaiana, SE, Brazil

Renata C.K. Kaminski received a Chemistry diploma from the University of Paraná (UFPR) in 2000. She completed her PhD degree in Chemistry at the São Paulo State University (2006) studying TiO_2-based thin films and powder. In 2008 she had a post-doctoral position at the Synchrotron SOLEIL (Saint-Aubin), where she worked as chemical engineer and researcher for 1 year. Now, she works as researcher at University of Sergipe (UFS), her research foccuses on TiO_2-based nanoparticles for photoprotection and antioxidants delivery via emulsified or liquid crystalline systems.

Bruno Leonardo Caetano
Chemistry Institute of São Paulo State University, UNESP, Prof. Francisco Degni Street, 55, Araraquara, SP, Brazil

Bruno Leonardo Caetano received a Chemistry diploma from the University of Franca (2003). He completed his PhD degree in Chemistry at the São Paulo State University (2010) studying the formation and growth of ZnO quantum dots. He completed his first post-doctoral in 2011 at the Synchrotron SOLEIL (Saint-Aubin). Now, his research for his second post-doctorate is focused on the nucleation and growth of nanoparticles, organic-inorganic hybrid materials and magnetic nanoparticles for drug delivery systems and hyperthermia.

Valérie Briois
Synchrotron SOLEIL, L'Orme des Merisiers, BP48, Saint Aubin, 91192 Gif-sur Yvette, France

Valérie Briois received a Chemical Engineering diploma from the National School of Chemistry of Paris (ENSCP) in 1988. She completed her PhD degree in Chemistry at the Université Pierre et Marie Curie-Paris VI in 1991 on the study of the genesis of oxysulfate of cerium(IV) by synchrotron radiation techniques. Then she joined the CNRS as researcher first at the Laboratoire pour l'Utilisation du Rayonnement Electromagnétique (LURE, Orsay) and then at the Synchrotron SOLEIL (Saint-Aubin) where she took the responsibility of hard X-rays beamlines dedicated to the X-ray absorption spectroscopy (XAS). She focuses her research interests on nanostructured materials prepared by soft-chemistry routes aiming to establish relationships between local range order structures determined by XAS and nanomaterials properties.

Leila Aparecida Chiavacci
Faculty of Pharmaceutical Sciences of São Paulo State University, UNESP, Araraquara-Jaú Interstate Highway, Km 1, Araraquara, SP, Brazil

Leila Aparecida Chiavacci graduated in Chemistry at São Paulo State University (UNESP) (1993), obtained her MSc in Chemistry/Physical Chemistry at UNESP (1996), and she completed her PhD in Chemistry/Physical Chemistry and in Materials Science in co-direction between UNESP and LURE, Université Paris-Sud (2001). Currently, she is a Professor at the Faculty of Pharmaceutical Sciences – UNESP – Araraquara. She has experience in the area of Chemistry and Materials, with an emphasis in Physical Chemistry and Nanomaterials, acting on the following topics: colloids, nanomaterials, controlled release of drugs, SAXS, EXAFS, and sol-gel hybrid organic-inorganic materials.

Claudie Bourgaux
University Paris-Sud, Institut Galien, CNRS, UMR 8612, LabEX LERMIT, F-92296 Châtenay-Malabry, France,
claudie.bourgaux@u-psud.fr

Claudie Bourgaux joined the CNRS as researcher in 1982, first at ESPCI (PARIS) and then at the "Laboratoire pour l'Utilisation du Rayonnement Electromagnétique" (LURE, ORSAY) as co-responsible of SAXS beamline. Currently, she works at "Institut Galien Paris-Sud". Her research interests include supramolecular assemblies of lipids and amphiphiles, either for the delivery and controlled release of drugs or for the study of interactions of drugs with model membranes.

ÉCOLE DOCTORALE
Sciences chimiques : molécules, matériaux, instrumentation et biosystèmes

Titre : Conception de Quantum dots à base d'oxyde de zinc (ZnO) pour des applications en bio-imagerie de nanosystèmes lipidiques

Mots clés : ZnO, Quantum Dots, bioimagerie et nanosystèmes lipidiques

Résumé : Les systèmes théranostiques, consistant en un dispositif unique contenant des agents de diagnostic et des principes actifs, suscitent un interêt accru car ils peuvent améliorer le traitement de maladies telles que le cancer. L'objectif de ce travail était d'insérer des Quantum Dots (QDs) à base de ZnO dans des nanoparticules lipidiques pouvant délivrer un principe actif anti-cancéreux. Nous avons étudié des QDs présentant une structure coeur-coquille ZnO/ZnS, des QDs dopés par des ions Mg, la modification de leur surface par de l'acide oléique (OA) et leur incorporation dans des nanoparticules lipidiques pour suivre l'internalisation des nanoparticules par les macrophages.

Title : Zinc oxide (ZnO) based quantum dots for bioimaging applications of lipid nanocarriers

Keywords : ZnO, Quantum Dots, bioimaing, and lipid nanocarriers

Abstract : Theranostic systems consist of a single device containing therapeutic and diagnosis agents and receive increased attention because these devices can improve the therapy of diseases such as cancer. The aim of this work was to incorporate ZnO based quantum dots (QDs) into lipid based nanocarriers allowing to encapsulate a model drug for cancer therapy. It was studied QDs presenting ZnO/ZnS core-shell structure, Mg-doped ZnO QDs, oleic acid (OA) surface modified QDs and their incorporation into lipid nanoparticles to study the internalization of the luminescent nanoparticles by macrophages.

Université Paris-Saclay
Institut Galien Paris Sud, UMR CNRS 8612
5, Rue Jean Baptiste Clément / 92296 Châtenay-Malabry, France